Formation Mechanism of Extended Defects in AlN Grown on SiC {0001} and Their Reduction by Initial Growth Control

February 2012

Hironori OKUMURA

Electronic Science and Engineering
Kyoto University

Abstract

AlN, which is a direct transition semiconductor with a wide band gap (6.0 eV), has attracted attention as a material for deep-ultraviolet (UV) light-emitting diodes (LEDs) as well as a underlying template of GaN-based high-electron-mobility transistors (HEMTs). However, existence of high-density extended defects in the AlN heteroepitaxial layers is obstructing realization of superior-performance devices. Improvement of crystalline quality of the AlN layers is a key issue.

For high-quality AlN growth, SiC is one of the most suitable substrates because of the small lattice mismatch between AlN and SiC (Δa ~0.9%). In AlN growth on SiC, there are two critical issues, i. e., polytype (2H/4H or 6H) and valency (Ⅲ-V/IV-IV) mismatch. The polytype mismatch generates planar defects, called stacking mismatch boundaries (SMBs), and the valency mismatch enhances a three-dimensional (3D) growth mode, generating a high threading dislocation density (TDD) ($\sim 10^{10}$ cm^{-2}). The author had attempt to overcome these problems by controlling SiC-surface structures and initial AlN growth, and achieved high-quality AlN growth (TDD: 4×10^{8} cm^{-2}) without SMBs.

In this thesis, high-quality heteroepitaxial growth of AlN on SiC {0001} by molecular-beam epitaxy (MBE) is presented. In addition, extended defects and optical properties of the AlN layers are characterized. The major results obtained in this study are as follows.

Due to the polytype difference, 2H-AlN layers on 4H- or 6H-SiC {0001} with 1-bilayer-high steps have SMBs. By controlling the step height of SiC to one-unit cell, the SMB can be eliminated. In Chapter 3, control of surface structures and chemical compositions of SiC {0001} is discussed. The author controls the step heights of SiC {0001} vicinal substrates by H_2-gas etching. Through optimization of gas-etching conditions and off-directions of the substrates, the 6-bilayer-high steps are obtained in the 30 % area of 2-inch 6H-SiC (0001) wafers, while the 3-bilayer-high steps are uniformly formed in the whole area of them. In a similar manner, 6H-SiC $(000\bar{1})$ with 3-bilayer-high steps and 4H-SiC {0001} with 2-bilayer-high steps are obtained. In addition, the author confirms that an *ex-situ* HF-chemical cleaning and *in-situ* Ga deposition-and-desorption process sufficiently remove residual oxygen on 4H- and 6H-SiC {0001} surfaces.

In Chapter 4, crystalline quality of AlN layers on SiC {0001} is improved especially by focusing on initial growth. First, growth conditions of Al-polar AlN on SiC (0001) with controlled step heights are optimized, realizing a layer-by-layer growth mode from 10 to 30 sec after starting AlN growth. In the AlN growth on 6H-SiC (0001) with 3- or 6-bilayer-high steps, the SMBs are not observed, but a high density of TDs (2×10^{10} cm^{-2}) in the AlN

layer, threading dislocation (TD) rows, is generated at the step edges of SiC before growth.

For further reduction of TDD in AlN layers on 6H-SiC (0001), an initial growth control is studied. To improve wettability of initial AlN growth, metallic Ga is deposited just before AlN growth. 2-monolayer (ML)-Ga pre-deposition allows early realization of the layer-by-layer growth mode (still not just after the growth) and reduces TDD in the AlN layer to 2×10^9 cm^{-2}. Next, a nitrogen-plasma stabilization process for 10 min before growth is focused on. In *in-situ* XPS measurements, the author finds that slight active-nitrogen species reach the SiC surface with a closed plasma-cell shutter during its stabilization process. An unintentional nitrogen-exposure before AlN growth is suppressed by starting growth after nitrogen-plasma ignition, achieving the layer-by-layer growth mode from the first AlN layer. The full-width at half-maximum (FWHM) values of the (0002) and $(01\bar{1}2)$ ω-scan diffraction peaks are 40 and 41 arcsec, respectively, and TDD in the AlN layers is decreased to 4×10^8 cm^{-2} (TDD on SiC terrace: 9×10^7 cm^{-2}). And, all impurity concentrations of Si, C, and O in the AlN layer are reduced to be below 1×10^{18} cm^{-3}.

N-polar AlN growth on 6H-SiC $(000\bar{1})$ with controlled step heights is also investigated. The N-polar AlN layer has multinucleation growth, resulting in a rough surface. By decreasing supersaturation, i. e., nitrogen-plasma power, the smooth surface with a step-and-terrace structure is obtained: RMS roughness is 0.6 nm. TDD is reduced to 2×10^9 cm^{-2}.

In Chapter 5, extended-defect structures, such as SMBs and TD rows generated at the step edges of SiC, are investigated by transmission electron microscopy (TEM). By the addition of a sacrificial oxidation process for SiC substrates with controlled step heights, stacking sequences of the topmost SiC surface can be modified. In the AlN layer on 6H-SiC with the modified 3-bilayer-high steps, SMBs are generated at the step edges of SiC. The SMBs consist of zigzag structures with $(\bar{2}110)$ and $(11\bar{2}0)$ planar defects. For example, the $(\bar{2}110)$ SMBs have the displacement vectors of $\mathbf{R}$=1/2$[01\bar{1}1]$. On the other hand, the TD rows consist of many U-shaped dislocation loops, i. e., TD pairs with Burgers vectors of opposite directions. These TD pairs result from dislocations along the step edges of SiC.

Critical thickness of AlN growth on SiC is investigated by x-ray diffraction (XRD), Raman scattering spectroscopy, cathodoluminescence (CL), and TEM. The critical thickness of AlN growth on SiC is estimated to be 3.5 nm by the Matthews-Blakeslee model, while all experimental results show that it is over 700 nm.

In Chapter 6, optical properties of AlN layers on 6H-SiC {0001} are characterized by CL and photoluminescence (PL) measurements. In the AlN layer coherently grown on 6H-SiC (0001), the peak energy of near-band-edge (NBE) emission is high (6.16 eV) at 300 K due to the biaxial strain, and well agrees with theoretical estimation for coherent growth. A donor bound exciton (D^0X) peak is clearly separated from a free A-exciton (FX_A) peak in the PL measurement at 8.8 K. The small FWHM values of the D^0X and FX_A lines, which are 2.7 and 7.1 meV, respectively, are obtained owing to the good crystalline quality.

In Chapter 7, a summary of the present work is given, together with the remaining issues to be solved and suggestions for future work.

Acknowledgements

First, I would like to express my deepest gratitude to Professor Tsunenobu Kimoto for his supervision, continuous guidance, and helpful advice. I would like to thank Associate Professor Jun Suda for his continuous guidance concerning experimental details, helpful suggestions, and constructive discussions throughout this work. They also gave me kind encouragement and the opportunity to conduct this research activity freely.

I would like to thank Professor Minoru Suzuki for his kind encouragement through the discussions. I acknowledge Associate Professor Mitsuru Funato for not only his helpful advice on this dissertation, but also his assistance with transmission electron microscopy (TEM), x-ray diffraction (XRD), and photoluminescence (PL).

I would like to appreciate Assistant Professor Masahiro Horita for maintenance of molecular-beam epitaxy (MBE) as well as his kind instruction of many experiment apparatuses. I am also indebted to Assistant Professor Yusuke Nishi for maintenance management of whole experiment system. I am very much obliged to Mr. Daisuke Harata, Mr. Hiroki Miyake, Mr. Mitsuaki Kaneko, Mr. Ryosuke Kikuchi, and Mr. Shunsaku Ueta for helping MBE maintenance.

I am truly indebted to collaborative research groups. I would like to appreciate Dr. Christian Kisielowski and Dr. ChengYu Song at the National Center for Electron Microscopy (NCEM) in Lawrence Berkeley National Laboratory (LBNL) and Dr. Petra Specht at University of California, Berkeley for their meaningful comments, the observation technique, sample processing methods, and the image simulation for high-resolution TEM (HRTEM) observation. They and Ms. Jane Cavlina at NCEM gave me the valuable opportunity to learn HRTEM more deeply. I also thank to Professor Yoichi Kawakami, Dr. Ryan G. Banal, Mr. Ryota Ishii, and Mr. Takao Oto at Kyoto University for helpful advices and helping PL measurements. I wish to offer my gratitude to Professor Akinori Koukitu, Associate Professor Yoshinao Kumagai, and Dr. Kazuhiro Akiyama at Tokyo University of Agriculture and Technology for collaborative study on H_2 gas-etching rate of SiC surfaces. I would like to thank Mr. Hiroyuki Kinoshita, Mr. Keiichi Ikeda, Dr. Shin Sasaki, Mr. Taro Nishiguchi, Mr. Toshihiko Hayashi, and Mr. Yoshimitsu Yoshioka from SiXON Ltd., Japan for supplying gas-etched 6H-SiC (0001) substrates.

I thank to all the members of Semiconductor Science and Engineering Laboratory for their kindness and supports: Dr. Atsushi Koizumi, Dr. Gan Feng, Dr. Giovanni Alfieri, Dr.

Hironori Yoshioka, Dr. Katsunori Danno, Dr. Masato Noborio, Dr. Robert Armitage, Mr. Daisuke Horie, Mr. Hiroki Niwa, Mr. Katsuhiko Fukunaga, Mr. Kazuki Yamaji, Mr. Kei Senga, Mr. Koichi Amari, Mr. Kouhei Adachi, Mr. Koutaro Kawahara, Mr. Muneharu Kato, Mr. Naoki Kaji, Mr. Naoki Okimoto, Mr. Naoki Watanabe, Mr. Naoya Morioka, Mr. Ryouhei Kanno, Mr. Ryota Suzuki, Mr. Seigo Mori, Mr. Sho Sasaki, Mr. Shuhei Ichikawa, Mr. Takashi Okuda, Mr. Tatsuya Iwata, Mr. Toru Hiyoshi, Mr. Yibo Zhang, Mr. Yuichiro Hayashi, and Mr. Yuichiro Nanen. I am grateful to secretaries, Ms. Yoriko Ohnaka and Ms. Mizuki Yamada for kindly supporting my daily work.

This work was supported by Grant-in-Aid for Research Fellow (21.5229) from Japan Society for the Promotion of Science (JSPS). This work was also financially supported in part by New Energy and Industrial Technology Development Organization (NEDO), Japan, Kyoto Environmental Nanotechnology Cluster, Japan, and the Global Center of Excellence Program (C09), the Ministry of Education, Culture, Sports, Science, and Technology of Japan.

Finally, I really thanks my parents, my brother, and all my friends for their understanding, continuing care, support, and heartfelt encouragement.

February, 2012
Hironori Okumura

Contents

Chapter 1

Introduction

1.1 Background

The present all-human society is based on advances in electronics and optoelectronics. In 20th century, semiconductor materials have provided the hardware backbone of the electronics and optoelectronics. Especially, developments of new semiconductor material have played an important role in evolution of our society and daily lives.

Since germanium (Ge) opened a field of solid state electronics in 1948, many kinds of semiconductor materials have been developed, and their material properties have been maximized for electronic products. In particular, silicon (Si) has provided the foundation of high-speed integrated circuits (ICs) and played a important role to build information technology (IT) society. And, group-Ⅲ arsenides (GaAs, AlAs, InAs) and group-Ⅲ phosphides (GaP, InP) have also provided superior performance as optical devices as well as high-frequency devices. GaAs-based devices, such as infrared/red laser diodes (LDs) in CD/DVD systems and metal-semiconductor field-effect transistors (MESFETs) for power amplifier, are indispensable for our daily lives. However, recently, higher-power microwave devices, and light-emitting diodes (LEDs) and LDs operating at short visible wavelength had been demanded strongly. To fulfill these demands, Si- and GaAs-based materials can not be used due to theoretical limits originating from their material properties, and development of new semiconductor materials is required. Then, wide bandgap semiconductors, especially gallium nitride (GaN), have attracted much attention.

GaN, which has bandgap of 3.4 eV, is a promising material for high-frequency and high-power devices due to the excellent property. In addition, not only GaN but also other group–Ⅲ nitrides (Ⅲ–Ns) (aluminum nitride (AlN) and indium nitride (InN)) are the most promising materials for the optical devices operating at wavelength of visible range. Last two decades, there have been extensive research and development of GaN-based LEDs and LDs.

1.2 Properties of Group-Ⅲ Nitrides

The physical properties and material parameters of GaN and AlN are listed in Table 1.1 and Table 1.2, respectively. Ⅲ–Ns are Ⅲ-V compound semiconductors composed of tetrahedrally bonded cation and anion atoms in a closed-packed structure. These alloys crystallize in a wurtzite structure as a thermodynamically stable structure [1]. The Ⅲ–Ns have attracted much attention as the candidates for LEDs [1] [2], because these compounds are direct-transition-type semiconductors [2] [3]. The Ⅲ–Ns can cover continuously from 0.7 eV (bandgap of wurtzite InN) to 6.0 eV (bandgap of wurtzite AlN) by appropriate alloying, as shown in Fig. 1.1.

Applications of the Ⅲ–Ns are not limited to LED and LDs. In comparison with other semiconductor materials, GaN has high breakdown field, high thermal stability, and high electron saturation velocity (Table 1.1). From these excellent properties, GaN is also used as electronic devices. Using GaN and its alloys with AlN and InN, we can utilize heterojunctions, i. e., bandgap engineering, expanding the design of device structures, such as high-electron-mobility transistor (HEMT) and heterojunction bipolar transistor (HBT). In particular, GaN-based HEMTs have attracted attention as high-power and high-frequency devices.

1.3 Current Status of Group-Ⅲ Nitride Devices

In the Ⅲ–N devices, recently, AlGaN-based deep-ultraviolet (UV) LEDs and GaN-based HEMTs have attracted much attention. In this section, current status of these devices is described.

1.3.1 AlGaN-based deep-UV LEDs

Recnetly, high-Al-content AlGaN deep-UV LED operating at the shorter wavelength (400–220 nm) attracts much attention for high-density optical data storage, sterilization, chemical analysis, and illumination lamps. Taniyasu *et al.* demonstrated AlN deep-UV LEDs operating at 210 nm (i. e., the shortest wavelength among Ⅲ–Ns) under current injection [4]. However, devices based on the AlGaN active layers have much lower efficiency than the InGaN-based devices; for instance, the external quantum efficiency (EQE) of LEDs operating at 285–240 nm is limited to 1% and that of the AlN LED is 10^{-6}% [4–10]. One of the factors is the high density of threading dislocations (TDs) originated from the heteroepitaxial growth of AlN or AlGaN. The AlN or AlGaN growth with a smooth surface and low defect density is a requisite to realize high-efficiency devices.

[1] Excitons are capable of stable existence in GaN due to the large binding energy of 28 meV than the thermal energy of room temperature (RT).

[2] Zinc-blende AlN is theoretically expected to have an indirect bandgap. The indirect bandgap of zinc-blende AlN changes to direct structure with tensile strain.

Table 1.1: Physical properties of GaN, AlN, SiC and most common other semiconductor materials.

Properties	GaN	AlN	SiC			Si	GaAs
			4H	6H	3C		
Crystal structure	WZ	WZ	4H	6H	ZB	Dia.	ZB
Lattice constant [Å]	3.189^a 5.186^c	3.112^a 4.982^c	3.081^a 10.05^c	3.081^a 15.12^c	4.36	5.43	5.65
Band structure	D.	D.	I.D.	I.D.	I.D.	I.D.	D.
Bandgap [eV]	3.42	6.05	3.26	3.02	2.3	1.12	1.42
Electron mobility [cm^2/Vs]	900	400	$1000^{\perp c}$ $1200^{/\!/c}$	$450^{\perp c}$ $100^{/\!/c}$	1000	1500	8500
Hole mobility [cm^2/Vs]	20	14	100	50	50	450	400
Electron saturation velocity [10^7 cm/s]	2.7	1.9	2.2	1.9	2.7	1	1
Breakdown field [MV/cm]	3.3	1.5	3	3	2	0.3	0.4
Thermal conductivity [W/cmK]	1.3	2.9	4.9	4.9	4.9	1.5	0.46
Relative dielectric constant	$9.5^{\perp c}$ $10.4^{/\!/c}$	8.5*	$9.7^{\perp c}$ $10.2^{/\!/c}$	$9.7^{\perp c}$ $10.2^{/\!/c}$	10	11.9	12.8
Conductivity control	△	△	◯	◯	△	◯	◯
Thermal oxide	×	×	◯	◯	◯	◯	×
Conductive wafer	△ (SiC)	△ (SiC)	◯	◯	△ (Si)	◯	◯
Insulating wafer	△ (Sap.)	△ (Sap.)	◯	◯	×	△ (SOI)	△

WZ: Wurtzite ZB: Zincblende Dia.: Diamond
D.: Direct I.D.: Indirect
◯: Excellent △: Fair ×: Difficult
Sap.: Sapphire SOI: Silicon on insulator
*Data of anisotropy reported are uncertain.

Table 1.2: Typical material parameters for GaN, AlN, and SiC.

Properties	GaN	AlN	6H-SiC
Elastic stiffness [GPa]			
C_{11}	390 [13]	396 [13]	501
C_{12}	145 [13]	137 [13]	111
C_{13}	106 [13]	108 [13]	52
C_{33}	398 [13]	373 [13]	553
C_{44}	105 [13]	116 [13]	163
Deformation potential [eV]			
$a - D_1$	-4.9 [13]	-6.9 [14]	
$a - D_2$	-11.3 [13]	-15.2 [14]	
D_3	8.2 [13]	8.3 [14]	
D_4	-4.1 [13]	-4.15 [14]	
Phonon deformation potential [cm^{-1}]			
a_λ for E_2^h	-740 [15]	-877 [15]	
b_λ for E_2^h	-727 [15]	-911 [15]	
Poisson ratio ν	0.20	0.20	0.085
Young' modulus $E(0001)$ [GPa]	360	330	540
Biaxial modulus $Y(0001)$ [GPa]	480	470	600

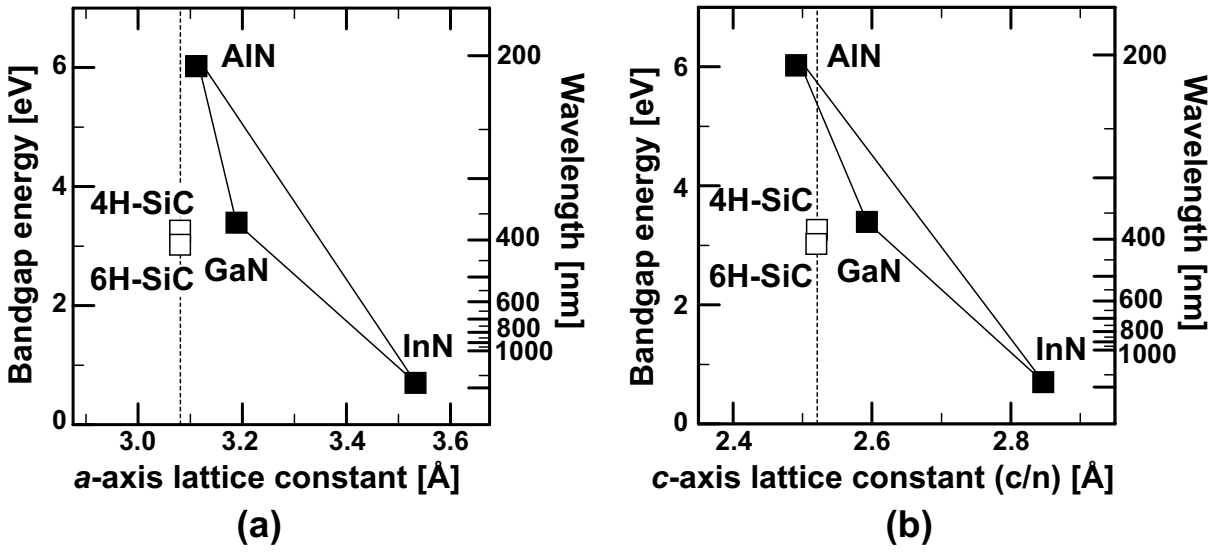

Figure 1.1: Relationships between bandgap and (a) *a*-axis / (b) *c*-axis lattice constant for hexagonal Ⅲ–Ns and SiC. Dashed lines show lattice constants of 4H-SiC.

1.3.2 GaN-based HEMTs

Properties of GaN-based HEMTs

As applications in Ⅲ–Ns high-power and high-frequency electronic devices, AlGaN/GaN HEMTs attract much attention. In the HEMTs, a strong built-in electrostatic field can exist in the ⟨0001⟩ direction because the noncentrosymmetric nature of the wurzite structure generates spontaneous and piezoelectric polarization [11, 12]. These internal fields form two-dimensional electron gas (2DEG) near an AlGaN/GaN heterointerface, as shown in Fig. 1.2. This electron channel layer near the heterointerface permits a short gate length, improving the high-frequency property in a microwave band. The 2DEG density in AlGaN/GaN is one order of magnitude higher than that in AlGaAs/GaAs, achieving high-current handling capability. A electron mobility of the 2DEG is higher than that of bulk because of no ionized-impurity scattering, realizing the high-speed performance. As listed in Table 1.1, GaN shows approximately one order higher-breakdown field than that of GaAs. High-voltage operation enables the highly-efficient performance. Consequently, GaN-based HEMTs are the most promising for future applications in high-power and high-frequency electronics.

Current status of GaN-based HEMTs

Most of the AlGaN/GaN HEMTs have been fabricated on (0001) or Ga-polar orientation, which is superior in terms of crystalline quality. The Ga-polar AlGaN/GaN HEMTs have already achieved high performance. Recently, research on $(000\bar{1})$ or nitrogen-polar (N-polar) orientation also attracts much interest due to its strong electron confinement and low contact resistance (Fig. 1.2 (b)) [16–20]. However, both Ga-polar and N-polar AlGaN/GaN HEMTs have too low reliability to be in practical use. One of the factors is a high density of TDs in the GaN films, 10^8–10^9 cm^{-2} [21–23]. High-quality GaN growth is a key issue to realize high reliability in the AlGaN/GaN HEMTs.

Substrates for GaN-based HEMTs

For high-quality GaN films, using GaN substrate, i. e., homoepitaxial growth, is the most suitable. Although bulk GaN and AlN is available now, high-quality and large-area wafers are unachieved at a reasonable cost. Heteroepitaxial growth of GaN on foreign substrates is inevitable. Among foreign substrates, sapphire (Al_2O_3) and Si are candidates for GaN growth, because large-area Al_2O_3 and Si wafers are commercially available at a low cost. However, GaN films on Al_2O_3 and Si are highly defective due to the large lattice mismatches more than 14%. Additionally, Al_2O_3 and Si substrates have a problem with a heat dissipation of the high-power devices owing to the low thermal conductivity. Then, silicon carbide (SiC) has been studied as a suitable substrate for GaN-based high-power devices owing to its excellent thermal conductivity as well as its close lattice constant ($\Delta a \sim 3.5\%$). Recently, 4-inch SiC wafers are available at a reasonable cost.

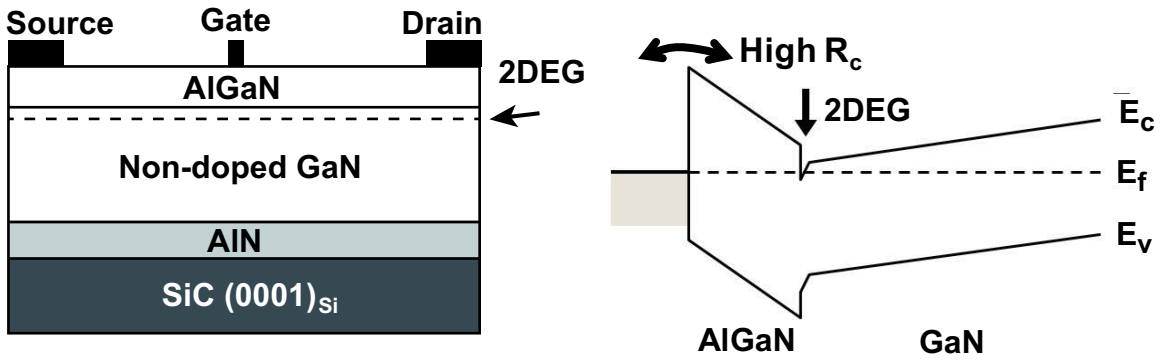

(a) Ga-polar GaN HEMT

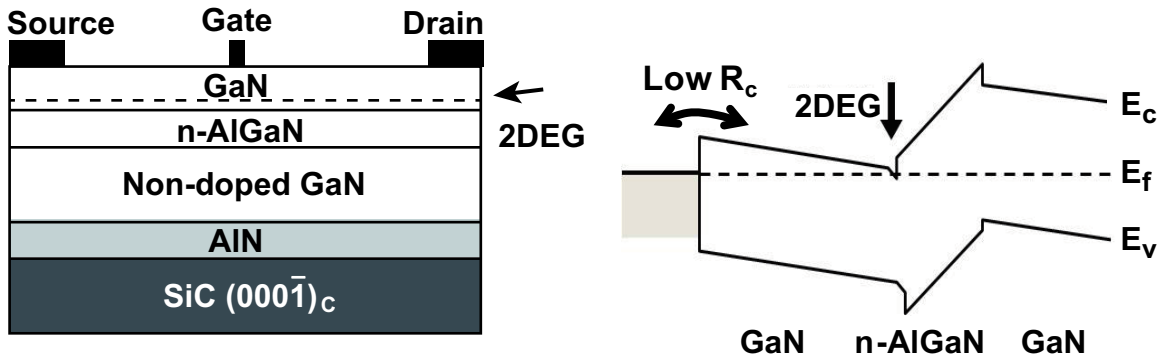

(b) N-polar GaN HEMT

Figure 1.2: Basic device structures and band diagrams of (a) Ga-polar and (b) N-polar GaN HEMTs.

SiC is a IV-IV compound semiconductor with Si and carbon (C) atoms with the ratio of unity and has more than 200 kinds of polytypes: the difference in stacking sequences along a hexagonal ⟨0001⟩ direction brings various crystal forms. Considering the Si-C pair as a sphere, there are three possible occupation sites denoted by A, B, and C (Fig. 1.3). In their polytypes, now, bulk SiC with 4H (ABCB) and 6H (ABCACB) structures [3] are commercially available (Fig. 1.4). The 4H- and 6H-SiC have high crystalline quality (threading dislocation density (TDD) less than 10^4 cm^{-2}) and conductivity control, such as n-type, p-type, and semi-insulating (SI). The SI substrate with high resistivity is effective to reduce a leak current and parasitic capacitance in high-power and high-frequency devices.

Above all, {0001} faces can have strong polarization-induced fields parallel to the ⟨0001⟩ direction in the strained layers and have an advantage in 2DEG of HEMTs. In GaN growth on SiC, the GaN films have the same crystal faces as the SiC substrate: i. e., GaN films on SiC (0001) and (000$\bar{1}$) have Ga polarity and N polarity, respectively [24–27]. Therefore, 4H- and 6H-SiC {0001} SI substrates are suitable for the GaN-based HEMTs.

GaN growth on SiC (0001)

For GaN growth on SiC, an AlN buffer layer is usually used because of the small lattice mismatch between AlN and SiC ($\Delta a \sim 0.9\%$). Although a nucleation layer (NL) of AlN can enhance an annihilation of TDs in the GaN films, the TDD in the GaN films have not be reduced to less than 10^8 cm^{-2} because the annihilation is limited to TDs close to each other. Then, the author has proposed a high-quality AlN template as an underlying layer of the GaN growth. The AlN templates with TDD under than 10^8 cm^{-2} would allow the GaN films to have higher crystalline quality. In this thesis, high-quality AlN growth on SiC {0001} substrates is presented.

1.4 Heteroepitaxial Growth of AlN

1.4.1 Current status of AlN growth

MOCVD growth

High-quality heteroepitaxial growth of Ⅲ–Ns has been accomplished via metal-organic chemical vapor deposition (MOCVD) techniques. AlN films are also generally grown by MOCVD, but have a high TDD of $\sim 10^{10}$ cm^{-2}.

The most popular technique to reduce the TDD is epitaxial lateral overgrowth (ELO), which can annihilate or trap the TDs in a plane normal to the surface direction of the

[3] H for hexagonal, C for cubic, and R for rhombohedral. Wurtzite and zinc-blende structures are referred to as 2H and 3C structures, respectively.

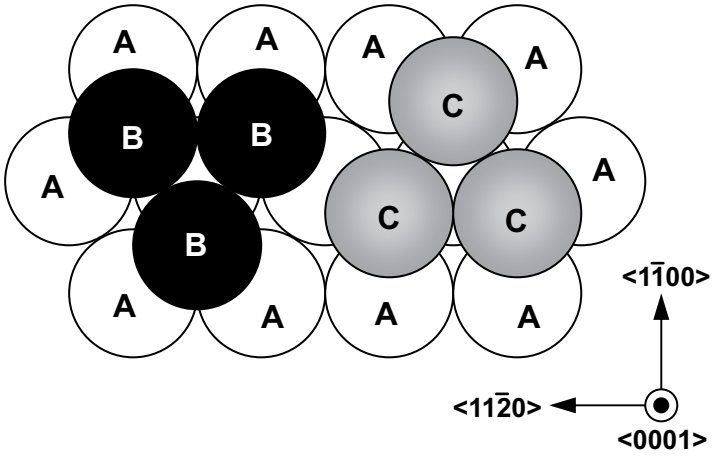

Figure 1.3: Hexagonal closed packing of Si–C or III–N pairs.

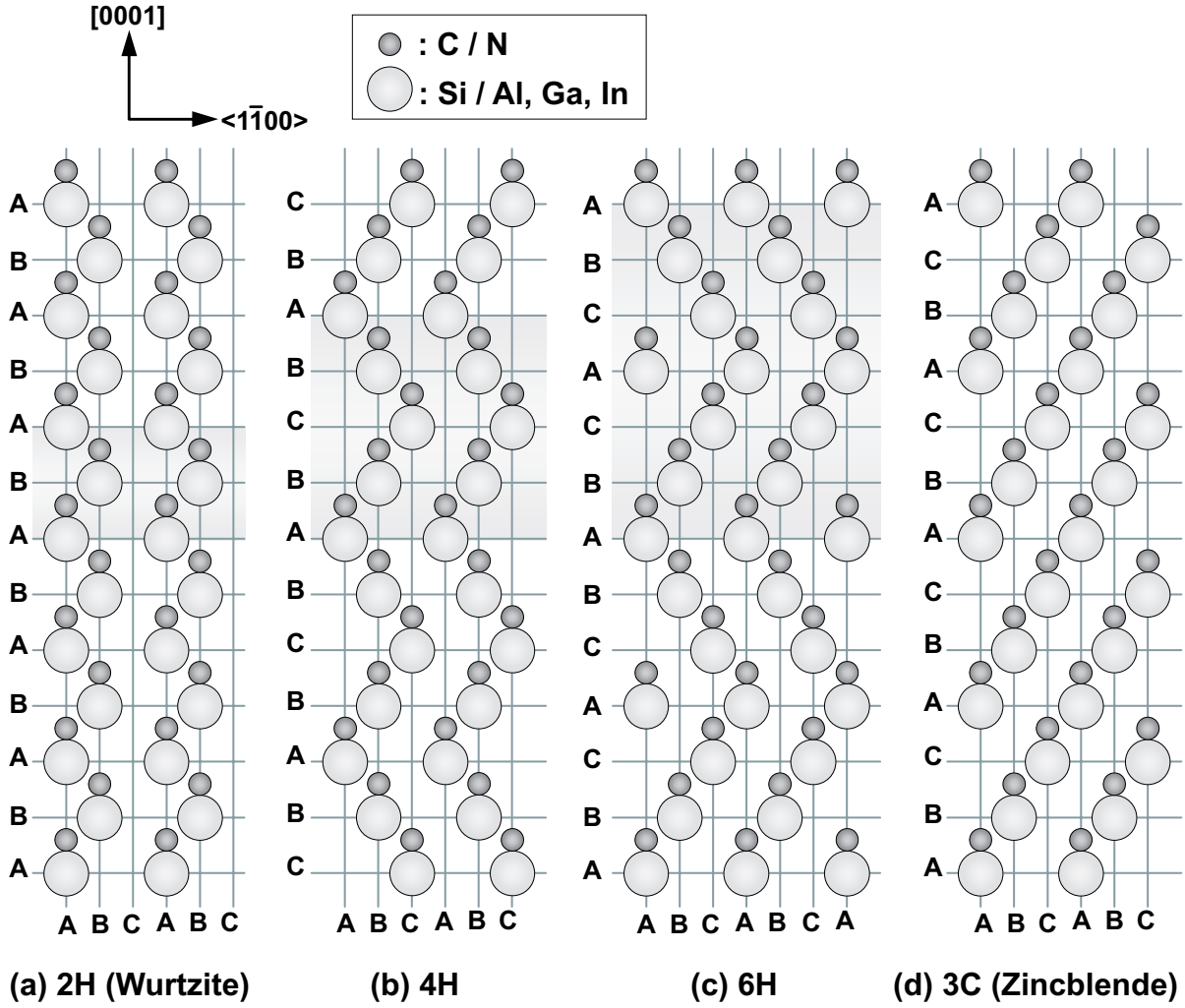

Figure 1.4: Stacking orders along [0001] (*c*-axis) for (a) 2H-, (b) 4H-, (c) 6H- and (d) 3C-structures of SiC or III–Ns.

substrate. However, remarkable reduction of the TDD by ELO is unexpectable because the dislocation bending is difficult in the AlN films . Taniyasu *et al.* reported that three-dimensional (3D) growth mode at an initial growth stage generated a high TDD, but the propagation direction of the dislocations could change horizontally due to larger-nuclei coalescence in thick growth, resulting in annihilation of the TDs [28]. Imura *et al.* reported that the annihilation of TDs was enhanced by generating the larger-nuclei coalescence at high growth temperature above 1300°C, achieving TDD of $10^8 - 10^9$ cm^{-2} [29, 30]. However, the TDD in the AlN layers has not be reduced to less than 10^8 cm^{-2} because of the limitation of the annihilation of TDs. To reduce further TDD, the two-dimensional (2D) growth mode from an initial growth stage is thought to be effective. Banal *et al.* enhanced Al adatom migration and the 2D growth mode by using a modified migration enhanced epitaxy (MEE), which is characterized by a combination of simultaneous source supply and conventional MEE, realized high-quality AlN growth on Al_2O_3 substrates [31]; FWHM values of (0002) and $(01\bar{1}2)$ ω-scan diffraction peaks were 38 and 250 arcsec, respectively.

In most of the AlN growth by MOCVD, Al_2O_3 substrates have been used. The author expects that AlN growth on SiC (0001) substrates can enhance further the 2D-growth mode due to the small lattice mismatch, improving the crystalline quality of the AlN layer.

MBE growth

Molecular-beam epitaxy (MBE) has an advantage of the 2D-growth mode at an initial growth stage because of a growth control at an atomic level and *in-situ* observation of the growth mode. In the previous study from our group, AlN growth on SiC (0001) by plasma-assisted MBE (PAMBE) achieved the layer-by-layer growth mode by optimization of the growth condition and control of the SiC-surface structure [32]. The full-width at half-maximum (FWHM) values of the (0002) and $(01\bar{1}4)$ ω-scan diffraction peaks were 75 and 518 arcsec, respectively. The author considers that there is still room to improve the AlN-film quality, because no reflection high-energy electron diffraction (RHEED) intensity oscillation was observed at a very initial growth stage, indicating a 3D growth mode occurred just after starting AlN growth. In this thesis, the author tries to improve the crystalline quality of AlN growth by focusing on the AlN/SiC interface.

1.4.2 Issues of AlN growth on SiC

AlN growth on SiC has three kinds of mismatch; (a) polytype, (b) valency, and (c) lattice mismatches. These are factors generating extended defects. For the high-quality heteroepitaxial growth of AlN, these systems must be overcome.

(a) Polytype mismatch

AlN has a wurtzite (2H) structure (*AB*AB...), but the available SiC wafers have a 6H (*ABCACB*ABCACB...) or 4H (*ABCB*ABCB...) structure. The AlN layer follows stacking sequences of the topmost two bilayers of the SiC surface [33], i. e., if the 6H-SiC surface termination is AB<u></u>CACBA..., 2H-AlN layers have the stacking sequence ...AB<u></u>AB. In general, SiC substrates before growth are treated by chemical mechanical polishing (CMP), forming 1-bilayer-high steps. The surface termination of SiC with 1-bilayer-high steps changes on every adjacent terrace because 6H-SiC have six-type terminations (Fig. 1.5). AlN layers on the SiC substrates have different stacking sequences on each terrace of the SiC surfaces and generate planar defects threading the AlN layers, called stacking mismatch boundaries (SMBs) or prismatic stacking faults (PSFs) [34, 35]. The schematic figure of stacking sequences in 2H-AlN growth on 6H-SiC with 3-bilayer-high steps is shown in Fig. 1.6. SMBs are $\{11\bar{2}0\}$ planar defects generated at step edges of the SiC surface.

Step height of the 6H-SiC surface can be controlled to be 6 bilayer (full-unit-cell height) or 3 bilayer (half-unit-cell height) by high-temperature H_2-gas etching via micro-step-bunching mechanism [36]. 2H-AlN on 6H-SiC substrates with 1- and 3-bilayer-high steps forms SMBs, while we can expect that the AlN layer on 6H-SiC with 6-bilayer-high steps grows without SMBs due to the identical stacking sequences on adjacent terraces. In this thesis, the author attempts to control step heights of the SiC surface with high uniformity and realizes AlN growth without SMBs.

(b) Valency mismatch

AlN is a Ⅲ-V compound semiconductor, but SiC is a IV-IV compound semiconductor. The most favorite atomic arrangements at an abrupt interface between AlN and SiC {0001} are intermixed configurations of Si-N or Al-C bonds [37]. AlN growth on SiC {0001} with this heterovalent system has much interface energy of the epilayer/substrate, resulting in a 3D growth mode, i. e., generation of numerous defects.

For high-quality AlN growth, a 2D growth mode, especially a layer-by-layer growth mode, from the first layer is required. to reduce the TDD, the author tries to control initial growth of AlN.

(c) Lattice mismatch

There is a lattice mismatch between AlN and SiC ($\Delta a \sim 0.9\%$, $\Delta c \sim 1.0\%$) (Fig. 1.1). The critical thickness of AlN growth on SiC is estimated to be 3.5 nm by Matthews-Blakeslee model [38]. In the growth over the critical thickness, a high density of misfit dislocations, which can convert into TDs, are generated owing to the lattice relaxation.

To suppress the generation of the misfit dislocations, the author attempts to increase the critical thickness of AlN growth on SiC by controlling growth conditions, such as the growth temperature, TDD, and growth mode.

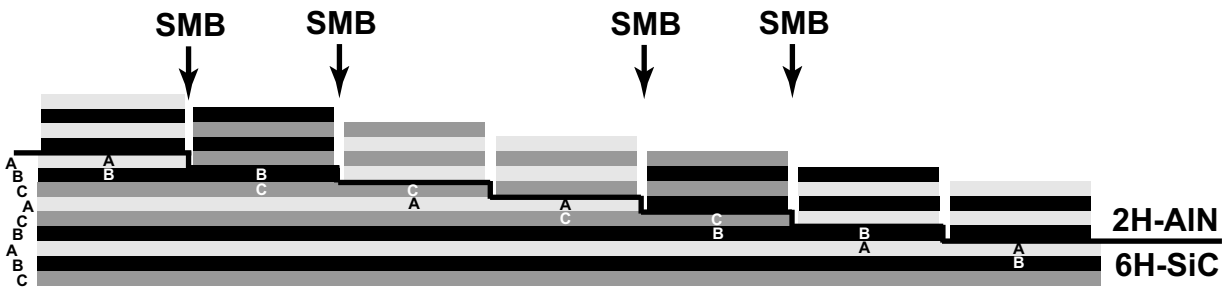

Figure 1.5: Schematic figure of stacking sequences in topmost two layers of 6H-SiC (0001) substrate with 1-bilayer-high steps.

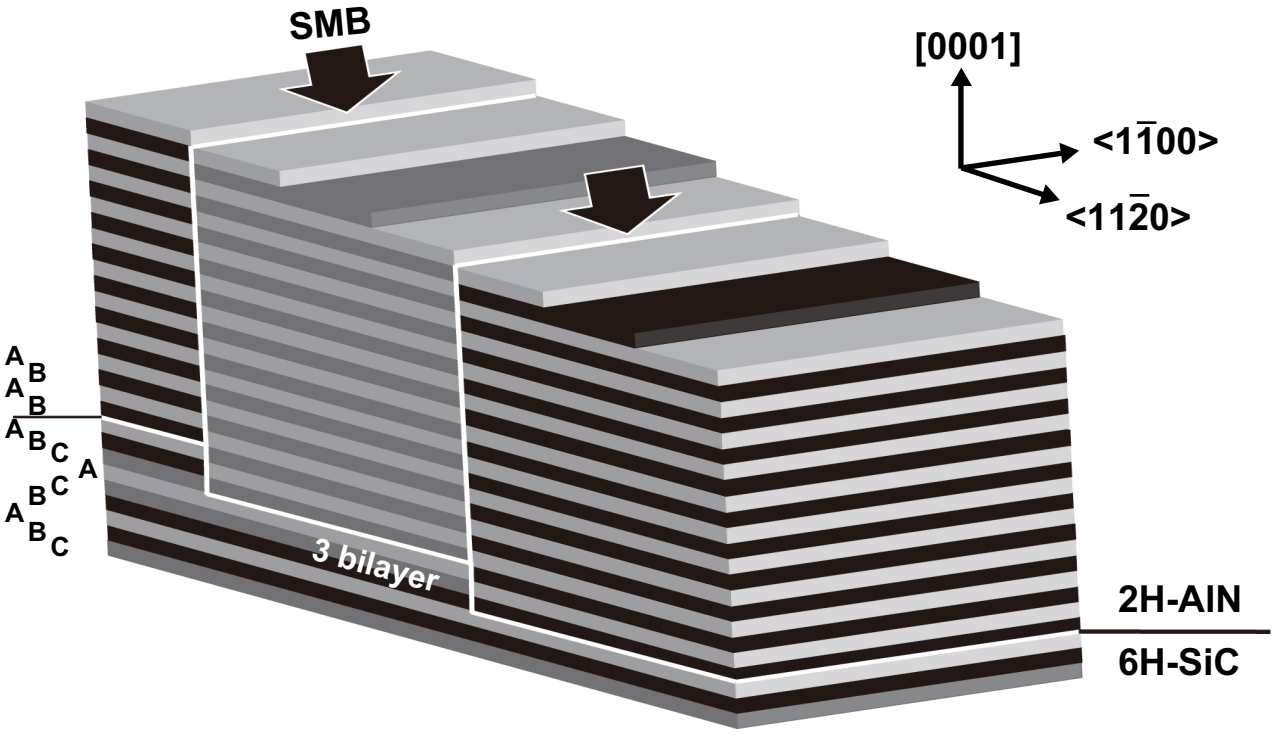

Figure 1.6: Schematic figure of stacking sequences in 2H-AlN grown on 6H-SiC (0001) substrate with 3-bilayer-high steps.

1.5 Outline of Thesis

In this thesis, high-quality heteroepitaxial growth of AlN on SiC {0001} by MBE is studied. Extended defect and optical properties of the AlN layers are characterized. The contents of this thesis are as follows.

In Chapter 2, MBE system and characterization methods are described. Typical AlN growth and pretreatment procedures for SiC substrates are also explained.

In Chapter 3, controls of surface status of SiC {0001} vicinal substrates are described. Step heights of 4H- and 6H-SiC {0001} are controlled to half- or one-unit-cell-high steps by micro-step-bunching phenomena in H_2-gas etching. Off directions as well as gas etching conditions are optimized to obtain the step heights with high uniformity at a large area. In addition, removal of residual oxygen on SiC {0001} surfaces by using *ex-situ* HF-chemical and *in-situ* Ga deposition-and-desorption process is presented.

In Chapter 4, realization of high-quality AlN growth by three methods (i)-(iii) is described: (i) step height control of SiC, (ii) group-III metal deposition just before growth, and (iii) avoidance of unintentional active-nitrogen exposure before growth. For (i), growth conditions of AlN layers on 4H- and 6H-SiC $(0001)_{\mathrm{Si}}$ with controlled step heights are optimized. And, an impact of the step heights (1, 3, or 6 bilayers) of 6H-SiC (0001) surfaces on the AlN layers is explained. For (ii), to reduce the AlN/SiC interface energy, deposition of metal Al or Ga just before AlN growth is proposed. Effects of deposited Al or Ga on the AlN layers are investigated. For (iii), the impact of an unintentional active-nitrogen exposure just before AlN growth is discussed. The chemical status of the SiC surfaces during a nitrogen-plasma stabilization process before growth is investigated, and an optimum growth process is proposed. Using these methods (i)-(iii), the layer-by-layer growth mode from the first layer and reduction of a TDD are successfully realized. In addition, N-polar AlN grown on 6H-SiC $(000\bar{1})_{\mathrm{C}}$ is presented. Impurity concentrations in AlN layers with various growth conditions, such as different crystalline quality, growth temperature, and polarity, are also studied.

In Chapter 5, extended-defect structures, such as SMBs and TDs, in the AlN layers on 6H-SiC (0001) are described. The author tries to clarify generation mechanism of the SMBs and TDs by transmission electron microscopy (TEM). Additionally, critical thickness and misfit dislocations in AlN growth on 6H-SiC (0001) are presented.

In Chapter 6, optical properties of the AlN layers are described by low-temperature cathodoluminescence (CL) and photoluminescence (PL) measurements.

In Chapter 7, a summary of this study and suggestions for future work are presented.

References

[1] H. Okumura, K. Ohta, G. Feuilet, K. Balakrishnan, S. Chichibu, H. Hamaguchi, P. Hacke, and S. Yoshida, J. Cryst. Growth **178**, 113 (1997).

[2] B. Monemar, Phys. Rev. B **10**, 676 (1974).

[3] F. A. Ponce and D. P. Bour, Nature **386**, 351 (1997).

[4] Y. Taniyasu, M. Kasu, and T. Makimoto, Nature **441**, 325 (2006).

[5] Y. Kida, T. Shibata, H. Naoki, H. Miyake, K. Hiramatsu, and M. Tanaka, phys. stat. sol. (a) **194**, 498 (2002).

[6] T. Takano, Y. Narita, A. Horiuchi, and H. Kawanishi, Appl. Phys. Lett. **84**, 3567 (2004).

[7] S. Heilman, S. Keller, S. Newman, Y. Wu, C. Moe, B. Moran, M. Schmidt, U. K. Mishra, J. S. Speck, and S. P. DenBaars, Jpn. J. Appl. Phys. **44**, L405 (2005).

[8] H. Hirayama, N. Noguchi, T. Yatabe, and N. Kamata, Appl. Phys. Exp. **1**, 051101 (2008).

[9] H. Harumasa, Y. Yamashita, M. Kuwabara, and H. Khan, Nature Photonics **2**, 551 (2008).

[10] T. Oto, R. G. Banal, K. Kataoka, M. Funato, and Y. Kawakami, Nature Photonics **4**, 767 (2010).

[11] O. Ambacher, J. Smart, J. R. Shealy, N. G. Weimann, K. Chu, M. Murphy, W. J. Schaff, L. F. Eastman, R. Dimitrov, L. Wittmer, M. Stutzmann, W. Rieger, and J. Hilsenbecm, J. Appl. Phys. **85**, 3222 (1999).

[12] O. Ambacher, B. Foutz, J. Smart, J. R. Shealy, N. G. Weimann, K. Chu, M. Murphy, A. J. Sierakowski, W. J. Schaff, L. F. Eastman, R. Dimitrov, A. Mitchell, and M. Stutzmann, J. Appl. Phys. **87**, 334 (2000).

[13] I. Vurgaftman and J. R. Meyer, J. Appl. Phys. **94**, 3675 (2003).

[14] G. Rossbach, M. Feneberg, M. Roppischer, C. Werner, N. Esser, C. Cobet, T. Meisch, K. Thonke, A. Dadgar, J. Blasing, A. Krost, and R. Goldhahn, Phys. Rev. B **83**, 195202 (2011).

[15] J. M. Wagner and F. Bechstedt, Appl. Phys. Lett. **77**, 346 (2000).

[16] S. Rajan, M. Wong, Y. Fu, F. Wu, J. S. Speck, and U. K. Mishra, Jpn. J. Appl. Phys. **49**, L1478 (2005).

[17] T. Kikkawa, Jpn. J. Appl. Phys. **44**, 4896 (2005).

[18] M. H. Wong, Y. Pei, T. Palacios, L. Shen, A. Chakraborty, L. S. McCarthy, S. Keller, S. P. DenBaars, J. S. Speck, and U. K. Mishra, Appl. Phys. Lett. **91**, 232103 (2007).

[19] S. Rajan, A. Chini, M. H. Wong, J. S. Speck, and U. K. Mishra, J. Appl. Phys. **102**, 044501 (2007).

[20] M. H. Wong, Y. Pei, J. S. Speck, and U. K. Mishra, Appl. Phys. Lett. **94**, 182103 (2009).

[21] K. Furuta, N. Nakamura, X. Q. Shen, M. Shimizu, T. Kitamura, K. Nakamura, and H. Okumura, J. Cryst. Growth **301**, 437 (2007).

[22] G. Meneghesso, F. Rampazzo, and M. Meneghini, IEEE Trans. Device Mater. Reliab. **8**, 332 (2008).

[23] N. Baron, Y. Cordier, S. Chenot, P. Vennrgues, O. Tottereau, M. Leroux, F. Semond, and J. Massies, J. Appl. Phys. **105**, 033701 (2009).

[24] S. P. Guan, A. L. Cai, J. S. Cabalu, H. L. Porter, and S. Huang, Appl. Phys. Lett. **77**, 2491 (2000).

[25] E. Monroy, E. Sarigiannidou, F. Fossard, N. Gogneau, E. Bellt-Amalric, J. L. Rouviere, S Monnoye, H. Mank, and B. Daudin, Appl. Phys. Lett. **84**, 3684 (2004).

[26] S. Keller, N. Fichtenbaum, F. Wu, G. Lee, S. P. DenBaars, J. S. Speck, and U. K. Mishra, Jpn. J. Appl. Phys. **45**, L322 (2006).

[27] D. F. Brown, S. Keller, F. Wu, J. S. Speck, S. P. DenBaars, and U. K. Mishra, J. Appl. Phys. **104**, 024301 (2008).

[28] Y. Taniyasu, M. Kasu, and T. Makimoto, J. Cryst. Growth **298**, 310 (2007).

[29] M. Imura, K. Nakano, N. Fujimoto, N. Okada, K. Balakrishnan, M. Iwaya, S. Kamiyama, H. Amano, I. Akasaki, T. Noro, T. Takagi, and A. Bandoh, Jpn. J. Appl. Phys. **46**, 1458 (2007).

[30] M. Imura, H. Sugimura, N. Okada, M. Iwaya, S. Kamiyama, H. Amano, I. Akasaki, and A. Bandoh, J. Cryst. Growth **310**, 2308 (2008).

[31] R. G. Banal, M. Funato, and Y. Kawakami, Appl. Phys. Lett. **92**, 241905 (2008).

[32] N. Onojima, J. Suda, and H. Matsunami, Jpn. J. Appl. Phys. **42**, L445 (2003).

[33] P. Ruterana and G. Nouet, phys. stat. sol. (b) **227**, 177 (2001).

[34] S. Tanaka, R. S. Kern, and R. F. Davis, Appl. Phys. Lett. **66**, 37 (1994).

[35] S. Yamada, J. Kato, S. Tanaka, I. Suemune, A. Avramescu, Y. Aoyagi, N. Teraguchi, and A. Suzuki, Appl. Phys. Lett. **78**, 3612 (2001).

[36] A. A. Burk and L. B. Rowland, J. Cryst. Growth **167**, 586 (1996).

[37] F. A. Ponce, C. G. Walle, and J. E. Northrup, Phys. Rev. B **53**, 7473 (1996).

[38] J. W. Matthews and A. E. Blakeslee, J. Cryst. Growth **27**, 118 (1974).

Chapter 2

Experimental Details of Crystal Growth

2.1 Introduction

AlN was grown by molecular-beam epitaxy (MBE). In an MBE system, *in-situ* analyses of growth kinetics and real-time monitoring of surface structures are possible owing to incorporated characterization tools in ultra-high vacuum (UHV) [1–3]. A growth mode at an initial growth stage also can be investigated in detail because the MBE system has an advantage of growth controls at an atomic level. In this chapter, the MBE system used in this study is described.

For high-quality AlN growth, surface conditions of a SiC substrate are important. Step heights of the SiC surface affect defect structures in the AlN layer [4, 5]. We controlled step heights of SiC {0001} by high-temperature H_2-gas etching in a hot-wall chemical vapor deposition (CVD). In addition, chemical conditions of the SiC substrates affect growth kinetics at the initial growth stage [6]. As pretreatment, a chemical wet cleaning and Ga deposition-and-desorption processes were carried out to remove residual oxygen adsorbed on the SiC surface. The characterization methods of the AlN layer as well as the pretreatments of the SiC surface are explained.

2.2 Molecular-Beam Epitaxy System

2.2.1 Vacuum systems

An MBE-growth system (EV-1000S, Eiko), as shown schematically in Fig. 2.1, was used for the epitaxial growth of AlN. The system consists of a sample-exchange chamber, a sample-transfer chamber, and a growth chamber. Because the sample-transfer chamber and sample-exchange chamber are separated by gate valves, no air can come directly into the growth chamber in loading and unloading samples. A schematic diagram of the pumping system for these chambers is presented in Fig. 2.1 (a).

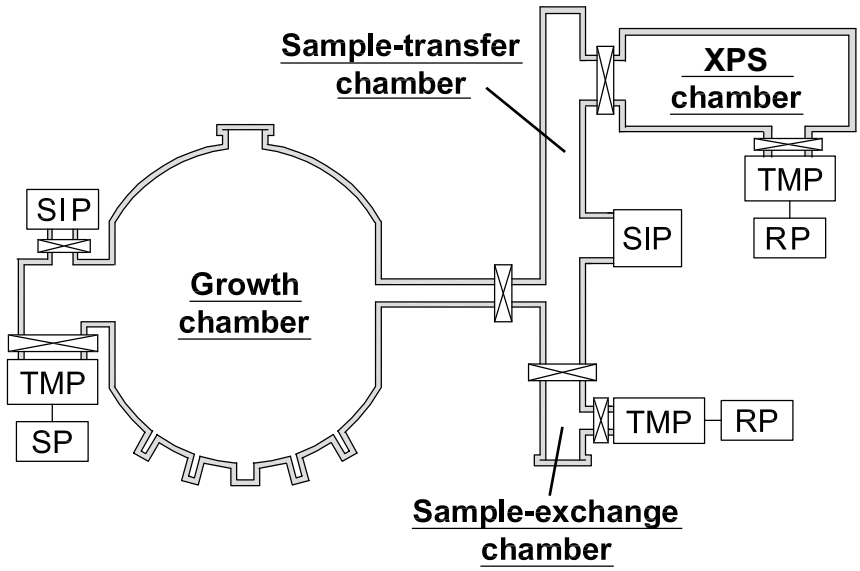

(a) Vacuum system

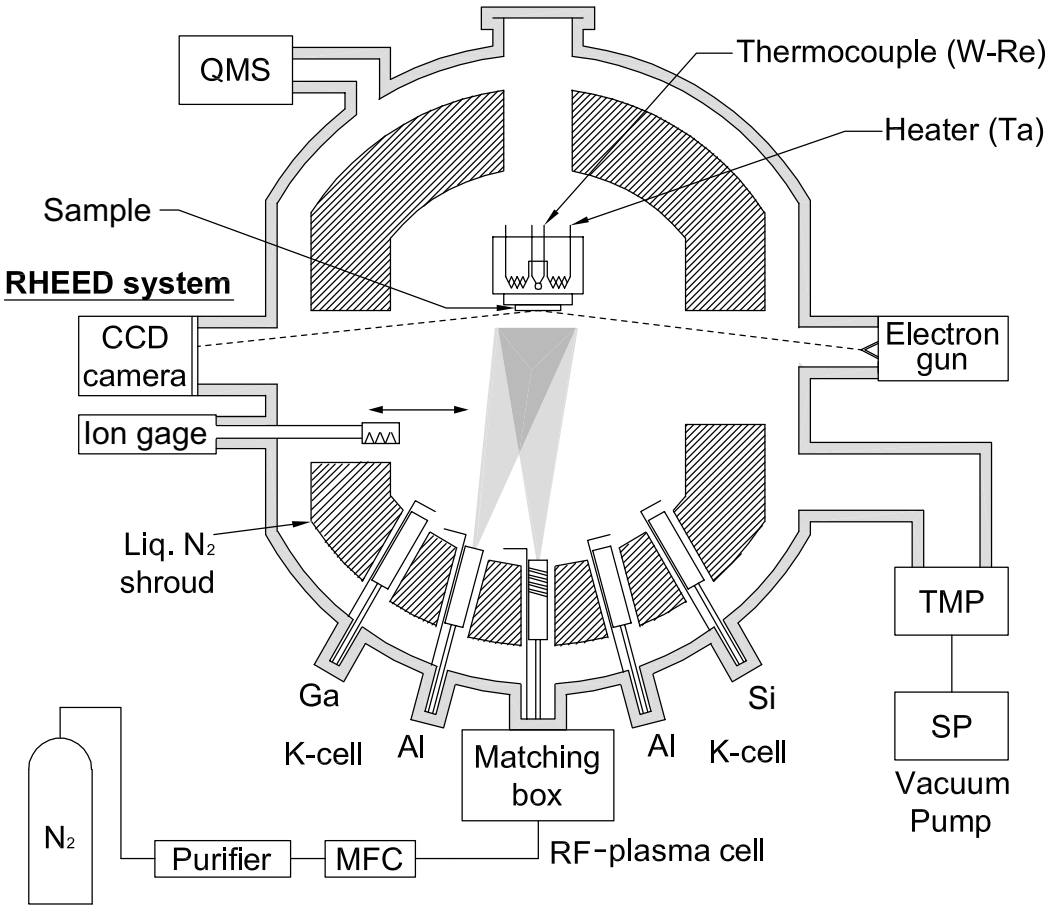

(b) Growth chamber

RP:	Rotary pump	QMS:	Quadrupole mass spectroscopy
SP:	Scroll pump	MFC:	Mass flow controller
TMP:	Turbo-molecular pump	SIP:	Sputter ion pump

Figure 2.1: Schematic views of MBE (a) vacuum system and (b) growth chamber.

The sample-exchange chamber is exhausted by a turbo-molecular pump connected to a rotary pump. The pressure reaches 1×10^{-5} Pa in one hour and the ultimate vacuum pressure is 3×10^{-6} Pa. The sample-exchange chamber is equipped with an infrared lamp which can heat samples to ∼200°C for degassing. The pressure in the sample-transfer chamber keeps lower than 7×10^{-7} Pa with a sputter-ion pump (Gamma Vacuum: 200 l/s).

The growth chamber, as shown in Fig. 2.1 (b), is pumped by a magnetically-suspended turbo-molecular pump (TG1300MCAB, Osaka Vacuum: 1300 l/s) connected to a scroll pump (ISP-250B, ANEST-IWATA: 250 l/m), achieving an oil-free condition. A sputter-ion pump (Perkin Elmer: 20 l/s) is also equipped as a back-up pump, and a gate valve for it is closed during growth. The pressure reaches 4×10^{-8} Pa. The growth chamber is equipped with a cryogenic shroud. The cryogenic shroud at liquid nitrogen temperature (77K) reduces the background pressure inside the chamber to below 6×10^{-9} Pa due to adsorption of residual gases. However, during epitaxial growth of AlN, the pressure increases to 10^{-3} Pa because of the inflow of nitrogen source gas. The growth chamber is also equipped with a quadrupole mass spectroscopy (QMS) system (QMS200, Pfeiffer Vacuum) which can detect impurity in nitrogen source gas as well as residual gases in UHV.

2.2.2 Sample holder and sample heating system

The samples are installed into a sample holder which is made of molybdenum (Mo). The sample holder can be heated up to 1000°C by a tantalum (Ta) heater placed behind it. The samples are secured to the holder by two retaining (snap) rings made of tungsten (W). A diffuser plate made of pyrolytic boron nitride (PBN) is used to improve heating uniformity. The sample temperature (T_{sub}) is measured by a thermocouple located just behind the sample. Although the actual sample temperature may be lower than the thermocouple temperature, we used the measured temperature without any corrections as the sample temperature. No sample rotation during growth was conducted.

2.2.3 Effusion cells and radio-frequency plasma source

The growth chamber is equipped with effusion cells for elemental aluminum (Al) and gallium (Ga) evaporation as well as a radio-frequency (RF) plasma cell. Each cell has an individual shutter blade made of Ta. The RF plasma cell is perpendicularly mounted to the sample, while the Al and Ga effusion cells are installed with 35° tilting to the perpendicular of the sample.

The RF-plasma cell is employed to produce active nitrogen species. A microwave of 13.56 MHz is applied for nitrogen activation. The plasma unit (UNI-Bulb RF Plasma Source, Applied EPI) is fitted with an optical emission detector which gives a photo-current reading correlated with the active-nitrogen flux intensity. Following a gettering-type purifier (PS10A-MC1-N, SAES Getters), nitrogen gas of 6N (99.9999%) purity (Extra Grade, Sum-

itomo Seika Chemicals) reaches the RF-plasma cell. The emission spectrum from the RF-plasma cell is dominated by atomic transition peaks at 745.2, 821.2, and 869.2 nm. In this study, the flow rate of nitrogen (N_2) gas was typically controlled to 0.75 sccm (2×10^{-3} Pa) by a mass flow controller (MFC) and the applied RF power was set to 300 W.

Elemental Al of 6N (99.9999%) purity (E&M cooperation) and Ga of 7N (99.99999%) purity (E&M cooperation) are evaporated from Knudsen-effusion cells (Applied EPI). Al and Ga metals are held in the effusion-cell crucibles made of PBN. The crucible is comprised of a cylindrical reservoir with a small tapered orifice, realizing large capacity with excellent flux uniformity. The Al-effusion cell crucible has a wide lip. The wide lip may damage the cell, but can prevent Al creep due to a thermally isolated cold zone. For the effusion cell, the 200g-SUMO^{TM} effusion cells are used. The SUMO effusion cells can increase charge capacity with superior material quality and cell performance. For Al, a cold-lipped SUMO-effusion cell with only the bottom filament is used. This cell prevents Al overflow in the PBN crucible under nitrogen atmosphere. The heat shielding and heater filament are carefully positioned to heat the crucible body efficiently with an intentional cold lip. For Ga, a hot-lipped SUMO-effusion cell with a dual filament configuration is employed because metallic Ga tends to recondense at the crucible orifice. The two different heater filaments provide a more efficient heating configuration so that the cells can operate at lower power with optimal heating of the crucible orifice.

In growth, the operating temperature for the Al and Ga effusion cells ranged from 1050–1200°C and 850–965°C, respectively. The temperature are controlled by a PID-temperature control system (EC5700, Ohkura Denki) and is stabilized within ±0.3°C. Intensities of the Al- and Ga-beam fluxes are measured by a retractable nude ion gauge located just below the sample.

2.3 Experimental Procedures

2.3.1 Preparation of SiC substrates

In this study, 6H-SiC $(0001)_{Si}$ on-axis (vicinal angle: 0.2-0.5°) wafers from SiXON Ltd. and 6H-SiC $(000\bar{1})_C$, 4H-SiC $(0001)_{Si}$, and 4H-SiC $(000\bar{1})_C$ vicinal wafers from CREE Inc. were used as substrates. These wafers except 6H-SiC $(000\bar{1})$ were semi-insulating (SI) and treated by chemical mechanical polishing (CMP) after mechanical polishing (MP).

To install in the sample holder for MBE growth, the wafers were diced into 7×8 mm^2 rectangular pieces. Before a H_2-gas etching, the substrates were immersed in a H_2SO_4/H_2O_2 mixture at 80°C and then were dipped in HCl, aqua regia and HF solutions [7], followed by rinse with deionized water and blow by dry N_2.

After these wet chemical cleaning, the substrates were introduced directly into a CVD system (TA-CVD1, Takeuchi Denki) and were etched at high-temperature H_2-gas atmosphere to eliminate the CMP damage and to control surface structures. The horizontal

hot-wall CVD system with the insulator was used (Fig. 2.2). SiC substrates are set on the floor of gas-flow channel formed on a SiC plate in a susceptor. On the graphite susceptor coated with SiC, six pieces of substrates (total area of 16×21 mm^2) are uniformly etched. The pressure in the reaction chamber can be changed from 2×10^3 –10^5 Pa by a pressure controller. For the etching, H_2 purified with a Ag-Pd purifier is used at a flow rate of 1–10 slm.

The etching was performed for 10–60 min in the temperature range of 1300–1550°C. After that, the susceptor temperature was reduced at around 160°C/min with the same pressure and H_2-flow rate as during the etching. In decreasing the temperature to below 700°C, the H_2-flow rate was changed to 1 slm. The optimum gas etching condition to achieve one-unit-cell high steps for SiC substrates is described in Section 3.2.

2.3.2 Pretreatment and growth procedures

The substrates treated by H_2-gas etching were loaded into the sample-exchange chamber for MBE growth. After the chamber evacuated to 10^{-5} Pa, the substrates were outgassed and then were transferred into the growth chamber via the sample-transfer chamber.

During the transfer from the CVD system to the MBE system, a few oxygen atoms adsorb on the SiC surface and form a (1×1) surface. To eliminate those residual oxygen atoms, *in-situ* Ga deposition-and-desorption processes are effective [8]. In this procedure, the following reaction process proceeds [9, 10];

$$SiO_2 + 2Ga \longrightarrow SiO \uparrow + Ga_2O \uparrow . \tag{2.1}$$

Particularly, the multiple Ga cleanings are more effective [6]. After the Ga cleaning, a $(\sqrt{3} \times \sqrt{3})$R30° surface of SiC is realized, corresponding to a 1/3 ML superstructure of Si or Ga adsorption [11, 12].

A typical procedure for epitaxial growth of AlN is shown in Figure 2.3. The substrate temperature was raised to 600°C at a ramp rate of 30°C/min. For the Ga cleaning, Ga metal was deposited to the substrate at 600°C and then the substrate temperature increased to 900°C. After the Ga deposition-and-desorption processes were performed twice, the substrate temperature was maintained at 1000°C for 10 min. Following the Ga cleaning, the temperature was decreased to growth temperature. Active nitrogen species were normally maintained for 10 min with the closed shutter to stabilize the gas flow, the growth chamber pressure, and the plasma condition, except for Section 4.5. After the stabilization of nitrogen plasma, vaporized Al and active nitrogen were introduced simultaneously to the substrate surface. At the end of growth, the cell shutters were closed simultaneously and then the substrate temperature decreased to room temperature at a rate of 20°C/min.

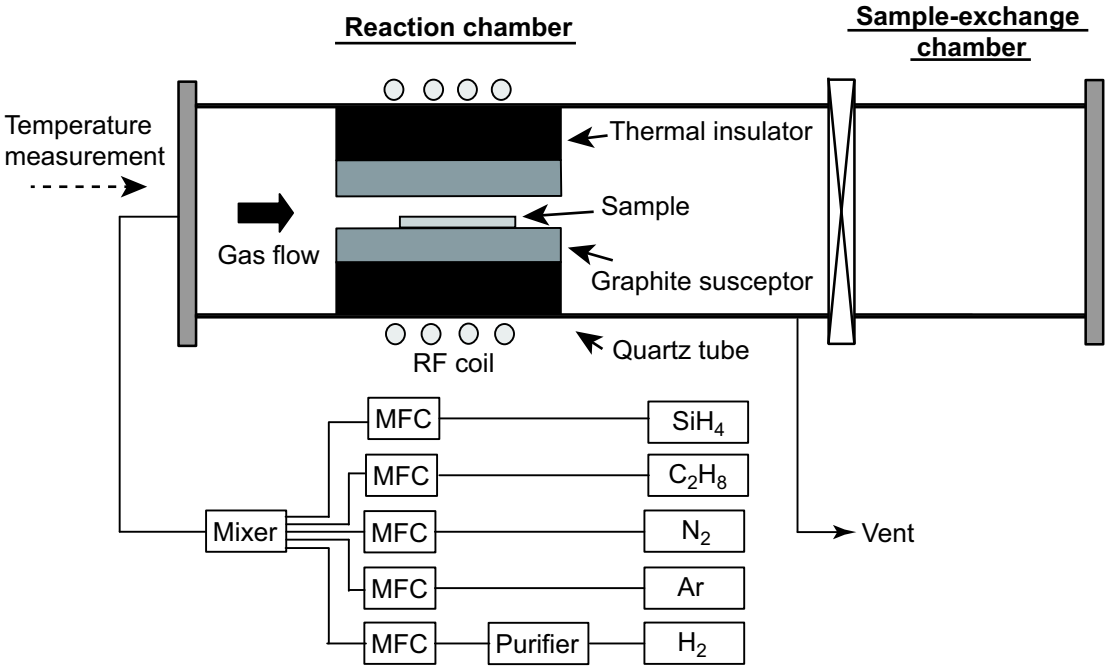

Figure 2.2: Schematic diagram of horizontal hot-wall CVD system.

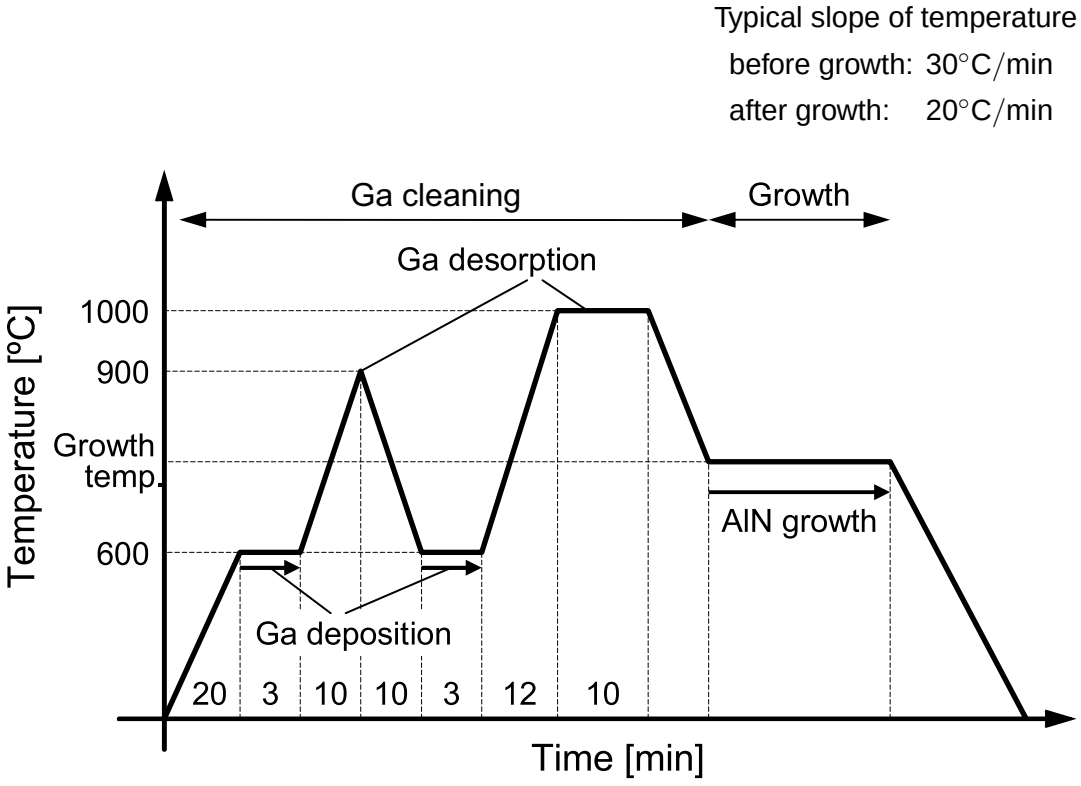

Figure 2.3: Typical procedure for epitaxial growth of AlN.

2.3.3 Characterization methods

Reflection high-energy electron diffraction (RHEED)

For *in-situ* analyses of kinetics during growth, RHEED was used. The electron beam accelerated by 20 kV is diffracted at the surface atoms of a sample and builds up a diffraction pattern on a fluorescent screen. The RHEED patterns are recorded through a 16-bit gradient Charge Coupled Device (CCD) camera. The monitoring of diffracted intensities is carried out by a real-time image processing system (kSA400 RHEED system, k-Space Associates).

X-ray photoelectron spectroscopy (XPS)

To examine a chemical composition and chemical bonding of surface atoms, XPS was used. The XPS chamber is exhausted by a turbo-molecular pump and the base pressure is as low as 9×10^{-7} Pa. Because the XPS chamber is connected through an UHV tunnel to the growth chamber (Fig. 2.1), the measurements can be performed *in-situ* after surface treatments or growth in the growth chamber. X-ray source is the $AlK_{\alpha 1}$ (1486.6 eV). XPS spectra is detected by a hemispherical electron energy analyzer (ESCA-1000 system, Shimadzu). The filament voltage and current are 10 kV and 20 mA, respectively. The analysis area is set to be ϕ 0.6 mm by slit. The beam linewidth and the pass energy are 0.85 eV and 0.3 eV, respectively.

X-ray diffraction (XRD)

To evaluate crystalline quality of films, the ω-scan and $2\theta/\omega$-scan was conducted using a triple crystalline x-ray diffractometer (SLX-2000, Rigaku) was used. The filament voltage and current are 50 kV and 300 mA, respectively. A copper (Cu) $K_{\alpha 1}$ line ($\lambda = 1.540562$ Å) was selected by a channel-cut double crystal germanium (Ge) (220) monochromator. The entrance-slit width of S1 and S2 were 1.0×0.1 mm^{-2} and 1.0×0.2 mm^{-2}, respectively. The receiving slit for the symmetric and asymmetric scan was 1.0×0.2 mm^{-2} and open (12×5.0 mm^{-2}), respectively.

To investigate strain of the films, the reciprocal space mapping (RSM) was measured using the other triple crystalline x-ray diffractometer (D8 Discover, Bruker AXS). The filament voltage and current are 50 kV and 100 mA, respectively. A Cu $K_{\alpha 1}$ line ($\lambda = 1.540562$ Å) was selected by a channel-cut double crystal Ge (220) monochromator. The entrance-slit width of S1 and S3 were 30×1.2 mm^{-2} and 30×1.0 mm^{-2}, respectively. The 2θ-directional resolution of one dimensional detector (VANTEC-1) is 0.007°.

Raman Scattering Spectroscopy

To evaluate the strain of films, the phonon mode was characterized by a triple monochromator micro Raman system (T64000, HORIBA) with an Ar^+ laser probe (488 nm). The laser power, laser current, and measurement time were 50 mW, 28A, and 3 min, respectively. The incident-slit and 2nd-intermediate-slit width were 100 μm and 16 mm, respectively. The resolution of an additive triple configuration (1800 grooves/mm) is 0.25 cm^{-1}. The phonon mode was obtained using the CCD camera cooled by liquid nitrogen (140 K).

Atomic force microscopy (AFM)

For surface observations, a Tapping-Mode AFM (Dimension 3100/Dimension V, Veeco Instruments) with silicon tips with ∼100 Å end-tip diameter (NCHR, Nanoworld) was used.

Transmission electron microscopy (TEM)

To observe defect structures in the films and convergent beam electron diffraction (CBED) patterns, a field-emission TEM (JEM-2100F, JEOL) accelerated at 200 kV was employed. The observed image was captured by the CCD camera.

For the High-resolution TEM (HRTEM) observation, transmission electron aberration-corrected microscopy (TEAM) 0.5 operated at 300 kV with a monochrometor was used. In plan-view (cross-sectional) observations, spherical aberrations of TEAM 0.5 were C3 = 1.614 μm (C5 = 371.5 μm) and C3 = 1.089 μm (C5 = 254.2 μm), respectively. The image was recorded near Scherzer defocus to compare with simulated images. For simulation of HRTEM images with the multislice method and of CBED patterns with the Broch wave method, JEMS software was used.

Sample was glued on the stainless steel ring with ϕ 2 mm for the support. Plan-view and cross-sectional samples were prepared by dimpling (656 Dimple Grinder, Gatan) down to 10 μm followed by Ar ion milling (691 PIPS, Gatan) at 5 kV until perforation occurred and at 0.5 kV for a cleaning.

Cathodoluminescence (CL)

For CL measurements, a single monochromator system (MONOCL3+, Oxford Instruments) combined with field-emission scanning electron microscopy (SEM) (JSM-6500F, JEOL) was used. The CL passed a parabolic mirror is converted into an electrical signal by Peltier-cooling photomultiplier tube (PMT). The grating is 2400 grooves/mm. The minimum sample temperature of 100 K can be achieved due to the stage cooled by liquid nitrogen. The probe current was changed for the measurements, while the acceleration voltage was kept constant (5 keV).

Photoluminescence (PL)

For PL measurements, an ArF Excimer laser (MPB Communications: wave length λ = 193 nm, pulse width 4 ns, maximum pulse rate 300 Hz) was employed. The laser power is tuned by film polarizer and $\lambda/2$ wave plate. The laser was incident from the surface normal, and the PL from the sample was collected at 60° from the surface normal. Before the PL signal goes into the monochromator (SP-2500, Acton Research Corporation Spectra) through the slit (opening: 20 μm), it is collimated by one lens and focused into the entrance slit. The resolution on the monochromator (2400 grooves/mm) is 0.045 nm, which is determined by CCD pixel size. The minimum sample temperature of 8.5 K can be achieved due to a cryogen-free cryostat. The PL from the AlN layer was obtained using the CCD camera cooled by liquid nitrogen (120 K).

References

[1] K. Balakrishnan, H. Okumura, and S. Yoshida, J. Cryst. Growth **189**, 244 (1998).

[2] N. Fujita, M. Yoshizawa, K. Kushi, H. Sasamoto, A Kikuchi, and K. Kishino, J. Cryst. Growth **189**, 385 (1998).

[3] M. H. Xie, S. M. Seutter, W. K. Zhu, L. X. Zheng, H. Wu, and S. Y. Tong, Phys. Rev. Lett. **82**, 2749 (1999).

[4] J. Bai, X. Huang, and M. Dudley, Mater. Sci. Process. **9**, 180 (2006).

[5] N. D. Bassim, M. E. Twigg, M. A. Mastro, C. R. Eddy, T. J. Zega, R. L. Henry, J. C. Culbertson, R. T. Holm, P. Neudeck, J. A. Powell, and A. J. Trunek, J. Cryst. Growth **304**, 103 (2007).

[6] N. Onojima, J. Suda, and H. Matsunami, Jpn. J. Appl. Phys. **42**, L445 (2003).

[7] J. Suda, K. Miura, M. Honaga, Y. Nishi, N. Onojima, and H. Matsunami, Appl. Phys. Lett. **81**, 5141 (2002).

[8] R. Kaplan and T. M. Parrill, Surf. Sci. Lett. **165**, L45 (1986).

[9] S. Wright and H. Kromer, Appl. Phys. Lett. **36**, 210 (1980).

[10] U. Starke, phys. stat. sol. (b) **202**, 475 (1997).

[11] V. van Elsbergen, T. U. Kampen, and W. Monch, Surf. Sci. **365**, 443 (1996).

[12] N. Onojima, J. Suda, and H. Matsunami, Jpn. J. Appl. Phys. **42**, L445 (2003).

Chapter 3

Surface Control of SiC {0001}

3.1 Introduction

As-received SiC substrates typically contain a high density of surface defects and scratches due to mechanical polishing (MP), forming additional defects during AlN growth [1]. Furthermore, they contain a distribution of stacking arrangements with random terminations, e. g., six types of the stacking arrangements for a 6H-SiC surface, so that AlN layers on the substrates have stacking mismatch boundaries (SMBs) [2, 3]. To minimize these defects in AlN layers, surface treatments of SiC substrates are necessary. H_2-gas etching and chemical mechanical polishing (CMP) was reported to be effective as the surface treatments of 6H-SiC (0001) substrates [4–7]. Gas etching removes the surface polishing scratches and realizes an atomically-flat terrace structure with one-unit-cell-high steps by macro step bunching. However, there are few reports on gas etching of 4H-SiC {0001} and 6H-SiC $(000\bar{1})$ surfaces. In this study, 4H-SiC and 6H-SiC {0001} surfaces were etched in H_2 atmosphere in a hot-wall chemical vapor deposition (CVD) reactor.

For SiC, both silicon and carbon atoms must be simultaneously removed. At temperature above 1200°C, SiC causes the following reactions with a H_2 carrier gas and is etched [8]:

$$\mathrm{SiC} + 2\mathrm{H_2} \longrightarrow \mathrm{CH_4} \uparrow + \mathrm{Si} \uparrow \tag{3.1}$$

$$2\mathrm{SiC} + \mathrm{H_2} \longrightarrow \mathrm{C_2H_2} \uparrow + 2\mathrm{Si} \uparrow . \tag{3.2}$$

The major components of the vapor are CH_4, C_2H_2, and Si [9]. To achieve a surface with half- or one-unit-cell-high steps, SiC must be slowly etched at low temperature. However, at temperature below 1600°C in the atmospheric pressure, CH_4 and C_2H_2 preferentially evaporate because the equilibrium pressure of CH_4 and C_2H_2 exceeds that of Si [10]. Excess silicon atoms remain on the surface, reducing the SiC etch rate as well as the condensation of Si droplets. To avoid generating Si droplets at low temperature, there are typically three methods: (i) addition of CH_4 to H_2 gas, (ii) addition of HCl to H_2 gas, and (iii) reduction of H_2-gas pressure [8–10]. For (i), the surface reaction ((3.1) and (3.2)) is reduced, inhibiting the excess stagnation of the silicon atoms on the surface. For (ii), the excess silicon atoms

react with HCl and are removed from the surface. For (iii), more silicon atoms can evaporate owing to the reduction of the stagnant layer thickness. Using methods (i)–(iii), the etching balance between the silicon and carbon atoms is maintained, increasing the etch rate of SiC. We selected method (iii) because severe control of the surface structures is possible. In this chapter, the etching condition and the off direction of the SiC substrates were optimized to obtain half- or one-unit-cell-high steps in a large area.

3.2 Step-Height Control of SiC Surfaces

3.2.1 Optimization of H_2-gas etching condition

4H-SiC $(0001)_{Si}$ surface

We used 4H-SiC {0001} vicinal-off (0.1-0.3°) substrates treated by CMP. After the chemical cleaning procedures, the substrates were loaded into a horizontal hot-wall CVD reactor. As a standard etching condition, the temperature, pressure, H_2-flow rate, and etching time were set to 1400°C, 3.3×10^4 Pa, 2 slm, and 30 min, respectively.

The surface morphologies of 4H-SiC (0001) etched for a temperature range of 1300–1500°C are shown in Fig. 3.1. All SiC surfaces were etched, and step-and-terrace structures were obtained. The steps are parallel and periodic over the SiC surfaces (Fig. 3.1 (d)). The step height was 0.5 nm, corresponding to the half-unit-cell (2 Si-C bilayer) height of the 4H-SiC (0001). The terraces were atomically smooth: RMS roughness was under 0.1 nm. The terrace width was about 200 nm, which corresponds 0.15° tilt, indicating the vicinal-off angle was conserved after gas etching. Below 1400°C, 2-bilayer-high steps were uniformly obtained at the large area. The edges of the 2-bilayer-high steps, however, are zigzag due to excess etching with 1-bilayer height (Fig. 3.1 (e)). Si droplets were sometimes observed on the surface by AFM (not shown in the figure). At 1500°C, huge step bunching was occurred, composed of 60-bilayer-high steps and 10-μm-wide terraces (Fig. 3.1 (c)). On the wide terraces, two 1-bilayer-high steps and 1-bilayer-high hollows (3×10^9 cm^{-2}) existed (Fig. 3.1 (f)). No Si droplets were observed on the surfaces at high temperature.

The surface morphologies of 4H-SiC (0001) etched for a pressure range of 1.3×10^4 – 6.7×10^4 Pa are shown in Fig. 3.2. A big step bunching over 16 bilayer was generated in the low pressure (Fig. 3.2 (a)). In 3.3×10^3 Pa, the step height was larger than 20 bilayer (not shown). There were two 1-bilayer-high steps on the terraces, like the etching at 1500°C. The 2-bilayer-high steps were achieved in the pressure above 3.3×10^4 Pa.

To avoid excess etching with 1-bilayer height at the step edges, the H_2-flow rate and etching time were also optimized. The surface morphologies of 4H-SiC (0001) etched for a flow rate range of 1–5 slm are shown in Fig. 3.3. The 2-bilayer-high steps were uniformly achieved independently of the flow rate. The higher the flow rate, the larger were the 1-bilayer-high surface defects (Fig. 3.3 (d)-(f)). The surface morphologies of 4H-SiC (0001) etched for 30–60 min are shown in Fig. 3.4. The surface etched for 60 min is only slightly

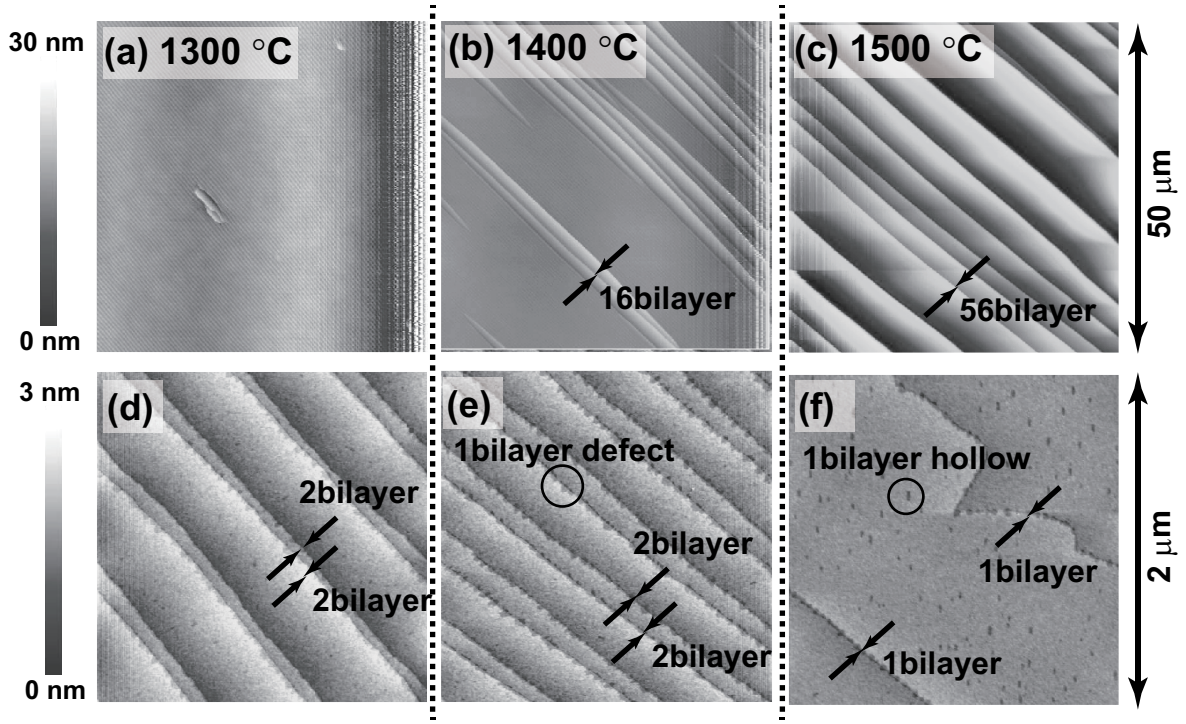

Figure 3.1: Surface morphologies of 4H-SiC (0001) etched at (a, d) 1300, (b, e) 1400, and (c, f) 1500°C in H_2 atmosphere. Pressure, H_2-flow rate, and etching time were 3.3×10^4 Pa, 2 slm, and 30 min, respectively.

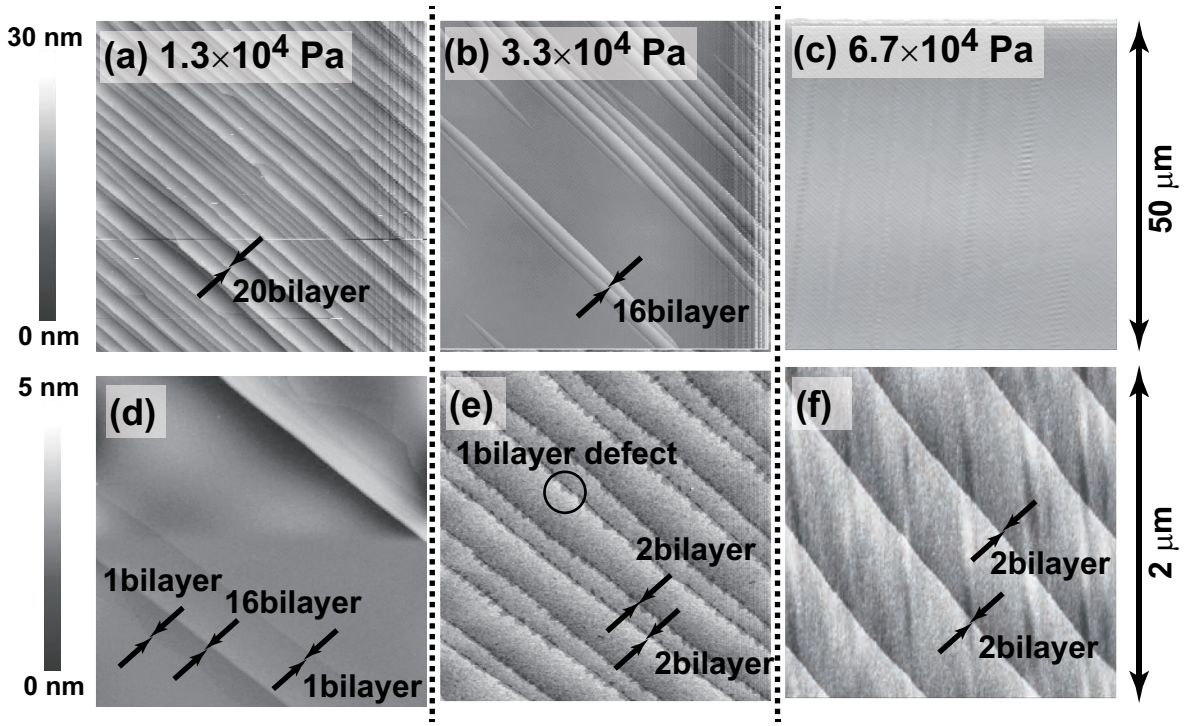

Figure 3.2: Surface morphologies of 4H-SiC (0001) etched in (a, d) 1.3, (b, e) 3.3, and (c, f) 6.7×10^4 Pa in H_2 atmosphere. Temperature, H_2-flow rate, and etching time were 1400°C, 2 slm, and 30 min, respectively.

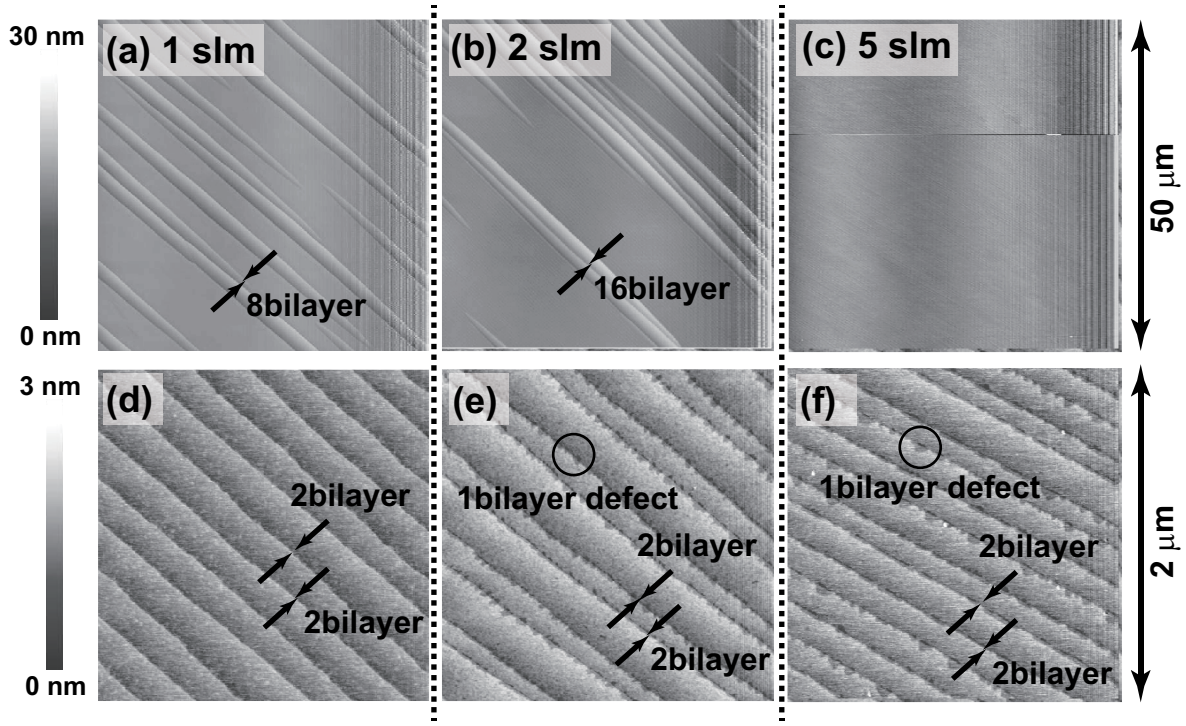

Figure 3.3: Surface morphologies of 4H-SiC (0001) etched at H_2-flow rate of (a, d) 1, (b, e) 2, and (c, f) 5 slm in H_2 atmosphere. Temperature, pressure, and etching time were 1400°C, 3.3×10^4 Pa, and 30 min, respectively.

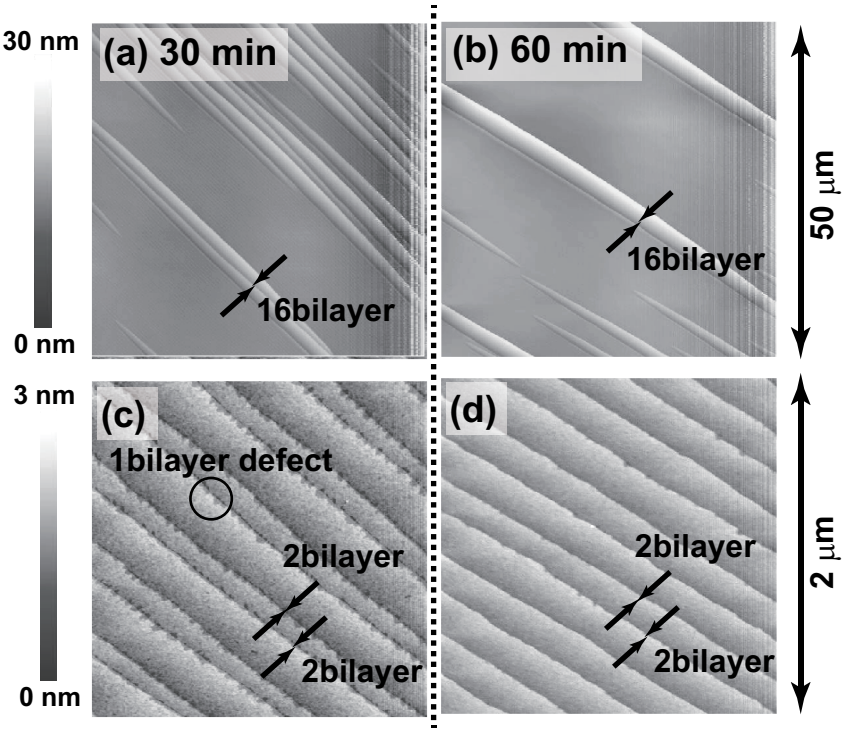

Figure 3.4: Surface morphologies of 4H-SiC (0001) etched at (a, c) 30 and (b, d) 60 min in H_2 atmosphere. Temperature, pressure, and H_2-flow rate were 1400°C, 3.3×10^4 Pa, and 2 slm, respectively.

different from that etched for 30 min. The best condition to obtain the 2-bilayer-high steps is 1400°C, 5×10^4 Pa, 2 slm, and 30 min.

4H-SiC (000$\bar{1}$) surface

The surface morphologies of 4H-SiC (000$\bar{1}$) etched for a pressure range of 1.3×10^4 – 6.7×10^4 Pa are shown in Fig. 3.5. Except for the pressure, the etching condition is the same as the standard condition. The tendency of the step bunching for 4H-SiC (000$\bar{1}$) is different from that for 4H-SiC (0001). The 2-bilayer-high steps were uniformly obtained independently of the pressure. However, the step edges of 4H-SiC (000$\bar{1}$) undulate hard. To achieve complete parallel steps, temperature and H_2-flow rate also must be optimized.

6H-SiC $(0001)_{Si}$ surface

We used 6H-SiC (0001) vicinal-off (0.1-0.3°) substrates treated by CMP and 6H-SiC (000$\bar{1}$) vicinal-off (0.1-0.3°) substrates only treated by MP. After the wet-chemical cleaning procedures, the substrates were loaded into a horizontal hot-wall CVD reactor. As a standard etching condition, the temperature, pressure, H_2-flow rate, and etching time were set to 1500°C, 2.6×10^3 Pa, 2 slm, and 30 min, respectively.

The surface morphologies of 6H-SiC (0001) after gas etching are shown in Fig. 3.6. The 6H-SiC (0001) surfaces etched in the standard condition have step-and-terrace structures with atomically smooth terraces and 3-bilayer-high steps (Fig. 3.6 (a)). At low temperature (1400°C) or in high pressure (1.3×10^4 Pa), 1-bilayer-high surface defects were observed at the step edges (Fig. 3.6 (b) and (c)). These results suggest that the surface defects were generated due to excess evaporation of carbon atoms. The 1-bilayer-high surface defects at the step edges had a $\{1\bar{1}00\}$ plane, which is energetically the most stable [11]. Unlike the 4H-SiC {0001} surfaces, no big step bunching over one-unit-cell height was observed on the 6H-SiC surfaces. In addition, the best etching pressure (2.6×10^3 Pa) for 6H-SiC (0001) with the 3-bilayer-high steps was much lower than that (3.3×10^4 Pa) for 4H-SiC (0001) with 2-bilayer-high steps, indicating that a (0001) plane of 6H-SiC is more stable than that of 4H-SiC, because the low pressure enhances the Si evaporation and increases the etch rate of SiC.

6H-SiC (000$\bar{1}$) surface

The surface morphologies of 6H-SiC (000$\bar{1}$) after gas etching are shown in Fig. 3.7. 6H-SiC (000$\bar{1}$) surfaces etched in the same standard condition as 6H-SiC $(0001)_{Si}$ have step-and-terrace structures with 3-bilayer-high steps (Fig. 3.7 (a)). In comparison with the 6H-SiC (0001), the terraces of 6H-SiC (000$\bar{1}$) surfaces were rough. This may depend on the atomic arrangements between the silicon and carbon atoms at the surface. Carbon atoms on a topmost (0001) surface are bound to silicon atoms with one bond. On the other hand, those on a topmost (000$\bar{1}$) surface are bound to silicon atoms with three bonds. At a high flow rate (5 slm), atomically smooth terraces were obtained. In high pressure (1.3×10^4 Pa), the surface had a two-dimensional (2D) nucleus, indicating layer-by-layer etching.

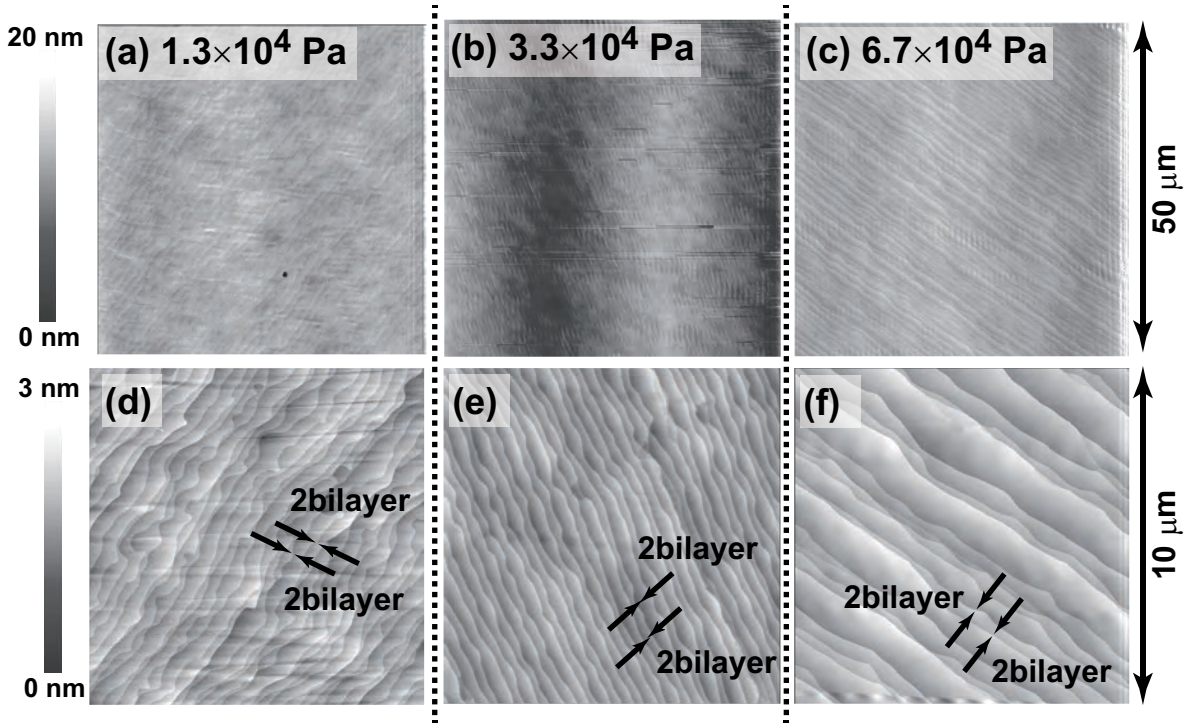

Figure 3.5: Surface morphologies of 4H-SiC $(000\bar{1})$ etched in (a, d) 1.3, (b, e) 3.3, and (c, f) 6.7×10^4 Pa in H_2 atmosphere. Temperature, H_2-flow rate, and etching time were 1400°C, 2 slm, and 30 min, respectively.

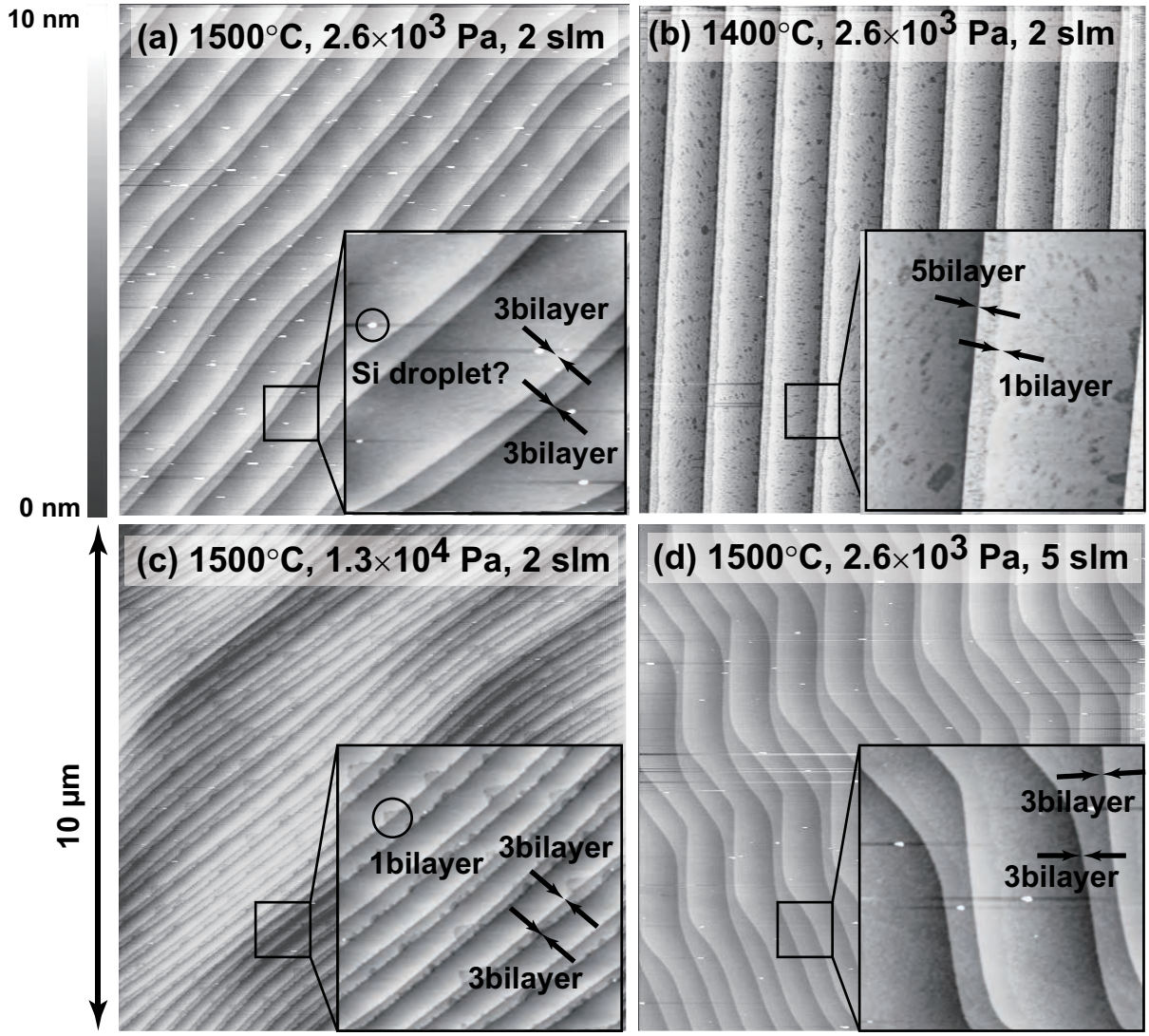

Figure 3.6: Surface morphologies of 6H-SiC (0001) etched in H_2 atmosphere for 30 min. Etching conditions were (a) standard (1500°C, 2.6×10^3 Pa, 2 slm), (b) low temperature (1400°C, 2.6×10^3 Pa, 2 slm), (c) high pressure (1500°C, 1.3×10^4 Pa, 2 slm), and (d) high H_2-flow rate (1500°C, 2.6×10^3 Pa, 2 slm).

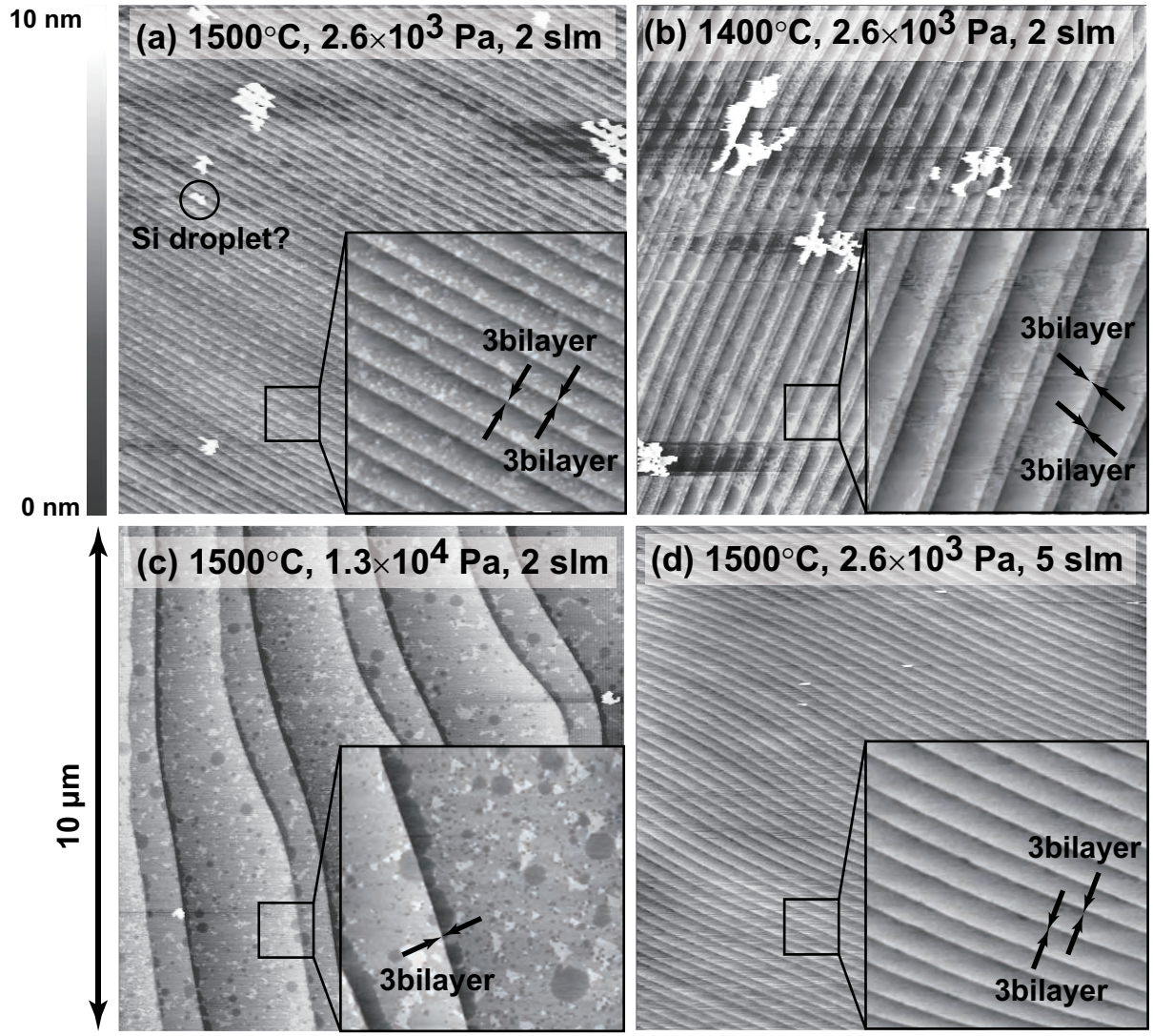

Figure 3.7: Surface morphologies of 6H-SiC $(000\bar{1})$ etched in H_2 atmosphere for 30 min. Etching conditions were (a) standard (1500°C, 2.6×10^3 Pa, 2 slm), (b) low temperature (1400°C, 2.6×10^3 Pa, 2 slm), (c) high pressure (1500°C, 1.3×10^4 Pa, 2 slm), and (d) high H_2-flow rate (1500°C, 2.6×10^3 Pa, 2 slm).

3.2.2 Discussion

Rate-limiting process

For SiC etching in the CVD reactor, mass transport phenomena is considered. In this model, the etch rate at low temperature is limited by the surface reaction ((3.1) and (3.2)), while that at high temperature is limited by the diffusion of products (C_2H_2 and Si). Using an *in-situ* gravimetric monitoring system, Akiyama *et al.* reported that the H_2-gas-etching process of 6H-SiC (0001) at 1350°C in atmospheric pressure is limited by the surface reaction [12]. We consider that etching in low pressure is the desorption limiting of Si because Si droplets were often observed.

Surface termination after gas etching

There are reports on one-unit-cell-high step bunching in the CVD growth of SiC {0001} [13]. The generation mechanism of multiple-step heights, which must be the same for growth and etching, is schematically shown in Fig. 3.8. In 6H-SiC (0001), there are three types of surface energies, i. e., the surfaces with steps of 6S1, 6S2, and 6S3. The desorption of a 6S2 step is the most favorable from the view-point of total surface energy, indicating the fastest etching velocity. The 6S2 step overtakes the 6S3 step and forms 2-bilayer-high steps. Borovikov *et al.* reported that the layer A was top of the surface [14]. This implies that the 2-bilayer-high steps proceed at a faster velocity than the 1-bilayer-high steps, and form 3-bilayer-high steps. The surface termination of 6H-SiC (0001) during gas etching is composed of layers ABC and ACB, indicating that all the topmost stacking arrangements are layers A. Although a similar mechanism is expected in 4H-SiC, the surface termination of 4H-SiC (0001) is composed of layers AB and CB, indicating different stacking arrangements (layers A or C) on each terrace.

Generation mechanism of huge step bunching in 4H-SiC (0001)

The dependence of the average step heights of the 4H-SiC (0001) surfaces on the etching temperature and pressure is shown in Fig. 3.9. The step heights were averaged in an area of 50×50 μm^2. The surface etched in the low pressure (2.6×10^4 Pa) had approximately 16-bilayer-high steps. Nakagawa *et al.* reported that 8 °-off 4H-SiC (0001) surfaces etched in an H_2 atmosphere form ordered nanofacets with high-index $(11\bar{2}n)$ (n=11-12) and a four-unit-cell height, corresponding to 16-bilayer height [15].

We consider that a big step bunching in 4H-SiC (0001) is attributed to the surface-termination difference. 6H-SiC (0001) has the same stacking arrangements on the topmost surface, so that one- or half-unit-cell high steps can be generated even at the high etch rate (in low pressure). However, the surface status of 4H-SiC (0001) is more unstable because each terrace (layers A or C) of the etched surface has different surface energy, forming the most stable $(11\bar{2}n)$ facets with 16-bilayer-high steps. In addition, in lower pressure (3.3×10^3 Pa) or at high temperature (1500°C), two 1-bilayer-high steps were formed on the terraces (Fig. 3.10). These 1-bilayer-high steps were etched not only at the lower step edges but also from the upper step edges owing to the strong driving force of etching. The etching from both sides on the terraces probably results in over-16-bilayer-high steps.

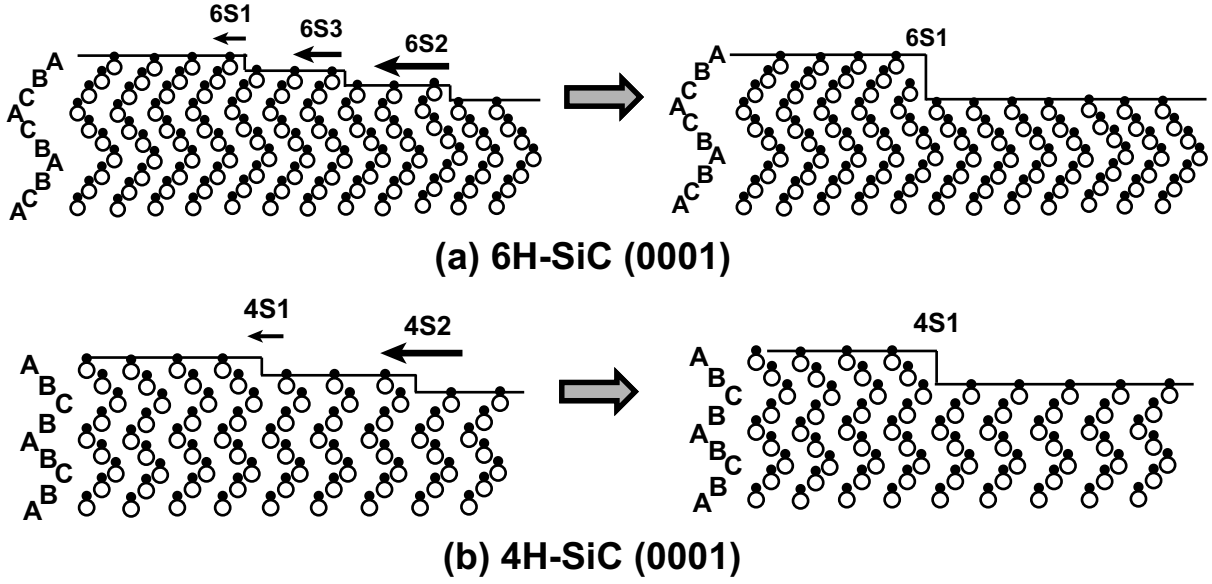

Figure 3.8: Generation mechanism of step bunching for 6H-SiC {0001} (a: before gas etching, b: during gas etching).

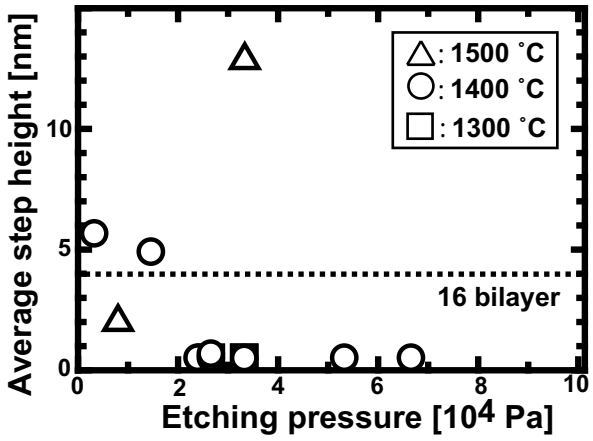

Figure 3.9: Relation between etching pressure and average step height of 4H-SiC (0001) surface.

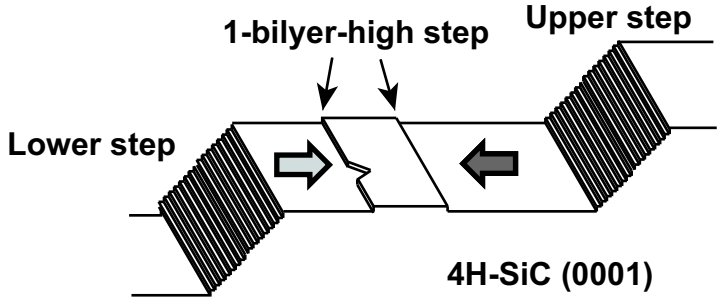

Figure 3.10: Schematic figure of huge step bunching of 4H-SiC (0001). 1-bilayer-high steps are etched from both sides of upper step and lower step in low pressure or high temperature conditions.

3.2.3 Off-direction dependence of step height

The step height of the 6H-SiC (0001) surfaces after H_2-gas etching depends on the off direction: the surface with steps in the $\langle 11\bar{2}0\rangle$ off direction has 3-bilayer-high steps, but that with steps in the $\langle 1\bar{1}00\rangle$ off direction has 6-bilayer-high steps [11, 16]. The step height of the 6H-SiC (0001) surfaces in the off direction between $\langle 11\bar{2}0\rangle$ and $\langle 1\bar{1}00\rangle$ has not been investigated systematically. To control the step height in a large area, we scrutinized the relation between the off direction and the step height of 6H-SiC (0001).

A 6H-SiC (0001) on-axis wafer was treated by CMP. This 2-inch-size wafer was etched in an H_2 atmosphere in a vertical hot-wall CVD reactor at SiXON Ltd. The etching temperature, pressure, and time were 1350°C, 2.7×10^3 Pa, and 30 min, respectively. The off directions distribute on an on-axis SiC wafer (Fig. 3.11), because strain in a SiC bulk occures a curvature of the (0001) plane.

We confirmed that the step height near the $\langle 11\bar{2}0\rangle$ off direction was 3 bilayer (Fig. 3.11 (a)). As the off direction approaches $\langle 1\bar{1}00\rangle$, two 3-bilayer-high steps gradually draw closer to each other, resulting in 6 bilayer in the off direction of 26 ° from $\langle 11\bar{2}0\rangle$ (Fig. 3.11 (d)). To evaluate the splitting ratio of these two 3-bilayer-high steps, we define W_s/W_l (Fig. 3.12 (a)). Here, W_s and W_l have shorter and longer terrace widths between 3-bilayer-high steps. In $W_s/W_l = 0.5$, the two 3-bilayer-high steps are completely separated, while in $W_s/W_l = 0$, they overlap, indicating 6-bilayer height. The dependence of the splitting ratio on the off direction is shown in Fig. 3.12 (b). In the off direction of 0-25 ° from $\langle 11\bar{2}0\rangle$, the steps were split into two 3 bilayers, and in the off direction of 25-30 °, the steps had complete 6 bilayers. We found that the off direction of the 6H-SiC (0001) surfaces with 6-bilayer-high steps must be controlled within 5 ° from $\langle 1\bar{1}00\rangle$.

For 6H-SiC {0001}, the mechanism of the step bunching by H_2-gas etching was suggested to be the minimization of surface free energy: i.e., step bunching is attributed to different etching speeds between the 3-bilayer step edges with one and two dangling bonds [17]. In the $\langle 1\bar{1}00\rangle$ off direction, the 3-bilayer step edges with two dangling bonds are etched more easily and reached the 3-bilayer step edges with one dangling bond, forming 6-bilayer-high steps (Fig. 3.13). On the other hand, in the $\langle 11\bar{2}0\rangle$ off direction, the dangling bonds of all 3-bilayer step edges have crystallographically the same status, so that the step height maintains 3 bilayer during gas etching. Williams *et al.* reported that surface energy reduction can be induced by the presence of attractive step-step interaction between closely spaced bimonolayer steps [18]. The step height in the off direction between $\langle 1\bar{1}00\rangle$ and $\langle 11\bar{2}0\rangle$ is decided by the balance between the etch-rate difference and the step-step interaction.

Vicinal-off angle of SiC {0001} should be over 0.1 °, because etch pits are generated for small off-axis substrates by spiral etching [19]. Additionally, the elimination of the polishing damage using CMP is necessary to obtain uniform steps by H_2-gas etching at temperature below 1500°C. Based on the above results, we controlled the step height of 6H-SiC (0001). 3-bilayer-high steps were uniformly achieved in the whole area of a 2-inch wafer, and 6-bilayer-high steps were achieved in the 30% area of the 2-inch wafer (Fig. 3.14).

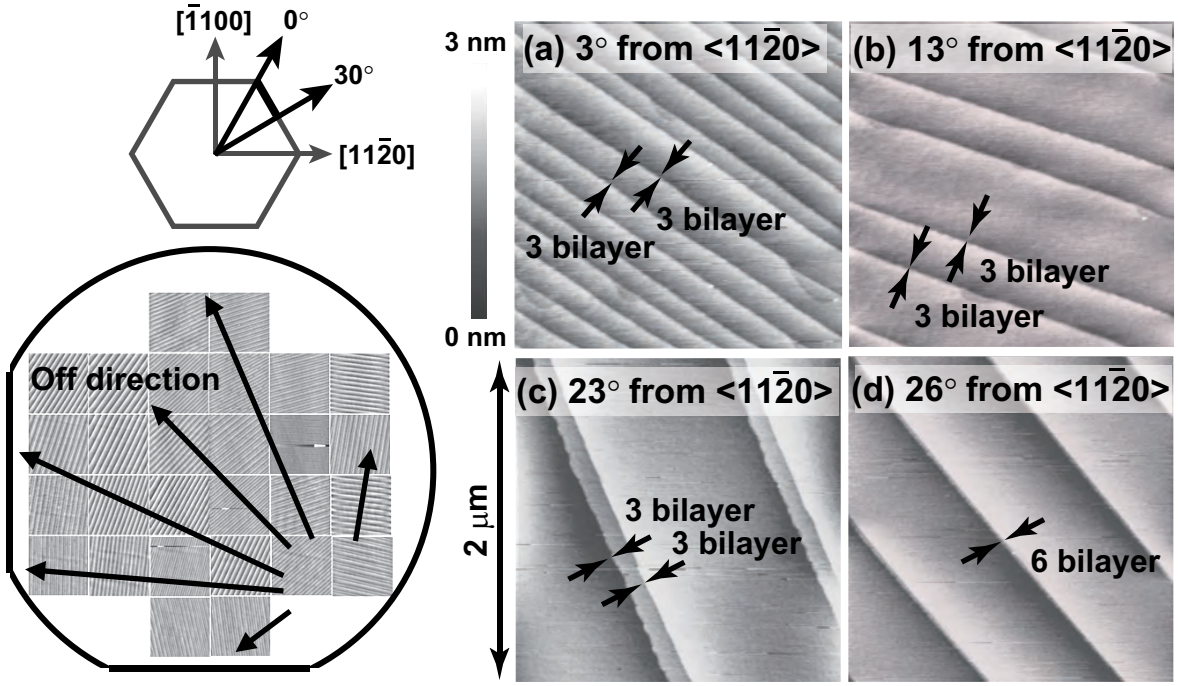

Figure 3.11: Surface morphologies of 6H-SiC (0001) on-axis wafer after H_2-gas etching. Step heights in various off directions (a: 3, b: 13, c: 23, and d: 26 ° from $\langle 11\bar{2}0 \rangle$) were observed.

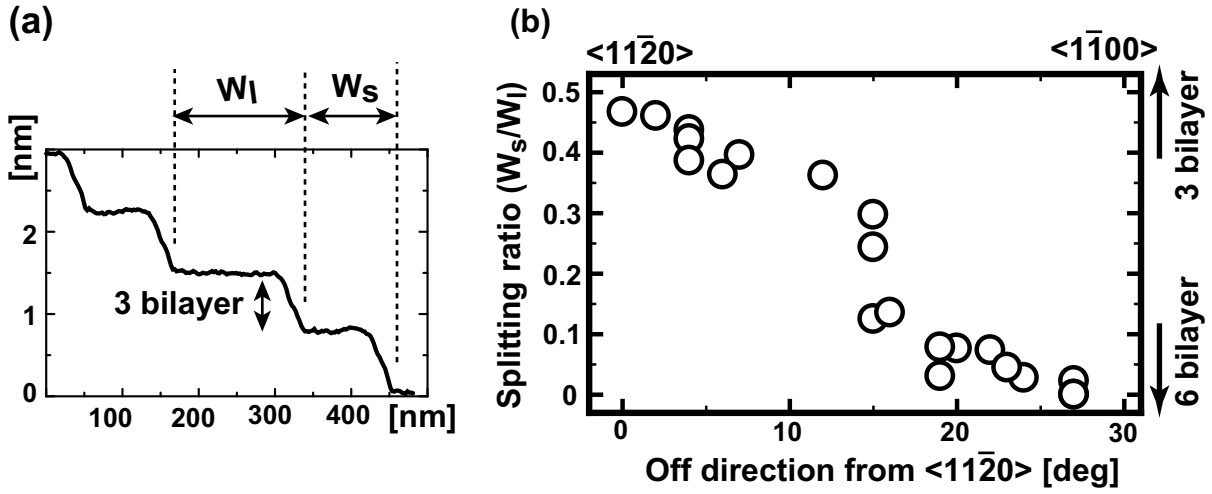

Figure 3.12: (a) Cross-sectional profile of 3-bilayer-high steps (W_l: longer terrace width between two 3-bilayer-high steps and W_s: shorter terrace width between two 3-bilayer-high steps) and (b) dependence of splitting ratio (W_s/W_l) on off direction from $\langle 11\bar{2}0 \rangle$.

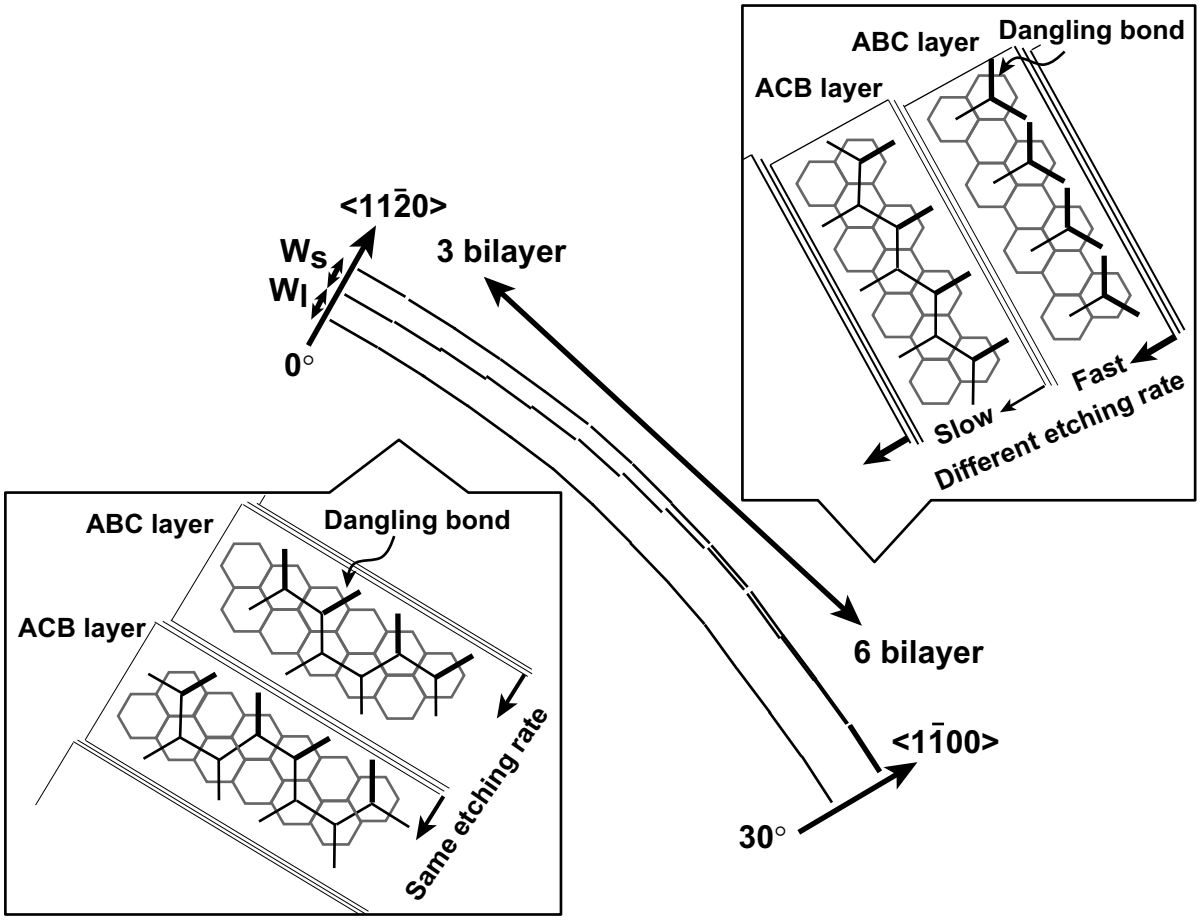

Figure 3.13: Formation mechanism of 6-bilayer-high steps in $\langle 1\bar{1}00 \rangle$ off direction.

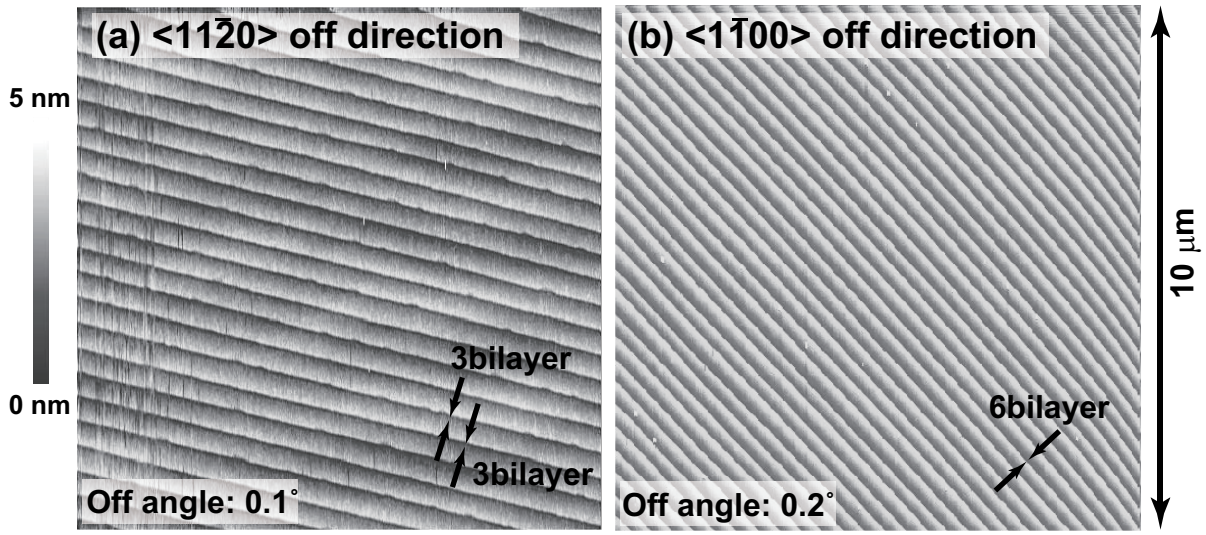

Figure 3.14: Surface morphologies of 6H-SiC (0001) with (a) 3-bilayer-high steps and (b) 6-bilayer-high steps by H_2-gas etching.

3.3 Chemical-Status Control of SiC Surfaces

3.3.1 Chemical analysis of SiC surfaces after pretreatments

The etched SiC substrates were loaded into an molecular-beam epitaxy (MBE) system via air. During the transfer and in decreasing temperature in the CVD reactor after the gas etching, a few oxygen atoms are adsorbed on the SiC surface [20]. These impurities can generate crystal defects during AlN growth [21]. To remove the native oxide films and residual oxygen on the surfaces, we carried out *ex-situ* HF-wet-chemical treatments and *in-situ* Ga cleaning, as described in Section 2.3, and investigated the chemical status of SiC {0001} surfaces after these pretreatments using *in-situ* x-ray photoelectron spectroscopy (XPS). The chemical composition is unevaluated because the peak position of XPS spectra for the semi-insulating substrates shifts due to the charge builtup. All peak intensities were normalized as Si $2p$ peaks had the same intensity.

4H-SiC $(0001)_{\mathrm{Si}}$ surface

The XPS spectra of a 4H-SiC (0001) surface after gas etching, wet-chemical cleaning, and Ga cleaning are shown in Fig. 3.15. As expected, the adsorbed oxygen was reduced by the wet-chemical cleaning. To analyze the topmost surface status, the SiC surfaces were determined at a tilt of 85° (Fig. 3.16). We confirmed that silicon dioxide films on the surface were removed by wet-chemical cleaning. Although the Ga cleaning was even more effective to remove the residual oxygen, just a little oxygen remained on the surface. This is because the residual oxygen is strongly adsorbed at the step edges with more dangling bonds or is newly adsorbed during the transfer or XPS measurement. Reflection high-energy electron diffraction (RHEED) patterns of 4H-SiC (0001) after pretreatments are shown in Fig. 3.17. The surface after gas etching is expected to be composed of a (1×1) structure due to the oxygen [22]. However, a $(\sqrt{3} \times \sqrt{3})$R30° phase was observed, as shown in Fig. 3.17 (a) and (b). Additionally, a (3×3) phase was observed after the Ga cleaning. 4H-SiC (0001) may adsorb excess Si on the surface after gas etching.

4H-SiC $(000\bar{1})$ surface

The XPS spectra of 4H-SiC $(000\bar{1})$ after pretreatment are shown in Fig. 3.18 and Fig. 3.19. Ga cleaning effectively removed the residual oxygen. The O $1s$ peak of the 4H-SiC $(000\bar{1})$ surface after the wet-chemical cleaning, however, was comparable to that after the Ga cleaning, because the $(000\bar{1})$ surface adsorbs less oxygen than the (0001) surface [23]. In addition to impurities, the C/Si ratio of SiC surfaces may affect AlN growth on the SiC substrate. In gas etching at a low pressure, silicon atoms can excessively evaporate during the temperature reduction. The C $1s$/Si $2p$ area ratio of the 4H-SiC (0001) and $(000\bar{1})$ surfaces was 0.7 and 1.2, respectively. This difference is attributed to the chemical nature of the emitter and scatter atoms, and the silicon forward scattering amplitude is twice that of carbon one [24]. The C $1s$/Si $2p$ area ratios of both 4H-SiC (0001) and $(000\bar{1})$ surface correspond the stoichiometry condition. Fig. 3.20 shows the RHEED patterns of 4H-SiC $(000\bar{1})$ after pretreatments. The surface reconstructed from (1×1) to $(\sqrt{3} \times \sqrt{3})$R30°. This

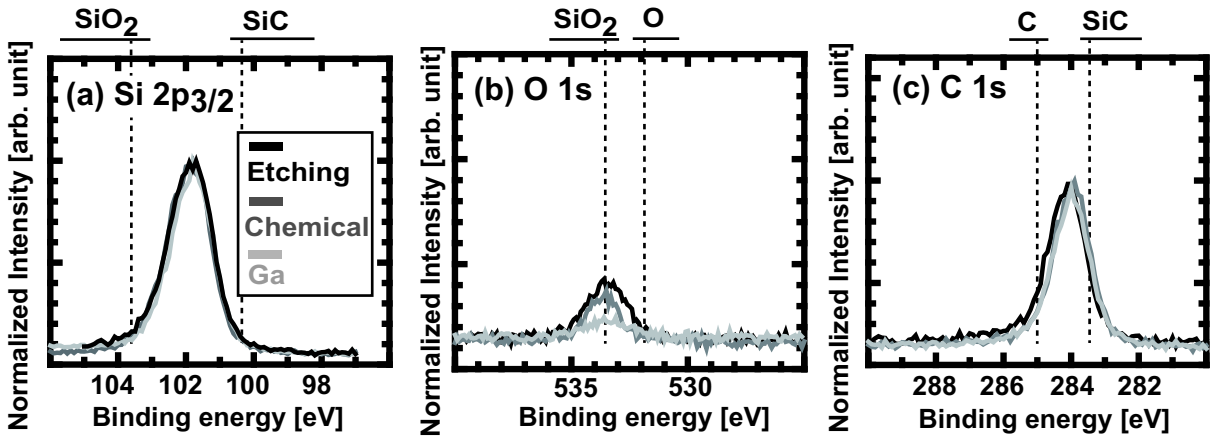

Figure 3.15: XPS spectra of (a) Si $2p3/2$, (b) O $1s$, and (c) C $1s$ obtained from 4H-SiC $(0001)_{\mathrm{Si}}$ surface after wet-chemical and Ga cleaning.

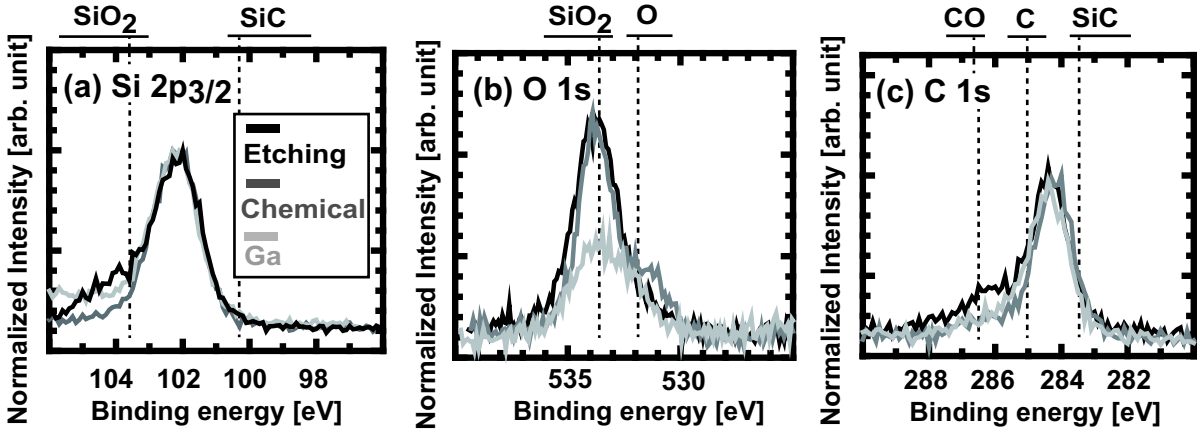

Figure 3.16: XPS spectra of (a) Si $2p3/2$, (b) O $1s$, and (c) C $1s$ obtained from 4H-SiC $(0001)_{\mathrm{Si}}$ surface tilted 85 ° after wet-chemical and Ga cleaning.

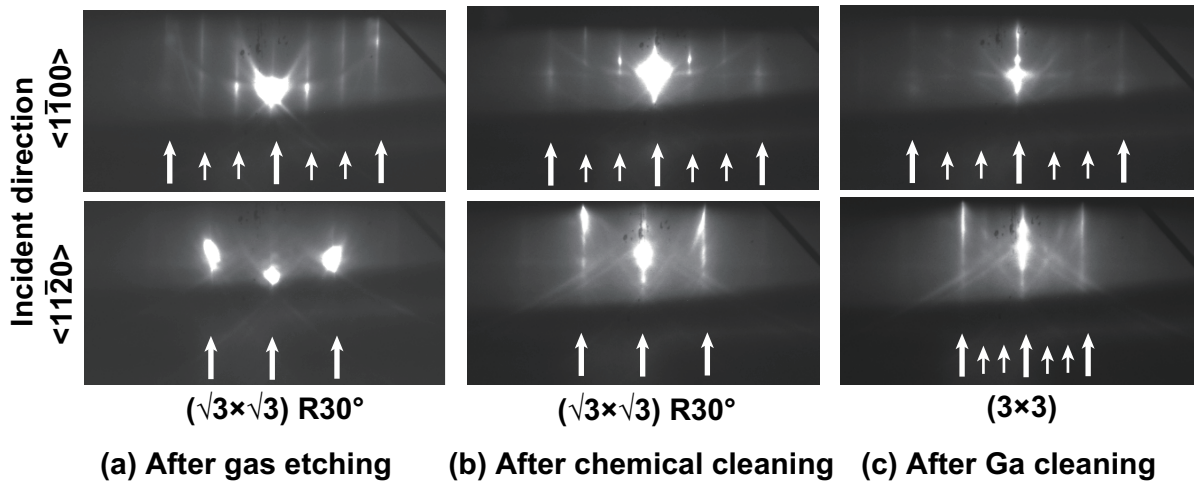

Figure 3.17: RHEED patterns of 4H-SiC $(0001)_{\mathrm{Si}}$ after (a) H_2-gas etching, (b) wet-chemical cleaning and (c) Ga cleaning.

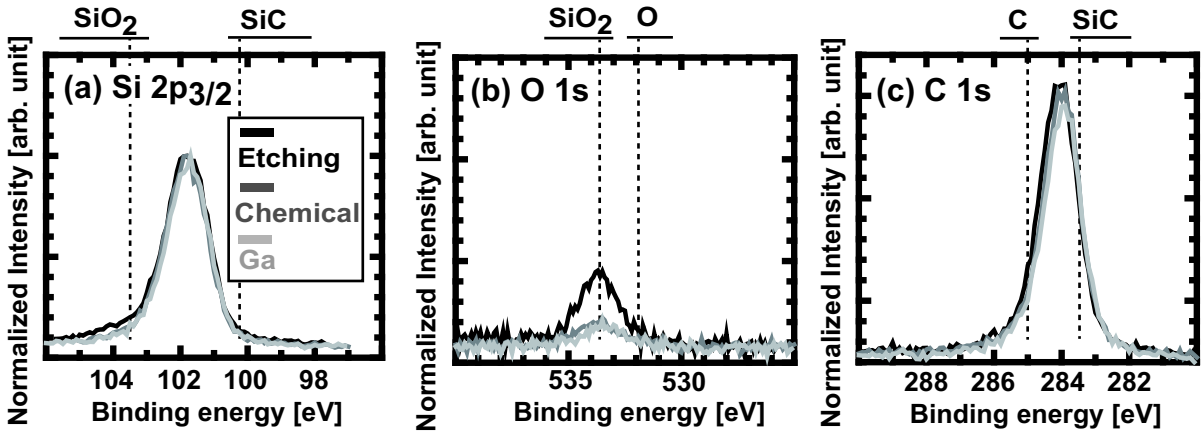

Figure 3.18: XPS spectra of (a) Si $2p3/2$, (b) O $1s$, and (c) C $1s$ obtained from 4H-SiC $(000\bar{1})_C$ surface after wet-chemical and Ga cleaning.

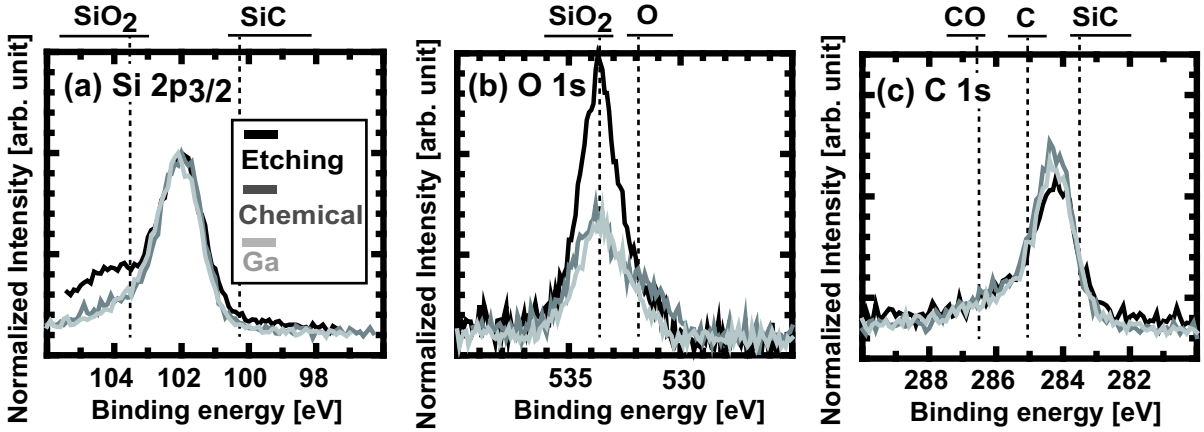

Figure 3.19: XPS spectra of (a) Si $2p3/2$, (b) O $1s$, and (c) C $1s$ obtained from 4H-SiC $(000\bar{1})_C$ surface tilted 85 ° after wet-chemical and Ga cleaning.

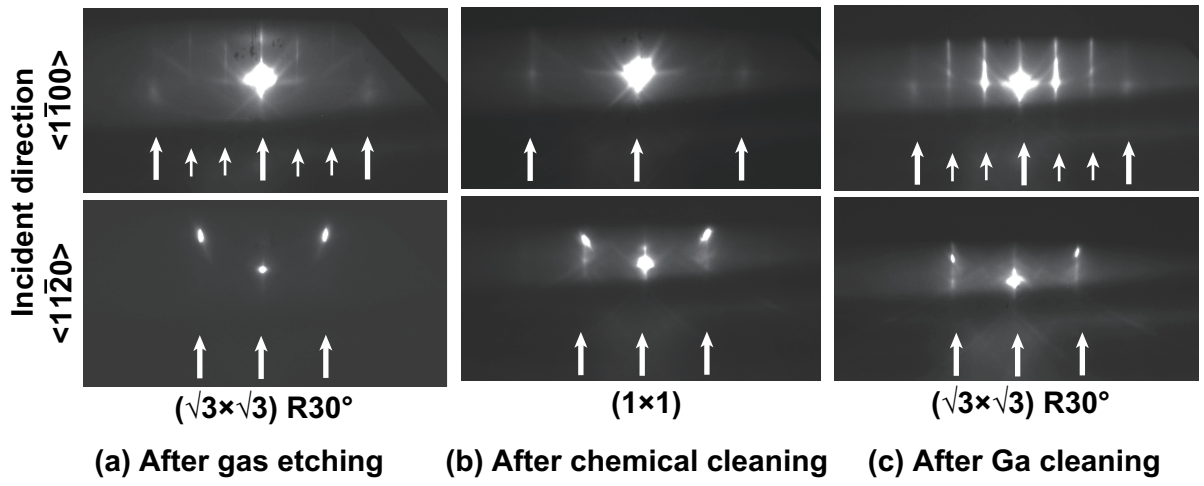

Figure 3.20: RHEED patterns of 4H-SiC $(000\bar{1})_C$ after (a) H_2-gas etching, (b) wet-chemical cleaning and (c) Ga cleaning.

is because 1/3 monolayer (ML) Si or Ga atoms were adsorbed on the surface by the Ga cleaning [20].

6H-SiC {0001} surface

The XPS spectra and RHEED patterns of 6H-SiC {0001} after pretreatment are shown in Fig. 3.21 and Fig. 3.22. As with 4H-SiC {0001}, the residual oxygen on 6H-SiC {0001} was considerably reduced by the Ga cleaning. The surface structure of the 6H-SiC {0001} was also reconstructed from (1×1) to $(\sqrt{3}\times\sqrt{3})$R30°. We found that the chemical condition of the 6H-SiC (0001) surface had the same tendency as that of the 4H-SiC (0001).

3.3.2 Discussion

Bernhardt *et al.* reported that H_2-gas etching of the SiC (0001) surface and subsequent exposure to oxygen in ambient air produced a highly-ordered $(\sqrt{3}\times\sqrt{3})$R30° silicate adlayer [25], corresponding to our results. They carried out quantitative low-energy electron diffraction (LEED) analysis of the $(\sqrt{3}\times\sqrt{3})$R30° phase and detected a SiO_x overlayer on the SiC substrate. A schematic diagram of the surface structure with a silicate adlayer has been proposed (Fig. 3.23 (a)). It was suggested that the two silicon atoms per unit cell of this adlayer formed a honeycomb arrangement [25]. Each oxygen atom is connected to two of the silicon atoms, completing a ring-type structure. The silicate and substrate are not connected by Si-Si bonds but by linear bridges by oxygen, Si-O-Si. This structure, which maintains a high degree of order even during exposure to ambient air, is stable up to 1000°C in ultra-high vacuum (UHV) conditions due to the saturation of all the dangling bonds. Elsbergen *et al.* reported that Si-O-Si can be removed by HF-wet-chemical cleaning [23]. This is the reason why the O 1*s* peak was reduced by the chemical cleaning. On the other hand, on the SiC $(000\bar{1})$, the silicon atoms are bound to the carbon atoms of the topmost SiC bilayer in the surface normal direction (Fig. 3.23 (b)) [23]. We consider that less adsorbed oxygen on SiC $(000\bar{1})$ is attributed to the structure of the silicate adlayer.

3.4 Summary

In this chapter, step-height and chemical-status controls of SiC {0001} surfaces were explained. H_2-gas-etching treatments in a hot-wall CVD reactor were effective for the step-height control as well as the removal of polishing damages of SiC {0001} surfaces. The 6-bilayer-high steps were achieved in their 30% area of the 2-inch 6H-SiC (0001) wafers, and 3-bilayer-high steps were uniformly achieved in the whole area of them. 6H-SiC $(000\bar{1})$ with 3-bilayer-high steps and 4H-SiC {0001} with 2-bilayer-high steps were also uniformly obtained. In addition, we confirmed that *ex-situ* wet-chemical and *in-situ* Ga cleaning procedures removed residual oxygen on all the SiC {0001} surfaces.

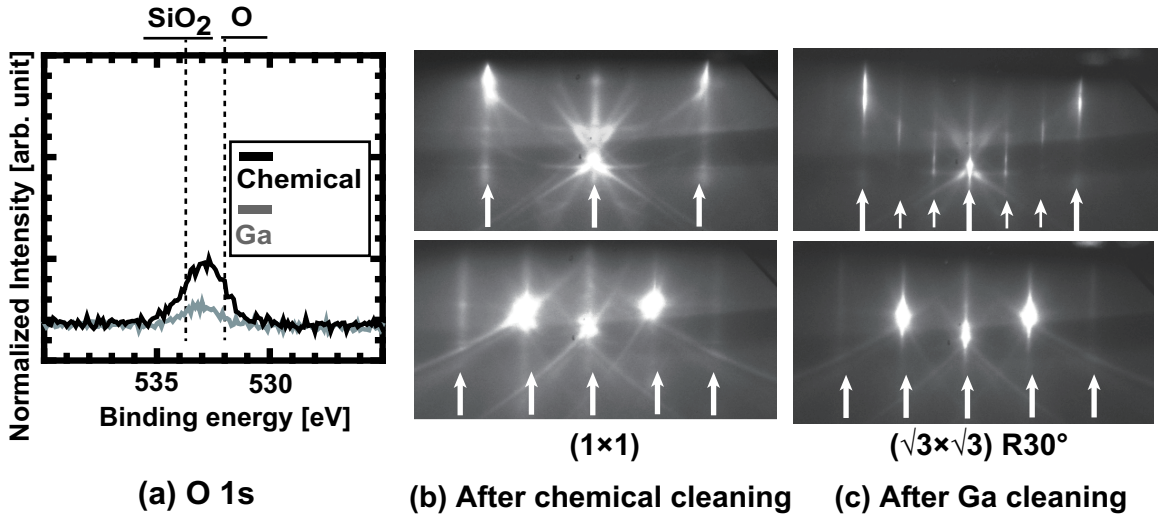

Figure 3.21: (a) XPS spectra of O 1*s* obtained from 6H-SiC $(0001)_{\mathrm{Si}}$ surface after chemical and Ga cleaning. RHEED patterns after (b) wet-chemical cleaning and (c) Ga cleaning.

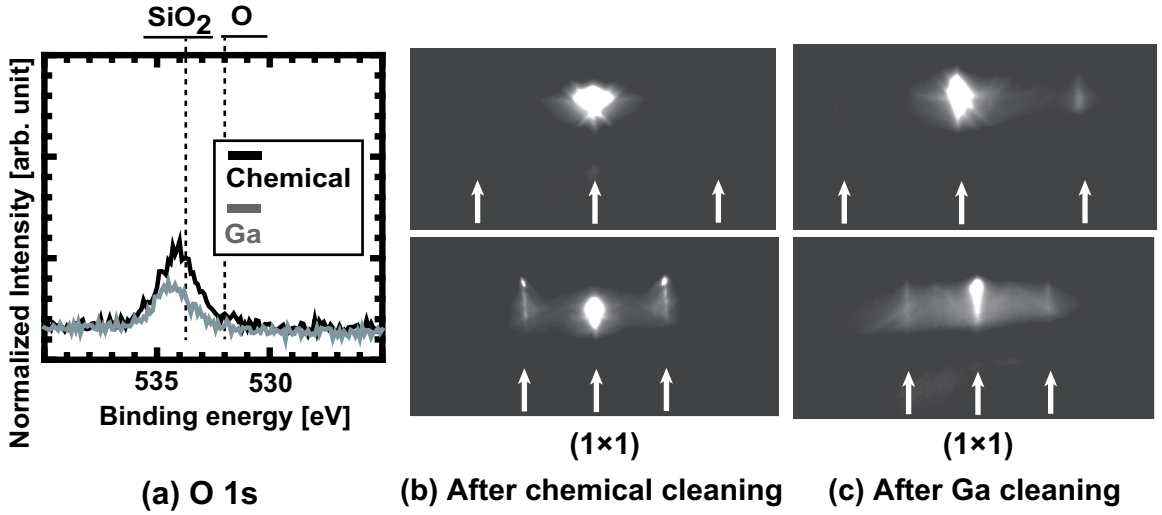

Figure 3.22: (a) XPS spectra of O 1*s* obtained from 6H-SiC $(000\bar{1})_{\mathrm{C}}$ surface after chemical and Ga cleaning. RHEED patterns after (b) wet-chemical cleaning and (c) Ga cleaning.

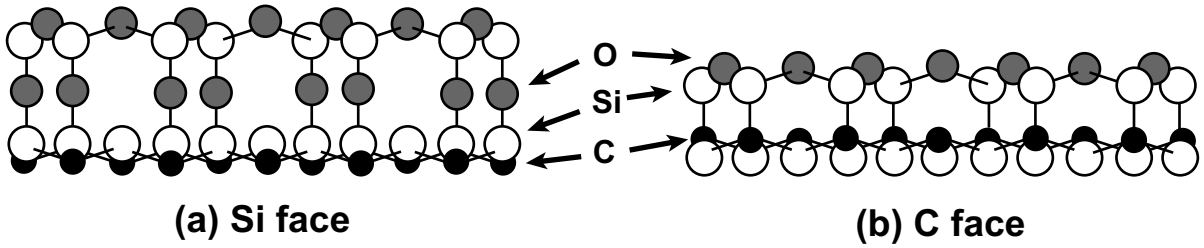

Figure 3.23: Sideview of oxide structures on (a) SiC $(0001)_{\mathrm{Si}}$ and (b) SiC $(000\bar{1})_{\mathrm{C}}$ in $[1\bar{1}00]$ projection.

In the next chapter, AlN growth on these SiC substrates with half- or one-unit-cell-high steps is performed in the MBE system. By focusing on an AlN/SiC interface and initial growth stage, we try to improve crystalline quality of the AlN layers.

References

[1] G. Ferro, H. Okumura, and S. Yoshida, J. Cryst. Growth **209**, 415 (2000).

[2] R. F. Davis, S. Tanaka, and R. S. Kern, J. Cryst. Growth **163**, 93 (1996).

[3] S. Yamada, J. Kato, S. Tanaka, I. Suemune, A. Avramescu, Y. Aoyagi, N. Teraguchi, and A. Suzuki, Appl. Phys. Lett. **78**, 3612 (2001).

[4] F. Owman, C. Hallin, P. Martensson, and E. Janzen, J. Cryst. Growth **167**, 391 (1996).

[5] L. Zhou, V. Aururier, and P. Pirouz, J. Electrochem. Soc. **144**, L161 (1997).

[6] V. Ramachandran, M. F. Brady, A. R. Smith, R. M. Feenstra, and D. W. Greve, J. Elect. Mat. **27**, 308 (1998).

[7] Z. J. Reitmeier, S. Einfeldt, R. F. Davis, X. Zhang, X. Fang, and S. Mahajan, Acta Mat. **58**, 2165 (2010).

[8] C. Hallin, F. Owman, P. Martensson, A. Ellison, A. Konstantinov, O. Kordina, and E. Janzén, J. Cryst. Growth **181**, 241 (1997).

[9] Z. Y. xie, C. H. Wei, L. Y. Li, Q. M. Yu, and J. H. Edgar, J. Cryst. Growth **217**, 115 (2000).

[10] A. A. Burk and L. B. Rowland, J. Cryst. Growth **167**, 586 (1996).

[11] S. Nakamura, T. Kimoto, and H. Matsunami, Appl. Phys. Lett. **76**, 3412 (2000).

[12] K. Akiyama, Y. Ishii, S. Abe, H. Murakami, Y. Kumagai, H. Okumura, T. Kimoto, J. Suda, and A. Koukitu, Jpn. J. Appl. Phys. **48**, 095505 (2009).

[13] T. Kimoto, A. Itoh, H. Matsunami, and T. Okano, J. Appl. Phys. **81**, 3494 (1997).

[14] V. Borovikov and A. Zangwill, Phys. Rev. B **79**, 245413 (2009).

[15] H. Nakagawa, S. Tanaka, and I. Suemune, Phys. Rev. Lett. **91**, 226107 (2003).

[16] A. Nakajima, H. Yokoya, Y. Furukawa, and H. Yonezu, Appl. Phys. Lett. **97**, 104919 (2005).

[17] H. Matsunami and T. Kimoto, Mat. Sci. Eng. **R20**, 125 (1997).

[18] E. D. Williams, R. J. Phaneuf, J. Wei, N. C. Bartelt, and T. L. Einstein, Surf. Sci. **294**, 219 (1993).

[19] J. Suda and T. Kimoto, Appl. Phys. Exp. **2**, 101603 (2009).

[20] N. Onojima, Dr. Thesis, Faculty of Engineering, Kyoto University, Kyoto, 2004.

[21] A. Nakajima, Y. Furukawa, S. Koga, and H. Yonezu, J. Cryst. Growth **265**, 351 (2004).

[22] K. Heinz, U. Starke, J. Bernhardt, and J. Schardt, Appl. Surf. Sci. **162**, 9 (2000).

[23] V. van Elsbergen, T. U. Kampen, and W. Monch, Surf. Sci. **365**, 443 (1996).

[24] L. Simon, J. L. Bischoff, and L. Kubler, Phys. Rev. B **60**, 11653 (1999).

[25] J. Bernhardt, J. Schardt, U. Starke, and K. Heinz, Appl. Phys. Lett. **74**, 1084 (1999).

Chapter 4

Growth of High-Quality AlN by Initial Growth Control

4.1 Introduction

In AlN growth on SiC substrates, surface structures and chemical status of the substrates were downplayed. These AlN layers had three-dimensional (3D) growth mode and were highly defective because a small lattice mismatch between AlN and SiC was insufficiently exploited [1–4]. By controlling surface status of the 6H-SiC (0001) substrates, Onojima *et al.* and Kim *et al.* achieved a layer-by-layer growth mode at an initial growth stage [5, 6]. However, an influence of step heights of SiC on the AlN layers has not been investigated because 3- and 6-bilayer-high steps mixed on the 6H-SiC substrates. In previous chapter, we obtained SiC {0001} with identical step heights at a large area. In this chapter, we grow AlN on SiC {0001} substrates with various step heights and investigate crystalline quality of their AlN layers.

To improve crystalline quality of an AlN layer, layer-by-layer growth mode from the first layer is necessary. However, in heteroepitaxial growth of AlN on SiC, no reflection high-energy electron diffraction (RHEED) intensity oscillation was observed at a very early growth stage [5]. The major factors to determine the growth mode are the surface energy of substrate, interface energy of the epilayer/substrate, and energy of epilayer. These energies should be reduced for two-dimensional (2D) growth mode. To improve a wettability of initial AlN growth, we propose group-Ⅲ-metal (aluminum (Al) or gallium (Ga)) pre-deposition just before growth. If SiC surfaces just before growth are covered with Ⅲ-metal, surface energy of the SiC substrates is expected to decrease, resulting in the 2D growth mode. In this chapter, optimal amount of metallic Al or Ga is deposited just before growth. In addition, we focus on the chemical surface status of SiC just before growth, and review a growth process again. By improving the growth process, layer-by-layer growth mode is achieved from the first layer.

4.2 Optimization of AlN Growth on SiC $(0001)_{Si}$

As SiC {0001} substrates, there are SiC $(0001)_{Si}$ and $(000\bar{1})_C$. In general, GaN layers grown on SiC (0001) and $(000\bar{1})$ planes have Ga polarity and N polarity, respectively [7]. It has been reported that the growth kinetics of Ga-polar and N-polar GaN layers is different; Ga-polar GaN has an advantage in crystalline quality. AlN is also expected to represent the same polarity as GaN on SiC {0001}, i. e., AlN on SiC (0001) and $(000\bar{1})$ are Al- and N-polar, respectively. In this section, the growth condition for the Al-polar AlN on SiC (0001) is optimized.

4.2.1 Experimental procedures

6H-SiC $(0001)_{Si}$ was treated by mechanical polishing (MP) and chemical mechanical polishing (CMP), whereas 4H-SiC $(0001)_{Si}$ was treated by MP and H_2-gas etching. 300-nm-thick AlN layers were grown on 6H-SiC (0001) by molecular-beam epitaxy (MBE). After growth, Al droplets were observed in half of the sample, indicating that AlN was grown under slightly Al-rich condition. Growth temperature ranged for 600–900°C, because the growth temperature of 500°C was too low for AlN growth to crystallize. To determine the polarity, the convergent beam electron diffraction (CBED) patterns of AlN on 6H-SiC {0001} were observed, as shown in Fig. 4.1. By comparing with the simulation data, the AlN layer grown on 6H-SiC (0001) was confirmed to have Al polarity.

4.2.2 Growth-temperature dependence

To examine growth mode, RHEED intensity profiles at an initial growth stage of AlN were investigated. The RHEED intensity profiles in 700 and 900°C growth are shown in Fig. 4.2. The RHEED intensity in the 700°C growth oscillated, indicating that the AlN layer has layer-by-layer growth mode. Just after starting the AlN growth, no RHEED intensity oscillated until 8 sec growth. We speculate that the AlN layers have 3D growth mode at very early growth stage.

The atomic force microscopy (AFM) images of the AlN layers are shown in Fig. 4.3. The AlN layer grown at 900°C had a step-and-terrace structure. The step height of the AlN layer was 1 Al-N bilayer (0.25 nm) and the step direction corresponded to an off direction of the SiC substrate, indicating that AlN was grown with the step-flow growth mode at high temperature. On the other hand, in low temperature growth, the layer-by-layer growth mode is likely to be realized because of a smaller Al migration. These results correspond to the Onojima's report [8].

In 600°C growth, a high density of spiral hillocks, 3×10^9 cm^{-2}, was observed. It has been reported that the spiral hillocks are resulted from screw-type threading dislocations (TDs) [9]. The density of the hillocks decreased with increasing the growth temperature and reached 8×10^6 cm^{-2} in the 900°C growth. The size of the hillocks increased

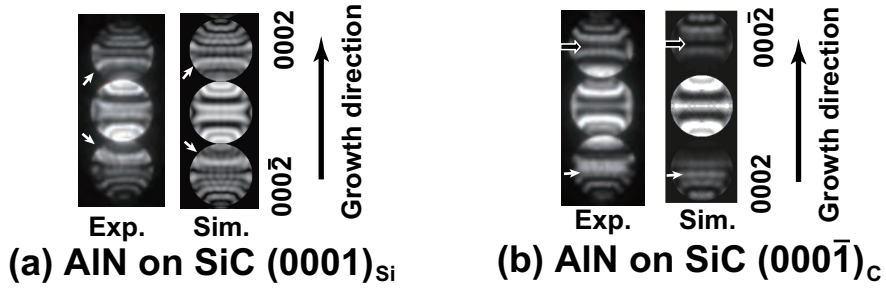

Figure 4.1: CBED patterns of (a) AlN on 6H-SiC $(0001)_{Si}$ and (b) AlN on 6H-SiC $(000\bar{1})_C$. Left side is experimental data and right side is simulation (a: 150 nm, b: 100 nm thickness).

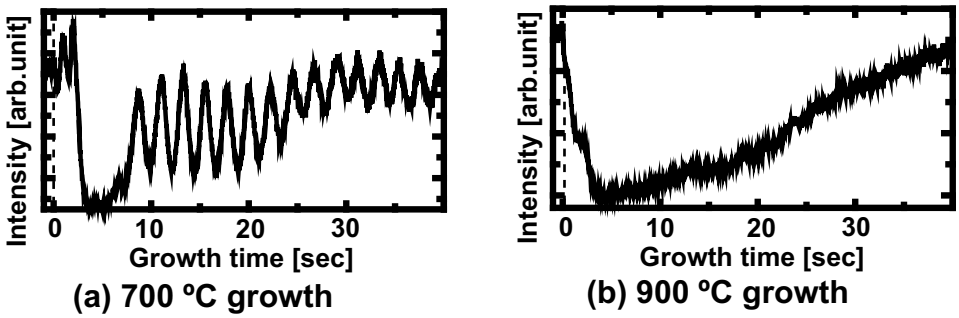

Figure 4.2: RHEED intensity profile of AlN growth on 6H-SiC (0001) at (a) 700 and (c) 900°C just after growth.

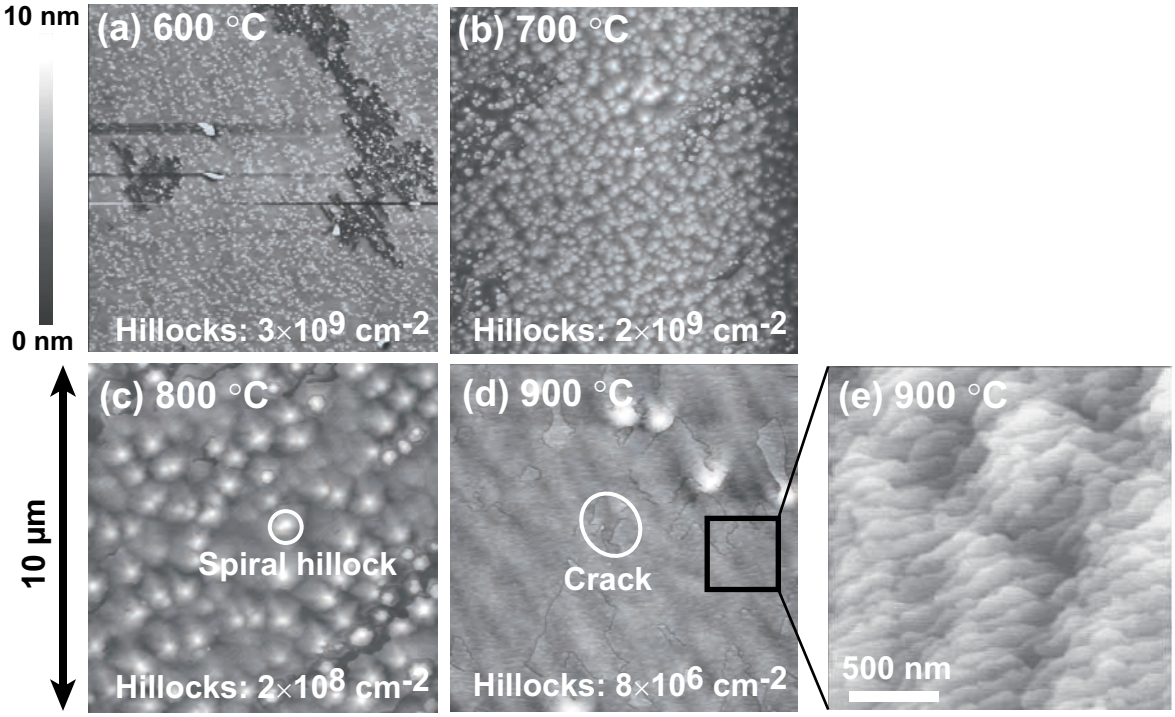

Figure 4.3: AFM images of 300-nm-thick AlN grown at (a) 600, (b) 700, (c) 800, and (d) 900°C on 6H-SiC (0001) treated by CMP.

with the growth temperature. The reason is described at Section 4.3.4. Only in the 900°C growth, there were micron-scale cracks due to difference of thermal expansion coefficient between AlN and SiC.

The crystalline qualities of AlN layers grown at various temperatures were investigated by x-ray diffraction (XRD). The full-width at half-maximum (FWHM) values for (0002) and $(01\bar{1}2)$ ω-scan diffraction peaks of the AlN layers are shown in Table 4.1 (a). The FWHM values for the (0002) diffraction peaks decreased with increasing growth temperature. X-ray rocking curves (XRCs) of the symmetric diffractions reflect on the out-of-plane rotation of columns perpendicular to the surface normal [10]. The spiral hillock density, or screw-type TDs, is supposed to affect the FWHM values for the (0002) diffractions. Meanwhile, the FWHM values for $(01\bar{1}2)$ diffraction peaks had little change for the growth temperature. This result disagrees with Onojima's results that the FWHM values for $(01\bar{1}2)$ diffraction peaks increased with growth temperature [8]. Although the layer-by-layer growth mode is enhanced at lower growth temperature, the control of the growth mode is effective in the just case of AlN growth on the atomically smooth SiC surfaces. Because our SiC surfaces without the gas etching are atomically rough, the enhancement of layer-by-layer growth mode is unbenefited.

4.2.3 Ⅲ/V-ratio dependence

300-nm-thick AlN layers were grown on 6H-SiC (0001) with various Ⅲ/V ratios at 700°C. The RHEED patterns after 300-nm growth in Al-rich and N-rich conditions are shown in Fig. 4.4. Both AlN layers after growth had a (1×1) phase [11]. The RHEED pattern of the AlN layer grown in the Al-rich condition was streak, while that in the N-rich condition showed the spotty pattern soon after growth, indicating a rough surface. Surface morphologies of the AlN layers grown in Al-rich, slightly Al-rich, and N-rich conditions are shown in Fig. 4.5. The AlN layer grown in the Al-rich condition had the step-flow growth mode with a spiral growth, while that in the N-rich condition had 3D growth mode. These results correspond to the RHEED pattern. We identified that AlN growth in the Al-rich condition was suitable for the smooth surface.

The FWHM values for (0002) and $(01\bar{1}2)$ ω-scan diffraction peaks of the AlN layers are shown in Table 4.1 (b). AlN growth under N-rich and excess Al-rich conditions exhibited low crystalline quality. Experiments show that epitaxial AlN thin films are generally superior under the Al-rich condition, which can be related to the presence of excess Al adlayers on surface. We confirmed that the slightly Al-rich condition was suitable for the high-quality AlN growth by MBE.

The AlN layers on 4H-SiC (0001) had the same tendency as that on 6H-SiC (0001): low growth temperature (600–700°C) and the slightly Al-rich condition is best to improve the crystalline quality of AlN. And then, the AlN layers had the layer-by-layer growth mode.

Table 4.1: FWHM values for (0002) and (01$\bar{1}$2) ω-scan diffraction peaks of AlN layers on 6H-SiC (0001) without gas etching; (a) temperature dependence and (b) Ⅲ/V ratio dependence at 700°C [arcsec]

(a) Temperature

	(0002)	(01$\bar{1}$2)
700°C	160	660
800°C	82	620
900°C	71	710

(b) Ⅲ/V ratio

	BEP [Pa]	(0002)	(01$\bar{1}$2)
Al rich	7.8×10^{-5}	570	1400
Slightly Al rich	7.3×10^{-5}	160	660
N rich	6.4×10^{-5}	410	1000

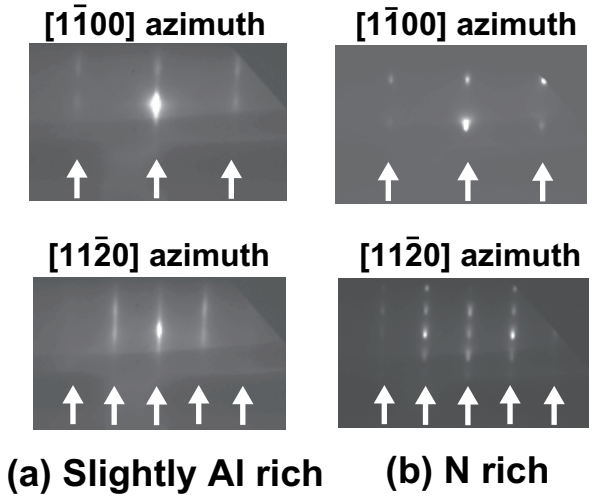

Figure 4.4: RHEED patterns after AlN growth on 6H-SiC (0001) with (a) slightly Al-rich and (b) N-rich conditions at 700°C.

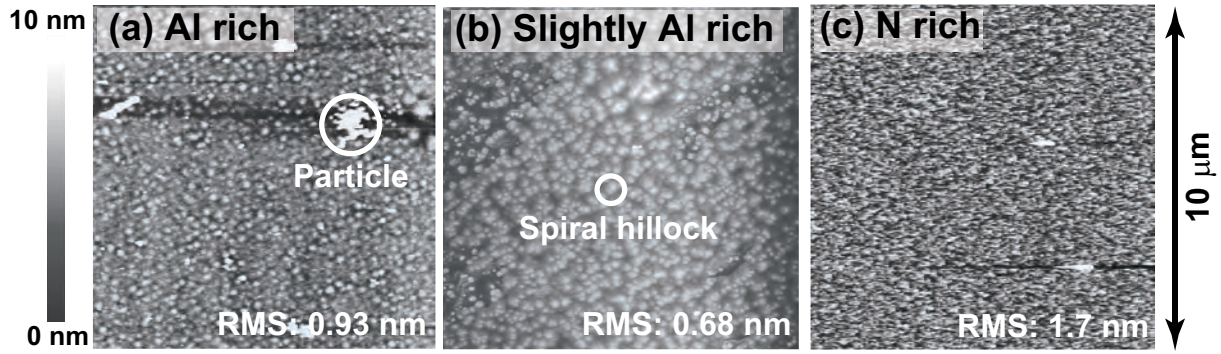

Figure 4.5: AFM images of AlN grown on 6H-SiC (0001) with (a) Al-rich, (b) slightly Al-rich, and (b) N-rich conditions at 700°C.

4.2.4 Discussion

Growth mode of AlN epilayer on SiC

Heteroepitaxial films are usually strained due to the lattice mismatch between an epilayer and a substrate. In the Volmer-Weber (VW) mode or 3D growth mode, the strain energy is elastically relaxed by lattice deformation in 3D nuclei. However, because the strain energy depends on the size of 3D nuclei and is different in each part of the nuclei, the lattice deformation causes incoherent coalescence of 3D nuclei, as shown in Fig. 4.6 (a), resulting in generation of numerous defects. Owing to the 3D growth mode, AlN grown on SiC (0001) in N-rich condition was high defective. To improve crystalline quality of AlN layers, Frank-van der Merwe (FM) mode or 2D growth mode is favorable (Fig. 4.6 (b)). This is the reason why Al-rich condition is suitable in high-quality AlN growth on SiC (0001) by MBE.

In a 2D growth mode, there are two types of growth mode: layer-by-layer and step-flow growth modes. In AlN growth on SiC {0001}, step-flow growth mode is unfavorable because of the polytype difference. AlN grown with the step-flow growth mode can follow the same polytype as the SiC substrate (Fig. 4.7 (a)). Actually, in AlN growth on nonpolar 4H-SiC, the 4H-AlN layer was realized by following the polytype of the substrate [12]. AlN grown on SiC {0001} with step-flow growth mode would have a 6H or 4H structure at the initial growth stage. However, the AlN layer with a wurtzite (2H) structure would grow on the 6H- or 4H-AlN layer because the 2H structure is the thermodynamically stable phase for AlN [7]. In the change of the crystal structure during growth, a high density of defects is generated at the interface of the different polytypes. On the other hand, AlN grown with layer-by-layer growth mode achieves the 2H structure from the first layer (Fig. 4.7 (b)), so that no defect is generated on the terrace of the SiC substrate. This is the reason why layer-by-layer growth mode is required for the higher-quality AlN growth on SiC {0001}.

Growth condition for layer-by-layer growth mode

Based on the BCF (Burton, Cabrera, and Frank) theory, a method to control the 2D growth mode is considered [13]. Adsorbed species diffuse on terraces toward steps. On the surface, the supersaturating ratio (α) takes a maximum value ($\alpha_{\max}$) at the center of the terrace. The $\alpha_{\max}$ is an essential parameter to determine the type of 2D growth mode, depending on the growth rate, growth temperature, and terrace width. In $\alpha_{\max} \geq$ a critical value (α_{crit}), step-flow growth mode is enhanced, while in $\alpha_{\max} \leq \alpha_{\mathrm{crit}}$, layer-by-layer growth mode is enhanced. Therefore, to realize layer-by-layer growth mode, both growth temperature and off angle of the substrate should be decreased. This explains that low growth temperature (600–700°C) enhanced layer-by-layer growth mode in AlN growth on SiC (0001). However, for 8 sec after starting AlN growth, no RHEED intensity oscillation was observed. To achieve the layer-by-layer growth mode from the first layer, the interface energy should be reduced by improving the wettability between the epilayer and the substrate.

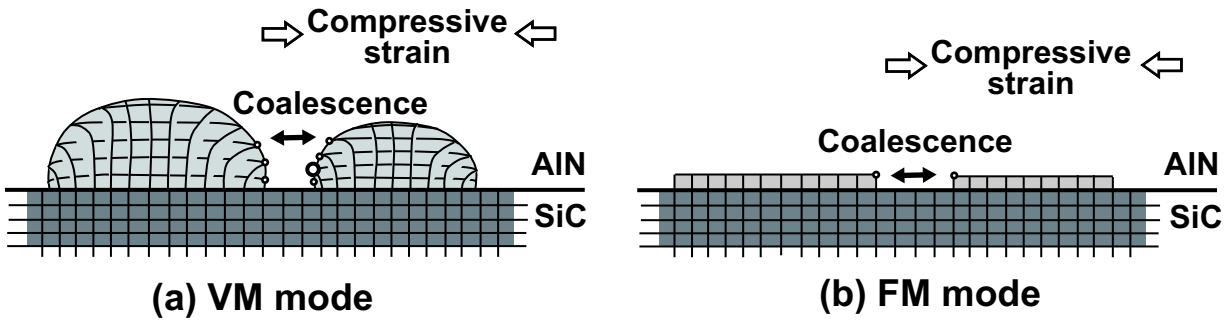

Figure 4.6: Schematic images of (a) incoherent coalescence of 3D nuclei with deformed lattices and (b) coherent coalescence of 2D nuclei.

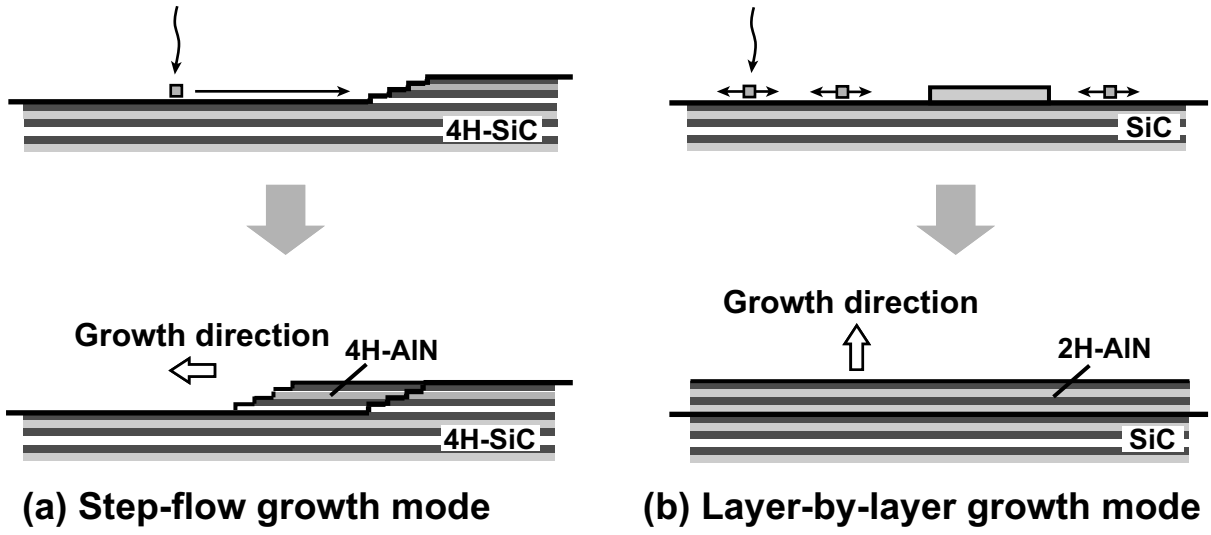

Figure 4.7: Schematic images of (a) 4H-AlN on 4H-SiC {0001} with step-flow growth mode and (b) 2H-AlN on SiC {0001} with layer-by-layer growth mode.

4.3 Effect of Step Height of SiC $(0001)_{Si}$ on AlN Epilayers

4.3.1 Experimental procedures

6H-SiC $(0001)_{Si}$ (vicinal angle $\sim$0.3°) substrates were used. The SiC substrates were treated by CMP and high-temperature H_2-gas etching. The standard condition for the H_2-gas etching is 1350°C, 30 min, and 20 Torr, as described in Section 3.2.3. The AFM images of 6H-SiC substrates after the gas etching are shown in Fig. 4.8 (a)-(c). Sample A with a $\langle 1\bar{1}00\rangle$-off direction had 6-bilayer-high steps, as shown in Fig. 4.8 (a), while sample B with a $\langle 11\bar{2}0\rangle$-off direction had 3-bilayer-high steps (Fig. 4.8 (b)). Sample C with the $\langle 11\bar{2}0\rangle$-off direction was treated by the gas etching in the higher pressure (100 Torr). With increasing pressure, the 3-bilayer-high steps of the 6H-SiC substrate are decomposed into 1+2 bilayer steps, as described in Section 3.2.1. We used this substrate as a SiC surface with 1-bilayer-high steps. In addition, the 6H-SiC substrate with an off direction near $\langle 1\bar{1}00\rangle$ sometimes includes both 3- and 6-bilayer-high steps. This substrate (sample D) was used to investigate the dependence of step heights of the SiC surface on defect structures in the AlN epilayers. After *in-situ* wet-chemical cleaning and *ex-situ* Ga cleaning procedures, AlN layers were directly grown on the SiC substrates at 700°C by MBE.

4.3.2 Surface morphology and crystalline quality of AlN epilayers

The surface morphologies of the AlN layers in samples A-C are shown in Fig. 4.8 (d)-(f). Due to the step-height control of SiC, all AlN layers exhibited a step-and-terrace structure with the 1-bilayer-high steps, indicating the step-flow growth mode. A step direction of the AlN layer corresponded to that of the SiC substrate. The terrace widths ($\sim$70 nm) of the AlN layers in sample A were sixth part of those ($\sim$400 nm) of the SiC substrates, i. e., an off angle of the AlN layer are consistent with that of the SiC substrate. In addition to the step-and-terrace structure, spiral-growth hillocks corresponding to screw-type TDs were observed. The spiral hillock densities of samples A and B were $\sim 10^7$ cm^{-2} (in an area of 10×10 μm^2), while that of sample C was 5×10^8 cm^{-2}, indicating that crystalline quality of sample C is inferior to others. Most spiral hillocks of sample C are formed into lines with a separation of $\sim$700 nm (Fig. 4.8 (f)), corresponding to a separation between steps of the SiC substrate (Fig. 4.8 (c)). The hillocks of sample A and B are randomly distributed. Although the spiral height of a 2H-AlN layer is supposed to be one-unit-cell height or 1**c**, the spiral height was **c**/2 (0.25 nm).

The FWHM values for the (0002) and $(01\bar{1}4)$ ω-scan diffraction peaks of AlN layers in samples A-C are given in Table 4.2. For the (0002) peaks, the FWHM values of all AlN layers were quite small, around 60 arcsec. The screw-type TD, which has the Burgers vector with a [0001] component, increases a FWHM value of the (0002) diffraction [10]. The influence of the screw-type TDs with the density less than 10^8 cm^{-2}, however, may be undetectable

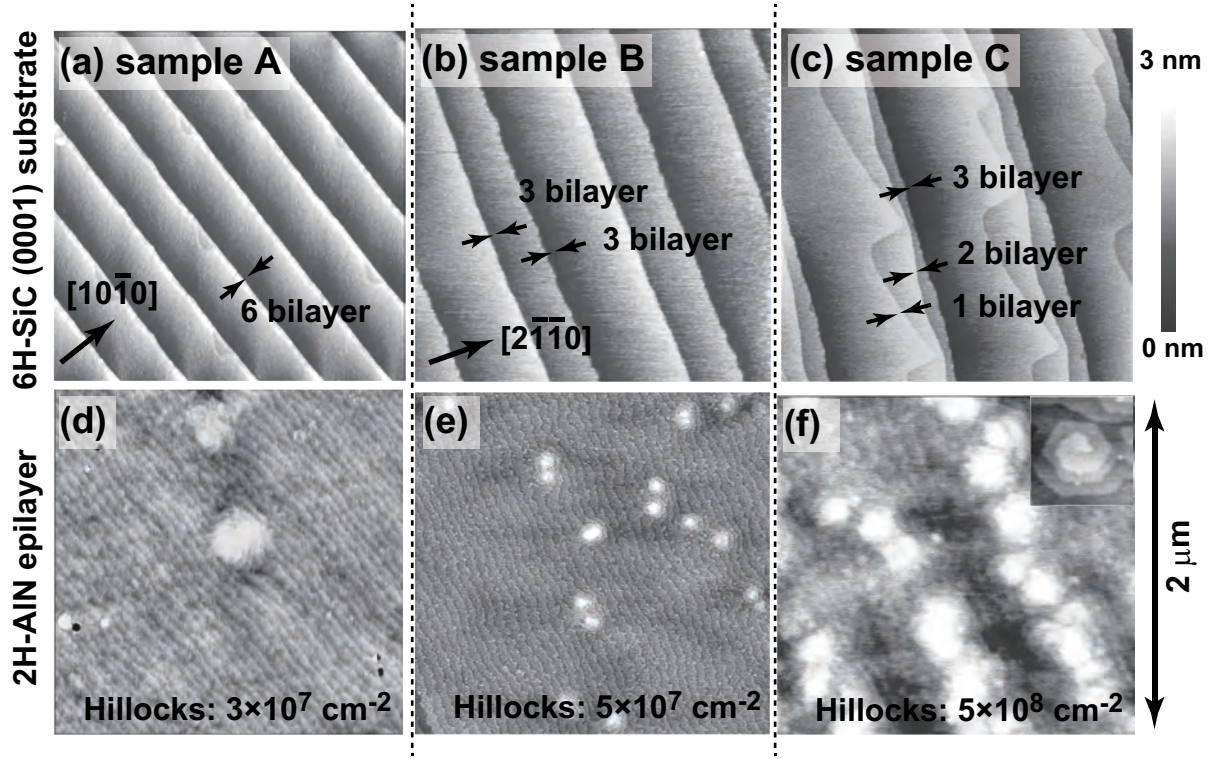

Figure 4.8: AFM images before and after AlN growth on vicinal 6H-SiC $(0001)_{Si}$ substrates with various step heights. SiC substrates of (a, d) sample A, (b, e) sample B, and (c, f) sample C have 6-, 3-, and 1-bilayer-high steps, respectively.

Table 4.2: FWHM values for (0002), $(01\bar{1}4)$, and $(01\bar{1}2)$ ω-scan diffraction peaks of 300-nm-thick AlN layers (samples A-E) on 6H-SiC (0001) with controlled surface structures [arcsec].

Sample	6H-SiC (0001) surface	(0002)	$(01\bar{1}4)$	$(01\bar{1}2)$
A	6-bilayer-high steps	61	370	620
B	3-bilayer-high steps	55	410	720
C	1-bilayer-high steps	62	700	990
E	3-bilayer-high steps with sacrificial oxidation process	57	86	62

in XRCs. On the other hand, edge-type TDs form no spiral hillocks. To evaluate edge-type TDs, XRC for asymmetrical diffraction is powerful tool. For the $(01\bar{1}4)$ peaks, the FWHM values for samples A and B were about 400 arcsec, while that for sample C was much larger (700 arcsec), indicating the higher density of edge-type TDs in sample C. Here, one puzzling result is that the crystalline quality of the AlN layer grown on 3-bilayer-high steps (sample B) was almost identical to that of the AlN layer grown on 6-bilayer-high steps (sample A). We believed that 6-bilayer-high steps were necessary for high-quality AlN growth on a 6H-SiC substrate, because the height of three units of 2H-AlN is equal to the 6-bilayer height. The 6H-SiC substrate with 3-bilayer-high steps was supposed to be unsuitable for the AlN growth, because stacking mismatch boundaries (SMBs) are generated. However, the crystalline quality of the AlN layer on 3-bilayer-high steps was equivalent to that on 6-bilayer-high steps.

4.3.3 Extended-defect structures in AlN epilayers

AlN layer on 6H-SiC with 3-bilayer-high steps

Bright-field plan-view transmission electron microscopy (TEM) images of the AlN layer on 6H-SiC with 3-bilayer-high steps are shown in Fig. 4.9 (a: [0001] zone-axis, b: with 15° tilt). Dark spots are TDs. As seen in Fig. 4.9 (a), TDs are arranged in rows with a separation of ∼100 nm, corresponding to the terrace width of the SiC substrate before growth. A direction perpendicular to the TD rows was 10° from $\langle 11\bar{2}0\rangle$, corresponding to the off direction of the SiC substrate. These results suggest that the TDs are generated at the step edges of the SiC substrate. A schematic diagram of defect structures in the AlN layer is shown in Fig. 4.10. Surprisingly, no SMB was observed in the AlN layer on 6H-SiC with 3-bilayer-high steps. The threading dislocation density (TDD) was 2×10^{10} cm^{-2} in an area of 200×200 nm^2. As shown in Fig. 4.9 (b), TDs were also observed on the terraces of the SiC substrate. The TDD on the terraces of SiC was 3×10^8 cm^{-2} and almost two orders of magnitude smaller than that generated at the step edges of SiC.

Dark-field cross-sectional TEM images of the AlN layer on 6H-SiC with 3-bilayer-high steps are shown in Fig. 4.11 (a: $\mathbf{g}$=0002, b: $\mathbf{g}$=$11\bar{2}0$). All TDs were generated at an AlN/SiC interface. The number of TDs was significantly more for the diffracting condition $\mathbf{g}$=$11\bar{2}0$ than for $\mathbf{g}$=0002. This implies that most TDs have $\mathbf{b}$=$1/3\langle 11\bar{2}0\rangle$ components, or pure edge type, according to the $\mathbf{g}\cdot\mathbf{b}$ invisibility criterion. The screw-type TDD is estimated to be $\sim 10^7$ cm^{-2}, corresponding to spiral hillock densities in the AFM image.

AlN layer on 6H-SiC with 6-bilayer-high steps

A bright-field plan-view TEM image of an AlN layer on a 6H-SiC (0001) substrate with both 3- and 6-bilayer-high steps (sample D) is shown in Fig. 4.12 (b). The TD rows were observed again and some TD rows were split in two. In terms of the separation width, a 6-bilayer-high step is thought to be split in two 3-bilayer-high steps, indicating that AlN layers on 6H-SiC with 6-bilayer-high steps also have the TD rows. No SMB was observed.

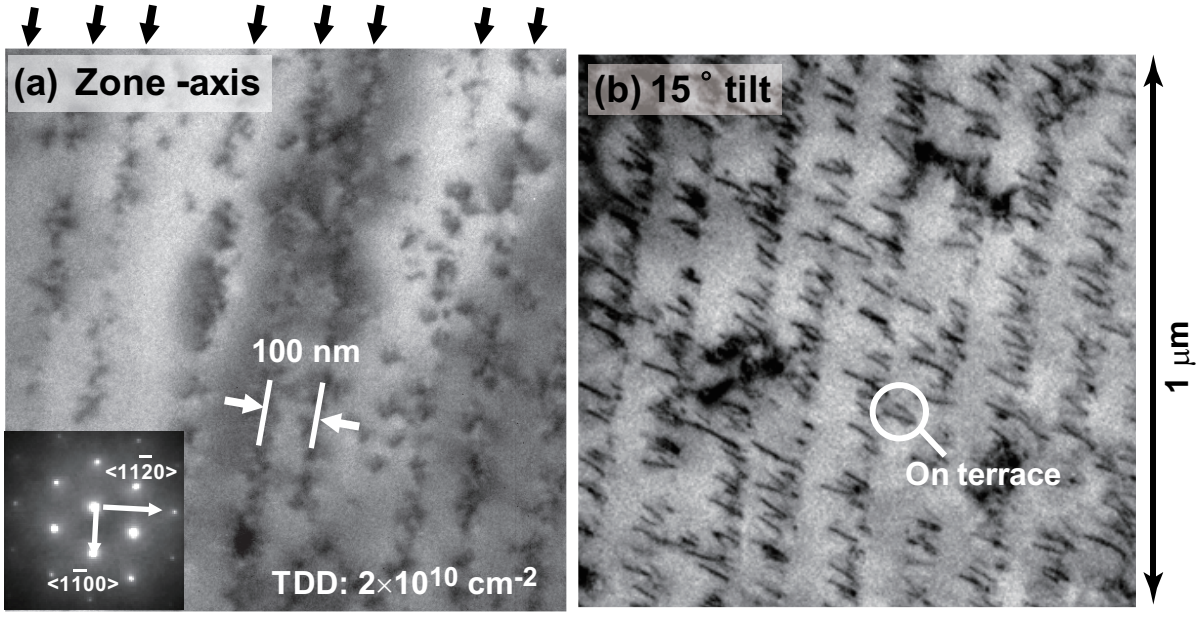

Figure 4.9: Bright-field plan-view TEM image of AlN layer on 6H-SiC (0001) substrate with 3-bilayer-high steps (a: zone-axis, b: 15° tilt).

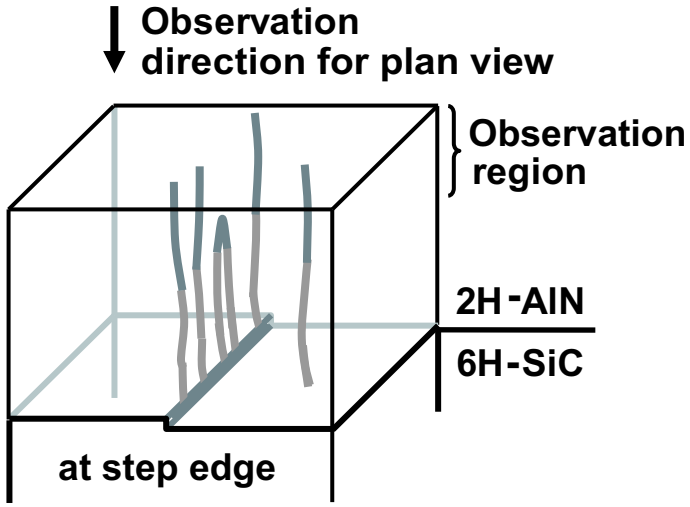

Figure 4.10: Schematic figure of defect structures in AlN layer on 6H-SiC (0001) substrate with 3-bilayer-high steps.

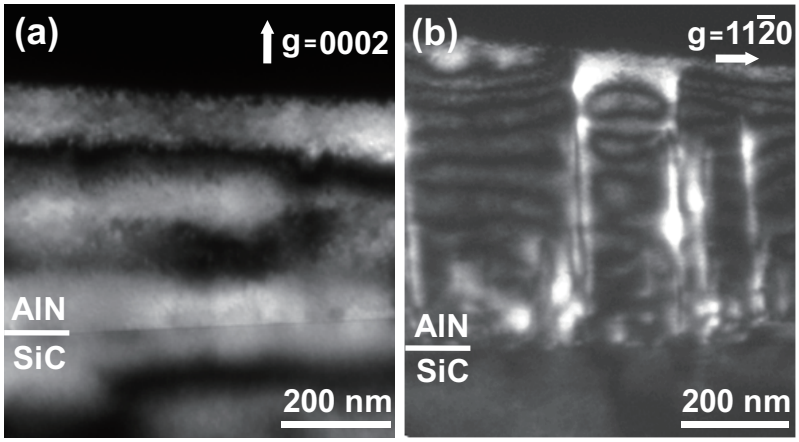

Figure 4.11: Dark-field cross-sectional TEM images of AlN layer on 6H-SiC (0001) with 3-bilayer-high steps (a: **g**=0002, b: **g**=11$\bar{2}$0).

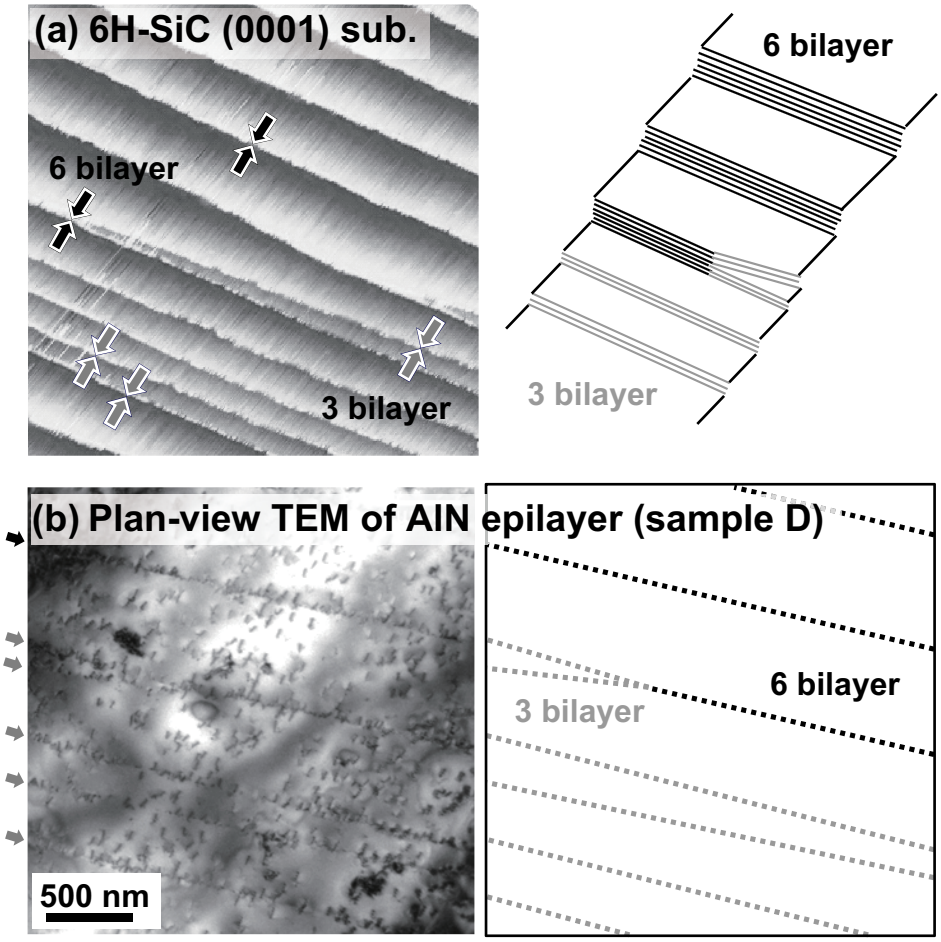

Figure 4.12: (a) Surface morphology of 6H-SiC (0001) with both 3- and 6-bilayer-high steps and (b) bright-field plan-view TEM image of AlN layer (sample D) on its substrate.

4.3.4 Discussion

Stacking arrangements of topmost SiC surfaces after gas etching

An unit cell of 6H-SiC consists of 6 Si-C bilayers stacked in a sequence following the ABCACB arrangement. The 6H-SiC surface terminates with three possible patterns for the stacking arrangement: (a) ABC/ACB, (b) BCA/CBA, and (c) CAC/BAB (Fig. 4.13). In the AlN layer on 6H-SiC with 3-bilayer-high steps, no SMBs were observed. We found that in these patterns, only the arrangement terminated by BCA/CBA (pattern (b)) would enable AlN growth without SMBs. During the gas etching, the arrangements terminated by ABC/ACB (pattern (a)) is favorable due to smaller surface energy, as described in Section 3.2.2. However, after the gas etching, a topmost SiC surface is oxidized due to exposure to air, as shown in Fig. 4.14 (a) [8]. The oxide films are removed by the wet-chemical and Ga cleaning procedures, so that the surface termination just before AlN growth becomes BCA/CBA (pattern (b)). AlN layers on SiC surfaces with the pattern (b) have BCBC... or CBCB... arrangements, resulting in no SMBs (Fig. 4.13 (b)).

As a generation source of TD rows, a conversion from SMBs is considered. No SMBs are supposed to be generated on 6H-SiC with 6-bilayer-high steps. However, the TD rows were observed in AlN layers on 6H-SiC with both 3- and 6-bilayer-high steps, suggesting that SMBs are inconvertible into TD rows. Another possibility is a partial dislocation generated between different stacking arrangements. If the AlN layers have two types of stacking arrangements on an identical terrace of the SiC substrates, partial dislocations are generated between them (Fig. 4.15). A first-AlN bilayer on the terrace of SiC has the same site (site B) as the stack layer below the topmost surface (site C). On the other hand, a first-AlN bilayer near the step edges of SiC has site A due to adsorption into step edges of SiC, so that partial dislocations are generated just near the step edge of the substrate. We consider that these partial dislocations form TD rows as follows. It can be understood as well-known decomposition of perfect dislocation b_1 into two partial dislocations b_2 and b_3: the directions of Burgers vector b_1 is $\langle 11\bar{2}0\rangle$, while that of Burgers vectors b_2 and b_3 are $\langle 1\bar{1}00\rangle$. The Burgers circuit follows that b_1=b_2+b_3; for example, b_1=1/3[1$\bar{2}$10], b_2 = 1/3[0$\bar{1}$10], and b_3 = 1/3[1$\bar{1}$00]. The TDs with Burgers vector b_1 are generated from partial dislocations with b_2 and b_3, and extend to the growth direction [0001] during growth. Therefore, TDs rows are formed between AlN layers of A- and B-site. In this model, AlN layers on SiC substrates with 6-bilayer-high steps also can have TD rows. For $\langle 1\bar{1}00\rangle$ off directions, the partial dislocations must bend many times because the partial dislocations are parallel to $\langle 1\bar{1}00\rangle$ directions, but for just $\langle 11\bar{2}0\rangle$ off directions, the partial dislocations would be in a straight line, not extending to growth direction. To minimize TD rows, the off-direction control of the substrates may be effective. As other causes of TD-rows generation, impurities adsorbed at step edges and lattice mismatch (1%) between AlN and SiC are considered. Detail generation mechanism of TD rows are described in Section 5.3.

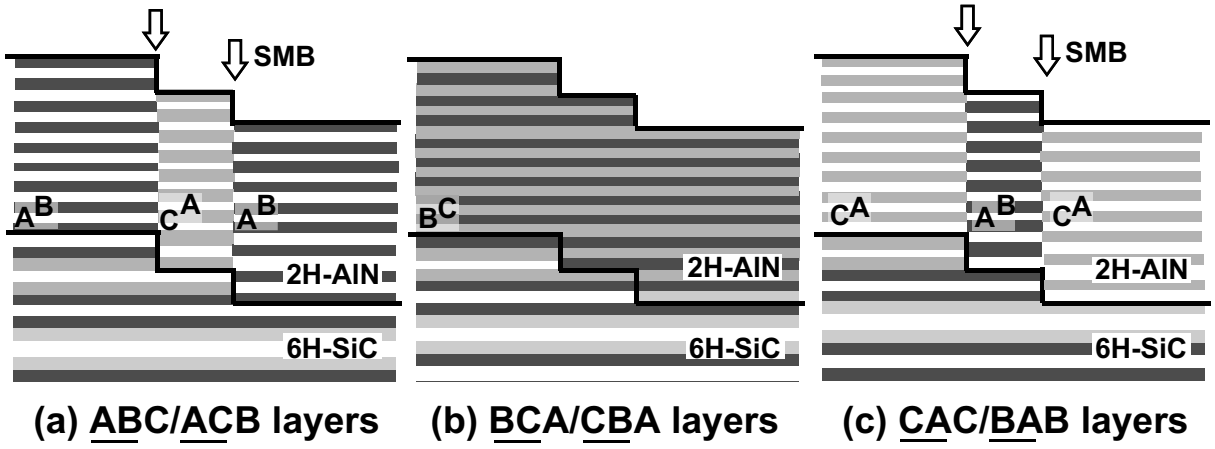

Figure 4.13: Stacking arrangements of 2H-AlN layer on 6H-SiC (0001) substrate with 3-bilayer-high steps. Three types of surface termination of SiC substrates are (a) ABC/ACB, (b) BCA/CBA, and (c) CAC/BAB layers.

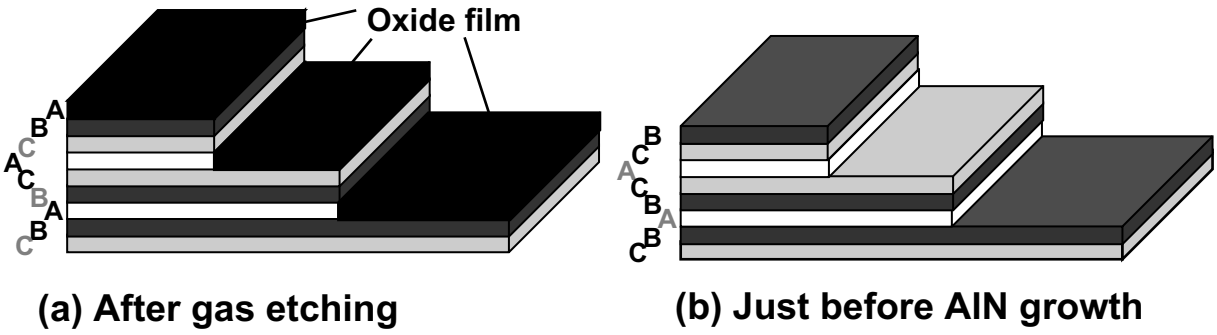

Figure 4.14: Surface termination of 6H-SiC (0001) with 3-bilayer-high steps (a) after gas etching (ABC/ACB layers) and (b) just before AlN growth (BCA/CBA layers).

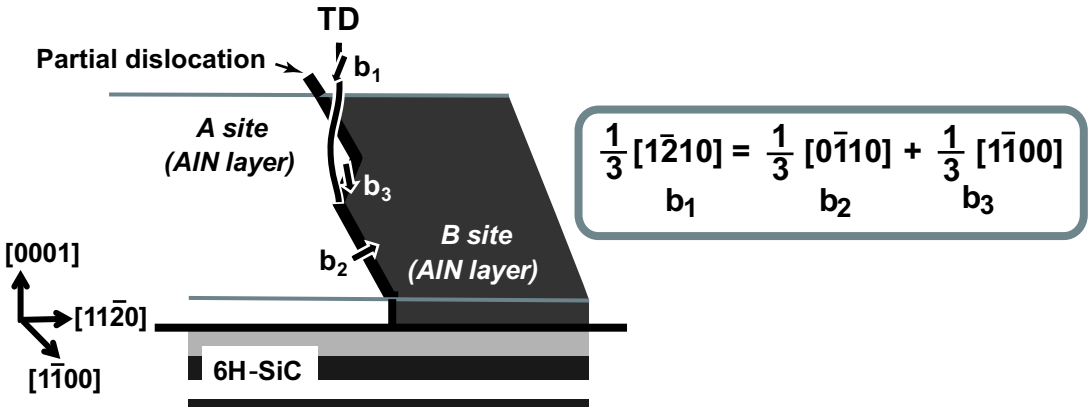

Figure 4.15: One of generation mechanisms of TD rows. Partial dislocations between different stacking arrangements generate TD; $1/3[0\bar{1}10] + 1/3[1\bar{1}00] = 1/3[1\bar{2}10]$ (TD).

Control of stacking arrangements of topmost SiC surfaces using sacrificial-oxidation process

We suggested that a 6H-SiC (0001) surface with 3-bilayer-high steps was terminated with BCA/CBA layers after the gas etching. If the topmost surface has the other pattern of stacking arrangements, SMBs should be generated in the AlN epilayer. To confirm this hypothesis, we carried out an additional sacrificial oxidation process after the gas etching. The process consists of 12-hour oxidation (forming an 80-nm-thick thermal oxide) and removal of the thermal oxide in HF solution. The 3-bilayer-high steps remained on the surface after this process. A 250-nm-thick AlN layer (sample E) was grown at 700°C. For the $(01\bar{1}2)$ peak, the FWHM value of the AlN layer was quite small, 62 arcsec.

Bright-field plan-view TEM images of the AlN layer are shown in Fig. 4.16 (a: [0001] zone-axis, b: 25 ° tilt). Many dark lines instead of TD rows were observed with zone axis and became bands with interference fringes in the tilted view, clearly indicating that they are planar defects threading through the AlN layer. The typical separation of the planar defects is ∼100 nm corresponding to the terrace width of the SiC substrate before growth. Based on these results, we believe that these planar defects are SMBs generated at the step edges of the SiC substrate. The SMBs consisted of $\{11\bar{2}0\}$ planes, as shown in Fig. 4.16 (a). Although the step edges of the SiC surface were straight, the SMBs formed continuous zigzag lines corresponding to the step direction of the SiC substrate. This is because the off direction of the SiC substrate is displaced by 10° out of $\langle 11\bar{2}0\rangle$. As shown in Fig. 4.17, all SMBs formed closed loops. The reason why some SMBs are generated on the SiC terraces is explained as follows. The oxide thickness by sacrificial oxidation is supposed to fluctuate significantly at the atomic scale. After the oxide removal, the step heights and stacking arrangements of the revealed SiC top layer may vary from position to position. Due to these fluctuations, some steps have no SMBs and other steps have SMBs.

As expected, SMBs were observed in the AlN layer on 6H-SiC (0001) with 3-bilayer-high steps and were inconvertible into TD rows. As discussed, the 6H-SiC substrate can have three patterns of surface terminations. We conclude that the stacking arrangement of the topmost SiC surface with the sacrificial oxidation process was ABC/ACB or CAC/BAB, generating SMBs in the AlN epilayer. On the other hand, the stacking arrangement without the sacrificial-oxidation process is BCA/CBA, generating TD rows instead of SMBs. Therefore, the 6H-SiC (0001) substrate with 3- and 6-bilayer-high steps enables AlN growth without SMBs unless the sacrificial oxidation is conducted. In particular, the substrate with the 3-bilayer-high steps may be profitable for AlN growth because it can be obtained in whole area of 2-inch wafer (Section 3.2.3).

As shown in Fig. 4.16 (a), TDs as well as the SMBs were observed on the terraces of SiC before growth. The TDD was 6×10^8 cm^{-2}. The very small FWHM value of the $(01\bar{1}4)$ diffraction peak is consistent with a small TDD. The SMBs may be detectable by X-ray. The detail of the SMBs is described in Section 5.2.

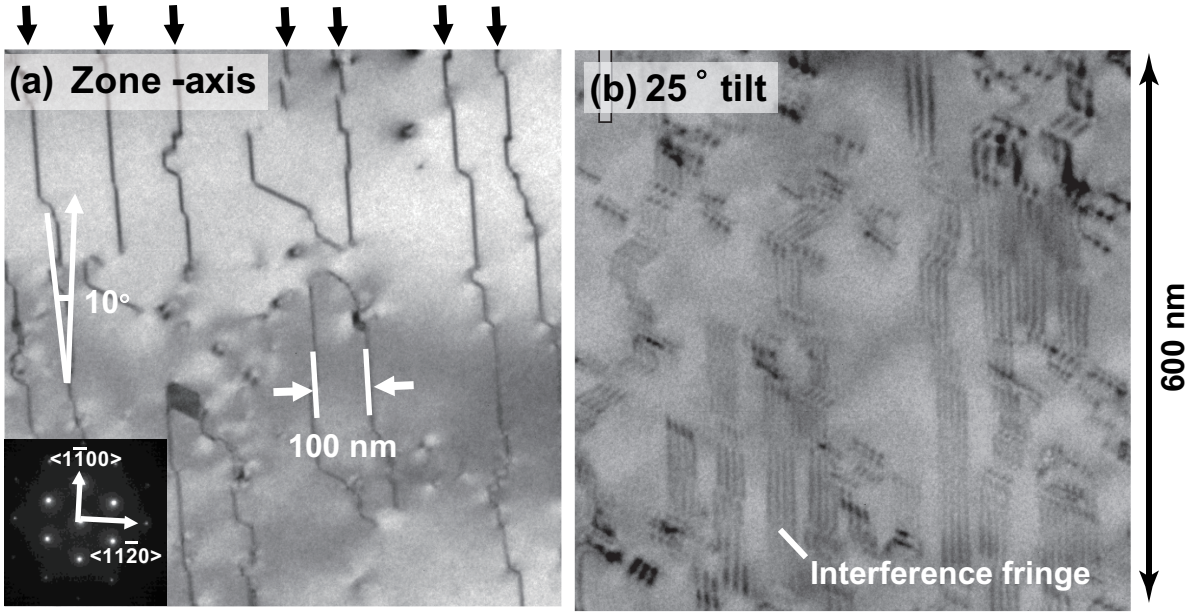

Figure 4.16: Bright-field plan-view TEM images of AlN layer on 6H-SiC (0001) with 3-bilayer-high steps after sacrificial oxidation process (a: [0001] zone-axis, b: 25 ° tilt).

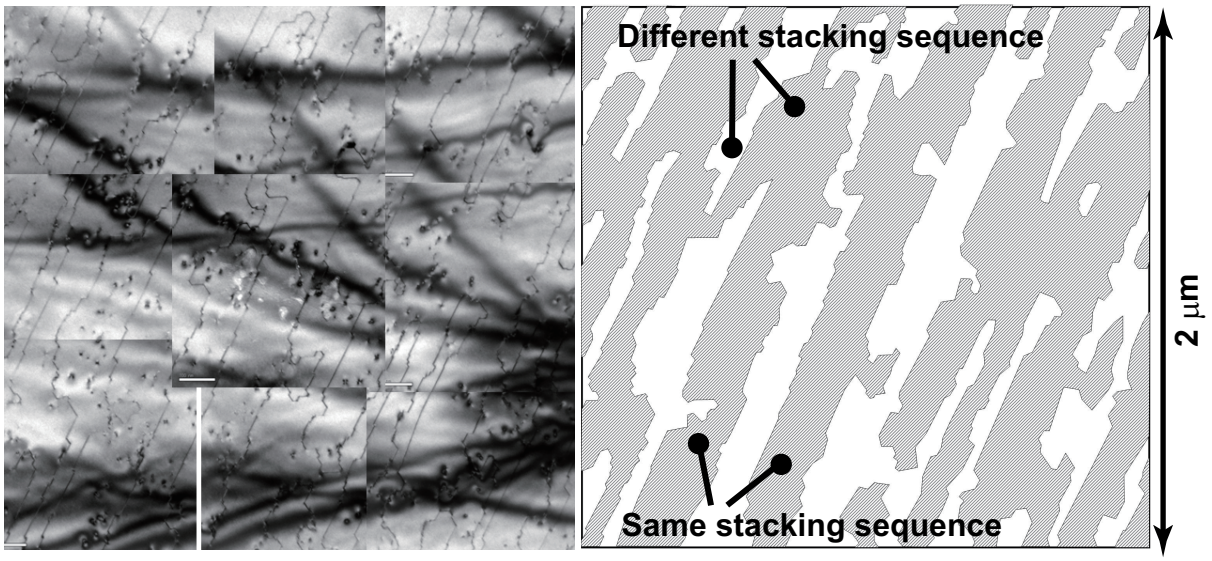

Figure 4.17: Large-scale bright-field plan-view TEM image of AlN layer on 6H-SiC (0001) with 3-bilayer-high steps after sacrificial oxidation process.

Generation mechanism of spiral hillocks

On AlN layers, there were spiral hillocks. Spiral hillocks arise from the lateral growth of pinned steps with small critical radii of curvature. As the pinned step bows out from screw-type TDs, it can wind into a spiral centered on the TDs. On the basis of BCF theory, Heying *et al.* reported that the radius of curvature of the pinned step line was limited to $\rho_c = \gamma a/[kT\ln(P/P_0)]$ (γ step energy per molecule, a monolayer height, k Boltzman constant, T temperature, P actual vapor pressure, and P_0 equilibrium vapor pressure of material) [13, 14]. This formula indicates that the radii of curvature, that is, the size of the hillocks increases with the growth temperature (Section 4.2.1).

Screw-type TDs were generated at an AlN/SiC interface. To clarify the origin of the screw-type TDs, we investigated an initial AlN growth. The surface morphology after 6-nm-thick AlN growth on 6-bilayer-high steps is shown in Fig. 4.18 (a). The triangle-shaped 2D islands with same direction existed on every terraces. 2D nuclei with the density of 1×10^8 cm^{-2}, however, face an opposite direction, suggesting that different stacking arrangements of the AlN layer exist on the identical terrace of SiC, e. g., stacking arrangements A and B on layer C. The density of the oppositely-directed 2D nuclei is close to that of spiral hillocks. In addition, AlN layers on SiC with 1-bilayer-high steps had the high density of spiral hillocks, and formed into lines with the same separation as the terrace width of the substrate. Based on these results, we suggest that different stacking arrangements on the identical terraces cause screw-type TDs. This suggestion supports the result that the spiral hillocks were randomly distributed on AlN layers grown on 6H-SiC with the 6- or 3-bilayer-high steps.

The schematic figure on generation mechanism of the screw-type TDs is shown in Fig. 4.19. First, in the AlN growth with the stacking arrangement of BCBC..., some different stacking layer A is formed on the layer C because of fluctuation of the crystal structure [15–17]. The layer A extends over the major stacking layer (B) due to accumulation of the strain energy, as shown in Fig. 4.19 (b). Then, dislocations are generated between the layers A and B. Adatoms are incorporated into the step of the layer A and the spiral is created because the step is pinned to the dislocation (Fig. 4.19 (c)). Next, the layer C is grown on the layer A, and the layer A wrapped with spiral again extends over the layer C (Fig. 4.19 (d) and (e)). Finally, the A and C layers grow the spiral and form a pair of spiral hillocks due to the pinned dislocations. To reduce the density of spiral hillocks, optimization of Ⅲ/V ratio and less interface energy are important.

In our considerations, the different stacking arrangements of AlN on the identical terraces can form TD rows, spiral hillocks, and SMBs. However, despite a lot of oppositely-directed 2D nuclei on the terraces of SiC, neither TD rows nor SMBs were observed on the terraces of SiC, indicating that the different stacking arrangements form no TD rows. TD rows would be generated by the other causes except for partial dislocations. The detail of generation mechanism of TD rows is described in Section 5.3.

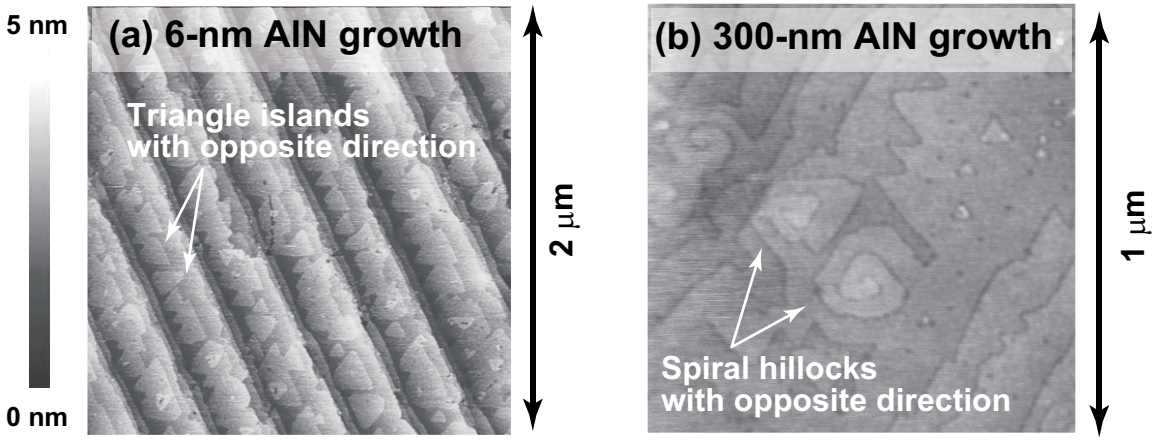

Figure 4.18: AFM images of (a) 6-nm- and (b) 300-nm-thick AlN layers on 6H-SiC (0001) with 6-bilayer-high steps.

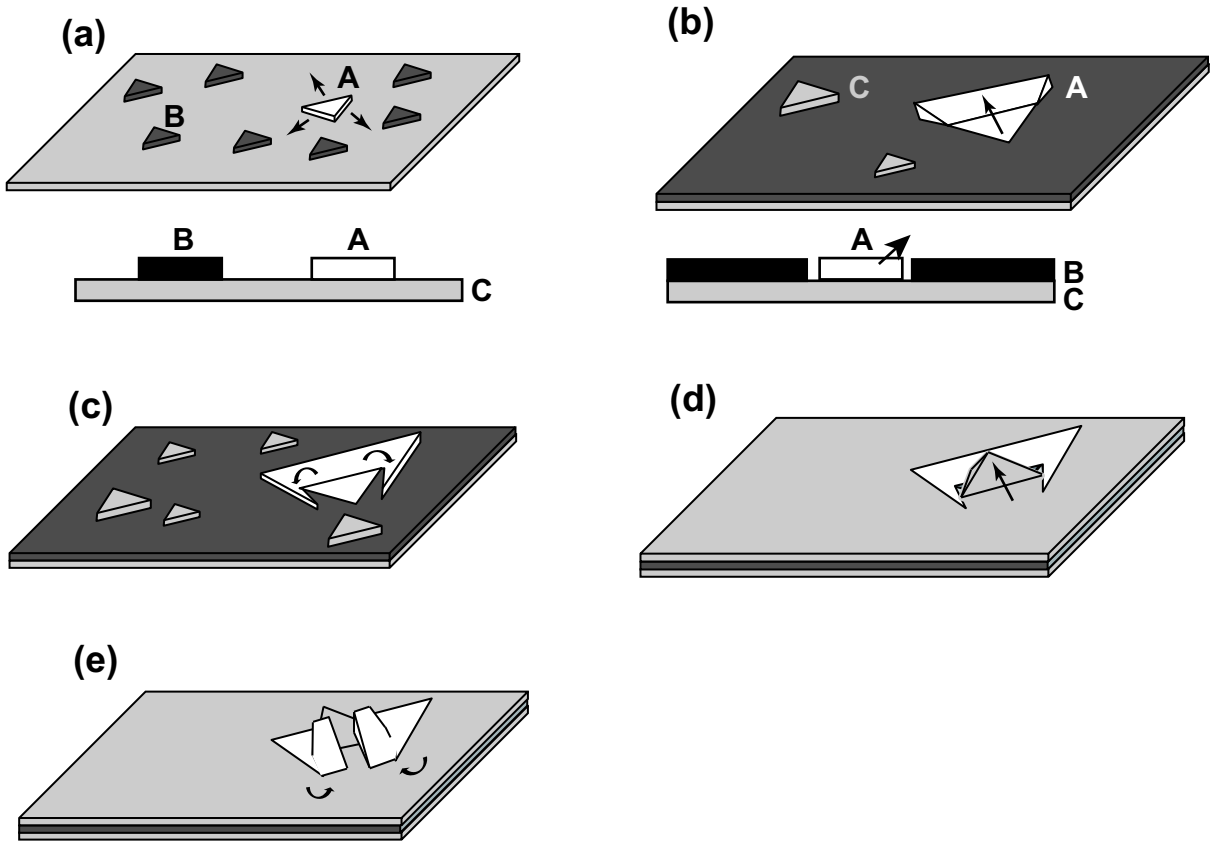

Figure 4.19: Schematic images of generation mechanism of spiral hillocks in AlN growth.

4.4 Al and Ga Pre-Deposition just before AlN Growth on SiC $(0001)_{Si}$

4.4.1 Experimental procedures

6H-SiC $(0001)_{Si}$ (vicinal angle $\sim$0.3°) substrates were used. The SiC substrates were treated by CMP followed by high-temperature H_2 gas etching to control the step height to be 3 bilayers. After the *ex-situ* wet-chemical cleaning and the *in-situ* Ga cleaning procedures, for reduction of the surface energy, the SiC surface was exposed to a Al metal (3×10^{-7} Pa) or a Ga metal (5×10^{-6} Pa) for 0–30 sec at the growth temperature of 600°C. Immediately after this, the 300-nm-thick AlN layer was grown by MBE. During AlN growth, no Ga was deposited. Growth sequence of AlN with the Al and Ga pre-deposition is shown in Fig. 4.20.

4.4.2 Effect of Al pre-deposition on AlN epilayers

RHEED intensity oscillations were slightly observed at the initial growth stage, indicating layer-by-layer growth mode. The surface morphologies of the AlN layers with Al pre-deposition time of 3, 7, and 10 sec are shown in Fig. 4.21. There were spiral hillocks caused by screw-type TDs. The spiral hillock density was over 10^8 cm^{-2}. The surface morphologies of the AlN layers are independent of the Al pre-deposition time.

FWHM values for the (0002) and $(01\bar{1}2)$ ω-scan peaks of the AlN layers with Al pre-deposition time of 0-10 sec are listed in Table 4.3. For the (0002) peaks, the FWHM values were small, under 60 arcsec. For the $(01\bar{1}2)$ peak, the FWHM values were also independent of the Al pre-deposition time, around 800 arcsec. From these results, we conclude that the Al pre-deposition has no significant effect on AlN growth including surface morphology and crystalline quality.

4.4.3 Effect of Ga pre-deposition on AlN epilayers

Growth mode and surface morphology of AlN epilayers

RHEED intensity profiles at an initial stage of AlN growth are shown in Fig. 4.22. In the AlN growth without Ga pre-deposition, the RHEED intensity oscillation was observed (Fig. 4.22 (a)). However, the RHEED intensity oscillates unclearly for 9 sec just after growth. By a Ga pre-deposition for 3 to 20 sec just before growth, a reduction of the initial-no-oscillation period in RHEED was observed, as shown in Fig. 4.22 (b)-(e). The shorter initial-no-oscillation period was 5 sec. Layer-by-layer growth mode from the earlier growth stage was achieved by the Ga pre-deposition. Meanwhile, the Ga pre-deposition time of 30 sec degraded the RHEED intensity oscillation. We found that there was the optimum Ga pre-deposition time to reduce the initial-no-oscillation time.

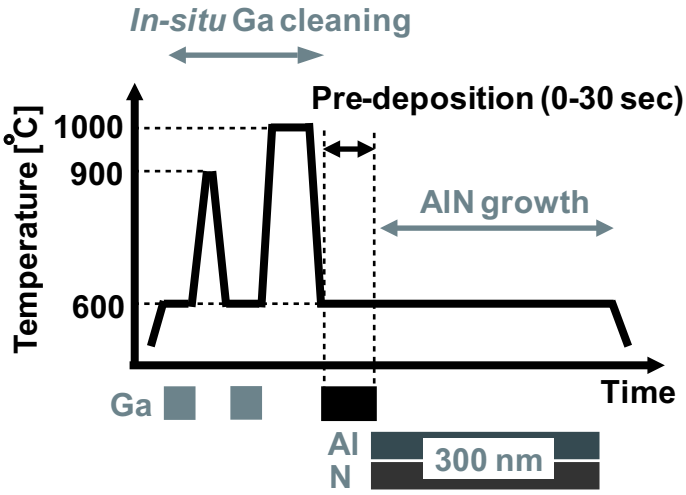

Figure 4.20: Procedure for AlN growth with Al and Ga pre-deposition.

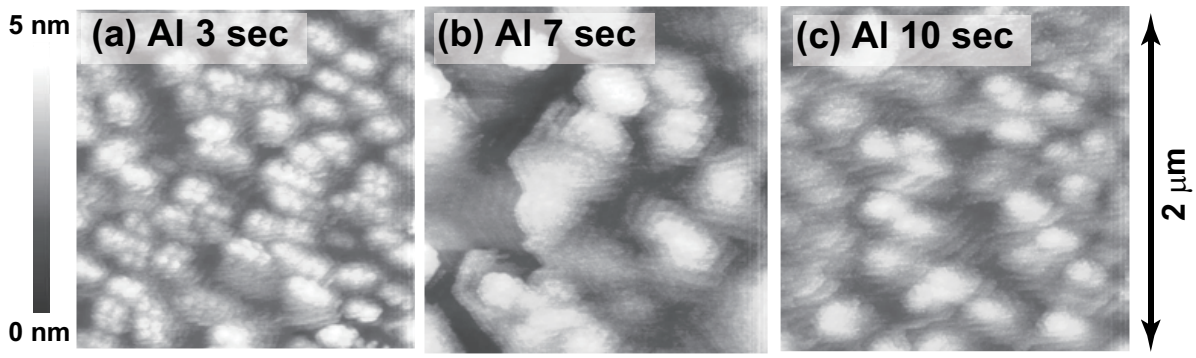

Figure 4.21: Surface morphology of AlN layers on 6H-SiC (0001) with Al pre-deposition time of (a) 3 sec, (b) 7 sec, and (c) 10 sec.

Table 4.3: FWHM values for (0002) and $(01\bar{1}2)$ ω-scan diffraction peaks of AlN layers on 6H-SiC (0001) with Al pre-deposition time of 0–10 sec [arcsec]

Al pre-deposition time [sec]	(0002)	$(01\bar{1}2)$
0	53	850
3	45	800
7	46	810
10	59	910

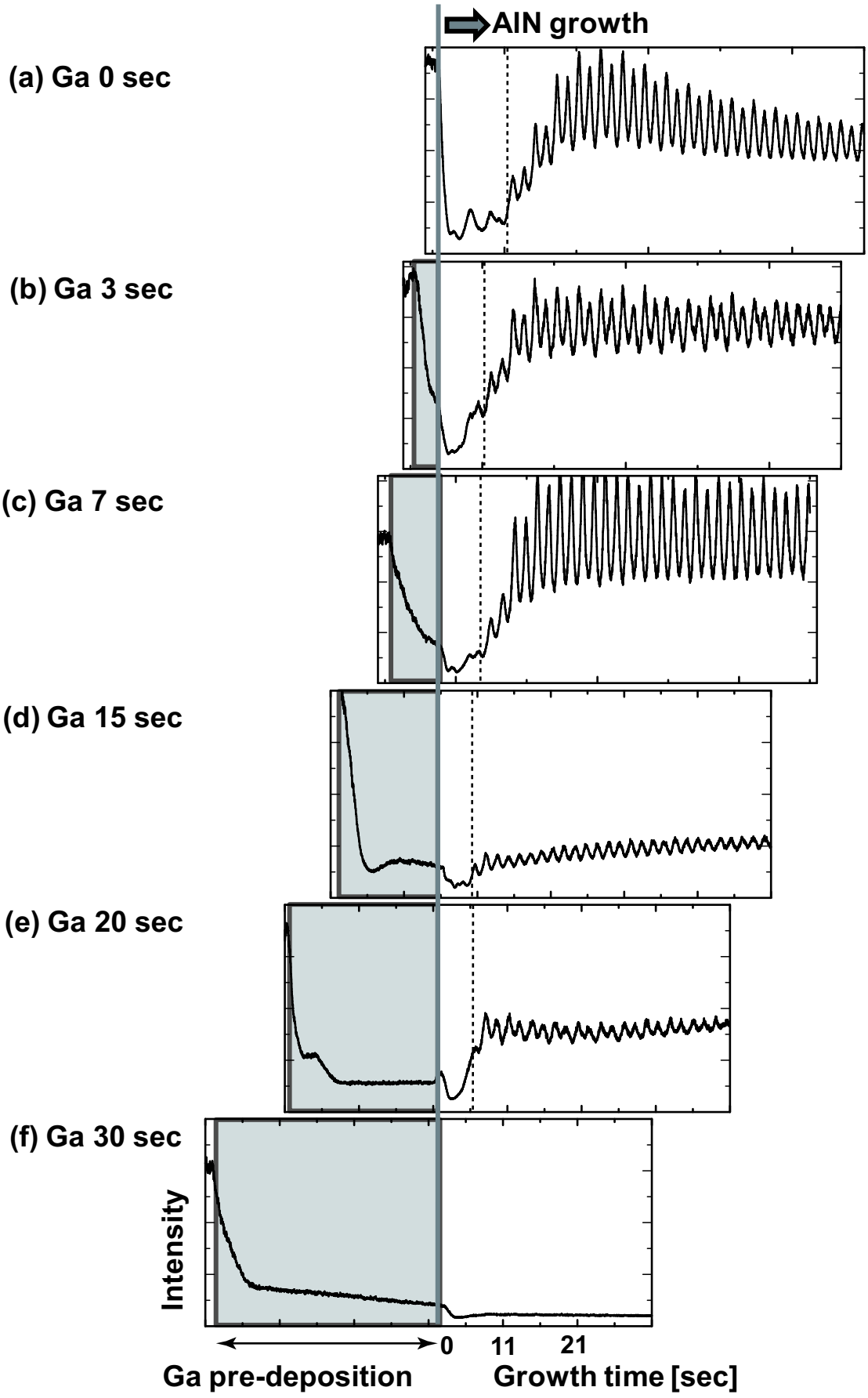

Figure 4.22: RHEED intensity profiles of AlN growth on 6H-SiC (0001) with Ga pre-deposition time of 0-30sec just after growth.

The surface morphologies of the AlN layers are shown in Fig. 4.23. All samples exhibit step-and-terrace structures with 1-bilayer-high steps of AlN, suggesting that the growth mode changed from layer-by-layer growth mode to step-flow growth mode with decomposition of 3-bilayer-high steps. Spiral hillocks were observed in the all samples. The spiral-hillock densities for Ga pre-deposition time of 0, 3, and 5 sec were 3×10^9 , 7×10^8 , and 4×10^8 cm^{-2}, respectively, and were lower on the AlN layers with the longer Ga pre-deposition time. Especially, the spiral hillock of AlN layers pre-deposited for 7 to 20 sec had the extremely low density, $\sim 10^6$ cm^{-2}, suggesting that pre-deposited Ga reduces the spiral hillock density. Although the AlN layer for Ga pre-deposition time of 30 sec also had the low density of spiral hillocks, the steps of the AlN layer undulated (Fig. 4.23 (f)).

Crystalline quality of AlN epilayers

The relationships between the Ga pre-deposition time and the FWHM values for the (0002) and $(01\bar{1}2)$ ω-scan diffraction peaks of the AlN layers are shown in Fig. 4.24. For the (0002) peaks, the FWHM values of most AlN layers were small, under 60 arcsec. For the $(01\bar{1}2)$ peak, significant improvement was observed for the Ga pre-deposition time of 5–10 sec and the FWHM values were less than 250 arcsec, suggesting reduction of the defect density due to Ga pre-deposition. The FWHM values for the (0002) and $(01\bar{1}2)$ ω-scan peaks of the AlN layers are listed in Table 4.4. We found that there was optimum condition for Ga pre-deposition.

The bright-field plan-view TEM images observed at [0001] zone-axis of the AlN layer with Ga pre-deposition for 3, 7, and 10 sec are shown in Fig. 4.25. A dark spot is a TD. It was found that the type of TDs was pure edge from a cross-sectional TEM image with two-beam condition. In the AlN growth for Ga pre-deposition time of 3 sec, the TD rows, which generated at step edges of the SiC surface, were observed, as in detail described at Section 5.3. The TDD of the AlN layer for Ga pre-deposition time of 7 sec was 2×10^9 cm^{-2}, one order of magnitude smaller than that of the AlN layer for Ga pre-deposition time of 3 sec. The low density of TDs observed by TEM was consistent with the small FWHM of the $(01\bar{1}2)$ diffraction peak.

In the AlN layer for Ga pre-deposition time of 10 sec, TDs had a zigzag structure. To investigate this defect structure, we observed the plan-view TEM images of the same defect in the AlN layer tilted within ± 15 ° in TX and TY directions, as shown in Fig. 4.26. A defect with the zigzag structure composed the V-shaped structure (Fig. 4.27 (a)). The TDs inclined to the growth direction are seen as the zigzag structure due to the interference with direct and diffracted beams. To confirm this structure, we observed cross-sectional TEM images of the AlN layer (Fig. 4.27 (b) and (c)). In the two-beam condition with $\mathbf{g}=11\bar{2}0$, V-shaped defects generated at an AlN/SiC interface were observed. We consider that the V-shaped defect consists of a pair of two pure-edge TDs. The V-shaped TDs have been observed in Si-doped AlGaN layers [18–20]. We speculate that AlGaN is grown at an initial growth stage due to excess Ga pre-deposition. The inclination of TDs may be caused by a misfit component owing to the lattice mismatch between AlGaN and AlN. Based on these

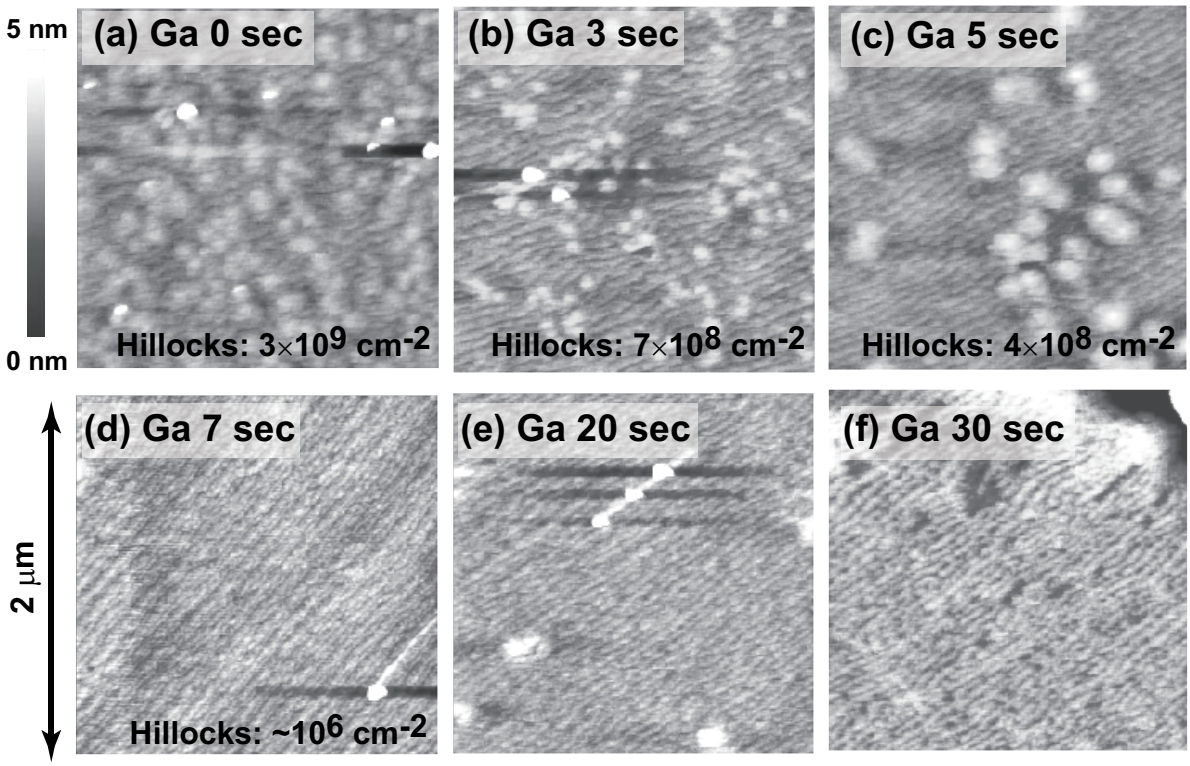

Figure 4.23: Surface morphology of AlN epilayers on 6H-SiC (0001) with Ga pre-deposition time of 0-30 sec.

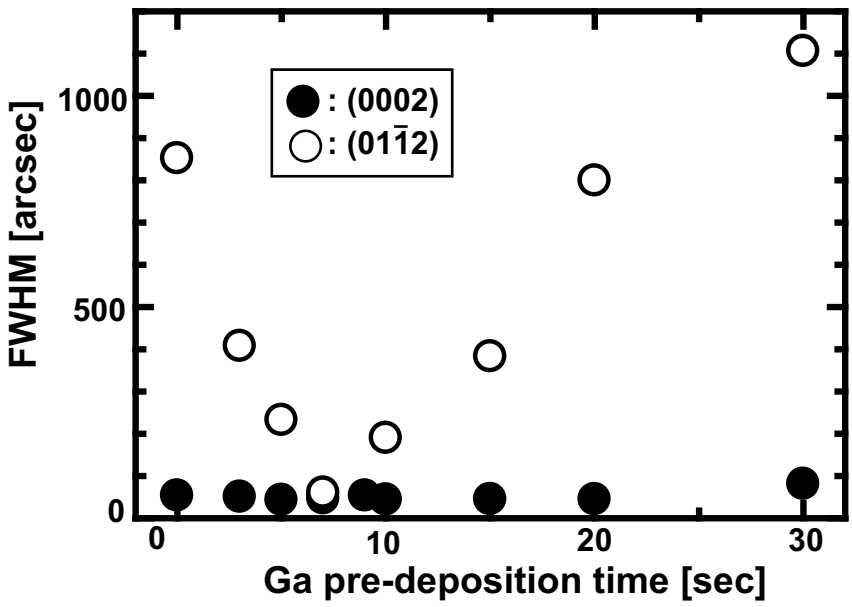

Figure 4.24: Relationship between Ga pre-deposition time and FWHM for (0002) and (01$\bar{1}$2) ω-scan diffraction peaks of AlN layers on 6H-SiC (0001).

Table 4.4: FWHM values for (0002) and (01$\bar{1}$2) ω-scan diffraction peaks of AlN layers on 6H-SiC (0001) with Ga pre-deposition time of 0–30 sec [arcsec]

Ga deposition time [sec]	(0002)	(01$\bar{1}$2)	Ga deposition time [sec]	(0002)	(01$\bar{1}$2)
0	53	850	10	44	190
3	51	410	15	45	380
5	43	230	20	45	800
7	46	60	30	81	1100

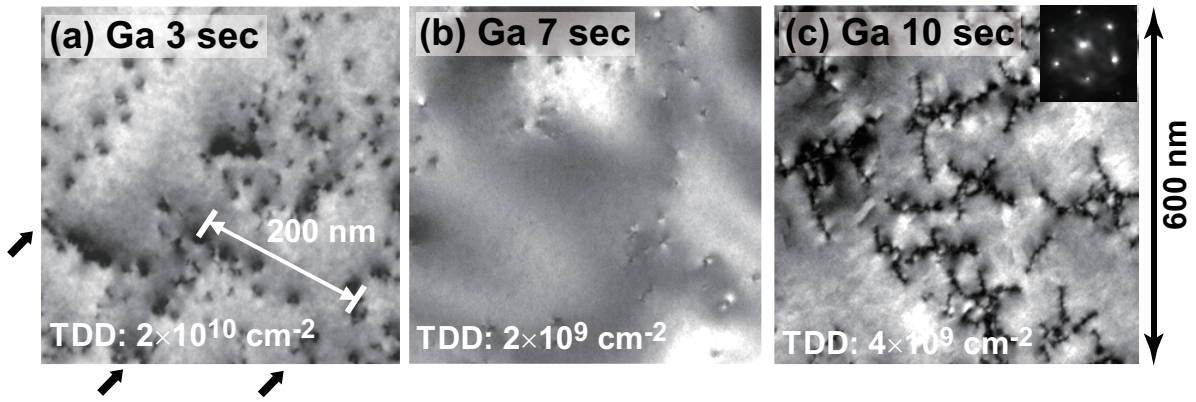

Figure 4.25: Bright-field plan-view TEM images of AlN layers with Ga pre-deposition time of (a) 3 sec and (b) 7 sec. Substrates are 6H-SiC (0001) with 3-bilayer-high steps.

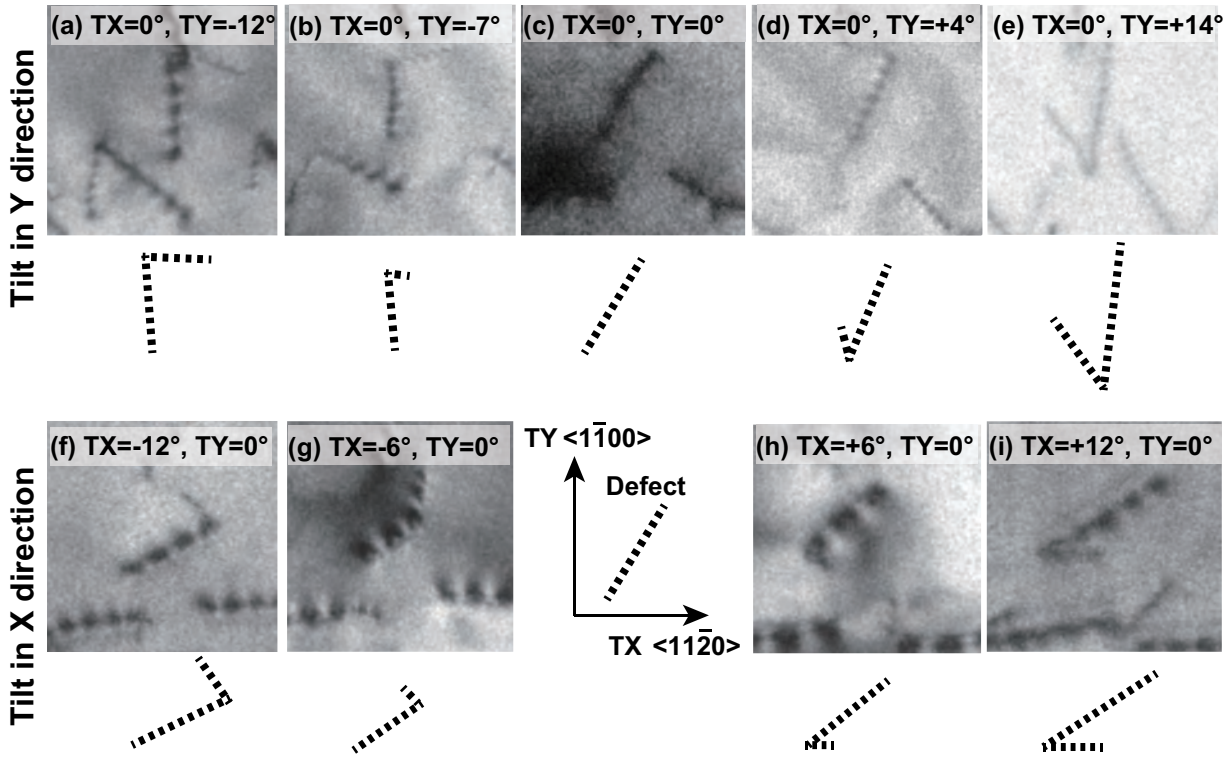

Figure 4.26: Bright-field plan-view TEM images of zigzag-structure defect in AlN layer on 6H-SiC (0001) with Ga pre-deposition time for 10 sec. (a)–(e) are tilted in Y direction (**g**=11$\bar{2}$0) and (f)–(i) are tilted in X direction (**g**=1$\bar{1}$00).

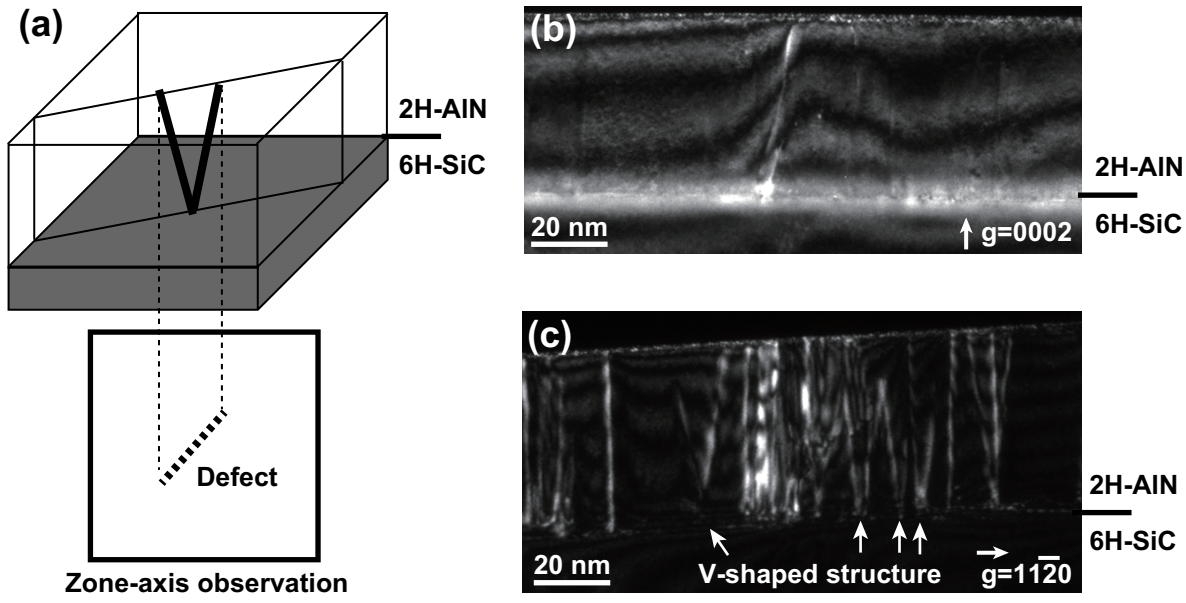

Figure 4.27: (a) Schematic figure of V-shaped defect in AlN layer on 6H-SiC (0001) with Ga pre-deposition time of 10 sec and dark-field cross-sectional TEM images of it (b: **g**=0002, c: **g**=11$\bar{2}$0).

results, TDD in this AlN layer is estimated at 4×10^9 cm^{-2}.

4.4.4 Discussion

Optimum Ga pre-deposition achieves layer-by-layer growth mode from the earlier stage of AlN growth, reducing the defect density including spiral hillocks and pure-edge type TDs. The reason why optimum Ga pre-deposition has this effect is discussed.

Al pre-deposition had no effect on the crystalline quality of the AlN layer. We consider that the metal Al can reduce the interface energy between an AlN epilayer and a SiC substrate, but the optimization for Al pre-deposition is severe because the metal Al is incorporated into the AlN layer with the growth. To improve the wettability using the metal Al, migration enhanced epitaxy (MEE) would be effective. On the other hand, the high wettability can be obtained and maintained by Ga pre-deposition. It is because the metallic Ga segregates on the AlN surface due to the smaller binding energy (2.20 eV) of Ga-N than that (2.88 eV) of Al-N [21–23]. Ga concentration in a 300-nm-thick AlN layer with Ga pre-deposition time of 7 sec was investigated by secondary ion mass spectroscopy (SIMS), as shown in Fig. 4.28 (a). Despite no Ga deposition during AlN growth, there are large Ga concentration (5×10^{20} cm^{-3}) on the AlN surface, indicating segregation of Ga. To confirm the Ga segregation, we also investigated the chemical surface state after 50-nm-thick AlN growth with and without Ga pre-deposition by *in-situ* x-ray photoelectron spectroscopy (XPS). Ga 2p peak was observed on the AlN surface only with Ga pre-deposition (Fig. 4.28 (b)). The energetically stable surface is achieved during the whole AlN growth due to the Ga segregation on the AlN layer.

For Ga pre-deposition, there was optimal condition. Ga deposited for 7 sec corresponds to 1.6 monolayer (ML) and residual Ga after the *in-situ* Ga cleaning is 0.3 ML because the SiC surface composes a $\sqrt{3} \times \sqrt{3}$ R30° pattern. The sum of the metal Ga adsorbed on the SiC substrate just before growth is about 2 ML. Northrup *et al.* have reported that laterally contracted 2 ML structures are energetically favorable under Ga-rich conditions because of the energy benefit of a reduced Ga-Ga spacing in the surface adlayers [24]. For GaN growth, the GaN lattice constant of 0.32 nm is substantially greater than the typical Ga-Ga spacing of 0.27 nm in bulk Ga, so that a 1×1 arrangement of Ga is under considerable tensile strain. With respect to the AlN growth, Northrup *et al.* have also reported that the 2 ML structures are energetically favorable under the Al-rich condition [25]. From these reports, we speculate that 2 ML Ga structure is the most stable even on the AlN surface [26].

Schematic figures of AlN growth with Ga pre-deposition are shown in Fig. 4.29. First, 2 ML Ga is deposited on the SiC substrate just before growth (Fig. 4.29 (a)). As active-nitrogen species and the metal Al reach this surface, AlN is preferentially grown on the SiC substrate due to the Ga segregation (Fig. 4.29 (b)). The 2 ML Ga reduces the surface energy just before growth, resulting in layer-by-layer growth mode at an earlier stage of the growth. In addition, the layer-by-layer growth mode maintains during AlN growth over 50-nm thickness, i. e., the pre-deposited Ga plays a role of surfactant for AlN growth.

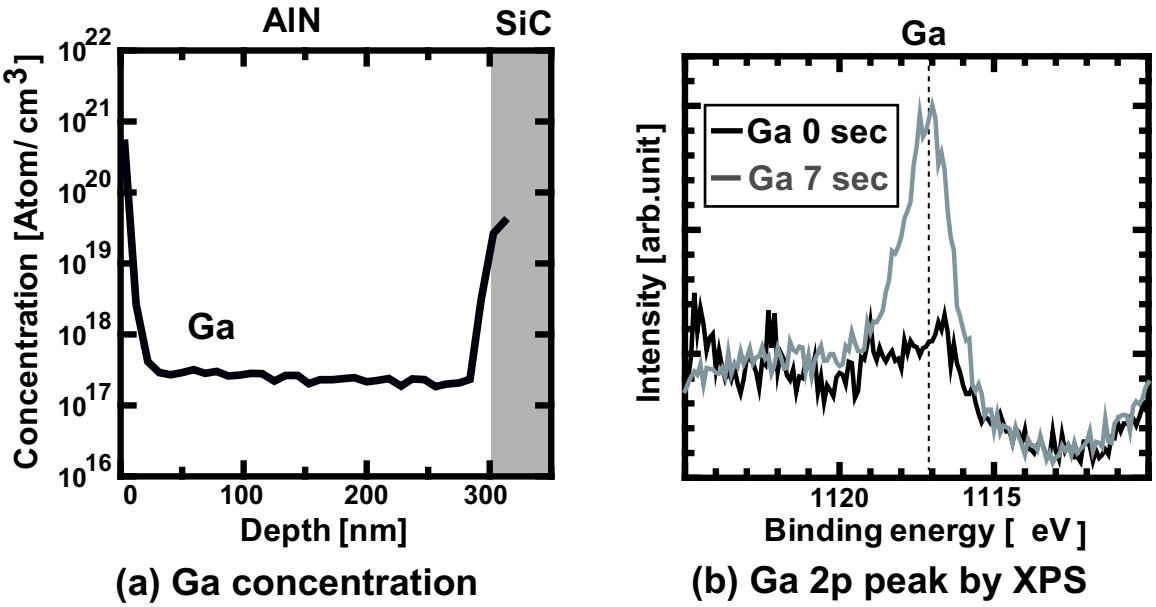

Figure 4.28: (a) Ga concentration in AlN layer by SIMS measurement and (b) Ga 2p peak of AlN surface by XPS spectra. Ga pre-deposition time is 7 sec.

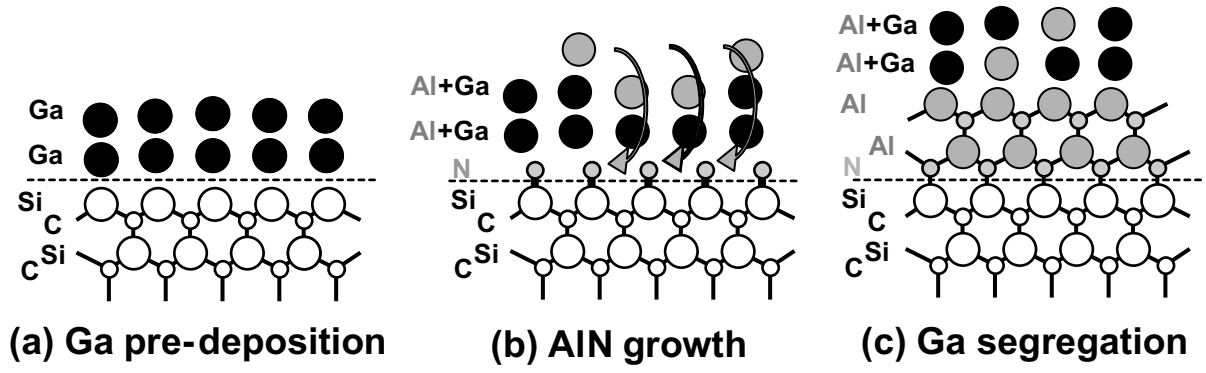

Figure 4.29: Schematics of AlN growth on SiC substrate with Ga pre-deposition at initial growth stage.

4.5 Avoidance of Nitrogen-Plasma Exposure before AlN Growth on SiC $(0001)_{Si}$

4.5.1 Introduction

In a general MBE process, nitrogen plasma is stabilized with a closed shutter for several minutes before the growth because the plasma condition fluctuates for around 10 min after the plasma ignition. To avoid an unoptimized Ⅲ/V ratio in the initial growth due to the fluctuation, we have employed this stabilization process. As long as the shutter is closed, no active-nitrogen species have been thought to reach the SiC surface because the active nitrogen species may be easily deactivated when they hit the shutter or the chamber walls. However, a slight change in the RHEED intensity of SiC substrates has been observed at 650°C after plasma ignition, suggesting that some active nitrogen species can reach the surface. Ohachi *et al.* showed very uniform nitridation of Si substrates with the closed plasma-cell shutter, suggesting that a certain amount of nitrogen reflected by the shutter or chamber walls remains active [27].

By XPS measurement, we investigated the surface composition of the SiC substrate held in the MBE chamber under nitrogen ambient at 650°C for 10 min. Before exposing the nitrogen ambient, the SiC substrates were treated by the *in-situ* Ga cleaning. One substrate was held in the nitrogen (N_2) flow of 0.75 sccm without plasma ignition. The other was held with an ignited plasma cell with the closed shutter. These N 1s peaks in XPS spectra are shown in Fig. 4.30. A small amount of Ga (less than 0.05 ML) was also detected on both substrates due to the *in-situ* Ga cleaning. For the case without plasma ignition, no nitrogen was detected on the SiC surface at all. Because the SiC surface is so inert, no nitrogen molecule can react with the surface. Meanwhile, for the case with the ignited plasma cell, small amount of nitrogen (much less than 1 ML) was detected on the SiC surface. In this measurement, how nitrogen atoms adsorb on the SiC was unclear. We have three possibilities; nitrogen atoms can (i) chemically adsorb on SiC terrace forming Si-N bonding, (ii) chemically adsorb preferentially at SiC step edges, and (ⅲ) bond with residual Ga and form GaN. Further investigation is necessary to understand the effect of nitrogen adsorption on initial growth of AlN.

The nitrogen adsorption on the SiC surface may inhibit the layer-by-layer growth at the very initial stage of growth, resulting in the TDD of 2×10^9 cm^{-2}. In this case, the unintentional nitrogen exposure should be avoided to reduce TDD.

4.5.2 Growth mode at initial growth stage

RHEED intensity versus growth time in sample D is shown in Fig. 4.31. Note that only in sample D, RHEED intensity oscillation started just after AlN growth, indicating the layer-by-layer growth mode from the first layer. We believe that nitrogen adsorbed on SiC surfaces

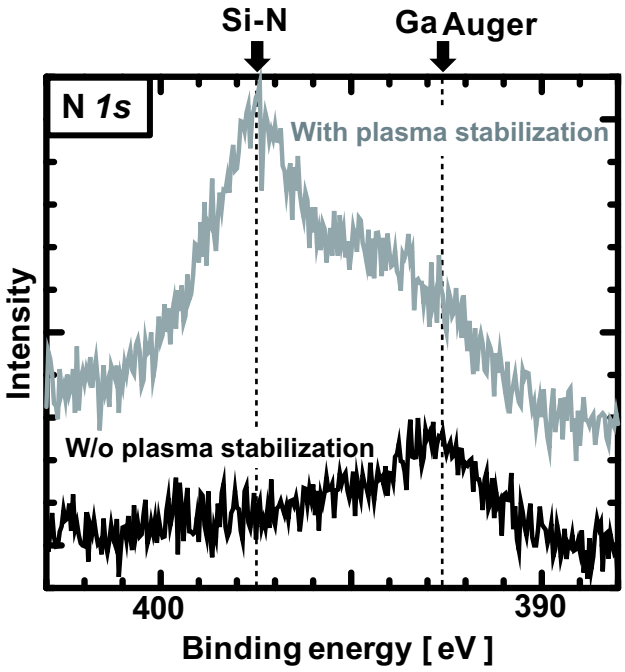

Figure 4.30: N 1*s* peak on 6H-SiC (0001) surface with and without nitrogen-plasma stabilization for 10 min.

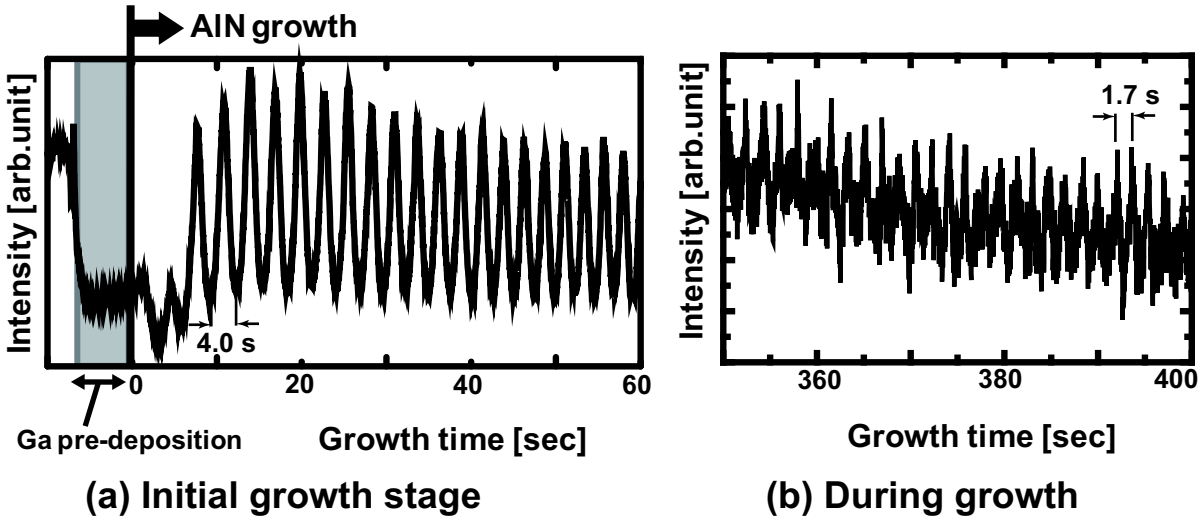

Figure 4.31: RHEED intensity profiles of AlN growth with both Ga pre-deposition and no active-nitrogen exposure just before growth.

resulted in unfavorable surfaces before growth and prevented the layer-by-layer growth mode from the first layer. One cycle of the RHEED intensity oscillation corresponding to growth time for 1-bilayer-thick AlN is 4.0 sec at the initial stage of AlN growth. However, the 1 cycle of the RHEED intensity oscillation gradually decreases during growth and reaches 1.7 sec after 60-nm-thick AlN growth. It takes 30 min for 290-nm-thick growth, indicating that the 1 cycle of the RHEED intensity oscillation is 1.6 sec. We consider that an AlN adsorption on SiC substrates is more difficult than that on AlN layer and the covered 2ML-Ga metal prevents nitrogen incorporation at the initial growth stage, resulting in the slow growth rate. Another possibility is that one cycle of the RHEED intensity oscillation corresponds to growth time for 2-bilayer-thick AlN. To confirm this, further investigation is necessary.

Surface morphologies of 1.5-nm-thick AlN layers are shown in Fig. 4.32 (a)-(c). The AlN layer without Ga pre-deposition seems to have 3D growth mode, as shown in Fig. 4.32 (a), while these with Ga pre-deposition have layer-by-layer growth mode (Fig. 4.32 (b) and (c)). These results correspond to RHEED intenisty profiles at the initial stage of AlN growth. The AlN growth with Ga pre-reposition and no active-nitrogen exposure has a lot of metal droplets (Fig. 4.32 (c)). We believe that the unintentional nitrogen exposure reacts pre-deposited Ga and reduces the amount of metal droplets.

Surface morphologies of 10-nm-thick AlN layers are shown in Fig. 4.32 (d)-(f). The AlN layer without Ga pre-deposition shifted to step-flow growth mode, as shown in Fig. 4.32 (d). This is consistent with the RHEED intensity oscillation observed only from 10 to 50 sec. This is because AlN grows with 3D growth mode on the SiC substrate adsorbed a few nitrogen atoms, followed by 2D growth mode on AlN layers. Meanwhile, the AlN layer with Ga pre-deposition maintains layer-by-layer growth mode even after 10-nm-thick growth (Fig. 4.32 (e) and (f)). This is due to Ga segregation as well as larger terrace width of the SiC substrate. However, the AlN layers have 4-bilayer-high (1 nm) dips near step edges. We speculate that excess Ga adsorbs with step edges and prevents AlN growth. To obtain atomically smooth surface, more severe optimization of Ga pre-deposition may be necessary.

4.5.3 AlN growth just after nitrogen-plasma ignition

Growth condition

6H-SiC $(0001)_{Si}$ (vicinal angle 0.15°) substrates were used. The substrates were treated by CMP and high-temperature H_2 gas etching to control the SiC step height to be 6 bilayers. After the *ex-situ* wet-chemical cleaning and the *in-situ* Ga cleaning procedures, 300-nm-thick AlN growth was started at growth temperature of 650°C. The growth procedure is illustrated in Fig. 4.33.

To minimize unintentional active-nitrogen exposure to the SiC surface, AlN was grown on 6H-SiC (0001) without plasma stabilization, i.e., just after the plasma ignition. If this unintentional exposure is the main cause of TDs, Ga pre-deposition may be unnecessary.

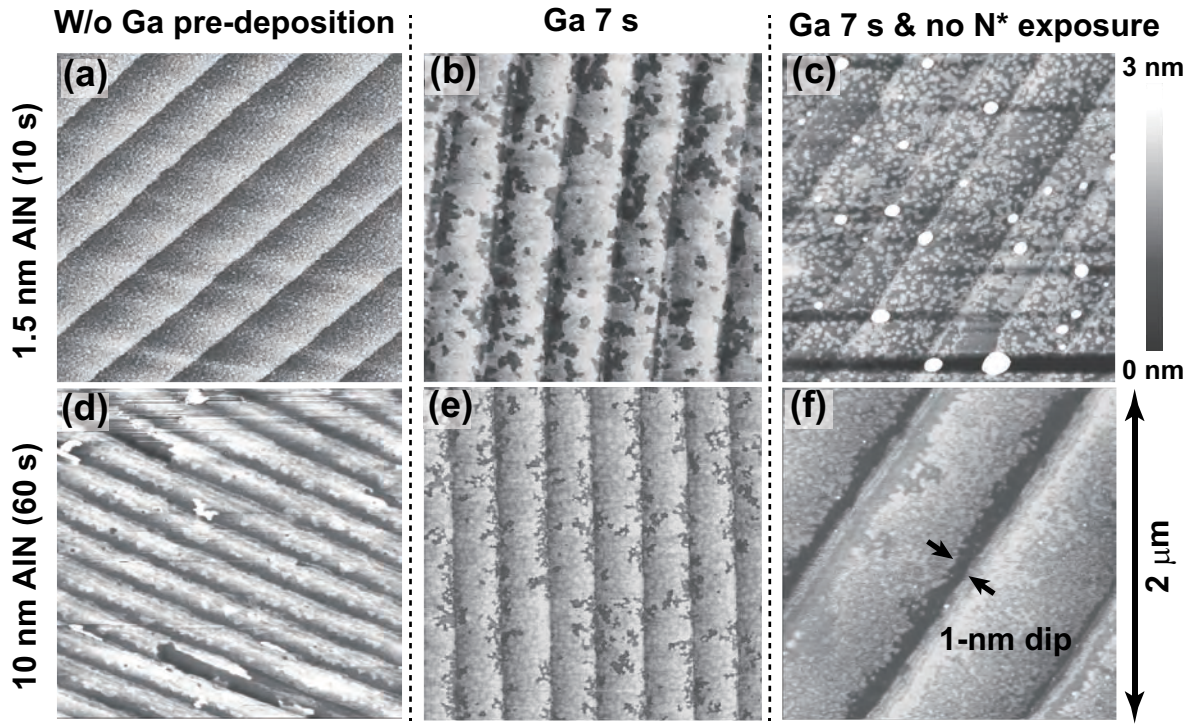

Figure 4.32: Surface morphologies of 1.5- and 10-nm-thick AlN layer on 6H-SiC (0001) with 3-bilayer-high steps ((a) and (d): direct AlN growth, (b) and (e): Ga pre-deposition for 7 sec, (c) and (f): Ga pre-deposition for 7 sec just after plasma ignition).

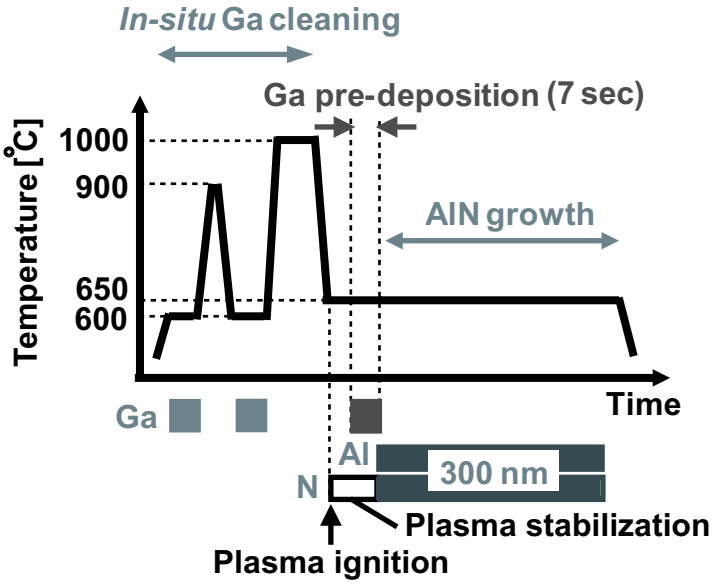

Figure 4.33: Procedure for AlN growth with Ga pre-deposition and no acrive-nitrogen exposure.

The effect of Ga pre-deposition on this process was also investigated. Samples A and B were grown after 10 min of stabilization of the plasma cell with the closed shutter, and samples C and D were grown as soon as the plasma was ignited. To investigate the effect of Ga pre-deposition, samples A and C were grown without Ga pre-deposition, and the SiC surfaces of samples B and D were exposed to a Ga beam just before AlN growth for 7 sec, corresponding to ∼2 ML. The growth conditions of samples A-D are listed in Table 4.5.

Surface morphology of AlN epilayers

The AlN surfaces of samples A-D had 1-bilayer-high step-and-terrace structures, indicating step-flow growth mode. Although AlN layers at an initial growth stage have layer-by-layer growth mode, 6-bilayer high steps decompose to six 1-bilayer-high steps with growth so that the AlN layers shift to step-flow growth mode. Surface morphologies of the SiC substrate and the AlN layer for sample D are shown in Fig. 4.34. It was confirmed that terrace width of the SiC substrate with 6-bilayer-high steps was just 6 times larger than that of the AlN layer.

Spiral hillocks corresponding to screw-type TDs existed on the all samples A-D. The hillock densities in samples A, B, and C were 3×10^{9} , 4×10^{8} , and 5×10^{6} cm^{-2}, respectively, while the density in sample D was much lower. As shown in Fig. 4.34 (c), only four spiral hillocks were observed in the 85-μm square area corresponding to a density of 6×10^{4} cm^{-2}. By combining the optimized Ga pre-deposition and no active nitrogen exposure, we achieved significant reduction of screw-type TDD.

Crystalline quality of AlN epilayers

The FWHM values for the (0002) and (01$\bar{1}$2) ω-scan diffraction peaks of samples A-D are also listed in Table 4.5. Both samples A and B have small FWHM values for the (0002) diffraction peak, less than 60 arcsec. For the (01$\bar{1}$2) diffraction, the FWHM value of sample B (190 arcsec) is much smaller than that of sample A (850 arcsec). As described in Section 4.4, optimal Ga pre-deposition enhances the layer-by-layer growth mode and reduces TDD. The FWHM values for the (0002) and (01$\bar{1}$2) diffraction peaks of sample C are very close to those of sample A. In the case of no Ga pre-deposition, the crystalline quality of AlN is nearly independent of the adsorption of nitrogen on SiC surfaces. On the other hand, in the case of Ga pre-deposition (sample D), the adsorption of nitrogen strongly impacts the crystalline quality. The FWHM value for the (01$\bar{1}$2) diffraction peak of sample D (41 arcsec) is considerably smaller than that of sample B (190 arcsec), as shown in Fig. 4.35. I believe that avoidance of unintentional active nitrogen exposure achieved layer-by-layer growth mode just after growth, resulting in an extremely small TDD.

The bright-field plan-view TEM image (10° tilt) of sample D is shown in Fig. 4.36. The TDD in sample D was low, 4×10^{8} cm^{-2} in an area of 4×4 μm^2. The TDs has edge type and TD rows were observed, indicating that TDs were generated at the step edges of the

Table 4.5: Growth conditions of samples A-D and FWHMs for (0002) and (01$\bar{1}$2) ω-scan diffraction peaks of samples A-D [arcsec]. Samples A-D are 300-nm-thick AlN layers on 6H-SiC (0001).

Sample	Plasma stabilization	Ga pre-deposition	FWHM (0002)	FWHM (01$\bar{1}$2)
A	Yes	No	53	850
B	Yes	Yes	46	190
C	No	No	62	800
D	No	Yes	40	41

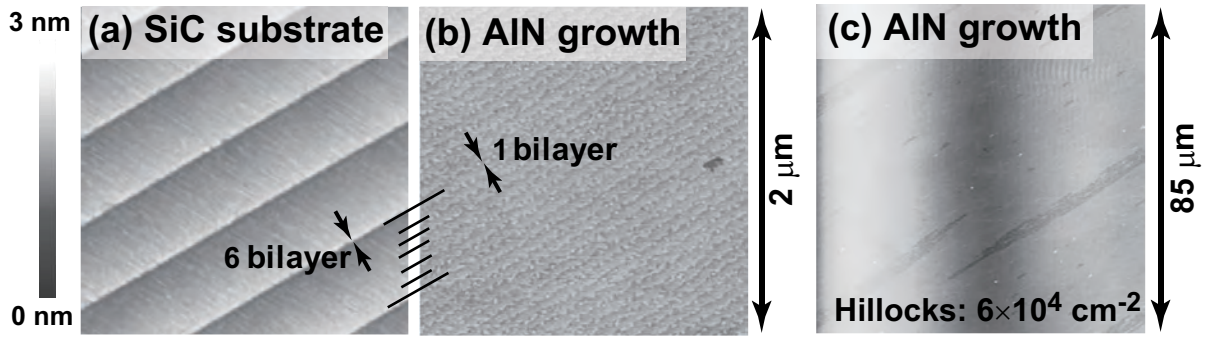

Figure 4.34: Surface morphology of AlN epilayers on 6H-SiC (0001) with Ga pre-deposition time of 7 sec just after nitrogen-plasma ignition.

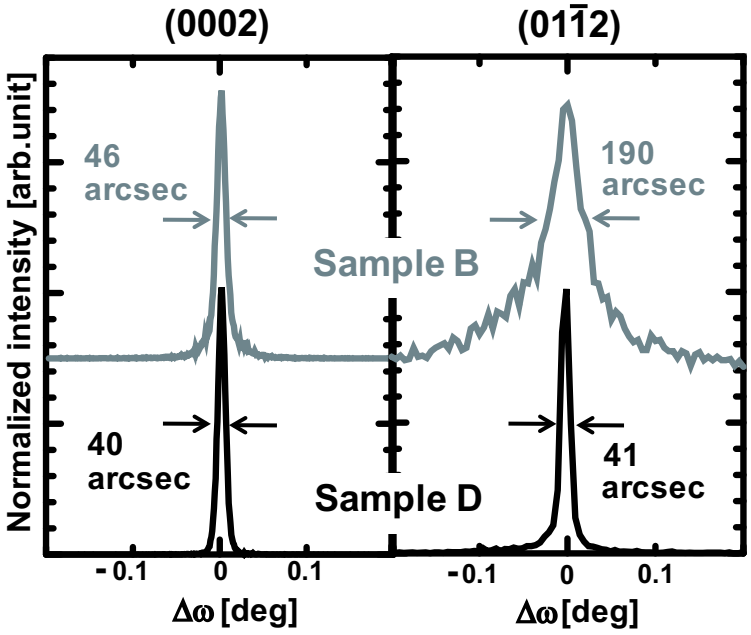

Figure 4.35: Relationship between Ga pre-deposition time and FWHM for (0002) and (01$\bar{1}$2) ω-scan diffraction peaks of AlN layers on 6H-SiC (0001).

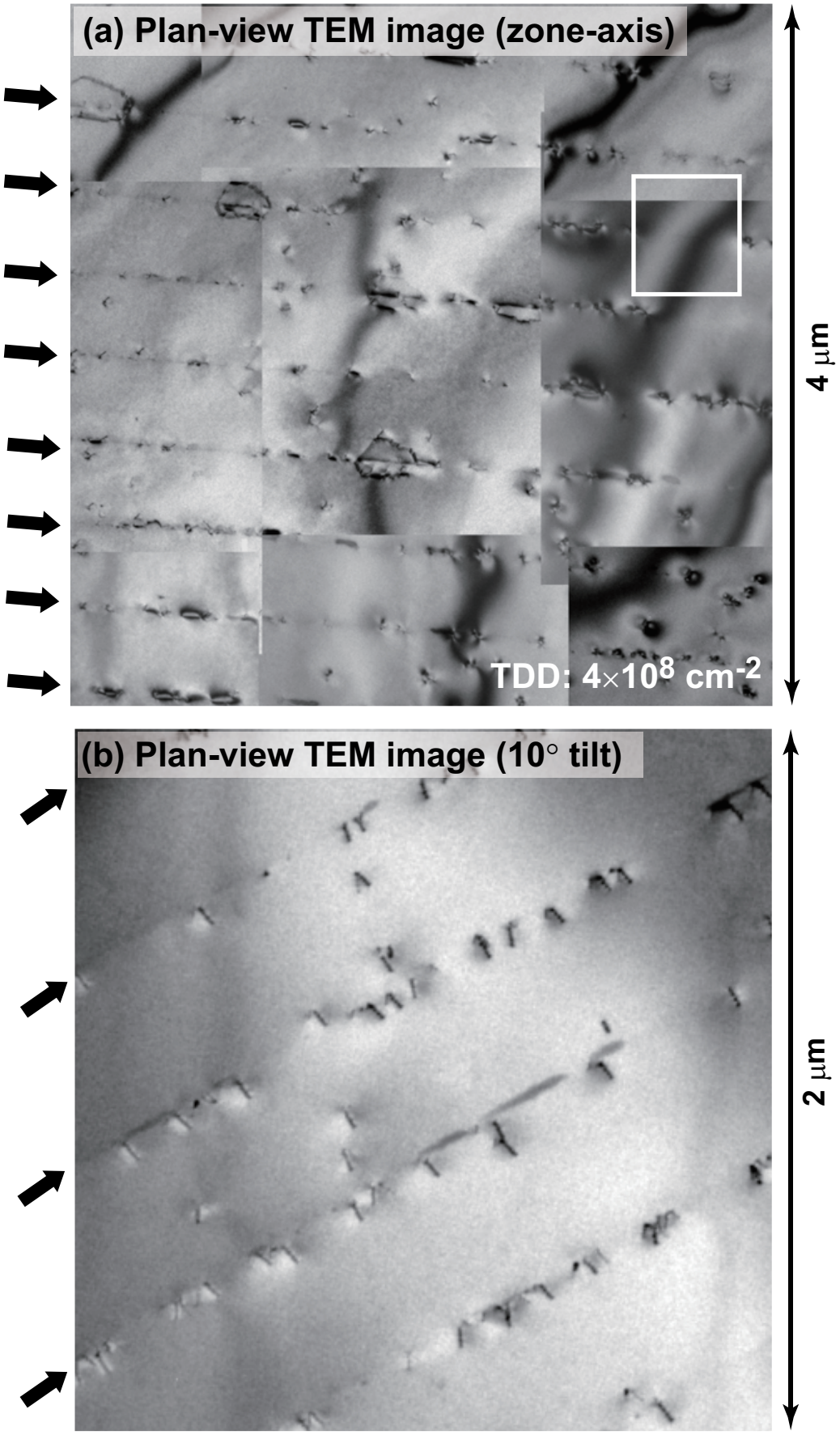

Figure 4.36: Bright-field plan-view TEM images of AlN layer on 6H-SiC (0001) with Ga pre-deposition time of 7 sec just after nitrogen-plasma ignition.

SiC substrates. The TDD generated on the terrace of the SiC substrates was very low, 8×10^7 cm^{-2}. The cross-sectional high-resolution TEM (HRTEM) image of the AlN/SiC interface is shown in Fig. 4.37. The abrupt interface was achieved in AlN heteroepitaxial growth on the SiC substrate. Despite including the AlN layer at the step edge of SiC, no TD was observed in the 1 μm $\times$ 1 μm area of Fig. 4.36 (a), suggesting that the TDD in the AlN layers can be reduced to less than 10^7cm^{-2} by controlling the TDs generated at the step edge of the SiC substrates.

4.5.4 Discussion

We found that active-nitrogen species reached the SiC surface even if the shutter closed. To confirm the effect of this unintentional active-nitrogen, we deposited 2ML Ga followed by nitrogen stabilization for 10 min. The RHEED pattern changed from streaky to spotty in 2 min after nitrogen ignition. We consider that the pre-deposited Ga bound with the excess nitrogen, resulting in the rough surface. For high-quality AlN growth, the unintentional-nitrogen-exposure time must be minimized. We still have a few seconds unintentional nitrogen exposure (for tuning matching unit). To eliminate this, installation of a gate valve and differential evacuation between main chamber and the plasma cell would be required. Remaining issue is the suppression of TDs generated at the step edges of SiC substrates. To solve this issue, dislocation structure (network) at step edges of SiC and its formation mechanism should be revealed.

4.6 AlN Growth on SiC $(000\bar{1})_C$

4.6.1 Experimental procedure

In this section, optimization of growth conditions of N-polar AlN layers is described. As a substrate for the N-polar AlN growth, 6H-SiC $(000\bar{1})_C$ treated by H_2-gas etching was used, as shown in Fig. 4.38 (a). A step-and-terrace structure with 6-bilayer-high steps was obtained. AlN was grown under slightly Al-rich condition for a temperature range 650-850°C. It was confirmed that the AlN layers on 6H-SiC $(000\bar{1})$ had N polarity by the CBED pattern, as shown in Fig. 4.1 (b).

4.6.2 Growth characteristics of N-polar AlN

Growth-temperature dependence

The surface morphologies of 300-nm-thick AlN layer grown at 650 and 850°C are shown in Fig. 4.38 (b) and (c), respectively. N-polar AlN surfaces had a lot of hillocks. The densities of the hillocks on AlN grown at 650 and 850°C were 6×10^9 and 5×10^8 cm^{-2},

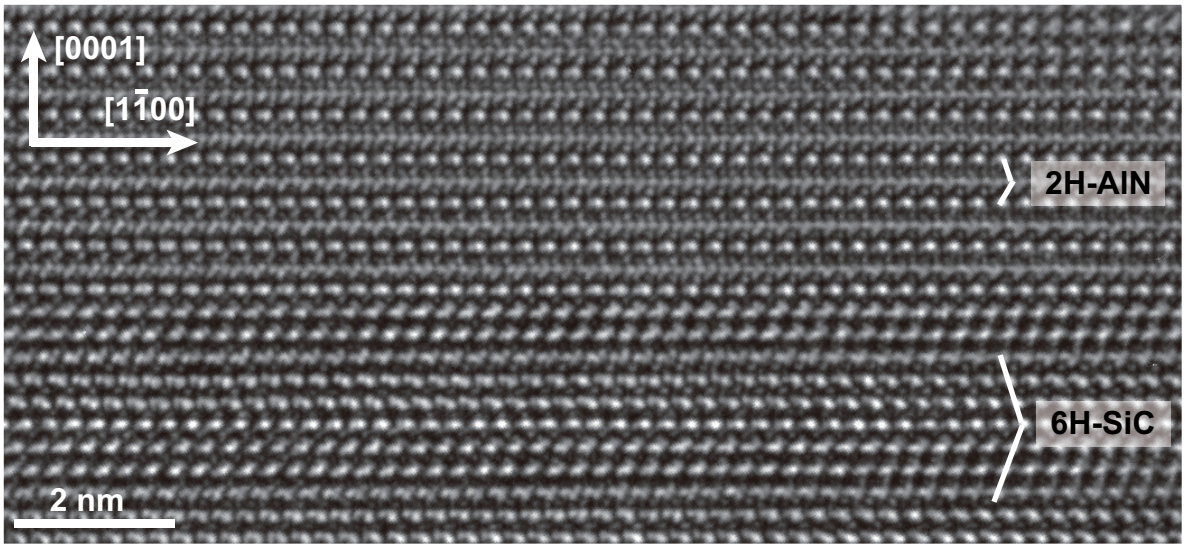

Figure 4.37: HRTEM image of 2H-AlN/6H-SiC (0001) interface ([11$\bar{2}$0] zone-axis).

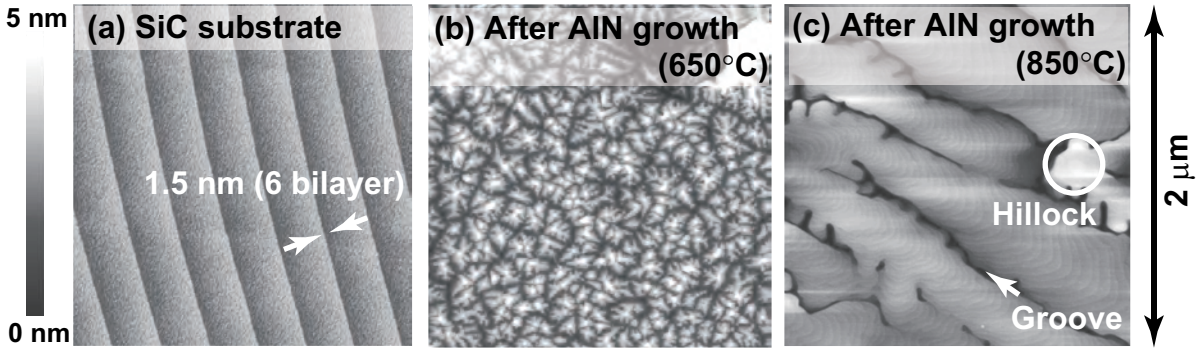

Figure 4.38: AFM images of (a) 6H-SiC (000$\bar{1}$) substrate and 300-nm-thick AlN layers grown on its substrate at (b) 650 and (c) 850°C.

respectively. Due to these hillocks, the root-mean-square (RMS) roughness was large. The RMS roughness of the AlN layer grown at 650°C was 5.5 nm, regardless of Ⅲ/V ratio. On the top of the hillocks, two-dimensional (2D) nucleus were observed, indicating that the hillocks are resulted from not spiral (screw dislocation) but multinucleation growth. On AlN grown at 850°C, parallel and long grooves existed between the hillocks. The grooves correspond to a step direction of the SiC surface before growth and the separation of the grooves are consistent with to the terrace width of the SiC surface. We believe that this multinucleation was generated on each terrace of the SiC substrates, so that the hillocks and the step-and-terrace structure with 1-bilayer-high steps were formed. In the case of Al-polar AlN growth on SiC (0001) with a similar growth rate, no multinucleation occurred, suggesting that the multinucleation growth may be typical of N-polar AlN growth.

Initial-growth mode of AlN epilayer

No RHEED intensity oscillation of AlN grown at 650°C was observed, while that of AlN grown at 850°C was observed for 30 seconds just after growth, as shown in Fig. 4.39 (a), indicating layer-by-layer growth mode. One cycle of the RHEED intensity oscillation is 4.0 sec, corresponding to growth time for 2-bilayer-thick AlN, like AlN growth on 6H-SiC (0001). After 30 seconds growth, the intensity of RHEED oscillations decreased. We found that in N-polar AlN growth, higher growth temperature was necessary to realize the layer-by-layer growth, in contrast with Al-polar AlN growth. Fig. 4.39 (b) shows a RHEED pattern of the AlN layer grown at 850°C. The RHEED pattern was streak, indicating the smooth surface of AlN.

The surface morphologies of AlN layers at the initial growth stage are shown in Fig. 4.40. Although AlN layers showed the layer-by-layer growth mode until 30 seconds (5-nm thickness) of growth, multinucleation growth occurred as growth proceeded, resulting in the formation of hillocks, as shown in Fig. 4.40 (c). This result corresponds to a RHEED intensity profile at the initial stage of AlN growth, as shown in Fig. 4.39. We believe that the formation factor for a multinucleation is high supersaturation in the N-polar AlN growth. Due to the high supersaturation, adatoms readily form into a 2D nucleus without being incorporated into the steps of the substrate, resulting in multinucleation growth and the formation of the hillocks. The adatom density under these growth conditions, such as a growth temperature of 850°C and a nitrogen-plasma power of 300 W, may be too high for N-polar AlN growth. To achieve a smooth surface in N-polar AlN growth, an increase in growth temperature, reduction in nitrogen-plasma power, and MEE growth are thought to be effective due to the low supersaturation. In addition, we think that a large off-angle substrate is also effective for the smooth AlN surface. By decreasing the terrace width of the substrate, adatom can be incorporated into the steps even in the high supersaturation, enhancing a step-flow growth mode without multinucleation growth.

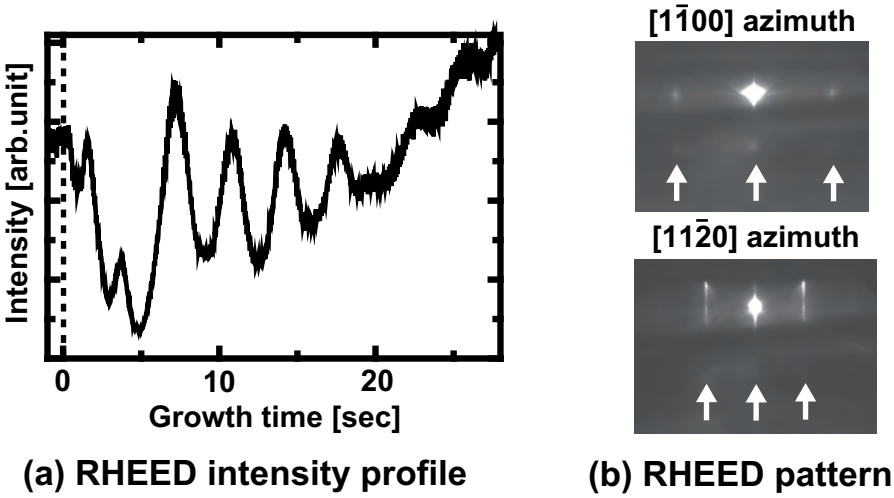

Figure 4.39: RHEED intensity profile of AlN growth at initial stage and RHEED pattern after growth in slightly Al-rich condition at 850°C.

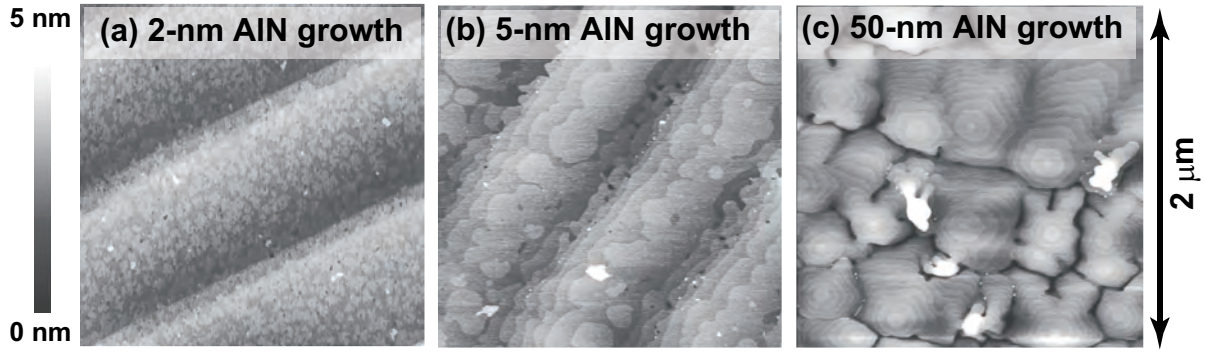

Figure 4.40: AFM images of 6H-SiC (000$\bar{1}$) substrate and 300-nm-thick AlN layers grown on its substrate at (b) 650 and (c) 850°C.

Crystalline quality of AlN epilayer

The FWHMs for $(000\bar{2})$ ω-scan diffraction peaks of the N-polar AlN layer grown at 650 and 850°C were 120 and 230 arcsec, respectively. Although spiral hillocks were hardly observed in AlN layers on SiC $(000\bar{1})$, these FWHM values are larger than those of AlN layers on SiC (0001) (under 60 arcsec). The large hillocks also may contribute to the mosaic tilt of XRC. Meanwhile, the FWHMs for $(01\bar{1}\bar{2})$ ω-scan diffraction peaks of the N-polar AlN layer grown at 650 and 850°C were 1200 and 500 arcsec, respectively. We found that a high growth temperature was suitable for N-polar AlN to achieve a smooth surface and high crystalline quality. No effect of Ga pre-deposition on the crystalline quality of AlN layers was observed for the AlN growth on SiC $(000\bar{1})$, unlike in the case of Al-polar AlN growth on SiC (0001). In 850°C growth, the reciprocal space mapping (RSM) of the AlN $(11\bar{2}\bar{4})$ epilayer and 6H-SiC $(11\bar{2}\ \bar{1}\bar{2})$ substrate is shown in Fig. 4.41. 300-nm-thick AlN is almost coherently grown on 6H-SiC $(000\bar{1})$. We consider that the coherent growth contributed to the high-quality AlN growth.

4.6.3 High-quality AlN growth by controlling supersaturation

We tried to reduce supersaturation by increasing the growth temperature to 950°C, but it was ineffective. As another method to reduce supersaturation, the nitrogen-plasma power was reduced to 200 W. Simultaneously, Al flux was also decreased to maintain a slightly Al-rich condition. AlN was grown on 6H-SiC $(000\bar{1})$ at 850°C for 30 min. The thickness of the AlN layer was 160 nm, indicating that this growth rate was 40% smaller than that of 300 W growth. The surface morphology of the AlN layer is shown in Fig. 4.42 (a). The RMS roughness of the AlN layer was 0.6 nm. As expected, smooth surface was achieved in the N-polar AlN growth. A step-and-terrace structure with 1-bilayer-high steps was clearly observed on the terrace of the substrate due to the smaller density of hillocks (3×10^7 cm^{-2}). Because the 1-bilayer-high steps radiate from the hillocks, the step direction was perpendicular to an off direction of the SiC substrate. The FWHM values for $(000\bar{2})$ and $(01\bar{1}\bar{2})$ ω-scan diffraction peaks of the AlN layer were small, 120 and 210 arcsec, respectively. By decreasing supersaturation, the crystalline quality of AlN was improved.

A bright-field plan-view TEM image of the 200-nm-thick AlN layer is shown in Fig. 4.42 (b). The dark spots are TDs. No planar defect called SMB was obtained, indicating that the step-height control of the SiC substrate is effective for eliminating SMBs in growth on C-face SiC. The type of TDs was found to be a pure edge by a cross-sectional TEM image obtained under a two-beam condition. The TDs are arranged in rows with a separation of approximately 200 nm. The separation ($\sim$300 nm) of TD rows closely corresponds to the terrace width of the SiC substrate before growth, indicating that most of the TDs are generated at the step edges of the SiC substrate. The TDD was low, 2×10^9 cm^{-2}, due to step-height control of SiC $(000\bar{1})$ by H_2-gas etching.

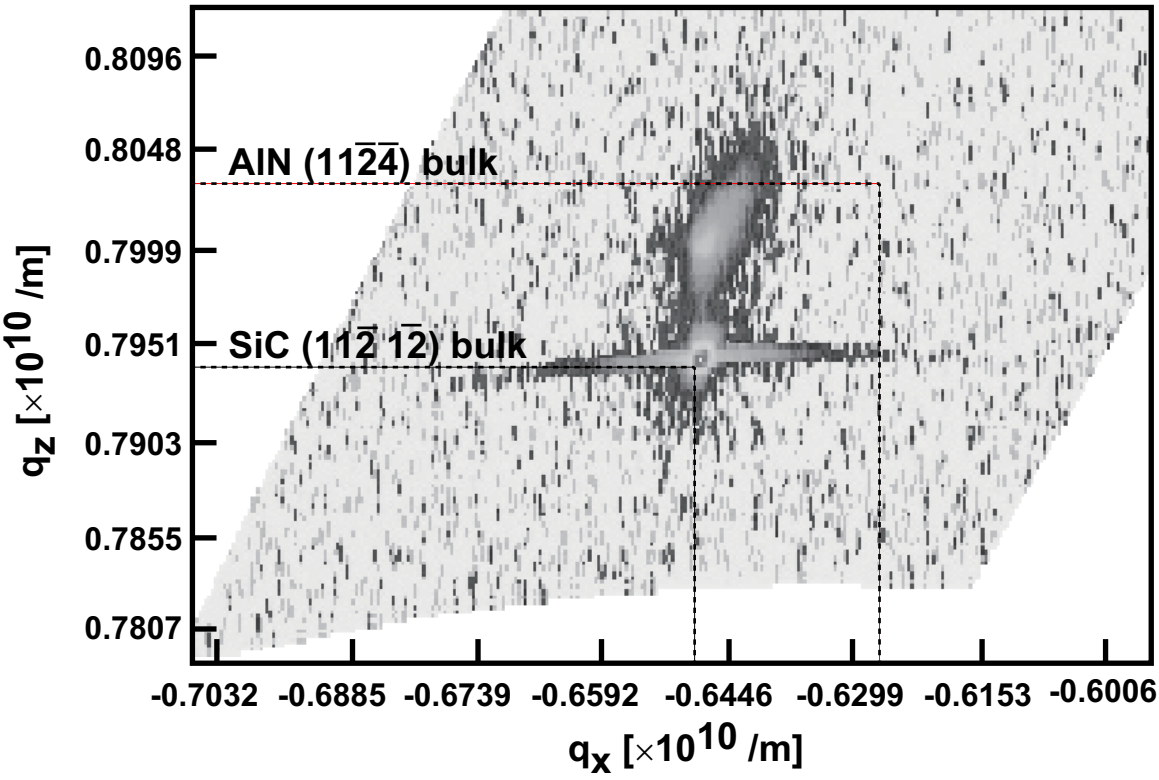

Figure 4.41: Reciprocal space mapping of N-polar AlN (11$\bar{2}\bar{4}$) epilayer and 6H-SiC (11$\bar{2}$ 1$\bar{2}$) substrate.

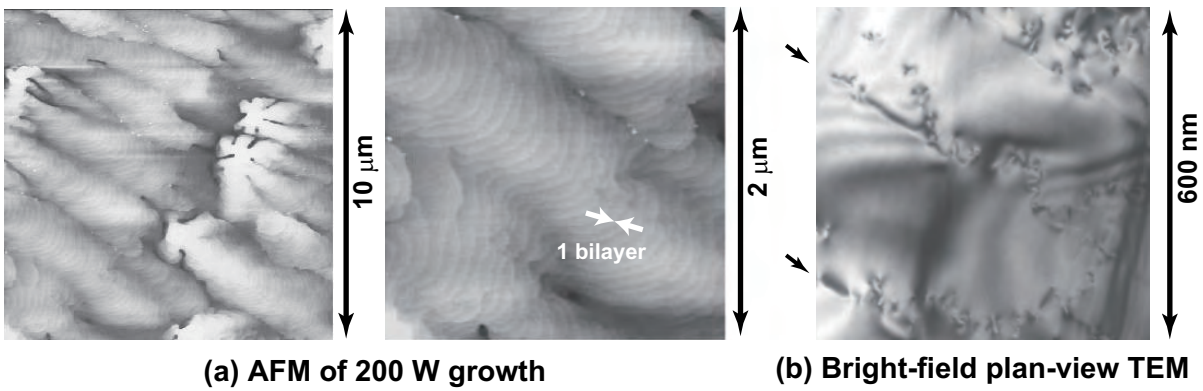

Figure 4.42: Surface morphology and bright-field plan-view TEM image of 200-nm-thick AlN grown with nitrogen-plasma power of 200 W.

4.7 Impurity Concentration in AlN Epilayers on SiC {0001}

4.7.1 Experimental procedures

To investigate the relation between the crystalline quality and impurity density, three kinds (samples A-C) of 300-nm-thick AlN layers on 6H-SiC (0001) were grown at around 600°C with slightly Al-rich condition. For sample A, AlN was grown without Ga pre-deposition. For samples B and C, 2ML-Ga was deposited just before AlN growth. The AlN layer of sample B was grown with nitrogen-plasma stabilization for 10 min before growth, while the AlN layer of sample C was grown without that. In addition, for sample D, a 300-nm-thick AlN layer was grown on 6H-SiC (0001) at high temperature (850°C) after the 50-nm-thick AlN layer was grown with the same condition as sample C. For sample E, the N-polar 200-nm-thick AlN layer was grown on 6H-SiC $(000\bar{1})$. The growth condition and crystalline quality of samples A-E are listed in Table 4.6. All the samples had no doping and Al droplets on the surface after growth.

Si, C, O levels were investigated using SIMS with an 8 keV Cs^+-primary ion beam to etch the samples. The measurements were performed at Evans Analytical Groups, Inc. The detection limits of the Si, C, and O atoms are shown in Table 4.7.

4.7.2 SIMS analysis of AlN epilayers

Crystalline-quality dependence

Impurity concentrations in the AlN layers with different crystalline quality (samples A-C) were investigated by SIMS (Fig. 4.43). The high concentration of the Si and C atoms near the AlN/SiC interface results from diffusion from the SiC substrate. All impurities of Si, C, and O atoms were less than 1×10^{18} cm^{-3} (Table 4.7). We consider that the C and O atoms are influenced by background in the MBE chamber. The concentration of Si atoms increases with increasing of TDD in AlN layers (Fig. 4.43 (a)). Elsner *et al.* reported that the stress filed produced by the TDs would accumulate electrically active impurities and point defects near the TDs [28, 29]. The Si atoms in the AlN layer also may accumulate along the core of the screw-type TDs [30].

Growth-temperature and polarity dependence

Impurity concentrations in the AlN layers of samples B, D, and E were investigated by SIMS (Fig. 4.44). The AlN layer in high-temperature growth (sample D) has the lower density of C atoms, like MOCVD growth of GaN [31, 32]. The N-polar AlN layer (sample E) has the high concentrations of Si, C, and O atoms. This results from the large surface roughness of the N-polar AlN layer as well as the low growth rate (5 nm/min).

Table 4.6: Growth condition (pretreatment, polarity, and growth temperature) and FWHM values for (0002) and (01$\bar{1}$2) ω-scan diffraction peaks of around-300-nm-thick AlN layers on 6H-SiC {0001} (samples A-E).

Sample	Pretreatment	Polarity	Growth temperature [°C]	(0002) [arcsec]	(01$\bar{1}$2) [arcsec]
A	Normal	Al	600	57	**970**
B	Ga depo.	Al	600	44	**190**
C	Ga depo., W/o plasma.	Al	650	39	**55**
D	Ga depo., W/o plasma.	Al	**850**	53	110
E	Normal	**N**	850	130	210

Ga depo. : 2ML-Ga pre-deposition just before growth (Section 4.4)
W/o plasma. : No nitrogen-plasma stabilization before growth (Section 4.5)

Table 4.7: Impurity concentrations and TDD in around-300-nm-thick AlN layers on 6H-SiC {0001} (samples A-E).

Sample	Si atoms [Atoms/cm^3]	C atoms [Atoms/cm^3]	O atoms [Atoms/cm^3]	Screw TDD [cm^{-2}]	Edge TDD [cm^{-2}]
A	1×10^{18}	1×10^{18}	5×10^{17}	3×10^{9}	2×10^{10}
B	1×10^{17}	9×10^{17}	5×10^{17}	2×10^{6}	2×10^{9}
C	2×10^{16}	2×10^{17}	2×10^{17}	6×10^{4}	4×10^{8}
D	1×10^{17}	1×10^{17}	1×10^{18}	2×10^{6}	1×10^{9}
E	2×10^{18}	1×10^{19}	1×10^{19}	3×10^{7}	2×10^{9}
Detection limit	1×10^{15}	6×10^{16}	1×10^{17}	-	-

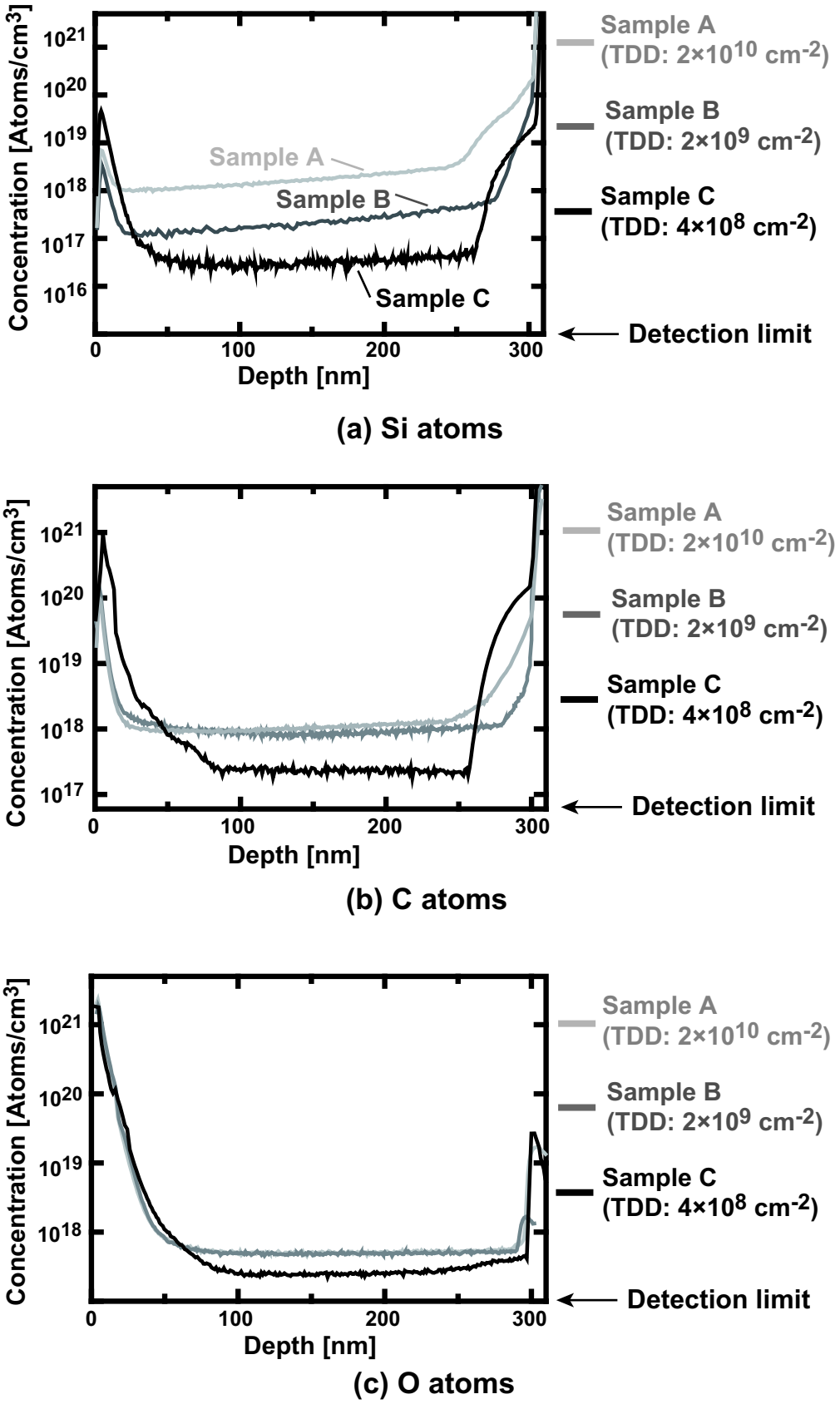

Figure 4.43: Distribution of impurity density ((a) Si, (b) C, and (c) O) in AlN layers (samples A-C) on 6H-SiC $(0001)_{Si}$.

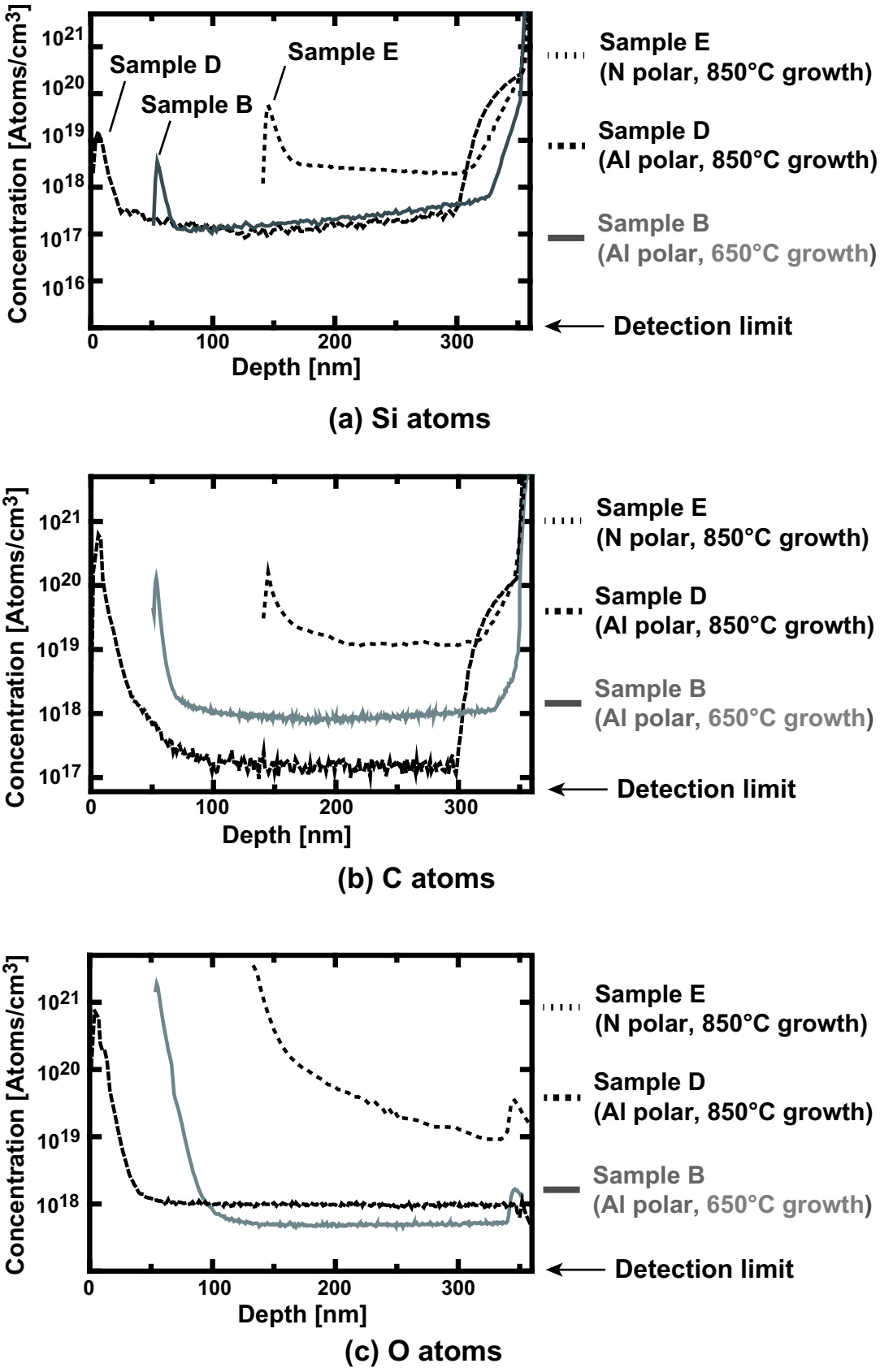

Figure 4.44: Distribution of impurity density ((a) Si, (b) C, and (c) O) in AlN layers (samples B, D, and E) on 6H-SiC {0001}.

4.8 Summary

We optimized the growth condition of AlN films on SiC {0001}. N-polar AlN on SiC (000$\bar{1}$) had multinucleation growth, indicating the rough surface. By decreasing the supersaturation, we achieved the smooth surface with a step-and-terrace structure and high-quality AlN growth (2×10^9 cm^{-2}). On the other hand, Al-polar AlN growth on SiC (0001) at low temperature (600–700°C) with the slightly Al-rich condition had the layer-by-layer growth mode at the initial growth stage. In AlN growth on 6H-SiC (0001) substrates with 3- and 6-bilayer-high steps, TDs were generated at the step edge of the SiC substrate before growth and arranged in rows. The TDD in the AlN layers was 2×10^{10} cm^{-2}. In addition, by the sacrificial oxidation process of the 6H-SiC (0001) with 3-bilayer-high steps, we achieved the large-area observation of SMBs for the first time.

To improve the crystalline quality of the Al-polar AlN growth, we focused on the initial growth stage. The Ga pre-deposition just before AlN growth was very effective to enhance the layer-by-layer growth mode and to reduce the TDD in the AlN layer. By 2ML-Ga pre-deposition, the TDD in the AlN layer was decreased to 2×10^9 cm^{-2}. Furthermore, AlN growth just after nitrogen-plasma ignition achieved the layer-by-layer growth mode from the first layer. The TDD in the AlN layer was 2×10^8 cm^{-2}.

In next chapter, generation mechanisms of TD rows and SMB are clarified by the HRTEM observation. We investigate the critical thickness of the AlN layer on SiC (0001) substrate. A estimation of TDD in the AlN layer using XRD is also described.

References

[1] Y. Wu, A. Hanlon, J. F. Kaeding, R. Sharma, P. T. Fini, S. Nakamura, and J. S. Speck, Appl. Phys. Lett. **84**, 912 (2004).

[2] A. Georgieva, P. O. Persson, A. Kasic, L. Hultman, and E. Janzen, J. Appl. Phys. **100**, 036105 (2006).

[3] Y. N. Picard, M. E. Twigg, M. A. Mastro, C. R. Eddy, R. L. Henry, R. T. Holm, P. G. Neudeck, A. J. Trunek, and J. A. Powell, Appl. Phys. Lett. **91**, 014101 (2007).

[4] Z. J. Reitmeier, S. Einfeldt, R. F. Davis, X. Xhang, X. Fang, and S. Mahajan, Acta Mater. **57**, 4001 (2009).

[5] N. Onojima, J. Suda, and H. Matsunami, Jpn. J. Appl. Phys. **42**, L445 (2003).

[6] M. Kim, J. Ohta, A. Kobayashi, H. Fujioka, and M. Ohta, Appl. Phys. Lett. **91**, 151903 (2007).

[7] P. Vermaut, P. Ruterana, and G. Nouet, Philos. Mag. **76**, 1215 (1997).

[8] N. Onojima, Dr. Thesis, Faculty of Engineering, Kyoto University, Kyoto, 2004.

[9] F. C. Frank, Discuss. Faraday Soc. **5**, 67 (1949).

[10] B. Heying, X. H. Wu, S. Keller, Y. Li, D. Kapolnek, B. P. Keller, S. P. DenBaars, and J. S. Speck, Appl. Phys. Lett. **68**, 643 (1996).

[11] C. D. Lee, Y. Dong, R. M. Feenstra, J. E. Northrup, and J. Neugebauer, Phys. Rev. B **68**, 205317 (2003).

[12] M. Horita, J. Suda, and T. Kimoto, Appl. Phys. Lett. **89**, 112117 (2006).

[13] W. K. Burton, N. Cabrera, and F. C. Frank, Philos. Trans. R. Soc. **243**, 299 (1951).

[14] B. Heying, E. J. Tarsa, C. R. Elsass, P. Fini, S. P. DenBaars, and J. S. Speck, J. Appl. Phys. **85**, 6470 (1999).

[15] M. H. xie, S. M. Seutter, W. K. Zhu, L. X. Zheng, H. Wu, and S. Y. Tong, Phys. Rev. Lett. **82**, 2749 (1999).

[16] H. Zheng, M. H. xie, H. S. Wu, and Q. K. Xue, Phys. Rev. B **75**, 205310 (2007).

[17] H. Zheng, M. H. xie, H. S. Wu, and Q. K. Xue, Phys. Rev. B **77**, 045303 (2008).

[18] P. Cantu, F. Wu, P. Waltereit, S. Keller, A. E. Romanov, U. K. Mishra, S. P. DenBaars, and J. S. Speck, Appl. Phys. Lett. **83**, 674 (2003).

[19] P. Cantu, F. Wu, P. Waltereit, S. Keller, A. E. Romanov, S. P. DenBaars, and J. S. Speck, J. Appl. Phys. **97**, 103534 (2005).

[20] Z. Wu, K. Nonaka, Y. Kawai, T. Asai, F. A. Ponce, C. Chen, M. Iwaya, S. Kamiyama, H. Amano, and I. Akasaki, Appl. Phys. Exp. **3**, 111003 (2010).

[21] E. Iliopoulos and T. D. Moustakas, Appl. Phys. Lett. **81**, 295 (2002).

[22] A. Nakajima, Y. Furukawa, H. Yokoya, S. Yamaguchi, and H. Yonezu, Jpn. J. Appl. Phys. **45**, 2422 (2006).

[23] W. E. Hoke, A. Torabi, J. J. Mosca, and T. D. Kennedy, J. Vac. Sci. Technol. B **25**, 978 (2007).

[24] J. E. Northrup, J. Neugebauer, R. M. Feenstra, and A. R. Smith, Phys. Rev. B **61**, 9932 (2000).

[25] J. E. Northrup, R. D. Felice, and J. Neugebauer, Phys. Rev. B **55**, 13878 (1997).

[26] J. S. Brown, G. Koblmuller, R. Averbeck, H. Riechert, and J. S. Speck, J. Vac. Sci. Technol. A **24**, 1979 (2006).

[27] T. Ohachi, N. Yamabe, H. Shimomura, T. Shimamura, O. Ariyada, and M. Wada, J. Cryst. Growth **311**, 2987 (2009).

[28] J. Elsner, R. Jones, P. K. Sitch, V. D. Porezag, M. Elstner, T. Frauenheim, M. I. Heggie, S. Oberg, and P. R. Briddon, Phys. Rev. Lett. **79**, 3672 (1997).

[29] Z. Weber, Y. Chen, S. Ruvimov, and J. Washburn, Phys. Rev. Lett. **79**, 2835 (1997).

[30] J. E. Northrup, Appl. Phys. Lett. **78**, 2288 (2001).

[31] G. Parish, S. Keller, S. P. DenBaars, and U. K. Mishra, J. Electron. Mater. **29**, 15 (2000).

[32] D. D. Koleske, A. E. Wickenden, R. L. Henry, and M. E. Twigg, J. Cryst. Growth **242**, 55 (2002).

Chapter 5

Extended Defects in AlN Epilayers on SiC

5.1 Introduction

In this chapter, we report on extended defects in AlN layers on 6H-SiC (0001): i. e., stacking mismatch boundaries (SMBs), TD rows, and misfit dislocations.

Depending on stacking sequences of topmost two bilayers of a SiC surface, an AlN layer grown on SiC (0001) can have planar defects threading [0001], i. e., SMBs. However, there are few reports on characteristic of the SMBs due to high defective. We successfully observed the SMBs at a micron scale due to a sacrificial-oxidation process of the SiC substrate and the realization of a layer-by-layer growth mode at an initial stage of growth (Section 4.3.4). In this chapter, we identify displacement vector of the obtained SMBs.

By controlling step heights of a 6H-SiC (0001) substrate to 3 or 6 bilayer, we achieved AlN growth without the SMBs. In addition, we realized a layer-by-layer growth mode from the first layer of AlN by Ga pre-deposition and avoidance of unintentional nitrogen exposure, so that threading dislocation density (TDD) was reduced to 4×10^8 cm^{-2}. However, most threading dislocations (TDs) were generated at step edges of the SiC substrate. Elimination of the TDs generated at the step edges, called TD rows, is a key issue for further reduction of TDD. To take a hint to reduce the TDD, we try to clarify the generation mechanism of the TD rows by transmission electron microscopy (TEM).

Both *c*-axis and *a*-axis lattice mismatches between AlN and SiC are 1 %. The critical thickness of $In_{0.15}Ga_{0.85}As$ growth on GaAs with the lattice mismatch of 1 % is under 100 nm [1]. However, surprisingly, the 300-nm-thick AlN layers were coherently grown on 6H-SiC substrates. To determine the critical thickness of the AlN growth on 6H-SiC (0001), we evaluated thick AlN layers by x-ray diffraction (XRD), laser Raman scattering spectroscopy, and cathodoluminescence (CL).

5.2 Characteristics of Stacking Mismatch Boundaries

5.2.1 Introduction

A SMB is a planar defect threading the [0001] direction. As similar planar defects, a prismatic stacking fault (PSF) and an inversion domain boundary (IDB) are well known. PSFs are formed by one shear part of a crystal, dissociation of a perfect dislocation, or insertion of an extra basal. In AlN or GaN heteroepitaxial growth on SiC nonpolar $(11\bar{2}0)$ substrates, PSFs are often observed with basal plane stacking faults (BSFs) [2, 3]. Drum observed PSFs in AlN crystals and proposed that PSFs were characterized by the displacement vector $\mathbf{R}=1/2[01\bar{1}1]$ [4]. Northrup's calculation showed that PSFs with $\mathbf{R}=1/2[01\bar{1}1]$ were energetically favorable [5, 6]. Zakharov *et al.* identified that PSFs in GaN/AlN layers on 4H-SiC $(11\bar{2}0)$ substrates had the displacement vector $\mathbf{R}=1/2[01\bar{1}1]$ [7]. On the other hand, IDBs are observed in GaN and AlN on sapphire (0001) [8]. AlN (0001) and AlN $(000\bar{1})$ have different polarities, Al polarity and N polarity, respectively. When the AlN layer with Al polarity and N polarity grows on the same substrate, the IDBs are generated between the AlN layers with their different polarities. SMBs and PSFs are $\{11\bar{2}0\}$ planar defects, while IDBs are $\{1\bar{1}00\}$ planar defects.

SMBs are formed in AlN or GaN growth on a SiC (0001) substrate due to the polytype difference. It is considered that SMBs have a displacement $\mathbf{R}=1/6[02\bar{2}3]$ because SMBs correspond to a simple change in stacking sequence, from ···BABA··· to ··· ACAC···. Tanaka *et al.* grew a 1.5-nm-thick AlN layer on a 6H-SiC (0001) substrate with 1-bilayer-high steps by molecular-beam epitaxy (MBE) and observed the SMBs using cross-sectional high-resolution TEM (HRTEM) [9]. However, characteristics of SMBs, such as the displacement vector, have not been reported because the crystalline quality of the AlN layers was insufficient for plan-view HRTEM observation. In this section, the SMBs were investigated in detail at an atomic scale using HRTEM.

5.2.2 Experimental procedures

6H-SiC (0001) (vicinal angle 0.2°) substrates were treated by high-temperature H_2-gas etching after chemical mechanical polishing (CMP), realizing the step-and-terrace structure. The SiC surface had 3-bilayer-high steps and around 200-nm-wide terraces. For the substrate, a sacrificial-oxidation process was carried out for 12 hours, forming an 80-nm-thick thermal oxide (Section 4.3.4). The thermal oxide was removed by a HF-wet-chemical solution. After an *ex-situ* wet-chemical cleaning and *in-situ* Ga cleaning, the SiC substrate was exposed to a Ga beam corresponding to around 2 monolayer (ML). Just after that, 50-nm-thick AlN growth was started at 650 °C. A reflection high-energy electron diffraction (RHEED) oscillation at an initial growth stage was observed, indicating the layer-by-layer growth mode. Defects in the AlN layers were observed by TEM and transmission electron aberration-corrected microscopy (TEAM).

5.2.3 Type and density of extended defects

The density of screw-type TDs was too low (under 10^7 cm^{-2}) to be observed by TEM. It was reported that screw-type TDs in AlN layers form spiral hillocks with 1**c**. In an atomic force microscopy (AFM) image after AlN growth, only two spiral hillocks were observed in an area 50×50 μm^2. The density of screw-type TDs was 8×10^4 cm^{-2}. Bright-field plan-view TEM images of the AlN layer were recorded with [0001] zone axis and 7° tilt, as shown in Fig. 5.1. A dark spot in Fig. 5.1 (a) is a TD. The TDs were distributed randomly and found to be pure-edge type from cross-sectional TEM images with the two-beam condition. The density of the TDs in the AlN layer was 8×10^8 cm^{-2}.

As shown in Fig. 5.1, a lot of dark lines were observed with zone axis and became bands with interference fringes in the tilted view, indicating that the dark lines are planar defects threading through the AlN layer. The typical separation of the planar defects was 200 nm, corresponding to the terrace width of the SiC substrate before growth. This indicates that the planar defects are generated at the step edges of the SiC substrate. The planar defects consisted of $\{11\bar{2}0\}$ planes. Although the step edges of the SiC surface before growth were straight, the planar defects formed continuous zigzag lines corresponding to the step direction of the SiC substrate. We consider that the off direction of the SiC substrate is displaced by 6° out of $\langle 1\bar{1}00\rangle$, causing the zigzag structure on the $\{11\bar{2}0\}$ planar defects. In a cross-sectional TEM image, the planar defects were generated at the AlN/SiC interface without insertion of an extra basal, indicating that the planar defects are not PSFs. The sign of the polarity is defined by the direction of the polar Al-N bonds aligned along the AlN c-axis. To determine the polarity around a planar defect in the AlN layer, convergent beam electron diffraction (CBED) patterns on the both sides of the planar defect were observed with $\langle 1\bar{1}00\rangle$ zone-axis. CBED patterns of the AlN layer are shown in Fig. 5.2. Compared with a simulation image, the AlN layer on the 6H-SiC (0001) substrate has Al polarity on both sides of the planar defects, indicating that the planar defects are not IDBs.

We conclude that the planar defects are $\{11\bar{2}0\}$ SMBs. A 6H-SiC substrate with 3-bilayer-high steps can have different surface terminations on each terrace. By the sacrificial-oxidation process, 2H-AlN on the 6H-SiC substrate grows with different stacking sequences on each terrace due to the polytype difference, so that SMBs are generated at the step edges, as shown in Fig. 1.6.

5.2.4 Displacement vector of SMBs

To investigate displacement vectors of the SMBs, plan-view images of the AlN layer was observed with various two-beam situations (see Fig. 5.3). The principles of the interpretation depend on the value of the phase factor $\alpha = 2\pi\mathbf{g}\cdot\mathbf{R}$ occurred in the expression $\exp(i\alpha)$ [4], where $\mathbf{g}$ is the reciprocal lattice vector of the operating reflection of a two beam situation and $\mathbf{R}$ is the displacement vector of the fault. When $\mathbf{g}\cdot\mathbf{R}$=0, the faults are out of contrast. The principal values of the phase factor in AlN are given in Table 5.1. Defect A in Fig. 5.3 (a) is out of contrast when $\mathbf{g}$=$\bar{1}2\bar{1}0$ and $10\bar{1}0$, suggesting that the fault vector is not $\frac{1}{6}\langle 2\bar{2}03\rangle$

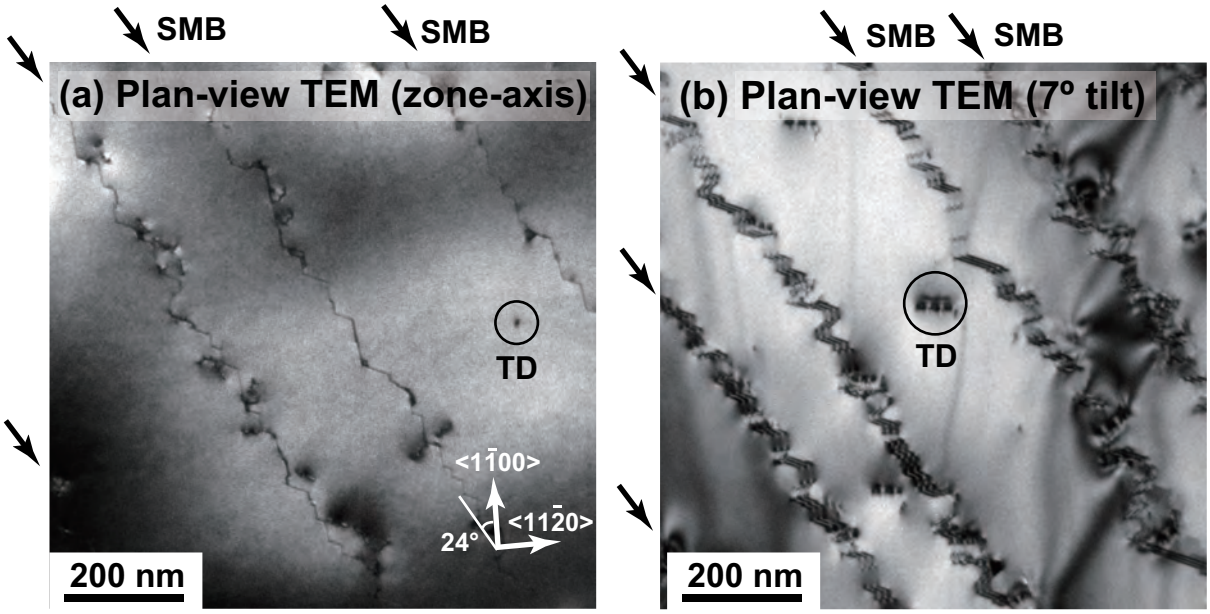

Figure 5.1: Bright-field plan-view TEM images of 50-nm-thick AlN layer on 6H-SiC (0001) substrate: (a) [0001] zone-axis and (b) 7° tilt.

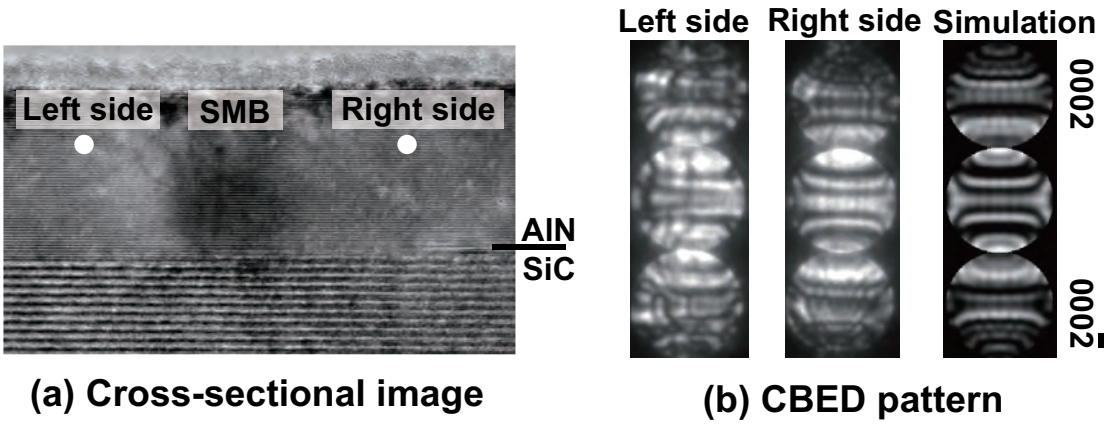

Figure 5.2: (a) Cross-sectional TEM image and (b) CBED patterns on both sides of SMB in AlN layer on 6H-SiC (0001) substrate.

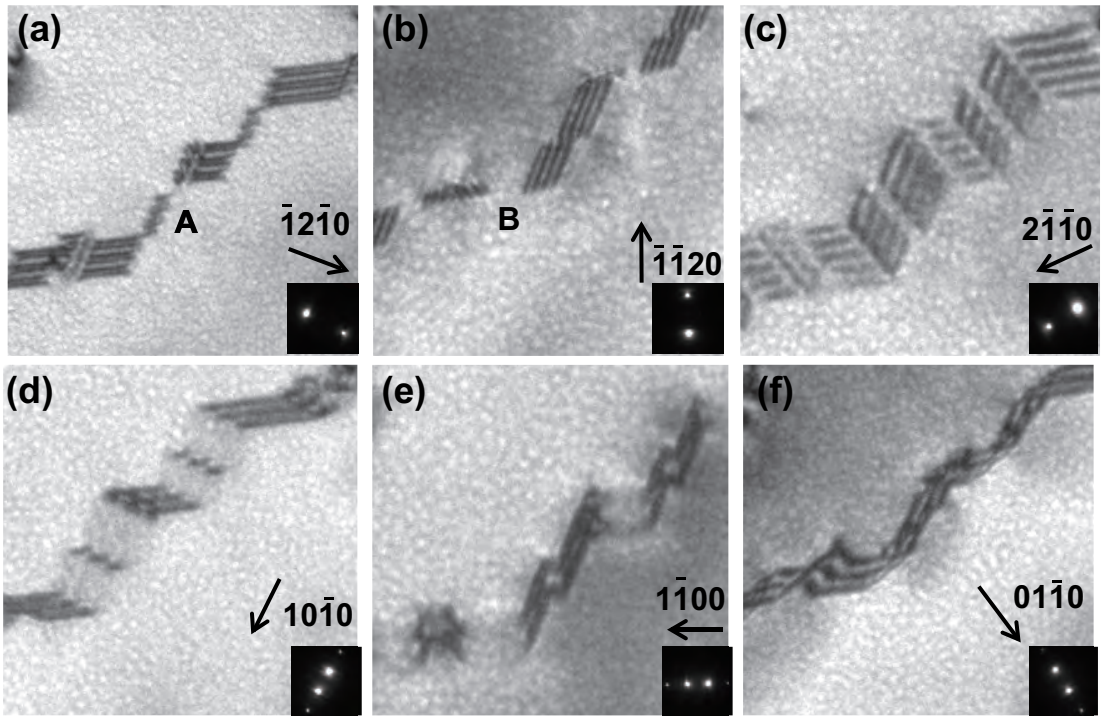

Figure 5.3: Plan-view TEM images of SMB in AlN layer on 6H-SiC (0001) with various two-beam conditions (a: $\mathbf{g}=\bar{1}2\bar{1}0$, b: $\mathbf{g}=\bar{1}\bar{1}20$, c: $\mathbf{g}=2\bar{1}\bar{1}0$, d: $\mathbf{g}=10\bar{1}0$, e: $\mathbf{g}=1\bar{1}00$, and f: $\mathbf{g}=01\bar{1}0$).

Table 5.1: Principle values of phase factor $\alpha = 2\pi\ \mathbf{g}\cdot\ \mathbf{R}$ for various $\mathbf{g}$ and $\mathbf{R}$ in AlN.

2π $\mathbf{g}$	$\frac{1}{2}\mathbf{c}=\frac{1}{2}[0001]$	$\frac{1}{2}\mathbf{a}=\frac{1}{6}[11\bar{2}0]$	$\frac{1}{3}\mathbf{p}=\frac{1}{3}[1\bar{1}00]$	$\mathbf{R}_1=\frac{1}{2}[1\bar{1}01]$	$\mathbf{R}_2=\frac{1}{6}[2\bar{2}03]$
$2\pi\ 11\bar{2}0$	0	0	0	0	0
$2\pi\ 1\bar{2}10$	0	π	0	π	0
$2\pi\ \bar{2}110$	0	π	0	π	0
$2\pi\ 1\bar{1}00$	0	0	$-\frac{2}{3}\pi$	0	$-\frac{2}{3}\pi$
$2\pi\ 10\bar{1}0$	0	π	$+\frac{2}{3}\pi$	π	$+\frac{2}{3}\pi$
$2\pi\ 01\bar{1}0$	0	π	$-\frac{2}{3}\pi$	π	$-\frac{2}{3}\pi$
$2\pi\ 02\bar{2}0$	0	0	$+\frac{2}{3}\pi$	0	$+\frac{2}{3}\pi$
$2\pi\ 03\bar{3}0$	0	π	0	π	0
$2\pi\ 0002$	0	0	0	0	0
$2\pi\ 01\bar{1}1$	π	π	$-\frac{2}{3}\pi$	0	$-\frac{1}{3}\pi$
$2\pi\ 03\bar{3}1$	π	π	0	0	π

(=$\mathbf{R}_2$). We predict that the displacement vector of the defect A is $\frac{1}{2}[\bar{1}011]$ (=$\mathbf{R}_1$). Although the fault vector of $\frac{1}{2}[\bar{1}011]$ can be checked by whether the contrast is produced in $\mathbf{g}=\bar{1}100$, $\bar{2}200$, and $\bar{3}300$, the high order reflection was difficult to isolate with confidence. Similarly, defect B in Fig. 5.3 (b) is out of contrast when $\mathbf{g}=\bar{1}\bar{1}20$ and $1\bar{1}00$, suggesting that the displacement vector of the defect B may be $\frac{1}{2}[\bar{1}101]$. Because one of the SMBs consists of defects A and B with different displacement vectors, there must be a new defect with $\mathbf{b}=\frac{1}{2}[0\bar{1}10]$ at the boundary of defects A and B due to Kirchhoff's law. However, no defects exist around the SMBs, as shown in Fig. 5.1. To clarify the displacement vector of the SMBs correctly, the other approach is necessary.

A plan-view HRTEM image of the AlN layer with the SMB is shown in Fig. 5.4. The image was obtained near the Scherzer defocus. The SMB was normal to a $\langle 11\bar{2}0\rangle$ direction. We assign a plane index of the observed $\{11\bar{2}0\}$ SMB with $(11\bar{2}0)$ for simplicity. Around the SMB, the 2-nm-wide AlN layer strained. We consider that the strain around the SMB results from the enforced binding between AlN layers with different stacking sequences. The SMBs are generated at the step edges of the SiC surface, as shown in Fig. 1.5. In GaN on 6H-SiC (0001), Sverdlov *et al.* observed one SMB at a 3-bilayer-high step of the SiC substrate [10]. However, in a nano-scale view, a 3-bilayer-high step consists of three 1-bilayer-high steps with separation of 1 nm. If SMBs are generated from each 1-bilayer-high step, three SMBs will be generated at one 3-bilayer-high step, so that the strain width around the SMB becomes over 2 nm. As shown in Fig. 5.4, it seems that just one SMB is generated at a 3-bilayer-height step and yields in the strain of the 2-nm width.

A cross-sectional HRTEM image of the AlN layer with $\{11\bar{2}0\}$ zone axis is shown in Fig. 5.5. The SMB threaded right through a [0001] direction from an AlN/SiC interface. In the cross-sectional image of the AlN layer, the strain width around the SMB was larger (4 nm) than that in the plan-view image because the cross-sectional image with $\{11\bar{2}0\}$ zone axis tilted at the angle of 30° to the $(11\bar{2}0)$ SMB. When we arbitrarily assign ...ABAB... to atomic columns at the right sides of the SMB, as shown in Fig. 5.5, the stacking sequence changes to ...CACA... at the left sides across the SMB, suggesting that the l component of the displacement $[hkl]$ is 1/2; the h and k components of the displacement $[hkl]$ cannot be precisely identified from the cross-sectional image.

To determine the displacement of the SMB, the images of filtered $\{1\bar{1}00\}$ lattice fringes from Fig. 5.4 (a) are shown in Fig. 5.6. $(1\bar{1}00)$ and $(10\bar{1}0)$ lattices shifted with half periodicity of an a-axis lattice across the SMB, as shown in Fig. 5.6 (a) and (b). The size of the a-axis lattice is $\mid 1/3\langle 11\bar{2}0\rangle \mid$. $(01\bar{1}0)$ lattice had no shift, as shown in Fig. 5.6 (c). These mean that a displacement vector $\mathbf{R}$ of the SMB includes the component of $1/2[01\bar{1}0]$ (h=1/2, k=0), as follows.

$$\mathbf{R} = \frac{1}{6}[11\bar{2}l] + \frac{1}{6}[\bar{1}2\bar{1}l] = \frac{1}{2}[01\bar{1}l] \tag{5.1}$$

Therefore, the displacement vector $\mathbf{R}$ of the $(11\bar{2}0)$ SMB is $1/2[01\bar{1}1]$. To confirm the displacement vector of the $(11\bar{2}0)$ SMB, experimental and simulated high-resolution (HR)

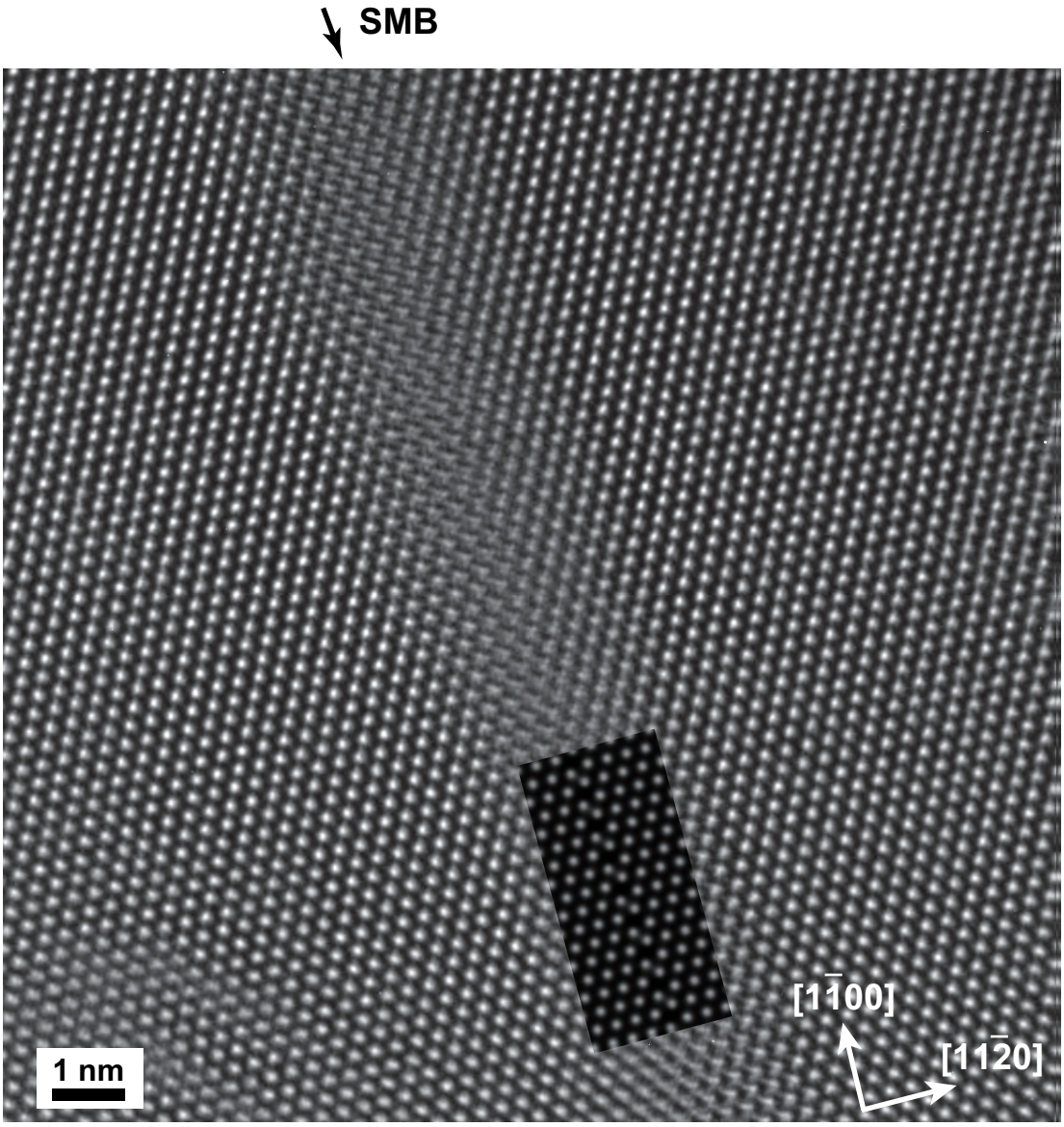

Figure 5.4: Plan-view HRTEM image of SMB in AlN layer on 6H-SiC (0001) substrate ([0001] zone-axis).

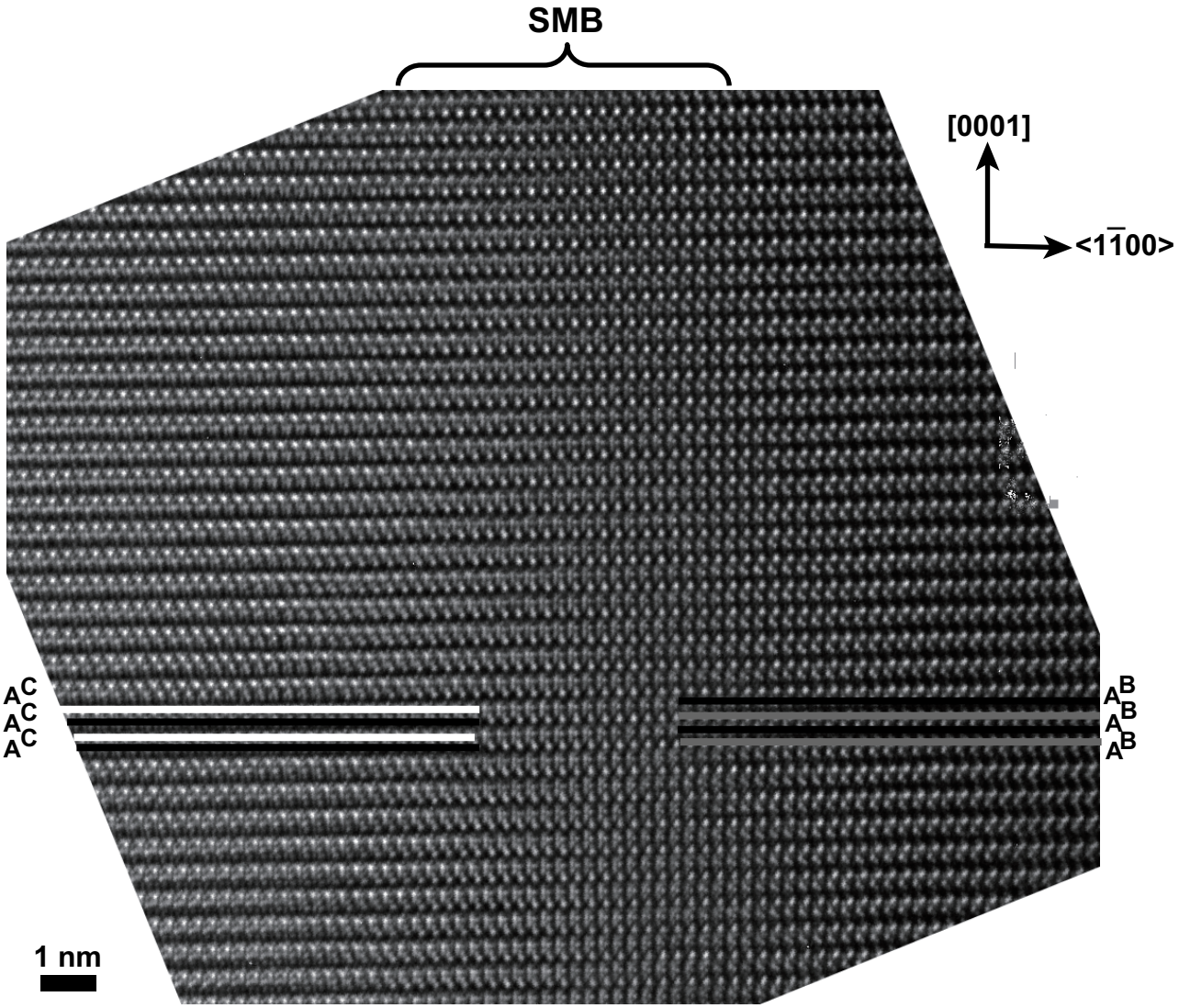

Figure 5.5: Cross-sectional HRTEM image of SMB in AlN layer on 6H-SiC (0001) substrate ([11$\bar{2}$0] zone-axis).

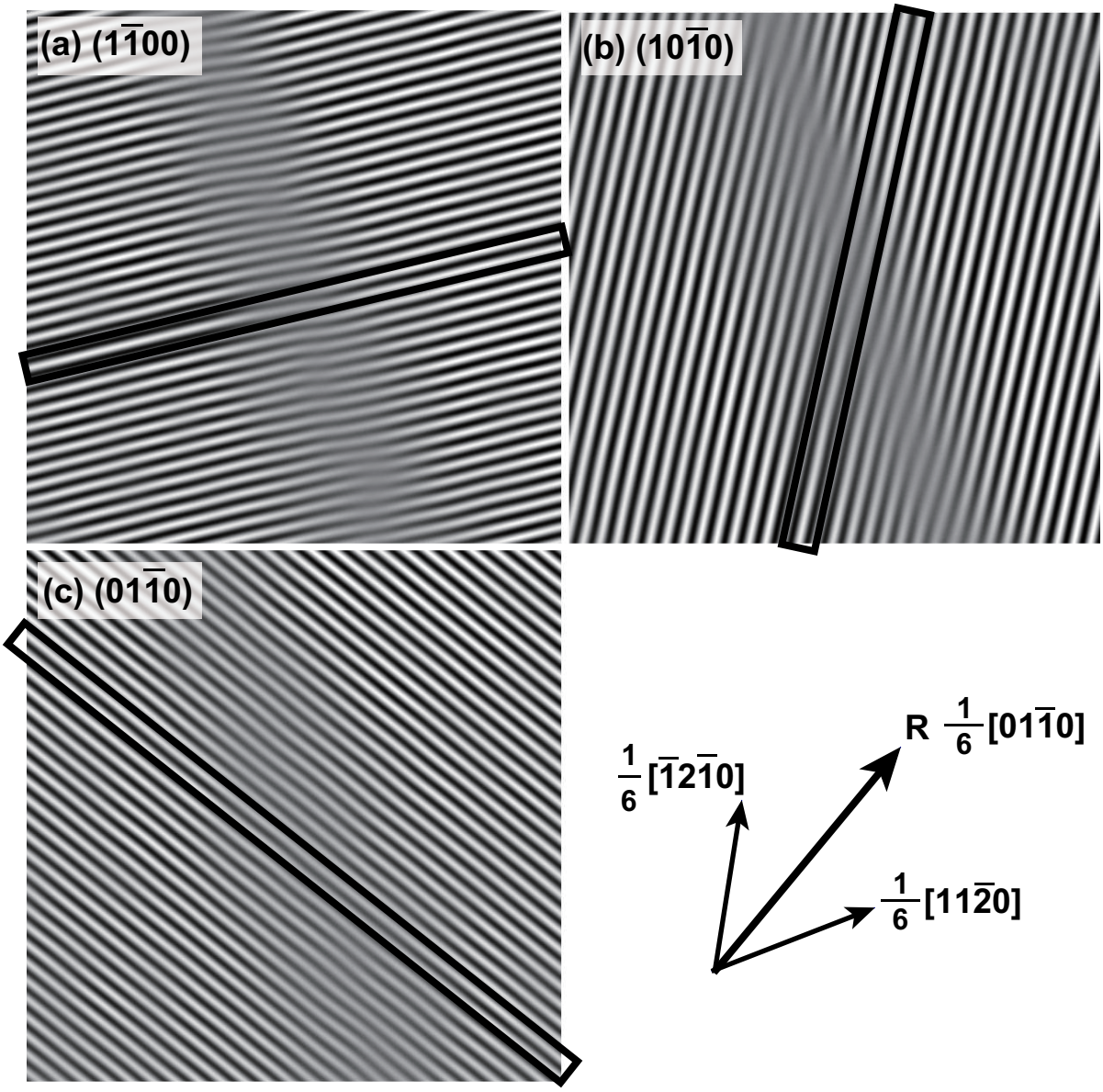

Figure 5.6: Filtered images of $\{1\bar{1}00\}$ lattice fringes around SMB in AlN layer using Fourier transform. (a): $(1\bar{1}00)$, (b): $(10\bar{1}0)$, and (c): $(01\bar{1}0)$. Only $(01\bar{1}0)$ lattice has no shift, indicating that displacement vector **R** is $1/2\ \langle 01\bar{1}1\rangle$.

images were compared. The simulation was measured near Scherzer defocus and sample thickness of 4.2 nm. The simulated HR image of the $(11\bar{2}0)$ SMB with $\mathbf{R}= 1/2[01\bar{1}1]$ was inserted in Fig. 5.4. The simulated HR image closely matches the experimental HR image at both sides across the SMB. We conclude that the $(11\bar{2}0)$ SMB has the displacement $1/2[01\bar{1}1]$.

When the stacking sequences of the AlN layer follow the topmost two layers of the SiC substrate, the displacement vector of the SMB generated at the step edges of the SiC substrate should be $1/6\langle 02\bar{2}3\rangle$. However, the displacement vector of the observed SMB was $1/2\langle 01\bar{1}1\rangle$. To form the SMBs with $\mathbf{R}=1/2\langle 01\bar{1}1\rangle$, the additional shift of $\frac{1}{6}\langle 01\bar{1}0\rangle$ is necessary, as follows.

$$\mathbf{R} = \frac{1}{2}\langle 01\bar{1}1\rangle = \frac{1}{6}\langle 02\bar{2}3\rangle + \frac{1}{6}\langle 01\bar{1}0\rangle \tag{5.2}$$

Northrup's calculations of an atomic structure for PSFs indicated that there are no wrong or broken bonds, but the PSFs with $\mathbf{R}=1/2\langle 01\bar{1}1\rangle$ are energetically more favorable than those with $\mathbf{R}=1/6\langle 02\bar{2}3\rangle$ due to large distortions from the tetrahedral bonding [5]. Although for the SMBs, their displacements at initial AlN growth have to be $1/6\langle 02\bar{2}3\rangle$ to follow the same stacking arrangement as the SiC surface, the SMBs also had the displacement $\mathbf{R}=1/2\langle 01\bar{1}1\rangle$. We consider that the displacement $\frac{1}{6}\langle 01\bar{1}0\rangle$ is added during growth due to favorable binding of AlN layers with different stacking arrangements. In AlN, the SMBs with $\mathbf{R}=1/2\langle 01\bar{1}1\rangle$ may be energetically more favorable than those with $\mathbf{R}=1/6\langle 02\bar{2}3\rangle$, such as PSFs.

A schematic figure of the atomic structure of the $(11\bar{2}0)$ and $(\bar{2}110)$ SMB with $\mathbf{R}= 1/2[01\bar{1}1]$ is shown in Fig. 5.7. The atomic structure of the $(\bar{2}110)$ SMB with $\mathbf{R}= 1/2[01\bar{1}1]$ corresponds to that of a favorable PSF reported by Northrup. In the case of Fig. 5.7, formation of the $(\bar{2}110)$ SMBs is most preferable. However, the SMBs are generated at the step edges of the SiC substrate with the off direction away from $\langle 1\bar{1}00\rangle$, so that the SMBs must compose the zigzag structure with the $(11\bar{2}0)$ and $(\bar{2}110)$ planes. The $(11\bar{2}0)$ SMB with $\mathbf{R}= 1/2[01\bar{1}1]$, which is unfavorable, must be formed. Due to the enforced formation, the 2-nm-wide AlN layer may strain around the $(11\bar{2}0)$ SMB. Although we observed just the $(11\bar{2}0)$ SMB with $\mathbf{R}= 1/2[01\bar{1}1]$, the $(\bar{2}110)$ SMBs with $\mathbf{R}= 1/2[01\bar{1}1]$ would have the smaller strain, as with the PSF observed by Zakharov *et al.* [5].

5.2.5 Discussion

Because an AlN layer on 3-bilayer-high steps also have the same abrupt interface, the AlN stacking layers on the terrace of the SiC substrate follow the same crystal arrangements as the SiC surface, as shown in Fig. 5.8 (a). When the surface termination of the SiC substrate with 3-bilayer-high steps is ...CBAB*CA* and ...BCAC*BA* on each terrace, AlN layers should have the stacking sequence of *CA*CA... and *BA*BA..., respectively.

The AlN layers with the different stacking arrangements coalesce at the step edges of the SiC substrate, generating the SMBs. In detail, near the step edges of the SiC substrate, the AlN layer should have step-flow growth mode due to preferable incorporation into the step.

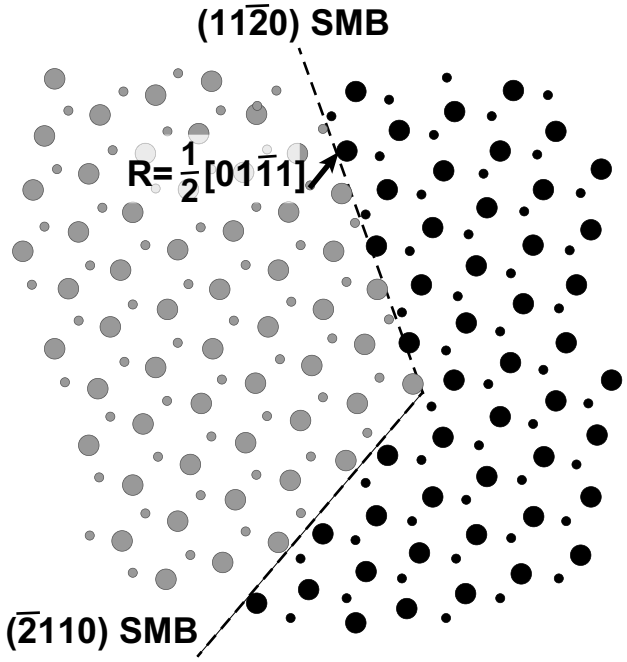

Figure 5.7: Schematic figure of SMB in AlN layer on 6H-SiC (0001). Displacement vector **R** is 1/2 $\langle 01\bar{1}1 \rangle$.

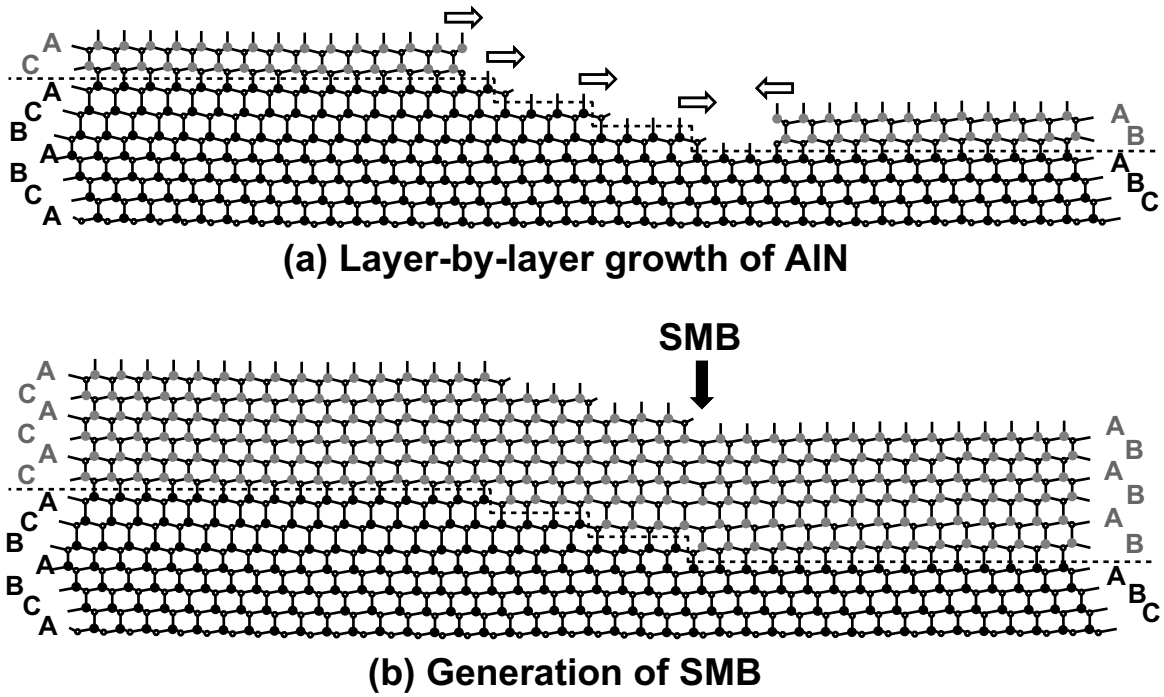

Figure 5.8: Cross-sectional schematic figures of SMB generated at step edge of 6H-SiC substrate with 3-bilayer-high steps. After AlN is grown in layer-by-layer growth mode, SMB is generated near step edge of SiC.

The AlN layers following the same stacking arrangements as the step of the SiC substrate are thought to coalesce with the AlN layers grown on the terrace, generating the SMB. Because no AlN layer near the step edges of the SiC substrate has layer-by-layer growth mode, just one SMB is generated from one 3-bilayer-high step, as shown in Fig. 5.8 (b). In the initial AlN growth, SMBs should have a displacement $1/6\langle 02\bar{2}3\rangle$ due to the simple change in stacking sequence, from ...BABA... to ...ACAC... . However, after further growth, the displacement $\frac{1}{6}\langle 01\bar{1}0\rangle$ is added because of favorable binding of AlN layers, changing the displacement vector to $1/2\langle 01\bar{1}1\rangle$. In cross-sectional HRTEM images, SMBs have no abrupt transformation of strain in growth direction, indicating that the displacement $\frac{1}{6}\langle 01\bar{1}0\rangle$ is gradually added.

The displacement vector of the SMB is decided by a direction in the first coalescence of the AlN layers. When the AlN layers with different stacking arrangements coalesce with a $[\bar{2}110]$ direction near the step edges of the SiC substrate, the $(\bar{2}110)$ SMBs are generated with the displacement $\mathbf{R}=1/2[01\bar{1}1]$. These $(\bar{2}110)$ SMBs with $\mathbf{R}=1/2[01\bar{1}1]$, as with PSFs reported by Northrup, have most preferable bonding. After that, the AlN layers completely coalesce in plane. When the off direction of the SiC substrate is out of $[\bar{2}110]$, the SMBs must have $(11\bar{2}0)$ planes as well as $(\bar{2}110)$ planes, forming the zigzag structure along with the step edges, as shown in Fig. 5.1 and Fig. 5.7. Both the $(11\bar{2}0)$ and $(\bar{2}110)$ SMBs have the displacement $\mathbf{R}=1/2[01\bar{1}1]$. Due to the same displacement vector, no other defect generates at the step edges of the SiC substrate. The $(11\bar{2}0)$ SMBs with $\mathbf{R}=1/2[01\bar{1}1]$ strain the 2-nm-wide AlN layer, as shown in Fig. 5.4, because of the enforced binding. The SMBs thread over 50 nm through the AlN layer.

We investigated why step heights of the 6H-SiC (0001) substrate depend on the off direction, as described at Section 3.2.3. It was found that the off direction within 10° out of $\langle 1\bar{1}00\rangle$ forms 6-bilayer-high steps, while that over 10° out of $\langle 1\bar{1}00\rangle$ forms 3-bilayer-high steps. The SiC substrate with just $\langle 11\bar{2}0\rangle$ off direction, corresponding to plane direction of SMBs, has 3-bilayer-high steps. The AlN layer on the SiC substrate with just $\langle 11\bar{2}0\rangle$ off direction would have the SMBs without zigzag structures and with the smaller strain.

5.3 Generation Mechanism of Threading Dislocation Rows

5.3.1 Experimental procedures

AlN layers on 6H-SiC (0001) with 3-bilayer-high steps without the sacrificial-oxidation process had TD rows (4×10^8 cm^{-2}), which were generated at the step edges of the SiC surface (Section 4.3.3). In this section, we try to clarify the generation mechanism of the TD rows using TEM.

6H-SiC (0001) substrates (vicinal angle 0.2°) were treated by high-temperature H_2-gas etching after CMP. The SiC surfaces had 3- or 6- bilayer-high steps. After an *ex-situ* wet-chemical and *in-situ* Ga cleaning procedures, AlN growth was started. Just after 2ML Ga

was deposited, AlN layers with thickness between 10–300 nm were grown at 650°C.

5.3.2 TD structures

Relation between TDs and crystal orientation

Surface morphologies of 6H-SiC (0001) substrates with different off directions were observed (Fig. 5.9). All SiC substrates with the off directions of 1, 19, and 25° from $\langle 11\bar{2}0\rangle$ had 3-bilayer-high steps. Bright-field plan-view TEM images of the 300-nm-thick AlN layer on these SiC substrates are shown in Fig. 5.9. TDs are observed as dark spots. Most TDs are arranged in rows with the separation width of around 500 nm, corresponding to the terrace width of the SiC substrate. We found that the TD rows were generated at the step edges of the SiC substrate, even though the separation with these step edges was small (10 nm) (Fig. 5.9 (c)). The TDD in the AlN layers is independent of the crystal orientation.

Structure of TD rows

We observed the TD rows using a weak-beam method. A plan-view TEM image of a 300-nm-thick AlN layer on 6-bilayer-high steps is shown in Fig. 5.10. Because the weak-beam image is tilted at 25° (Fig. 5.10 (a)), TDs are observed as thin bright lines. From the average length of TDs (100 nm), the thickness of the processed sample is estimated to be 270 nm, indicating that an AlN/SiC interface is unincluded in Fig. 5.10 (a). TDs on the terraces of the SiC substrate are composed of V-shaped half loops. On the other hand, TDs at the step edges of the SiC substrate have U-shaped structures, indicating that TD rows consist of dislocation networks.

A plan-view HRTEM image of TDs in a 100-nm AlN layer was observed (Fig. 5.11 (b)). Burgers vectors of the TDs are $\mathbf{b}=\frac{1}{3}[11\bar{2}0]$ and $\mathbf{b}=\frac{1}{3}[\bar{1}\bar{1}20]$, and both TDs have a edge-type component. In observing the TDs in Fig. 5.11 (a) at high magnification, all TDs are near the others with Burgers vector of an opposite direction, suggesting that the TD rows consist of many dislocation pairs. Two types of the TD pairs were observed: pair A was $\frac{1}{3}[11\bar{2}0]$ and $\frac{1}{3}[\bar{1}\bar{1}20]$, pair B was $\frac{1}{3}[\bar{2}110]$ and $\frac{1}{3}[2\bar{1}\bar{1}0]$. Each TD pair had the constant distance: pairs A and B was 10 and 30 nm, respectively. Average distance of the TDs was 25 nm.

5.3.3 Generation source of TD rows

TEM observation of AlN/SiC interface

To observe the AlN/SiC interface, we grew thin AlN layers. Fig. 5.12 shows a plan-view TEM image of a 50-nm-thick AlN layer on 3-bilayer-high steps. The sample was observed at a 20° tilt. From the length of observed TDs (40 nm), the thickness of this processed sample is estimated at 110 nm, indicating that the AlN/SiC interface is included in Fig. 5.12. The dark lines were observed at the same position as the TD rows, indicating that the dark lines are generated at step edges of SiC. The U-shaped structure was composed of a dark line and two TDs, corresponding to the result in Fig. 5.11. The defects with the U-shaped structure are arranged in rows without overlapping. We found that TD rows consisted of

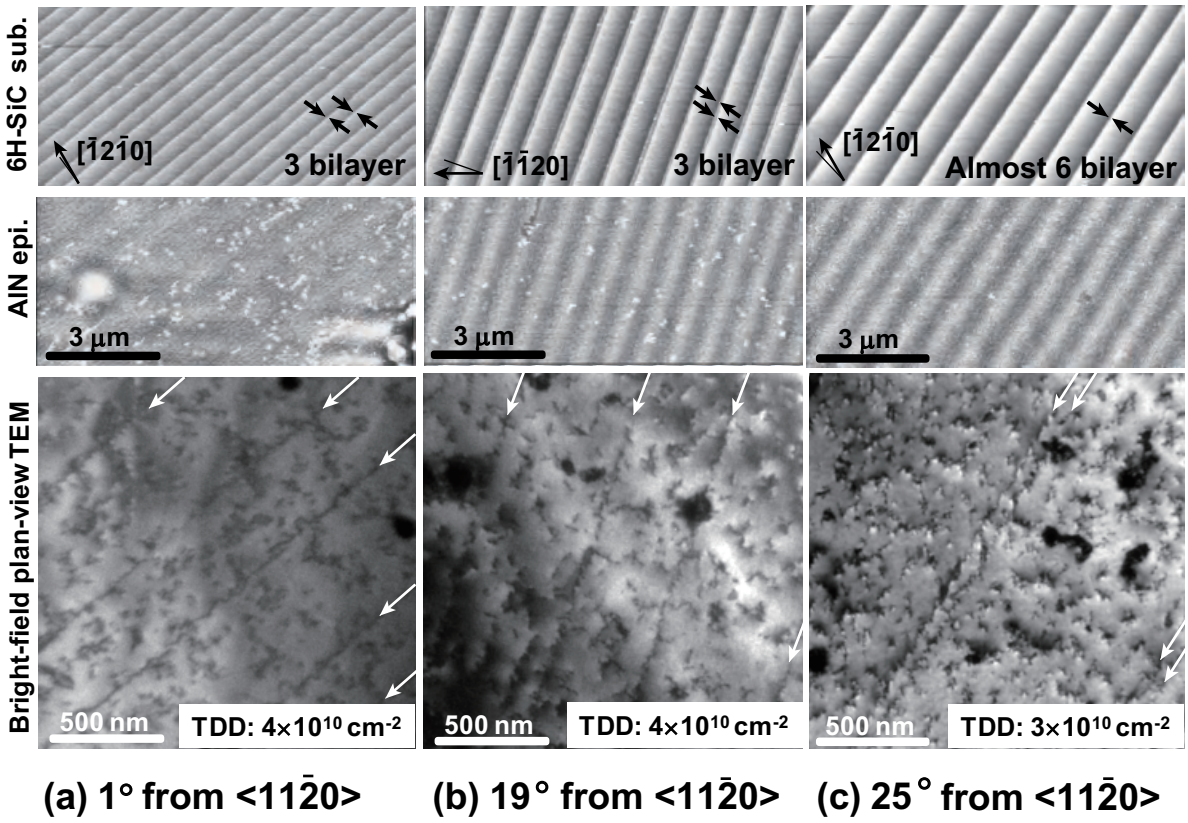

Figure 5.9: Bright-field plan-view TEM image and surface morphology of AlN layers on 6H-SiC (0001) with different off directions; (a) 1 , (b) 19 , and (c) 25° from $\langle 11\bar{2}0 \rangle$.

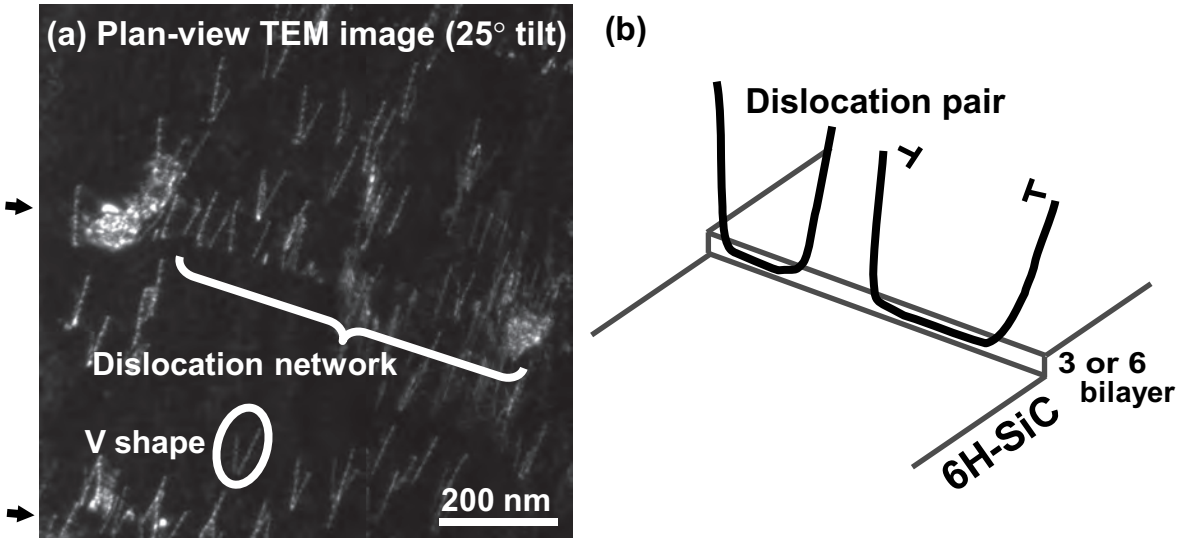

Figure 5.10: (a) Plan-view TEM image of 300-nm-thick AlN layer on 6H-SiC (0001) substrate with 6-bilayer-high steps (25° tilt with weak beam method) and (b) schematic figure of TD pairs generated at step edges of SiC.

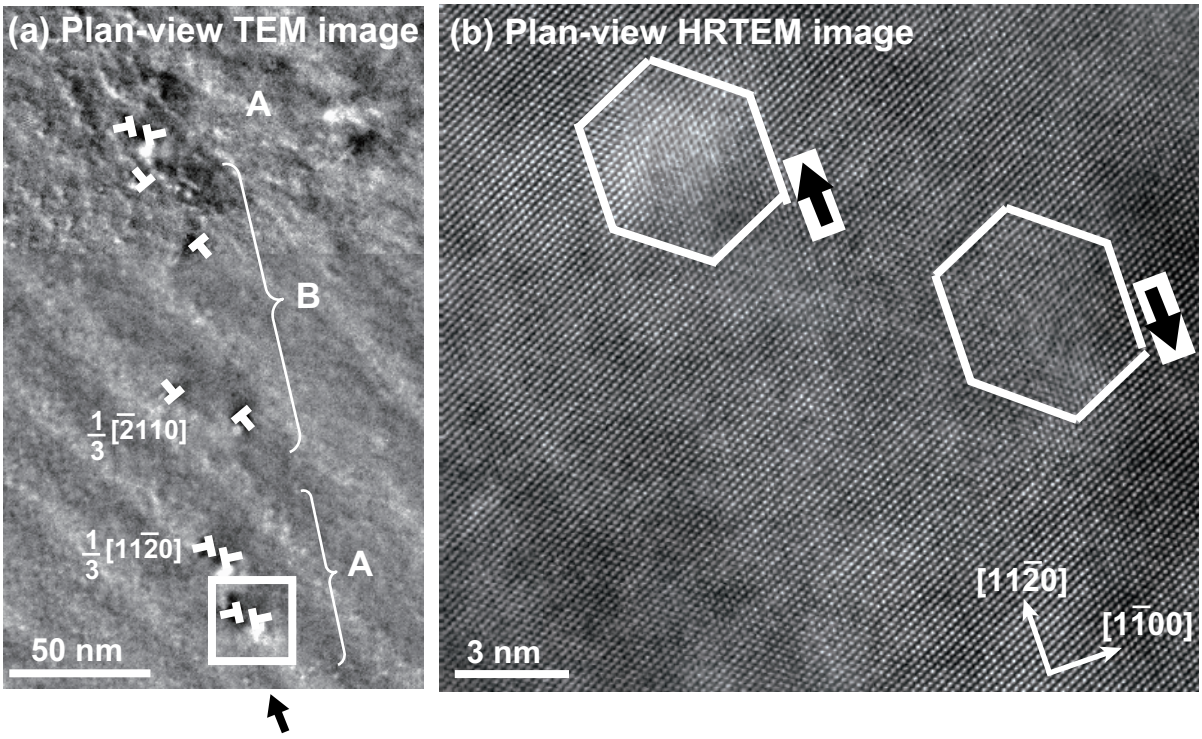

Figure 5.11: Plan-view HRTEM image of 100-nm-thick AlN layer on 6H-SiC (0001): (a) TD rows and (b) TD pair A.

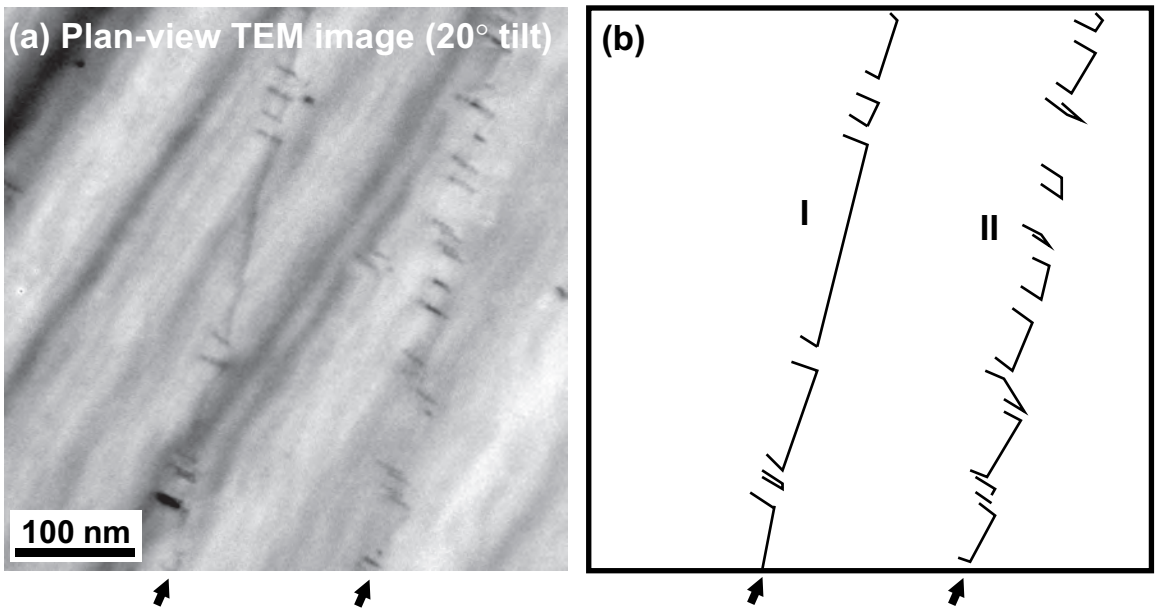

Figure 5.12: (a) Bright-field plan-view TEM images of 50-nm-thick AlN layer on 6H-SiC (0001) substrate with 3-bilayer-high steps (20° tilt) and (b) schematic figure of TD rows.

many TD pairs with a U-shaped structure (Fig. 5.10 (b)). TDD at each step edge (TD rows I and II) was different, as shown in Fig. 5.12 (b). High density of TDs consists of many short U-shaped defects (TD row II) and composes on the tortuous line.

A plan-view TEM image of a 10-nm-thick AlN layer on 3-bilayer-high steps is shown in Fig. 5.13. Although the SiC substrate as well as the AlN layer is included in Fig. 5.13, the TDs in the SiC substrate are not observed because the TDD of SiC is under 10^4 cm^{-2}. Straight dark lines were observed in Fig. 5.13 (a). The separation of dark lines corresponds to terrace width (100 nm) of the SiC substrate, indicating that the dark lines are generated at step edges of the SiC surface. Dark lines had no interference fringe in the tilted image and there was no relation between a direction of dark lines and crystal orientation. In addition, both sides of the dark line have same stacking structures (Fig. 5.13 (b)). These results indicate that dark lines are not SMBs. Fig. 5.13 (c) shows a magnified image of two dark lines. The two dark lines have different shapes, i. e., a straight line and tortuous line, like TD rows (I and II) in Fig. 5.12 (b). This is because the growth nuclei of AlN reflect the shape of these lines. An AlN crystal has threefold symmetry. The shape of the AlN two-dimensional (2D) nuclei is triangle and stacking arrangements of the AlN layer on 6H-SiC with 3-bilayer-high steps are different on each terrace, indicating that the shape of triangle islands are inverted. Additionally, a plan-view TEM image of the AlN layer at a two-beam condition (g=$10\bar{1}0$) is shown in Fig. 5.13 (d). The dark line was out of contrast at g=$1\bar{1}00$ and $\bar{1}100$, suggesting that the displacement has the component of $[1\bar{2}10]$. We consider that the dark lines are misfit dislocations due to the lattice mismatch (1%) between AlN and SiC. Relaxed AlN layers on SiC should generate a TD with a distance of 31 nm, closely corresponding to the average distance of TDs (25 nm), as shown in Fig. 5.11 (b).

RSM of AlN layer with and without TD rows

If misfit dislocations are generated at the step edges of 6H-SiC (0001), the AlN layers would be partially relaxed. We investigated the strain of the AlN layers on SiC using reciprocal space mapping (RSM). The q_x and q_y values of bulk AlN $(11\bar{2}4)$ are -0.643 and 0.803, respectively. The q_x and q_y values of bulk SiC $(11\bar{2}\ 12)$ are -0.650 and 0.794, respectively. The RSM of the AlN layer with TD rows is shown in Fig. 5.14 (a). X-ray was entered from three types of the directions: $[11\bar{2}0]$, $[2\bar{1}\bar{1}0]$, or $[1\bar{2}10]$. The off direction of the AlN layer with the TD rows was 50° from $[11\bar{2}0]$. In the incident direction of $[11\bar{2}0]$, the a-axis lattice constant of the AlN layer is identical with that of SiC, i. e., coherent growth, while in the incident direction of $[2\bar{1}\bar{1}0]$ and $[1\bar{2}10]$, the a-axis lattice constant for a main peak of the AlN layer corresponds to that of SiC, but a sub peak trails: i. e., the AlN layer is partially relaxed. For comparison, the RSM of the AlN layer with SMBs was also investigated (Fig. 5.14 (b)). The off direction of the AlN layer with SMBs was 118° from $[11\bar{2}0]$. The SiC $(11\bar{2}\ 12)$ has two peaks because the SiC substrate has the grain boundaries. The AlN layer with SMBs is coherently grown on 6H-SiC (0001), as expected.

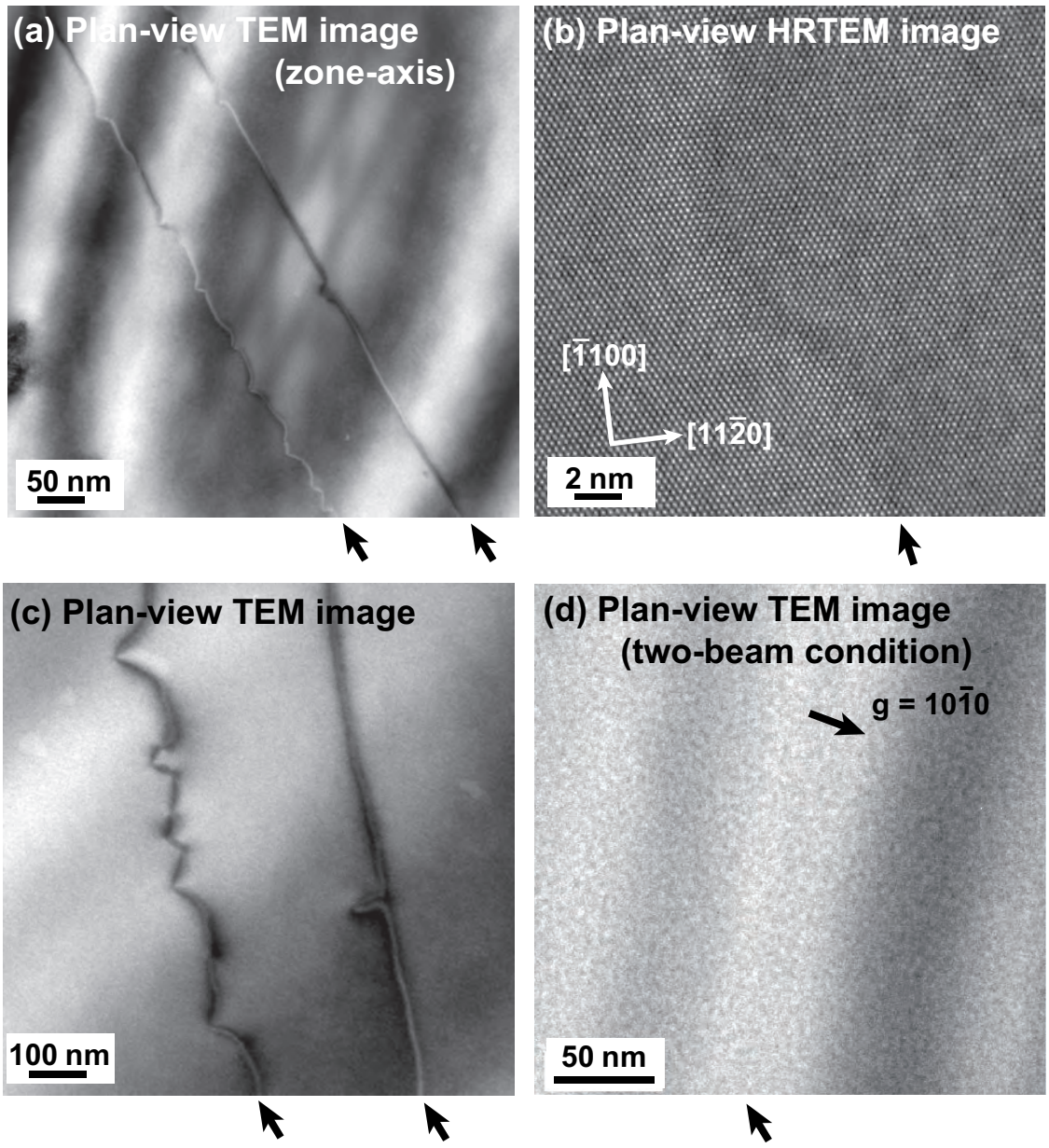

Figure 5.13: Bright-field plan-view TEM images of 10-nm-thick AlN layers on 6H-SiC (0001) substrate: (a, c) zone-axis, (b) HRTEM, and (d) two-beam condition ($\mathbf{g}$=10$\bar{1}$0).

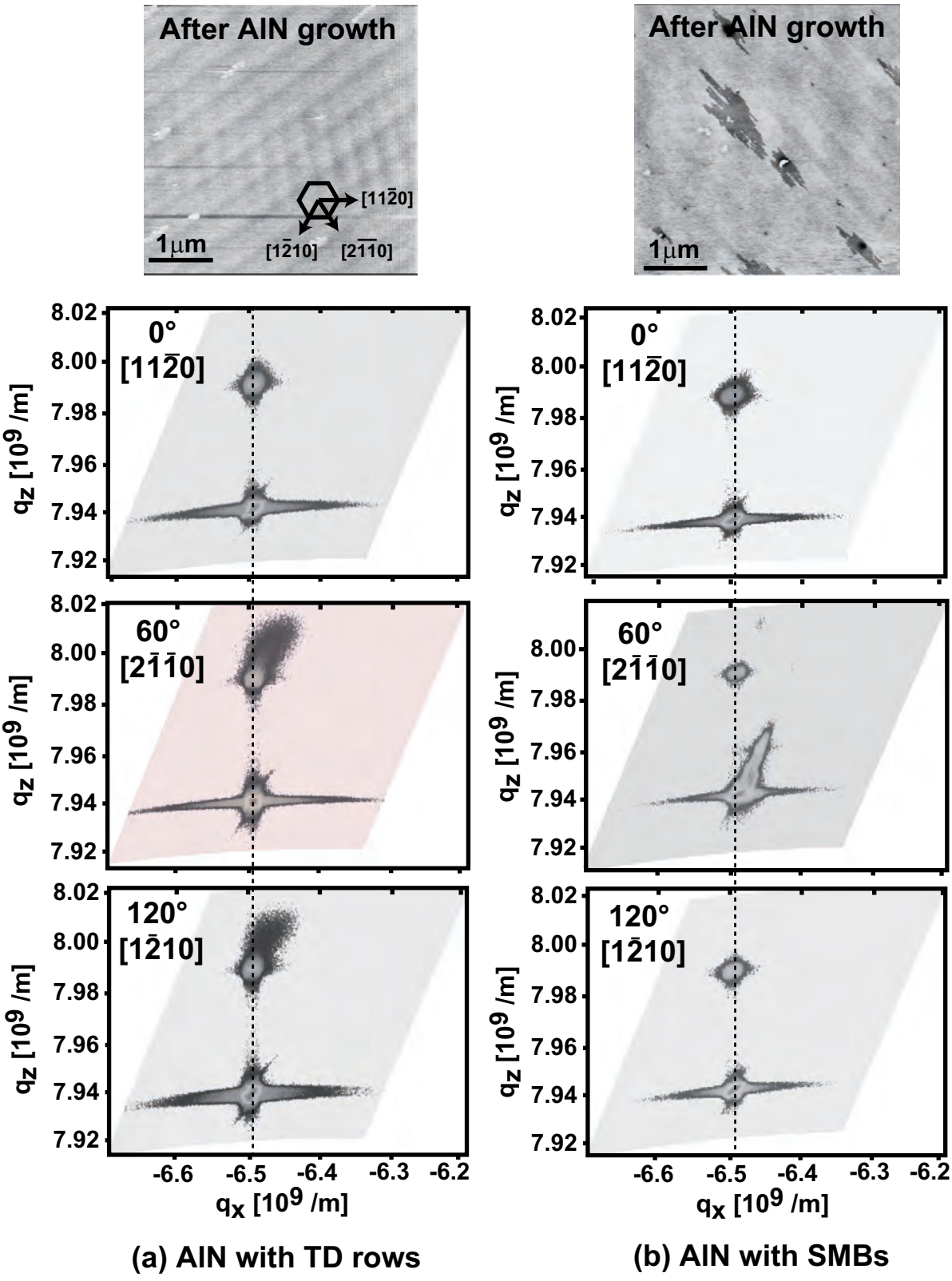

Figure 5.14: Surface morphology and RSM of 300-nm-thick AlN layer on 6H-SiC (0001) with different X-ray incident directions. AlN layers have (a) TD rows and (b) SMBs.

In the AlN layer with the TD rows, the RSM of the $(2\bar{1}\bar{1}0)$ plane, which is almost parallel to the steps of SiC, was relaxed, implying that the misfit dislocations were inserted parallel to the steps of SiC. In the TEM observation, misfit dislocations were generated at the step edges, corresponding to this RSM result. The reason why the whole AlN layer was coherently grown is that there are few misfit dislocations on the over-100-nm-wide terrace of SiC.

5.3.4 Estimation of threading dislocation density by XRD

Screw-type TD density

Out-of-plane misorientation (α), e. g., screw-type TDs including Burgers vector of [0001] component, as well as coherent length ($L_{\parallel}$) parallel to a SiC surface increase FWHM values (β_s) of ω-scan peaks of symmetric (0002), (0004), and (0006) reflections for an AlN layer. To separate these two broadening mechanism, we used a Williamson-Hall plot (Fig. 5.15) [11]. When TDs are randomly distributed, the screw-type TDD (N_s) can be estimated from the tilt angle (α), as follows, [12–14]

$$N_s^r = \frac{\alpha^2}{2\pi \ln 2 \times b_s^2} \tag{5.3}$$

where b_s is the size of Burgers vector in the c axis. For AlN layer on 6H-SiC (0001) (edge-type TDD: 4×10^8 cm^{-2}), $L_{\parallel}$ and N_s^r were 16 μm and 1×10^7 cm^{-2}, respectively. The estimated N_s^r is disagreement with the spiral hillock density (6×10^4 cm^{-2}), which corresponds the screw-type TDD.

The Williamson-Hall plot can be used for only high-quality and thick films because the x-ray intensity of high-order planes, e. g., (0006), is quite low. For low crystalline quality, the screw-type TDD is estimated using the FWHM value (β_s) instead of α in Eq. (5.3) [15]. The relation between β_s and the spiral hillock density for the AlN layers is shown in Fig. 5.16 (a). Solid line is the value calculated from Eq. (5.3). The spiral-hillock density has the linearly tendency to the FWHM values, but is one order of magnitude higher than the values calculated from Eq. (5.3).

Edge-type TD density

Edge-type TDD (N_e) can be estimated from the FWHM value (β_e) of $(01\bar{1}2)$ ω-scan diffraction peaks, as follows, [15]

$$N_e^r = \frac{\beta_e^2}{2\pi \ln 2 \times b_e^2} \tag{5.4}$$

where b_e is the size of Burgers vector in the a axis. When TDs are piled up in small-angle grain boundaries, the individual strain fields superimpose, and N_e follows to: [16, 17]

$$N_e^p = \frac{\beta_e}{\sqrt{2\pi \ln 2} \times b_e L_{\parallel}} \tag{5.5}$$

Because TDs in the AlN layer on 6H-SiC (0001) with 3- or 6-bilayer-high steps are arranged in rows, like the grain boundary, Eq. (5.5) is more suitable for the estimation of the low edge-type TDD. In addition, we converted the FWHM value of the $(01\bar{1}2)$ reflection measured in skew symmetry to an in-plane FWHM value (β_{e0}), as follows, [18, 19]

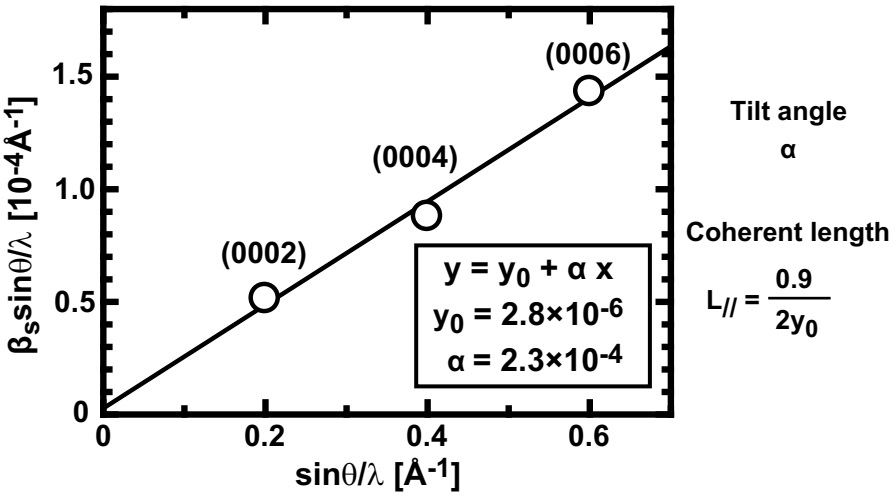

Figure 5.15: Williamson-Hall plot of 300-nm-thick AlN layer on 6H-SiC (0001) substrate with 3-bilayer-high steps. AlN was grown at 650°C just after 2ML-Ga pre-deposition and nitrogen-plasma ignition.

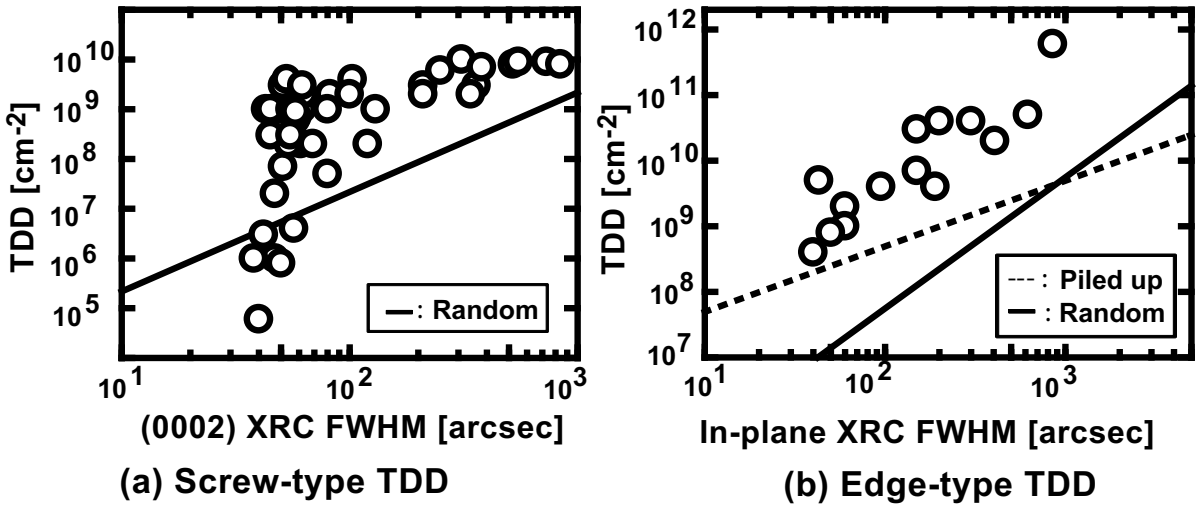

Figure 5.16: Relation between XRC-FWHM values and TDD in 300-nm-thick AlN layers on 6H-SiC (0001). (a) screw-type TDD (spiral-hillock density) was obtained from AFM images and (b) edge-type TDD was obtained from plan-view TEM images. Solid and dashed lines are value calculated from Eq. (5.4) and (5.5), respectively.

$$\beta_e^2 = (\beta_{e0} \cos\chi)^2 + (\beta_s \sin\chi)^2 \tag{5.6}$$

where χ is the inclination angle. The relation between β_{e0} and the TDD obtained from plan-view TEM images for the AlN layers is shown in Fig. 5.16 (b). Solid and dashed lines are the value calculated from Eqs. (5.4) and (5.5) about $L_{\parallel} = 200$ nm (terrace width of SiC), respectively. The density of edge-type TDs also is one order of magnitude higher than the values calculated from Eq. (5.5).

5.3.5 Discussion

Generation mechanism of misfit dislocations over step edges of SiC

In AlN layers on 6H-SiC (0001) with 3- or 6-bilayer-high steps, TD rows, which consist of many U-shaped dislocation pairs, were generated at the step edges of SiC. We found that these TD rows were caused by misfit dislocations over the step edges of SiC.

On the terrace of 6H-SiC with 3-bilayer-high steps, AlN is grown in layer-by-layer growth mode from the first layer. If AlN has a step-flow growth mode near the step edges of SiC, the stacking sequences of 2H-AlN adsorbed at the step edges follow that of the 6H-SiC substrate, generating SMBs. However, no SMBs were observed in the AlN layer with the TD rows. We consider that in 650°C growth, few adatoms are incorporated at the step edges of SiC (Fig. 5.17 (a)).

After 3-bilayer growth, each AlN nucleus on adjacent terraces coalesces over the step edge of SiC. Because AlN is coherently grown on SiC, in-plane strain (ϵ_{xx}) is caused due to the lattice mismatch. Then, normal strain (ϵ_{zz}) is given by

$$\epsilon_{zz} = -2\frac{C_{13}}{C_{33}}\epsilon_{xx} \tag{5.7}$$

where ϵ_{zz} is $(c_e - c_s)/c_s$, $\epsilon_{xx}(= \epsilon_{yy})$ is $(a_e - a_s)/a_s$, and C is an elastic constant. The strain of a and c axis for $C_{13} = 95$ and $C_{33} = 402$ GPa [20] are $+1 \times 10^{-2}$ (compressive) and -7×10^{-3} (tensile), respectively. In the AlN nuclei coalescence, misfit dislocations with $1/3[11\bar{2}0]$ component are generated over the step edge of SiC to relieve the strain energy of the a axis (Fig. 5.17 (b)). In the AlN layer, there is also the strain of c axis and the relaxation of the c-axis strain generates screw-type TDs. However, the screw-type TDD was very small, under 10^6 cm^{-2}. This may because the lattice mismatch of the c axis is reduced to 0.7 % due to the tensile strain.

Generation mechanism of TD pairs and effect of TD rows on XRC

Misfit dislocations had two types of structures, i. e., straight and zigzag (Fig. 5.13), because the misfit dislocations are generated by the coalescence of the AlN nuclei with threefold symmetry. We consider that the nuclei coalescence is intermittently generated, as shown in Fig. 5.18 (a). The each nuclei coalescence probably generates the different Burgers vector, so that the two or three types of the TD pairs with different Burgers vectors were generated at one step edge of SiC (Fig. 5.11). We anticipate that during growth, the

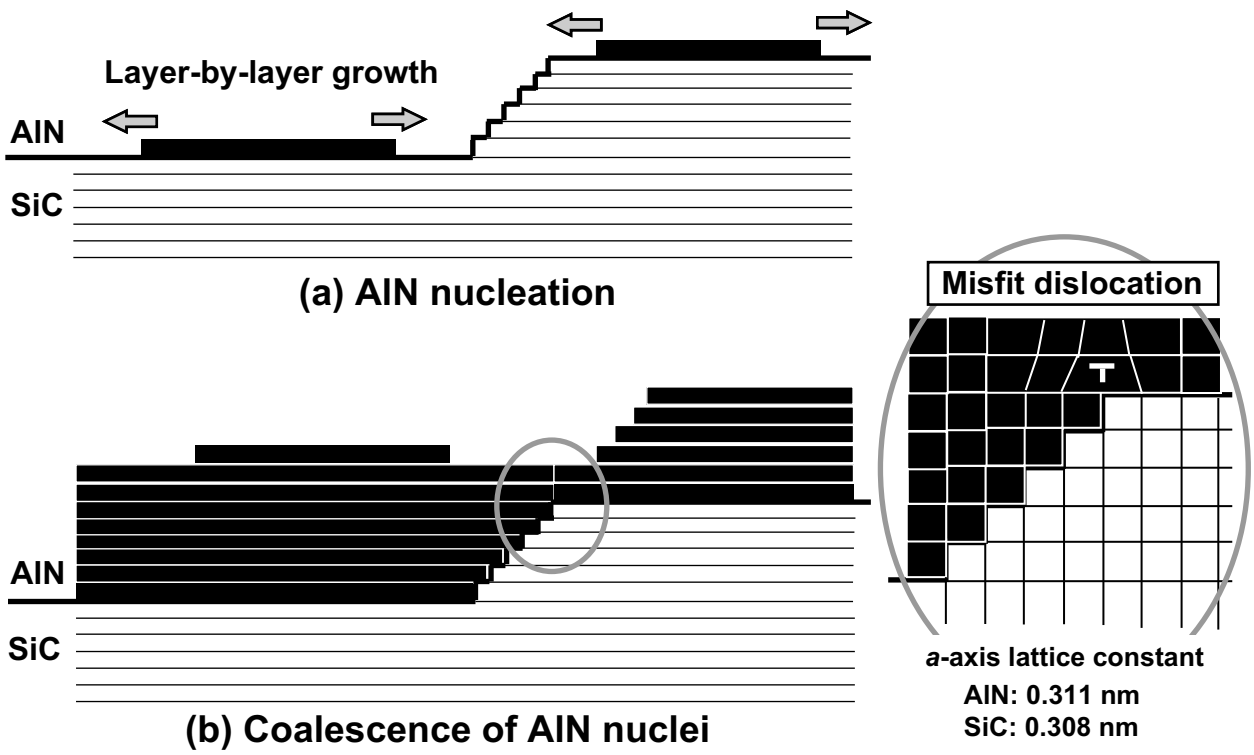

Figure 5.17: Schematic figure of misfit dislocation generated at step edge of 6H-SiC substrate with 6-bilayer-high steps.

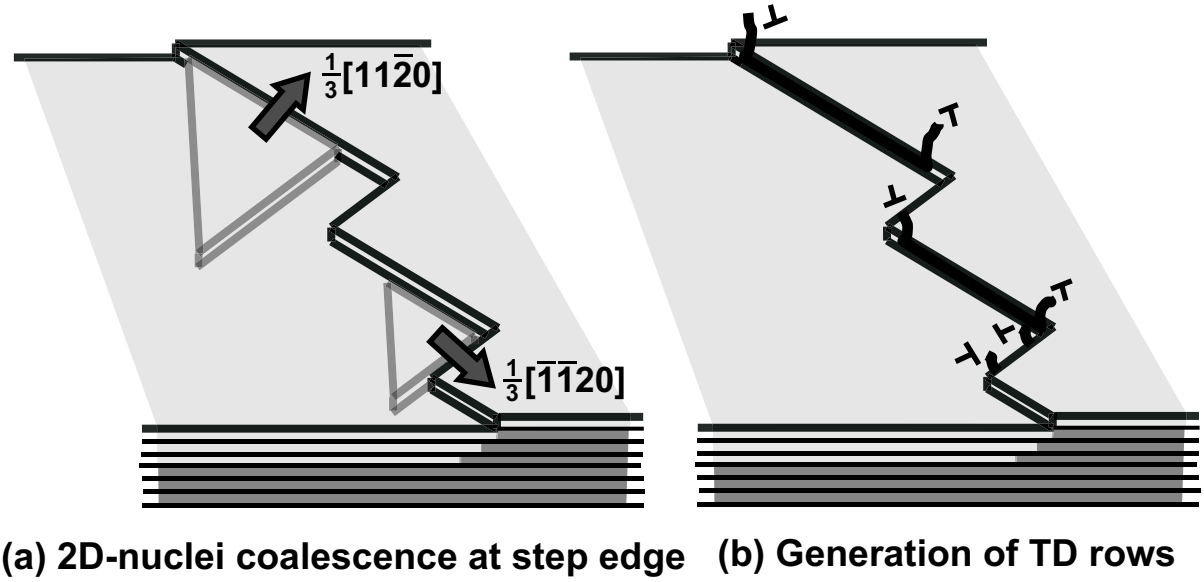

Figure 5.18: Schematic figure for generation mechanism of TD pairs at step edges of SiC.

misfit dislocations become edge-type TDs due to the glide on $(11\bar{2}0)$ and extend to growth direction (Fig. 5.18 (b)), resulting in many TD pairs, i. e., TD rows. The misfit dislocations with the straighter structure would generate less density of TD rows.

There was the difference between the TDD estimated from ω-scan FWHM values and the TDD observed by TEM and AFM. This is caused by the particular defect structure in the AlN layers on SiC. The TD pairs annihilate the strain fields each other due to opposite Burgers vectors. The small twist components of TDs result in the considerable reduction of the ω-scan FWHM values. In addition, the TD rows have a less influence on the ω-scan FWHM values than randomly distributed TDs.

5.4 Critical Thickness of AlN Epilayer on SiC

5.4.1 Strain of thick AlN epilayers on SiC

XRD $2\theta/\omega$ scan

A c-axis lattice constant c_s of the completely relaxed 2H-AlN layer is 4.982 Å. For 2H-AlN coherently grown on 6H-SiC (0001), the c-axis lattice constant c_e is estimated to be 5.005 Å by Eq. (5.7). To evaluate the critical thickness of AlN growth on 6H-SiC (0001) substrates, we investigated the c-axis lattice constant of the AlN layers with the thickness between the 100 and 1200 nm using XRD $2\theta/\omega$ scan. The relation between the thickness and c-axis lattice constant of the AlN layers is shown in Fig. 5.19 (a). The AlN layer grown on SiC without the Ga pre-deposition process, called normal growth, is gradually relaxed with the increasing the thickness. On the other hand, the AlN layer with the Ga pre-deposition process, called high-quality growth, is coherently grown on SiC until 900 nm, and the c-axis lattice constant abruptly decreases at the thickness between 900 and 1000 nm. This indicates that around 900 nm is a critical thickness of AlN growth on SiC. The normal strain of the AlN layers on SiC is listed in Table 5.2. The normal strain of the AlN layers gradually decreases with increasing the thickness.

RSM

The a-axis lattice constant of the 2H-AlN layers grown on 6H-SiC (0001) substrates was investigated using RSM, as shown in Fig. 5.20 (a). The a-axis lattice constant of the 700-nm-thick AlN layer corresponds to that of the SiC substrate, indicating that AlN is pseudomorphically grown on SiC. The c-axis lattice constant measured by RSM corresponded to that obtained from the $2\theta/\omega$ scan. For the 900-nm-thick AlN layer, the two peaks appeared because of the partially relaxed AlN layer. The 1000- and 1200-nm-thick AlN layer is relaxed. The in-plane relaxation α $(= [a_e - a_s]_{measure}/[a_e - a_s]_{free\ standing})$ of the 1000- and 1200-nm-thick AlN layer grown on the 6H-SiC (0001) substrate is 43 % [21].

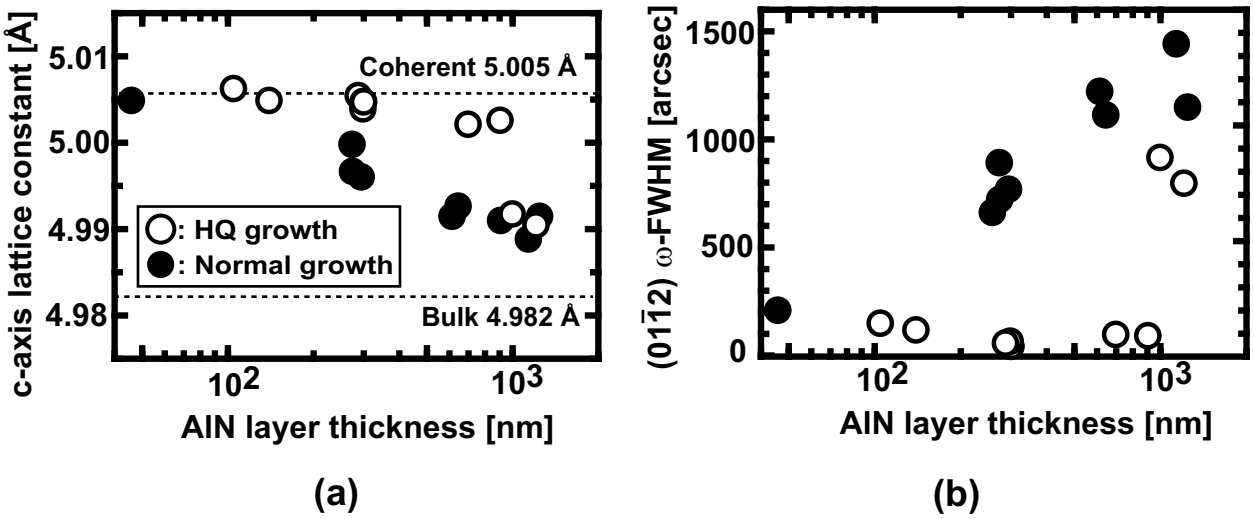

Figure 5.19: (a) Relation between thickness and c-axis lattice constant of AlN layers and (b) relation between thickness and (01$\bar{1}$2) FWHM values of AlN layers. High-quality and normal AlN layers are grown on 6H-SiC (0001) substrates with and without 2ML-Ga pre-deposition, respectively.

Table 5.2: Normal strain ϵ_{zz}, relax ratio α, and crystalline quality of AlN layers with various thickness. High-quality AlN on 6H-SiC (0001) substrates was grown with Ga pre-deposition at 650°C. Calculated values are for 2H-AlN layer coherently grown on 6H-SiC (0001) substrate.

Thickness [nm]	$\epsilon_{zz}^{\mathrm{XRD}}$ [10^{-3}]	α [%]	$\epsilon_{zz}^{\mathrm{Raman}}$ [10^{-3}]	NBE of CL [eV]	Hillock density [cm^{-2}]	(01$\bar{1}$2)-ω [arcsec]
1200	+1.69	43	+2.1	6.07	1×10^9	800
1000	+1.95	43	+2.1	6.07	2×10^9	910
900	+4.12	0, 28	+4.6	6.10	3×10^6	89
700	+4.03	0	+4.6	6.15	4×10^6	95
300	+4.55	0	+4.6	6.15	2×10^6	55
150	+4.58	-	+4.6	-	4×10^6	120
100	+4.86	-	+4.6	-	2×10^6	150
Calc.	+4.71	0	+4.71	6.18	-	-

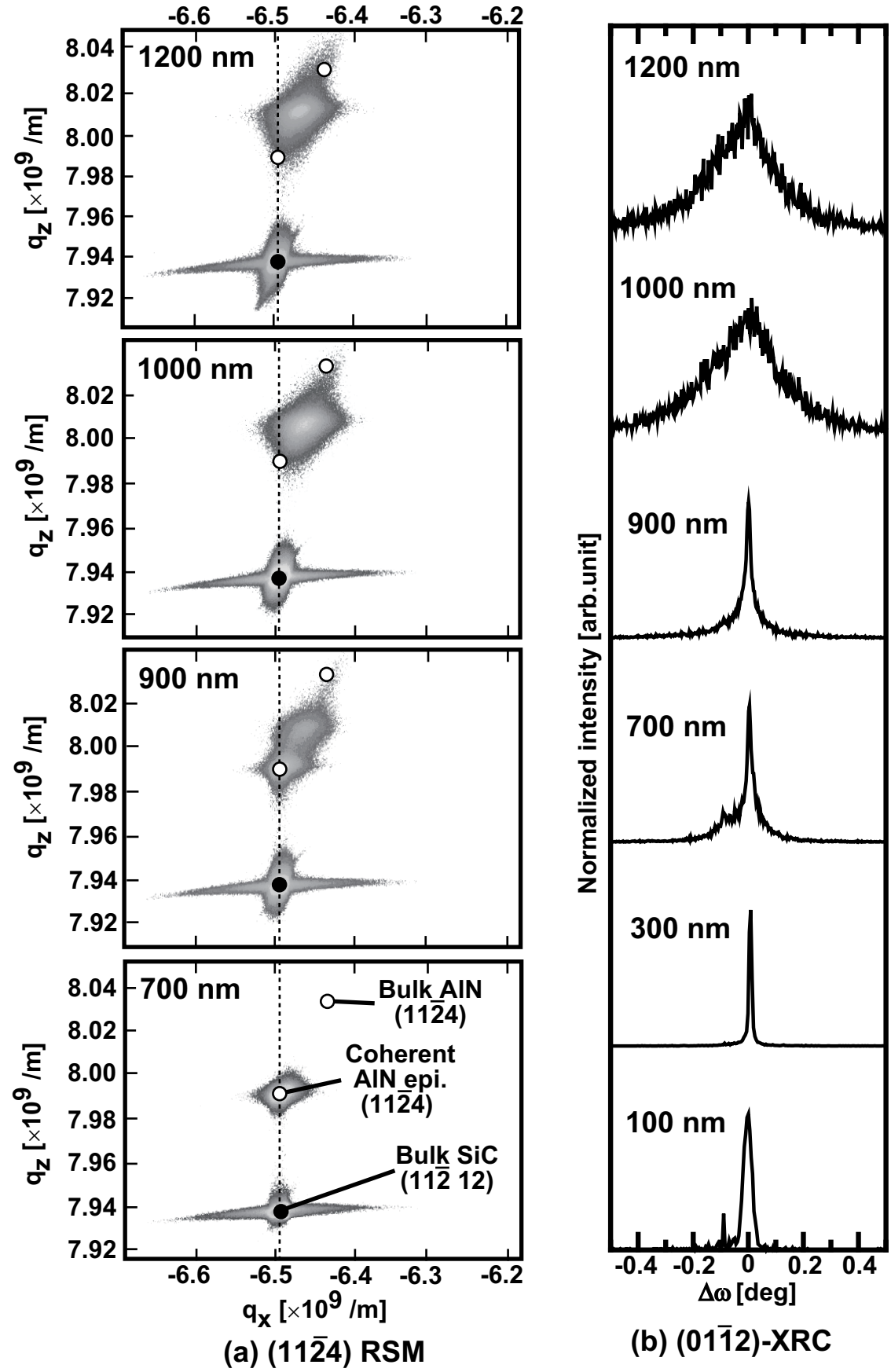

Figure 5.20: (a) RSM and (b) XRC of AlN layers with 100 – 1200 nm thickness, which were grown with Ga pre-deposition at 650°C, on 6H-SiC (0001) with 3-bilayer-high steps.

Raman Scattering Spectroscopy

The residual strain of the epilayer can be evaluated by microscopic Raman scattering spectroscopy as well as XRD. A backscattering geometry, z(x,xy)$\bar{z}$, was conducted by polarizing the incident light; z and x is the direction along [0001] and [11$\bar{2}$0], respectively. For a 2H-AlN (0001) layer, the observable phonon modes are A_1(LO) (611 cm^{-1}) and E_2 (248.6 and 657.4 cm^{-1}) [22]. In the range of the validity of Hooke's law, the magnitude of the frequency shift for phonon mode is determined by the two deformation potential constants a_λ and b_λ for given strain, as follows [23],

$$\Delta\omega_\lambda = a_\lambda(\epsilon_{xx} + \epsilon_{yy}) + b_\lambda\epsilon_{zz} \tag{5.8}$$

Using the Eqs. (5.7) and (5.8), the normal strain can be estimated from the Raman shift. Raman spectra of the AlN layers in the range of $640 - 700$ cm^{-1} at 300 K is shown in Fig. 5.21. The E_2^H phonon mode of the under-1000-nm-thick AlN layers was located at 670 cm^{-1}. Then, the normal strain is 4.6×10^{-3} (Table 5.2), corresponding to the strain of the AlN layer coherently grown on SiC. We confirmed that the AlN layer on SiC had the biaxial compressive strain parallel to the c axis. On the other hand, the Raman shift of the 1000-nm-thick AlN layer is small (+5 cm^{-1}), and the normal strain is 2.1×10^{-3} , which is in good agreement with the XRD results.

CL

The strain of an AlN layer contributes to a near-band-edge (NBE) peak shift of CL spectra. CL spectra of the AlN layers grown on the 6H-SiC (0001) substrates was measured at 300 K (Fig. 5.22). The NBE peak of the under-900-nm-thick AlN layers shifts to the high energy side due to the compressive strain. However, unlike the XRD and Raman measurements, the 900-nm-thick AlN layer is slightly relaxed. We consider that the AlN layer near the surface is relaxed because CL spectra is more sensitive to the property near the surface. The critical thickness of the AlN layer on SiC is between 700 and 900 nm. The detail of the CL spectra is described in Section 6.2.

5.4.2 Misfit dislocations in thick AlN epilayers

Screw-type TDD

Surface morphologies of 700-, 900-, 1000-, and 1200-nm-thick AlN layers on the 6H-SiC (0001) substrates are shown in Fig. 5.23. The step-and-terrace structures with 1-bilayer-high steps (0.25 nm) were obtained. There were also spiral hillocks, which correspond to the screw-type TDs, on the AlN surface. For the 1000-nm-thick AlN layer, the spiral hillock density is high (more than 1×10^9 cm^{-2}), indicating that screw-type TDs were generated by the lattice relaxation of the AlN layer.

Edge-type TDD

The relation between the thickness and FWHM values for (01$\bar{1}$2) ω-scan diffraction peaks of the AlN layers is shown in Fig. 5.19 (b) and Table 5.2. For the normal growth,

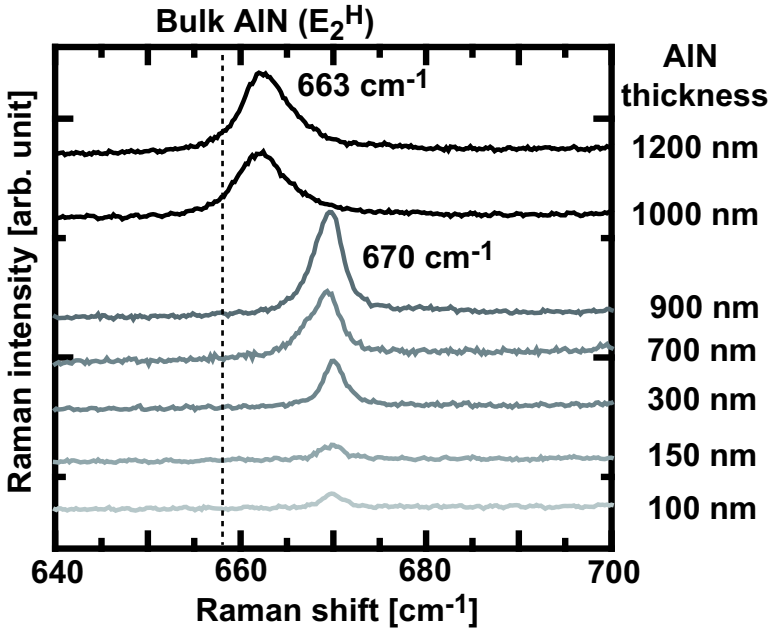

Figure 5.21: Raman spectra of AlN layers on 6H-SiC (0001). AlN layers with thickness between 100 and 1200 nm were grown with 2ML-Ga pre-deposition at 650°C.

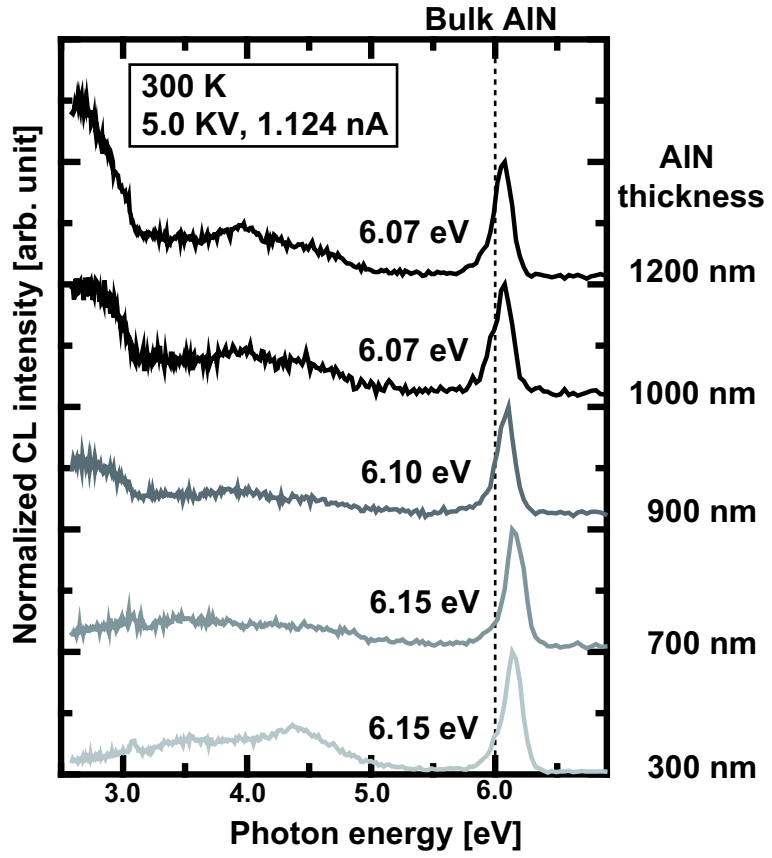

Figure 5.22: CL spectra of AlN layers on 6H-SiC (0001) at room temperature. AlN layers with thickness between 300 and 1200 nm were grown with 2ML-Ga pre-deposition at 650°C.

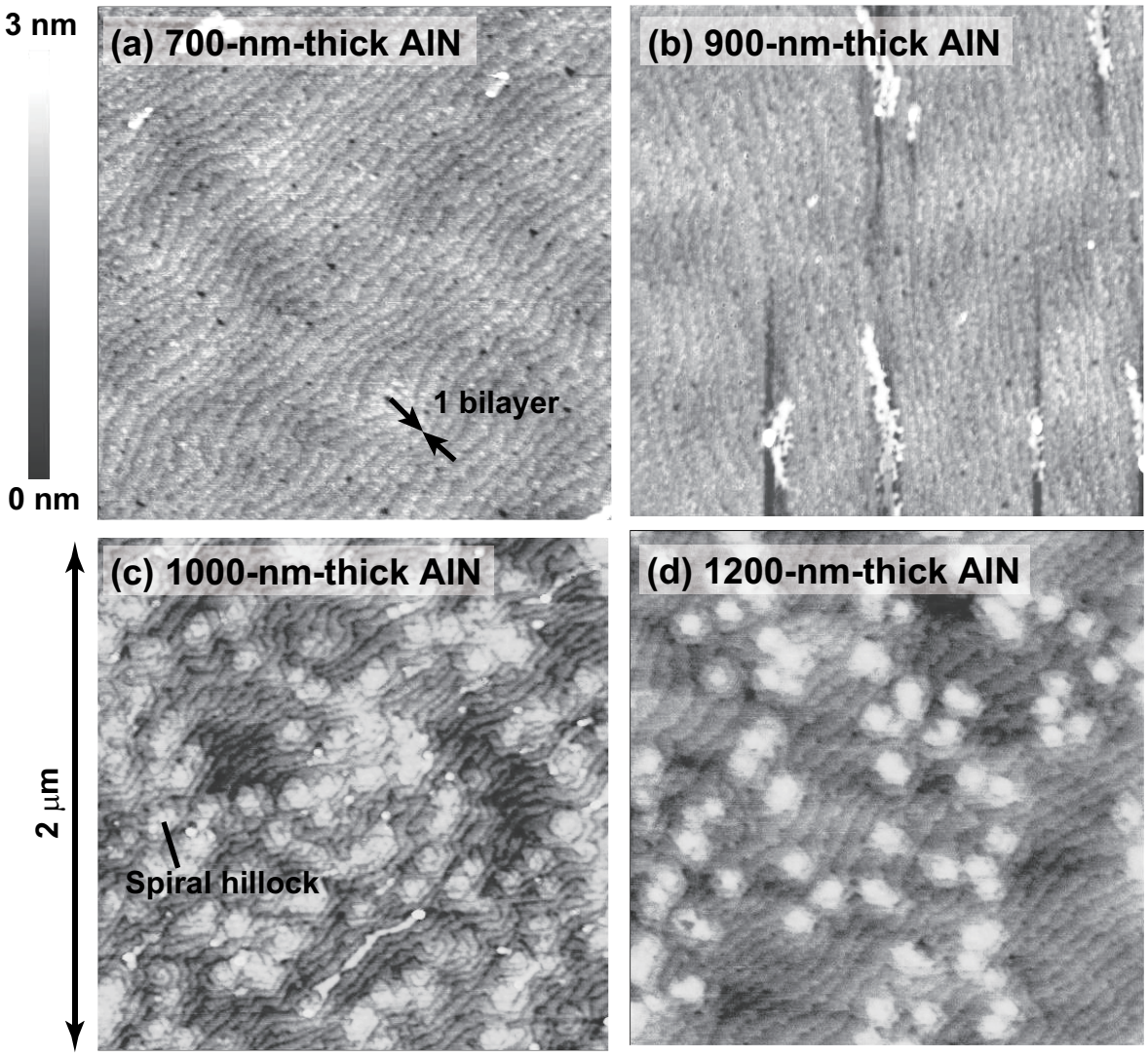

Figure 5.23: Surface morphology of AlN layers on 6H-SiC (0001) with 3-bilayer-high steps. Thickness of AlN layers are (a) 700, (b) 900, (c) 1000, and (d) 1200 nm.

the FWHM values gradually increase with the thickness, while for the high-quality growth, these suddenly increase at the 1000-nm thickness, indicating that the edge-type TDs were generated by the lattice relaxation of the AlN layer.

To investigate the defect structure in the thick AlN layer on the 6H-SiC (0001), bright-field plan-view TEM images were observed (Fig. 5.24). In the 700-nm-thick AlN layer, TDs are arranged in rows with the same separation as the terrace width of the SiC substrate before growth, indicating that TDs are generated at the step edges of the SiC substrate. Meanwhile, TDs in the 900-, 1000- and 1200-nm-thick AlN layers are randomly distributed, and the TDD is one order of magnitude higher than that of the 700-nm-thick AlN layer. We consider that the high density of the random TDs is caused by the misfit dislocations due to the lattice relaxation of the AlN layer.

Introduction of misfit dislocations

Cross-sectional TEM images of a 900-nm-thick AlN layer on 6H-SiC (0001) were observed with two-beam conditions (Fig. 5.25). In the case of diffraction vector $\mathbf{g} = 0002$, a dislocation with Burgers vector of [0001] component, i. e., a screw-type dislocation, is observed (Fig. 5.25 (a)). The dislocation loops were generated after around 600 nm growth, which closely corresponds to the critical thickness evaluated in Section 5.4.1. We consider that the screw-type dislocation loops were generated because of the relaxation of the AlN layer. On the other hand, for $\mathbf{g} = 11\bar{2}0$, an edge-type dislocation is observed (Fig. 5.25 (b)). Most edge-type TDs were generated at the AlN/SiC interface. The TDD is around 1×10^{11} cm^{-2}, corresponding to the result of the plan-view TEM observation. This indicates that edge-type TDs are generated at the AlN/SiC interface in the relaxation. The TDs generated during growth must climb to reach the AlN/SiC interface, but the growth temperature of 650°C is insufficient for the climb motion. We need to investigate further.

Although the 900-nm-thick AlN layer has already started relaxing in the view of the result of Section 5.4.1, the XRC FWHM value of this AlN layer was small. This is because the XRC peak intensity of the AlN layer coherently grown on SiC is stronger than that of the relaxed AlN layer (Fig. 5.20 (b)). When the crystalline quality of the AlN layer near the critical thickness is evaluated using XRD, we have to be careful to the XRD spectra.

5.4.3 Discussion

The energetic and kinetic parameters describing mismatch accommodation by in-plane strain and misfit dislocation are described using a Matthews-Blakeslee model [24]. Matthews *et al.* considered that the pre-existing TDs in the substrate replicates in the epilayer and bends over to create misfit dislocations in the interface when the force exerted by the misfit strain exceeds the tension in the dislocation line (Fig. 5.26). The critical thickness (h_c) is described as follows,

$$h_c = \frac{b}{8\pi f} \frac{1 - \nu \cos^2 \alpha}{(1 + \nu) \cos \lambda} (\ln \frac{h_c}{b} + 1) \tag{5.9}$$

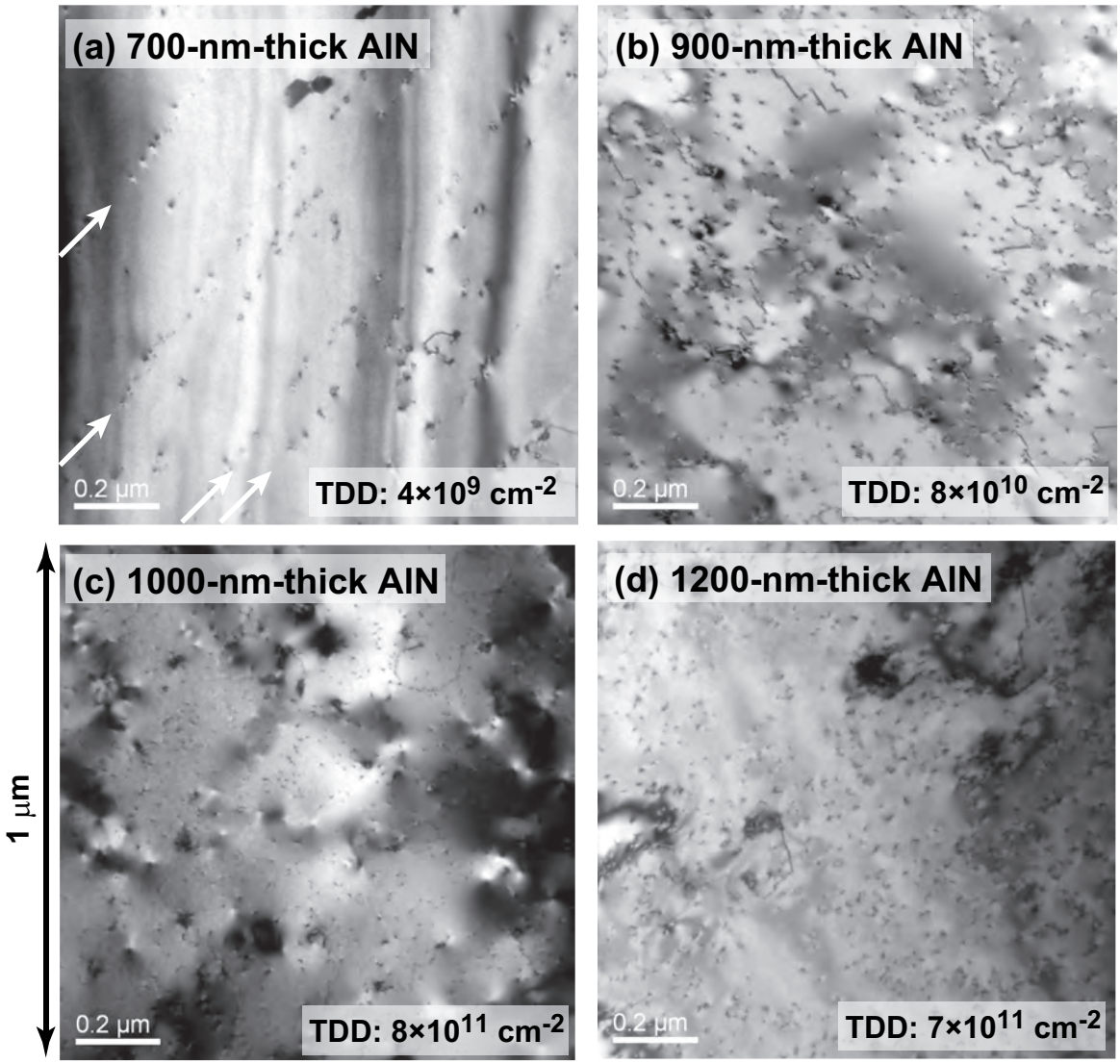

Figure 5.24: Bright-field plan-view TEM images of AlN layers on 6H-SiC (0001) with 3-bilayer-high steps. Thickness of AlN layers are (a) 700, (b) 900, (c) 1000, and (d) 1200 nm.

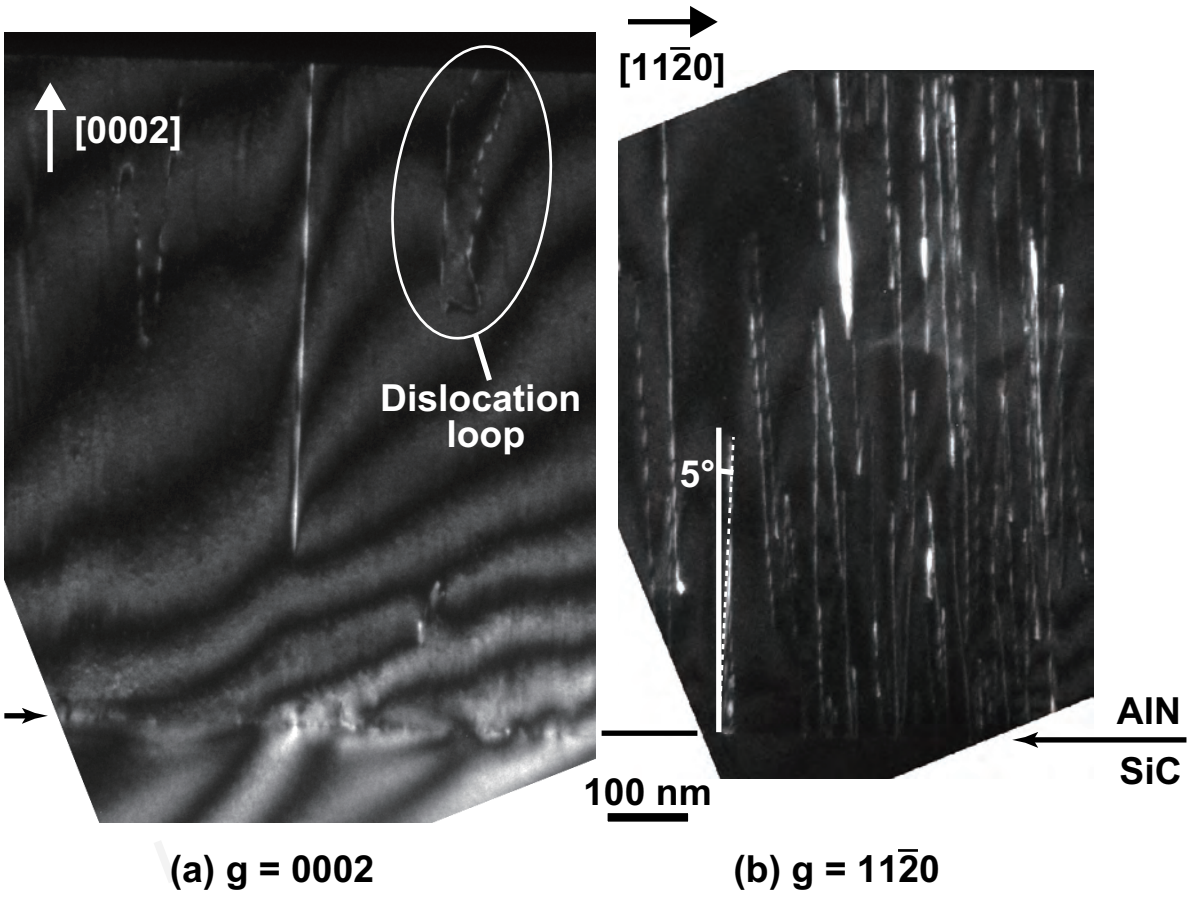

Figure 5.25: Dark-field cross-sectional TEM image of 900-nm-thick AlN layer on 6H-SiC (0001). (a) $\mathbf{g} = 0002$ and (b) $11\bar{2}0$.

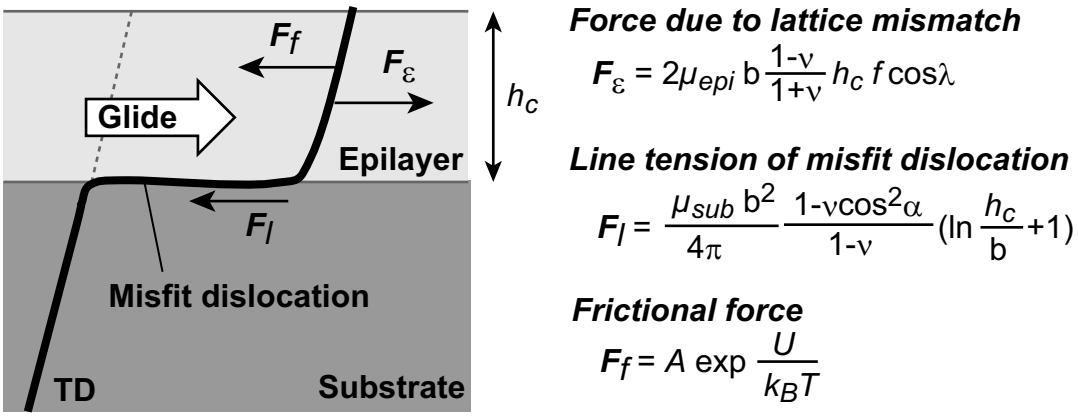

Figure 5.26: Matthews-Blakeslee model for critical thickness of heteroepitaxial growth.

where f is the lattice mismatch factor ($(a_s - a_e)/a_e$), ν is the Poisson ratio, $\mathbf{b}$ is the size of the Burgers vector, α is the angle between the dislocation line and the Burgers vector, and λ is the angle between the slip plane and the AlN/SiC interface. Fischer *et al.* improved the Matthews-Blakeslee model by including the elastic interaction between straight misfit dislocations [25]. The improved critical thickness is described as follows,

$$h_c = \frac{b}{8\pi f}\frac{1-\nu\cos^2\alpha}{(1+\nu)\cos\lambda}(\ln\frac{h_c}{b}+1) + \frac{b\cos\lambda}{2f} \tag{5.10}$$

The critical thickness of 2H-AlN epilayers on 6H-SiC is estimated to be 21 nm, which is much smaller than the experimental value (around 900 nm). This is because the Matthews-Blakeslee model considers the glide of the dislocations to introduce the misfit dislocations. In the MBE growth of AlN, the glide of the TDs has never been observed at the growth temperature of 650°C.

Price *et al.* reported that extremely large critical thickness was obtained at low temperature because of less force to activate dislocation movement [26], and Fox *et al.* proposed that the force for the dislocation activation should be added to the Matthews-Blakeslee model [27]. Then, the critical thickness becomes

$$2\mu_{epi}b\frac{1+\nu}{1-\nu}h_c f\cos\lambda - Ah_c\exp\frac{U}{k_BT} = \frac{\mu_{sub}b^2}{4\pi}\frac{1-\nu\cos^2\alpha}{1-\nu}(\ln\frac{h_c}{b}+1) \tag{5.11}$$

where μ is the shear modulus (131 GPa for 2H-AlN, 195 GPa for 6H-SiC [28]), A is a constant, and U is the activation energy. When $\ln A$ and U for $T = 650$°C are -30 and 2.392 eV, respectively, the critical thickness is estimated to be 840 nm (Table 5.3), which is in close agreement with the experimental result. The value of U is in the range of Peierls energies for semiconductors [29, 30].

The AlN layer with high TDD (2×10^{10} cm^{-2} on the SiC terraces) gradually relaxed with increasing the layer thickness, but that with low TDD (9×10^{7} cm^{-2} on the SiC terraces) abruptly relaxed at the thickness of around 900 nm. Although the dislocation movement at low temperature is difficult, for the AlN layer with the high TDD, the formation of TDs with V-shaped structure, i. e., a bend of the TDs (Fig. 5.25 (b)) [31, 32], can reduce the strain energy due to the introduction of misfit components. On the other hand, for the AlN layer with the low TDD, the strain energy can be insufficiently relieved by the pre-existed TDs, so that the high density of new TDs and misfit dislocations is generated after around-900-nm growth. The achievement of the 2D growth mode from the first layer also would contribute to increase the critical thickness of the AlN growth on the SiC substrate.

5.5 Summary

In the AlN layer on 6H-SiC (0001) substrates treated sacrificial-oxidation process, SMBs were generated at the step edges of the SiC substrate with the 3-bilayer-high steps due to the polytype difference between 2H-AlN and 6H-SiC. At micro-scale observation, the

Table 5.3: Critical thickness of 2H-AlN layer on 6H-SiC (0001) substrate.

Model	Force balance	Critical thickness [nm]
Matthews-Blakeslee	F_ϵ=F_l	3.5
Fischer	F_ϵ=F_l (with dislocation interaction)	21
Fox-Jesser	F_ϵ=F_l+F_f	840 (U = 2.392 eV)
People-Bean [33]	-	240
Experiment	-	∼900

SMBs consisted of zigzag structures with $(\bar{2}110)$ and $(11\bar{2}0)$ planar defects. We found that the $(\bar{2}110)$ SMBs had the displacement vectors of $\mathbf{R}=1/2[01\bar{1}1]$ with 2-nm-wide strain by high-resolution TEM images.

In the AlN layer on 6H-SiC (0001) substrate with 3-bilayer-high steps, TD rows were generated at the step edges of the SiC substrate. The TD rows, which consist of the many U-shaped TD pairs, are caused by misfit dislocations due to the lattice mismatch (1%). We expect that the TDD in the AlN epilayers is further reduced by controlling the initial growth mode.

In next chapter, the optical properties of the AlN layer coherently grown on 6H-SiC (0001) are investigated by CL and photoluminescence (PL).

References

[1] T. G. Andersson, Z. G. Chen, V. D. Kulakovski, A. Uddin, and J. T. Vallin, Appl. Phys. Lett. **51**, 752 (1987).

[2] V. Potin, P. Ruterana, and G. Nouet, J. Appl. Phys. **82**, 2176 (1997).

[3] P. Kandaswamy, C. Bougerol, D. Jalabert, P. Ruterana, and E. Monroy, J. Appl. Phys. **106**, 013526 (2009).

[4] C. Drum, Philos. Mag. **11**, 313 (1965).

[5] J. Northrup, Appl. Phys. Lett. **72**, 2316 (1998).

[6] J. Northrup, Appl. Phys. Lett. **86**, 071901 (2005).

[7] D. Zakharov, Z. Weber, B. Wagner, Z. Reitmeier, E. Preble, and R. Davis, Phys. Rev. B **71**, 235334 (2005).

[8] J. Bai, X. Huang, M. Dudley, B. Wagner, R. Davis, L. Wu, E. Sutter, Y. Zhu, and B. Skromme, J. Appl. Phys. **98**, 063510 (2005).

[9] S. Tanaka, R. S. Kern, and R. F. Davis, Appl. Phys. Lett. **66**, 37 (1995).

[10] B. N. Sverdlov, G. A. Martin, H. Morkoc, and D. J. Smith, Appl. Phys. Lett. **67**, 2063 (1995).

[11] G. Williamson and G. Hall, Acta Matel. **1**, 22 (1953).

[12] C. G. Dunn and E. F. Koch, Acta Matel. **5**, 548 (1957).

[13] J. E. Ayers, J. Cryst. Growth **135**, 71 (1994).

[14] R. Chierchia, T. Bottcher, H. Heinke, S. Einfeldt, S. Figge, and D. Hommel, J. Appl. Phys. **93**, 8918 (2003).

[15] T. Metzger, R. Hopler, E. Born, O. Ambacher, M. Stutzmann, R. Stommer, M. Schuster, H. Gobel, S. Chrestiansen, M. Alberecht, and H. P. Strunk, Philos. Mag. **77**, 1013 (1998).

[16] T. Bottcher, S. Einfeldt, S. Figge, R. Chierchia, H. Heinke, D. Hommel, and J. S. Speck, Appl. Phys. Lett. **78**, 1976 (2001).

[17] H. Wang, J. Zhang, C. Chen, Q. Fareed, J. Yang, and M. Khan, Appl. Phys. Lett. **81**, 604 (2002).

[18] V. Srikant, J. S. Speck, and D. R. Clarke, J. Appl. Phys. **82**, 4286 (1997).

[19] Y. J. Sun, O. Brandt, T. Y. Liu, A. Trampert, K. H. Ploog, J. Blasing, and A. Krost, Appl. Phys. Lett. **81**, 4928 (2002).

[20] R. Ishii, A. Kaneta, M. Funato, and Y. Kawakami, Phys. Rev. B , (submitted).

[21] P. F. Fewster, Thin Solid Films **319**, 1 (1998).

[22] H. Harima, J. Phys. Condens. Matter **14**, R967 (2002).

[23] J. M. Wagner and F. Bechstedt, Appl. Phys. Lett. **77**, 346 (2000).

[24] J. W. Matthews and A. E. Blakeslee, J. Cryst. Growth **27**, 118 (1974).

[25] A. Fischer, H. Kuhne, and H. Richter, Phys. Rev. Lett. **73**, 2712 (1994).

[26] G. L. Price, Phys. Rev. Lett. **66**, 469 (1991).

[27] B. A. Fox and W. A. Jesser, J. Appl. Phys. **68**, 2801 (1990).

[28] D. Gerlich, S. L. Dole, and G. A. Slack, J. Phys. Chem. Solids **47**, 437 (1986).

[29] P. Astie, J. J. Couderc, P. Chomel, D. Quelard, and M. Duseaux, phys. stat. sol. (b) **96**, 225 (1986).

[30] Q. Duo and A. Yoshida, Jpn. J. Appl. Phys. **33**, 2453 (1994).

[31] P. Cantu, F. Wu, P. Waltereit, S. Keller, A. E. Romanov, U. K. Mishra, S. P. DenBaars, and J. S. Speck, Appl. Phys. Lett. **83**, 674 (2003).

[32] P. Cantu, F. Wu, P. Waltereit, S. Keller, A. E. Romanov, S. P. DenBaars, and J. S. Speck, J. Appl. Phys. **97**, 103534 (2005).

[33] R. People and J. C. Bean, Appl. Phys. Lett. **47**, 322 (1985).

Chapter 6

Optical Properties of AlN Epilayers on SiC

6.1 Introduction

As critical issues for the high efficiency optoelectronic devices, there are threading dislocations (TDs) and impurities. TDs become the nonradiative recombination centers (NRCs) and decrease the peak intensity in the optical measurements. The high concentrations of impurities, such as Si and O, originates a strong violet luminescence (VL), which is detrimental to optoelectronic devices using AlN.

Presently, there are few reports on the optical property of AlN grown by molecular-beam epitaxy (MBE) with threading dislocation density (TDD) less than 10^9 cm^{-2}. We achieved low TDD of 4×10^8 cm^{-2} (screw-type TDD: under 10^6 cm^{-2}) and impurity concentrations less than 1×10^{18} cm^{-2} in the MBE growth of AlN (Section 4.5 and Section 4.7). In this chapter, the property of the fundamental optical transitions for this high-quality AlN layer is investigated. The optical properties of AlN are studied by cathodoluminescence (CL) and photoluminescence (PL) spectroscopy.

6.2 Violet-Band Cathodeluminescence of AlN Epilayers on SiC

6.2.1 Experimental procedures

We prepared three kinds (samples A-C) of 300-nm-thick AlN layers on 6H-SiC (0001) with different crystalline quality. The AlN was grown at 650°C with slightly Al-rich condition. The growth condition and crystalline quality of the AlN layers are listed in Table 6.1. In addition, for sample D, a 300-nm-thick AlN layer was grown on 6H-SiC (0001) at high temperature (850°C) after the 50-nm-thick AlN layer was grown at 650°C in the same condition as sample C. For sample E, a N-polar 200-nm-thick AlN layer was grown on 6H-SiC $(000\bar{1})$. All the samples had no doping and Al droplets on the surface after growth. The detail of the growth condition was described in Section 4.7.

Table 6.1: Growth conditions and intensity ratios of deep CL bands at 3.93 and 4.37 eV to NBE emission of AlN layers on 6H-SiC {0001} (samples A-E).

Sample	TDD [cm^{-2}]	Growth temperature [°C]	Polarity	$I_{3.93}/I_{NBE}$	$I_{4.37}/I_{NBE}$
A	2×10^{10}	600	Al	0.98	0.88
B	2×10^{9}	600	Al	0.49	0.61
C	4×10^{8}	650	Al	0.31	0.40
D	1×10^{9}	850	Al	0.32	0.48
E	2×10^{9}	850	N	1.93	1.56

6.2.2 Deep emission band in AlN epilayers

Crystalline-quality dependence

Wide-range CL measurements were projected at 5.0 kV with the electron-beam current density of 1.1 nA. The 300 K CL spectra of the 300-nm-thick AlN layers with the different crystalline quality (samples A-C) are shown in Fig. 6.1 (a). The series of CL spectra was normalized to the near-band-edge (NBE) peak intensity. All the sample exhibited a NBE excitonic emission peaks around 6.2 eV, which is larger than those of bulk AlN (6.0 eV) due to the biaxial strain (Section 5.4) [1].

The deep emission bands were observed at 4.37 and 3.93 eV. These VLs have been invoked to as donor-acceptor pair (DAP) recombinations involving a shallow donor and a V_{Al} deep acceptor, which is enhanced by the presence of impurities such as Si and O [2, 3]. The bands at 4.37 and 3.93 eV are assigned to originate from V_{Al} and V_{Al}-O complexes, respectively [4]. Accordingly to Nam *et al.*, the electron energy of the V_{Al}^{3-} level is approximately 0.5 eV higher than that of the $(V_{Al}\text{-complex})^{2-}$ level [5]. The band at 4.37 and 3.93 eV might be assigned as being due to the emission associated with $(V_{Al}\text{-complex})^{2-}$-O and V_{Al}^{3-}-O, respectively. Sample A has the highest intensity of the CL peak at 4.37 eV, suggesting that V_{Al} concentration may increase with TDD. We achieved the reduction of VL-peak intensities by half of the NBE peak for the high-quality AlN layer (sample C).

Growth-temperature and polarity dependence

The 300 K CL spectra of the around-300-nm-thick AlN layers (samples B, D, and E) are shown in Fig. 6.1 (b). Like the samples A-C, the deep emission bands were observed at 4.37 and 3.93 eV. In comparison with sample B (650°C growth), the VL intensity of sample D (850°C growth) is reduced, suggesting that V_{Al} concentration may decrease with increasing growth temperature. There were no emission associated with prismatic stacking faults (PSFs) [6]. Sample E (N-polar growth) has the highest VL-peak intensities (Table 6.1). This is because the high concentrations of O atoms, as discussed in Section 4.7. For N-polar AlN growth, further reduction of the impurity concentrations as well as the TDD are required.

6.2.3 Low-temperature measurement of AlN epilayer

The 100 K CL spectra of the high-quality AlN layer on 6H-SiC (0001) (sample C) are shown in Fig. 6.2. The deep emission bands were observed at 4.37 and 3.54 eV. Intensity ratios ($I_{\text{deep}}/I_{\text{NBE}}$) of deep CL band at 4.37 and 3.93 eV to NBE emission of the AlN layers were 1.04 and 9.45, respectively. The peak intensity at 3.54 eV increased more rapidly than the NBE peak, indicating that this peak relates to the impurities. We speculate that this peak position depicts a blue shift from 3.54 eV (100 K) to 3.93 eV (300 K) with increasing temperature.

High-resolution NBE CL spectra of sample C are shown in Fig. 6.3 (a). No thermal

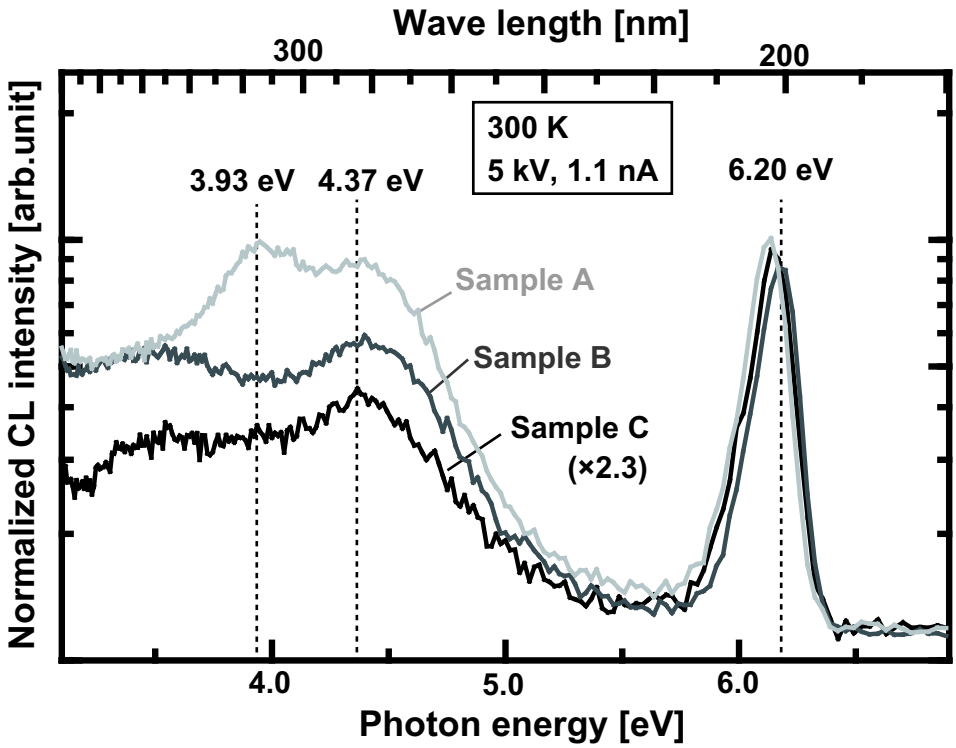

(a) CL spectra of AlN with different TDD

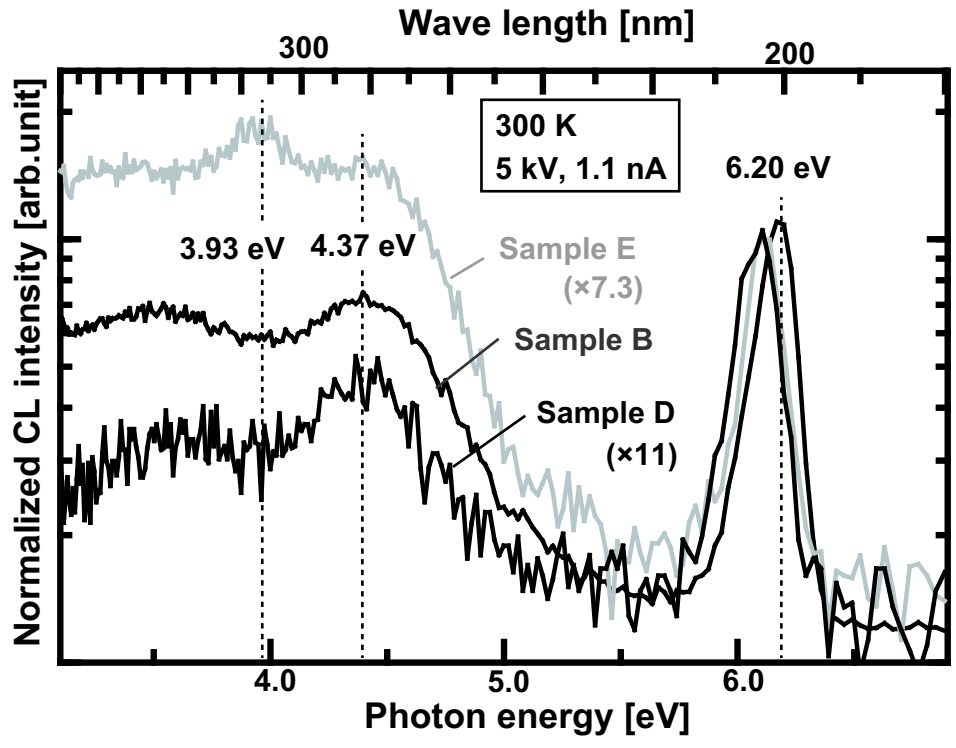

(b) CL spectra of AlN in different growth conditions

Figure 6.1: Wide-range 300 K CL spectra of around-300-nm-thick AlN layer grown on 6H-SiC (0001) (Samples A-E). Series of CL spectra was normalized to NBE peak intensity. (a) CL spectra of AlN layers with different TDD (samples A-C) and (b) CL spectra of AlN layers with different growth conditions, such as growth temperature and polarity (sample B, D, and E).

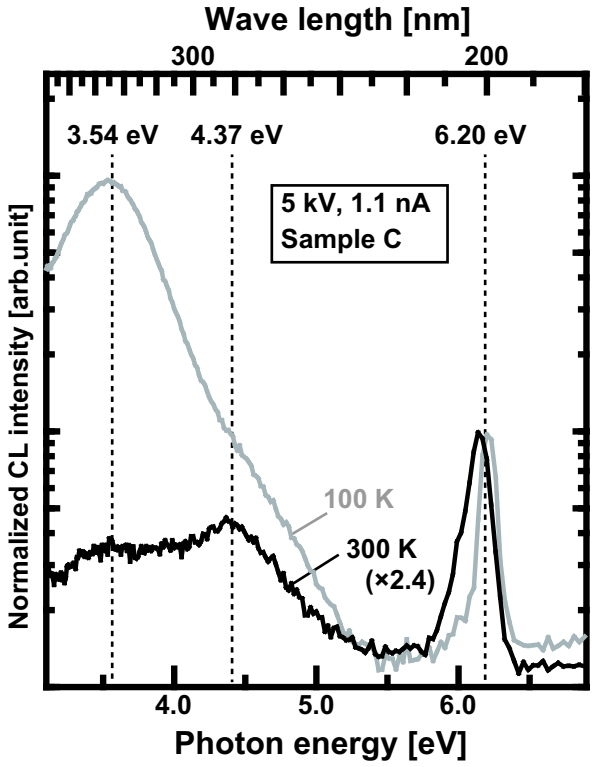

Figure 6.2: Wide-range CL spectra of 300-nm-thick AlN layer grown on 6H-SiC {0001} (Sample C). Series of CL spectra was normalized to NBE peak intensity. CL measurements were carried out at 300 and 100 K.

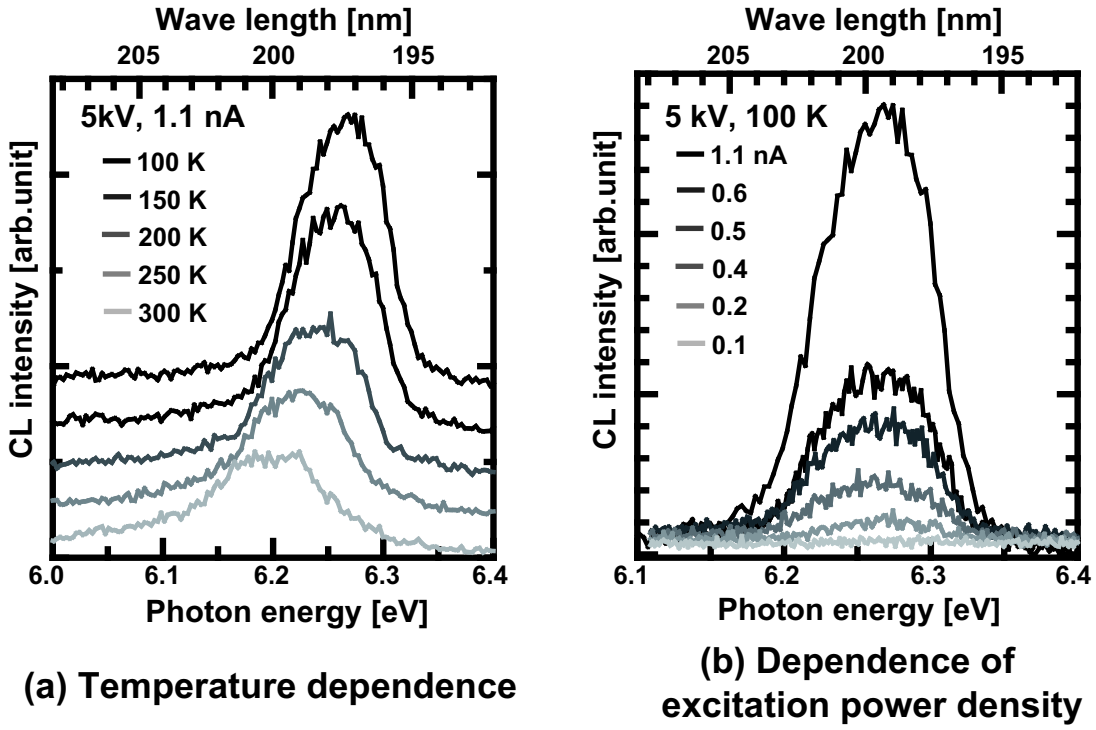

Figure 6.3: Dependence of (a) temperature and (b) excitation power density (100 K) of high-quality AlN layer on 6H-SiC (0001) (sample C).

quenching of peaks was observed above 100 K. We confirmed that the peak position shifted with the measurement temperature from 6.20 eV (300 K) to 6.27 eV (100 K). These peak positions may include an instrumental error (under 0.05 eV) because of no wavelength calibration, unlike a PL measurement. The dependence of the excitation power density on the high-resolution NBE CL spectra at 100 K is shown in Fig. 6.3 (b). No shift of the NBE emission peak was observed in more than one order of magnitude variation of the excitation power density.

6.3 Near-Band-Edge Photoluminescence of AlN Coherently Grown on SiC

6.3.1 Peak assignment of low-temperature PL spectra

A PL spectrum of the 300-nm-thick AlN layer coherently grown on 6H-SiC (0001) (sample C in Section 6.2) was measured at 8.8 K (Fig. 6.4). A NBE peak of the AlN layer largely shifts to the high-energy side due to the biaxial strain. We observed five peaks with positions given in Table 6.2. To assign these peaks, the spectra were evaluated for excitation densities varied between 40 and 670 kW/cm^{-2} (Fig. 6.5). At the lowest excitation-power density, the spectrum is dominated by the PL line (II) at 6.236 eV, which is attributed to the radiative recombination of excitons bound to neutral donors (D^0X). A second emission line (I) at the higher energy side (6.249 eV) is clearly resolved, which is attributed to free A-exciton transition (FX_A). The separation between the D^0X and FX_A peaks is 13 meV, corresponding to the reported values [7–9]. At the lowest excitation energy, the FWHM values of the D^0X and FX_A lines are 2.7 and 7.1 meV, respectively, suggesting that the AlN layer has a good film quality.

A PL line (III) has not been reported. To assign the PL line (III), the PL intensity of the FX_A line as a function of excitation-power density was investigated (Fig. 6.6 (a)). With the excitation-power density, the FX_A line almost linearly grows. The dependence of the FX_A intensity (I_{FX}) on the excitation-power density (I_P) gives $I_{FX} \propto I_P^{1.2}$. The PL intensities of the D^0X line and the line (III) as a function of excitation-power density are shown in Fig. 6.6 (b). The dependence of the PL intensities of the D^0X line and the line (III) on the excitation-power density gives $I_{DX} \propto I_P^{1.2}$ and $I_{\mathrm{III}} \propto I_P^{0.7}$, respectively. We consider that the PL line (III) is attributed to the radiative recombination of excitons bound to deep neutral donors (D_2^0X) because of the exponent of under 1. To confirm this, we need further investigation.

PL lines at 6.138 and 6.020 eV correspond to longitudinal optical (LO) phonon replicas of the $FX_{A,\mathrm{n=1}}$ with a phonon energy of about 110 meV [10]. The LO phonon replica of the D_1^0X probably is masked by the more intense luminescence of the LO phonon replica of the $FX_{A,\mathrm{n=1}}$. A $FX_{A,\mathrm{n=2}}$ peak was reported at the higher energy side from the $FX_{A,\mathrm{n=1}}$ peak to around 40 meV [11], but was unclearly observed in this sample because it is too close to the peak of the laser (6.424 eV).

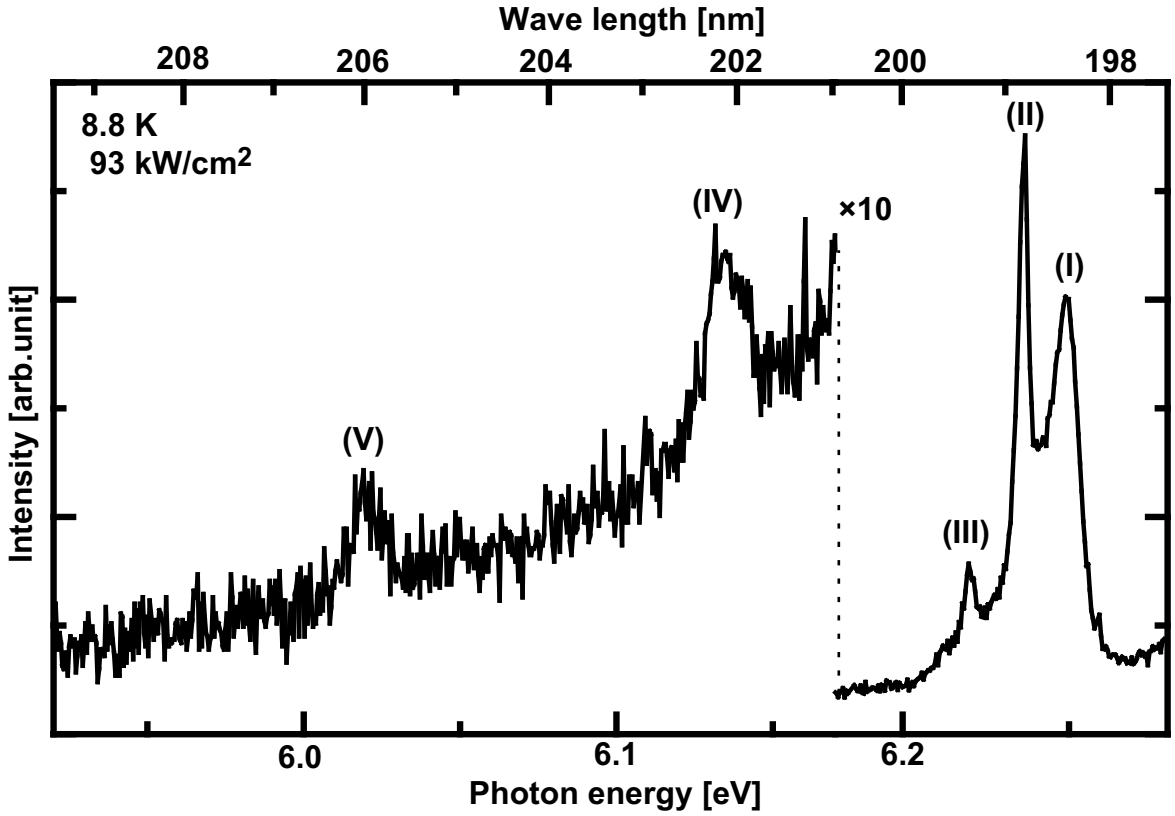

Figure 6.4: NBE PL spectrum of AlN layer coherently grown on 6H-SiC (0001) (sample C in Section 4.7). Measurement was carried out at 8.8 K and 93 kW/ cm^2.

Table 6.2: Energy positions and FWHM values of PL peaks for AlN layer on 6H-SiC (0001) (sample C in Section 4.7). Measurement was carried out at 8.8 K and 40 kW/cm^2.

Peak	Energy [eV]	FWHM [meV]	Energy spacing from $FX_{A,n=1}$ [meV]	Identification
(I)	6.249	7.1	0	$FX_{A,n=1}$
(II)	6.236	2.7	13	D_1^0X
(III)	6.220	4.2	29	D_2^0X?
(IV)	6.138	13.3	111	$FX_{A,n=1}$-LO (+ D_1^0X-LO?)
(V)	6.020	-	229	$FX_{A,n=1}$-2LO (+ D_1^0X-2LO?)

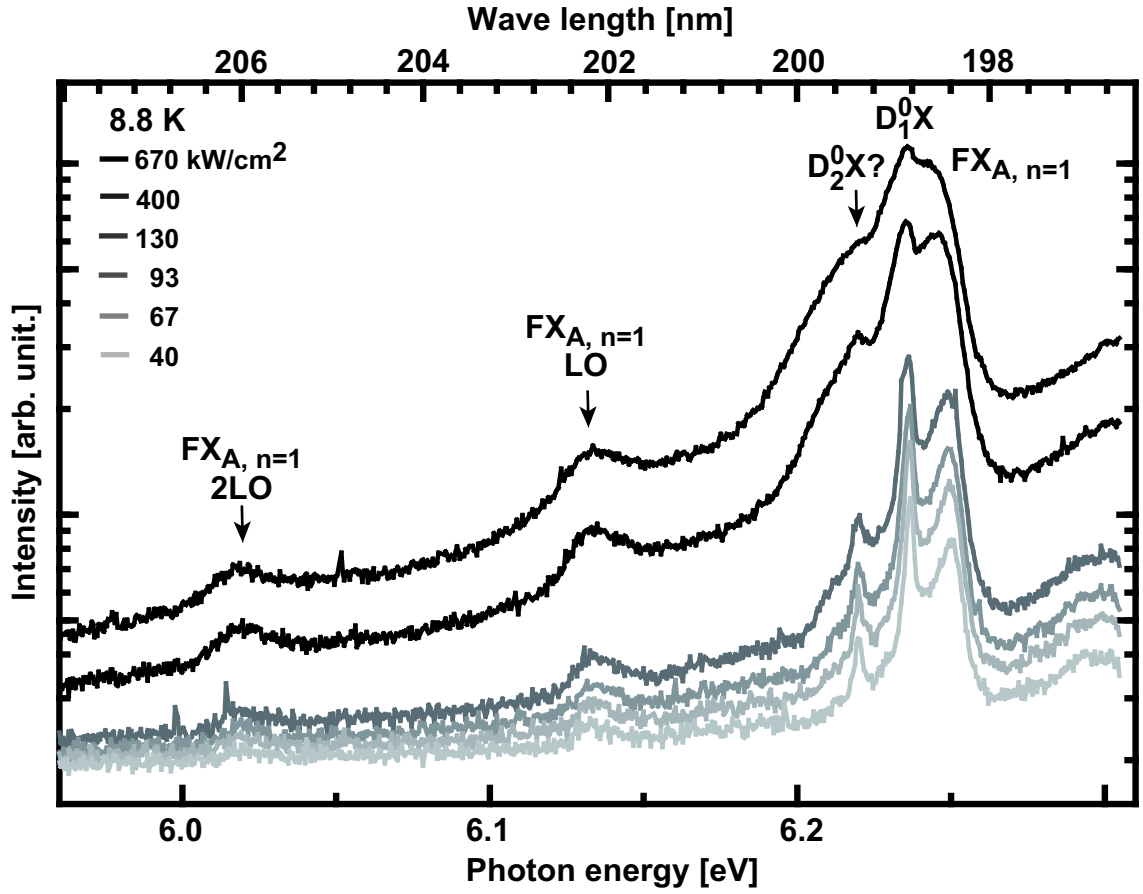

Figure 6.5: NBE PL spectra of AlN layer coherently grown on 6H-SiC (0001) at 8.8 K as function of excitation density.

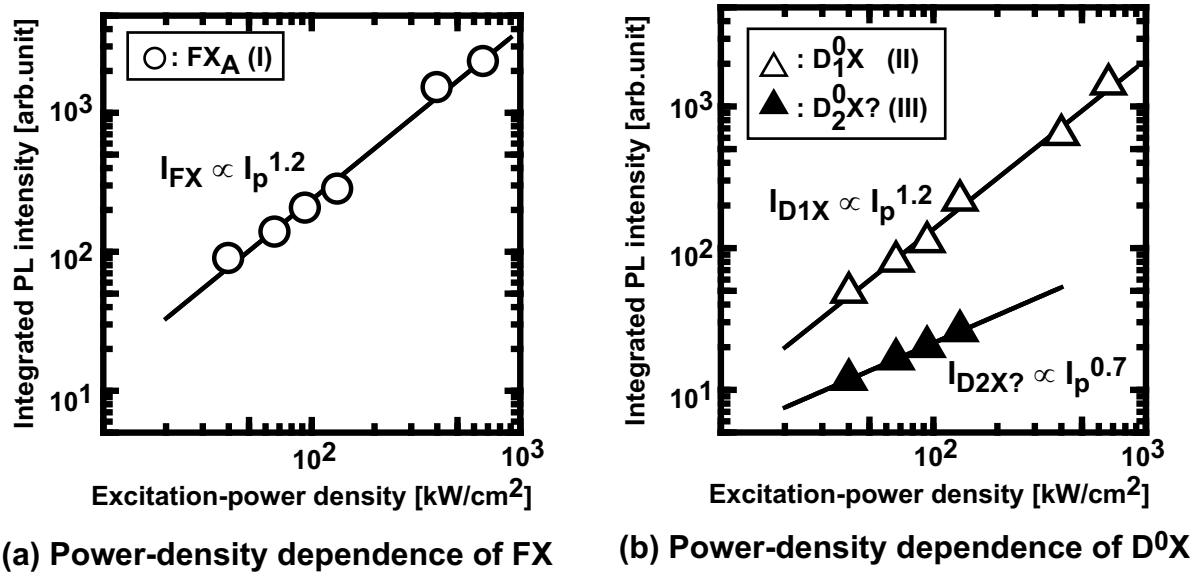

Figure 6.6: Variation of (a) free-exciton and (b) donor-bound-exciton photoluminescence intensity with excitation-power density at 8.8 K.

6.3.2 Temperature dependence of PL spectra

The temperature-dependent band-edge PL emission spectra for the AlN epilayer (sample C) is shown in Fig. 6.7. The D^0X peaks showed faster thermal quenching than the FX_A peaks. This is because the donor-bound excitons dissociate at higher temperatures into FX_A and neutral donors D^0, ($D^0X \rightarrow FX + D^0$). The band-gap energy decreases with increasing temperature (Fig. 6.8 (a)) because of the expansion of the lattice. The temperature dependence can be described with the following equation assuming Bose-Einstein statics [12],

$$E_g(T) = E_g(0) - \frac{2B}{\exp(\Theta/\mathrm{T}) - 1} \tag{6.1}$$

where $E_g(0)$ is the band gap of AlN at 0 K. At B = 150 meV, Θ was 470 K, closely corresponding to the reported values [13, 14]. Although the NBE-peak position largely shifted to the high energy side ($E_g(0)$=6.245 eV), we obtained the Θ corresponding to the energy maximum of the lower energy group of LO phonon branches near the Brillouin zone edge being 350-640 K [15]. The separation between the LO and $FX_{A,\mathrm{n}=1}$ peaks keeps around 110 meV independently of the temperature, indicating that the LO phonon replica results from the $FX_{A,\mathrm{n}=1}$.

The Arrhenius plot of the integrated PL intensity of the FX_A transition line is shown in Fig. 6.8 (b). The activation energy was fitted using the equation below [16]:

$$I(T) = \frac{I(0)}{1 + C\exp(-E_a/kT)} \tag{6.2}$$

where $I(T)$ and $I(0)$ are the PL intensities at a finite temperature T and 0 K, respectively, E_a is the activation energy. The E_a was estimated to be 80 meV. This corresponds to the free exciton binding energy E_x in AlN, indicating dissociation of the free exciton [17].

The energy gap at 10 K is 6.245 eV + 0.080 eV = 6.325 eV, which is about 0.2 eV larger than the bulk AlN (6.11 eV at 10 K) due to the biaxial strain. The ratio of the integrated peak intensity between 290 and 8.8 K was high, 17 % [18, 19]. The constant integrated-PL intensity was maintained until 100K, suggesting that the AlN layer has the good quality film.

6.3.3 Discussion

The AlN layer coherently grown on the SiC substrate has a biaxial strain, as described in Section 5.4. The free exciton transitions are given as [20]

$$E_g(\epsilon_{zz}) = E_g(0) + ((a - D_1) - \frac{C_{33}}{C_{13}}(a - D_2))\epsilon_{zz} \tag{6.3}$$

where E_g is the strain-dependent energy gap, a, D_1, and D_2 are the deformation potential energies, C_{jk} (j, k = 1-3) is the elastic constants. We used $a - D_1$ = -6.9 eV, $a - D_2$ = -15.2 eV, C_{13} = 95 GPa, C_{13} = 402 GPa [21], C_0 = 4.982 Å, and $E_g(0)$ = 5.974 eV [22]. The c-axis lattice constant of the AlN layer was evaluated by x-ray diffraction (XRD).

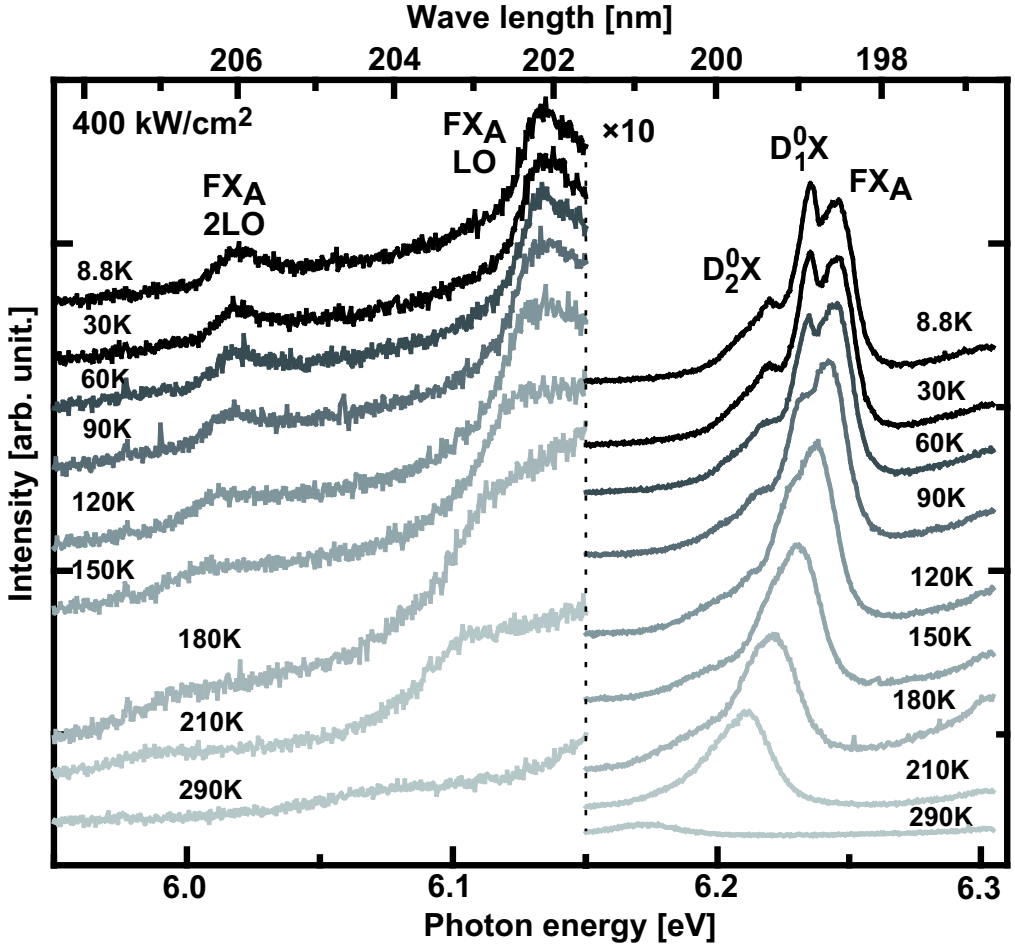

Figure 6.7: NBE PL spectra of AlN layer coherently grown on 6H-SiC (0001) at 400 kW/cm^2 as function of temperature.

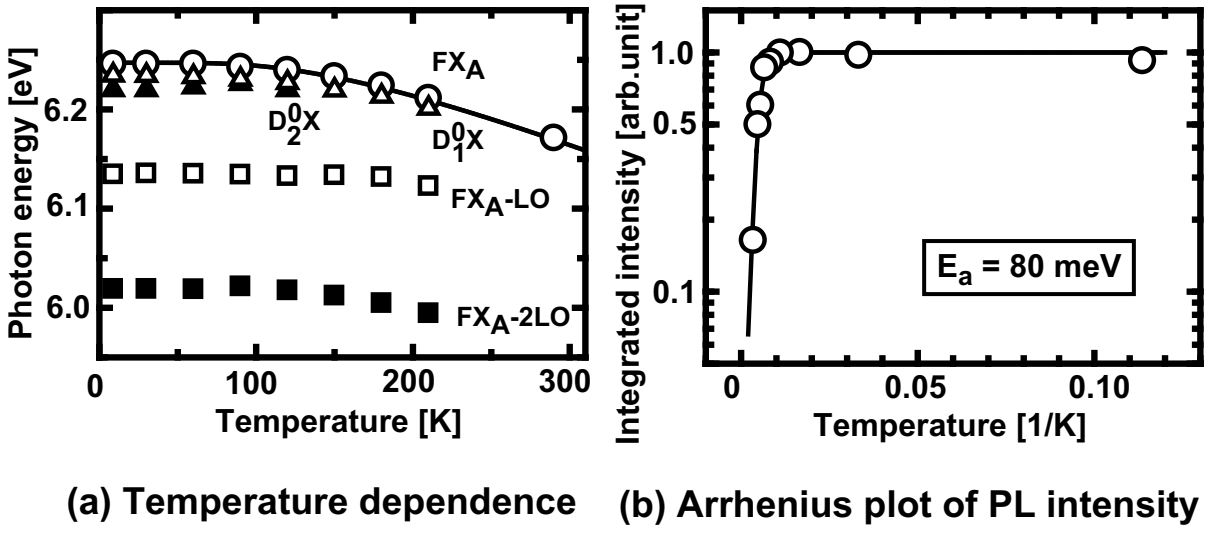

Figure 6.8: (a) PL peak energies as function of temperature. Solid line is fitting curve assuming Bose-Einstein statistics (b) Arrhenius plot of PL intensity for AlN layer on 6H-SiC (0001). Solid line is fitting curve using Eq. (6.2).

The lattice parameters and energy positions at 300 K PL spectra are given in Table 6.3. Using Eq. (6.3), strain dependence of free-exciton resonance energies is shown in Fig. 6.9. The calculated energy gap of the AlN layer coherently grown on SiC (sample C) becomes 6.195 eV, which is fairly close to the energy gap (6.173 eV) obtained from the PL measurement. The difference is caused by the value of $E_g(0)$ as well as the unclear deformation-potential parameters. Because Rossbach *et al.* measured and fitted the energy gap using absorbing spectrum, there is the difference of around thermal energy ($\sim$ 26 meV) for the $E_g(0)$ [22].

6.4 Summary

We confirmed that the AlN layers with low TDDs reduced the intensity of the VLs. In the AlN layer coherently grown on 6H-SiC (0001), the peak energy of NBE emission was 6.16 eV at 300 K due to the biaxial tensile strain. A donor bound excion peak was clearly separated from free A-exciton for the PL measurement at 10 K due to the good film quality. At the lowest excitation energy, the FWHM values of the D^0X and $X_{A,\mathrm{n}=1}$ lines were 2.7 and 7.1 meV, respectively.

References

[1] T. Onuma, T. Shibata, K. Kosaka, K. Asai, S. Sumiya, M. Tanaka, T. Sota, A. Uedono, and S. F. Chichibu, J. Appl. Phys. **105**, 023529 (2009).

[2] E. Monroy, J. Zenneck, G. Cherkashinin, O. Ambacher, and M. Hermann, Appl. Phys. Lett. **88**, 071906 (2006).

[3] G. A. Slack, L. J. Schowalter, D. Morelli, and J. A. Freitas, J. Cryst. Growth **246**, 287 (2002).

[4] T. Koyama, M. Sugawara, T. Hoshi, A. Uedono, J. K. Kaeding, R. Sharma, S. Nakamura, and S. F. Chichibu, Appl. Phys. Lett. **90**, 241914 (2007).

[5] K. M. Nam, M. L. Nakarmi, J. Y. Lin, and H. X. Jiang, Appl. Phys. Lett. **86**, 222108 (2005).

[6] R. Liu, A. Bell, F. A. Ponce, C. Q. Chen, J. W. Yang, and M. A. Khan, Appl. Phys. Lett. **86**, 021908 (2005).

[7] E. Silveria, J. A. Frietas, M. Kneissl, D. W. Treat, N. M. Johnson, G. A. Slack, and L. J. Schowalter, Appl. Phys. Lett. **84**, 3501 (2004).

[8] J. Li, K. B. Nam, M. L. Nakarmi, J. Y. Lin, and H. X. Jiang, Appl. Phys. Lett. **81**, 3365 (2002).

Table 6.3: Lattice parameters, strain states, and energy positions obtained from PL at 300 K. Samples A-E are around-300-nm-thick AlN layers on 6H-SiC {0001} in Section 4.7.

Sample	*c*-axis lattice constant [Å]	Strain ϵ_{zz} [10^{-4}]	Energy position (X_A) [eV]
A	4.9979	34.1	6.089
B	5.0018	42.0	6.145
C	5.0050	48.4	6.173
D	5.0018	42.0	6.135

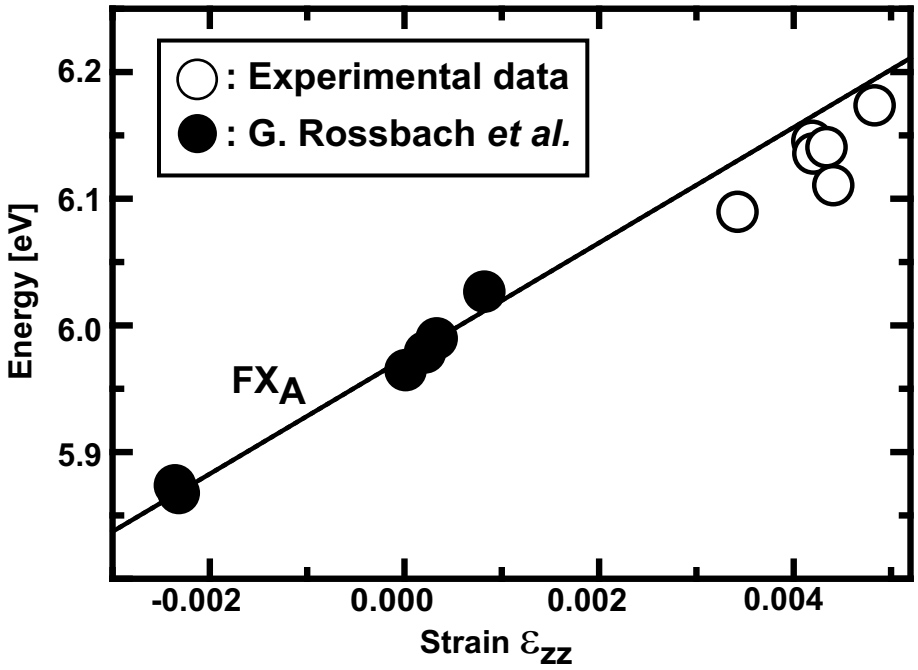

Figure 6.9: Energy positions of free exciton transitions at 300 K as function of ϵ_{zz} and correspondig calculations using Eq. (6.3).

[9] Y. Yamada, K. Choi, S. Shin, and H. Murotani, Appl. Phys. Lett. **92**, 131912 (2008).

[10] J. Shi, Phys. Rev. B **68**, 165335 (2003).

[11] R. A. Leute, M. Feneberg, R. Sauer, K. Thonke, S. B. Thapa, F. Scholz, Y. Taniyasu, and M. Kasu, Appl. Phys. Lett. **95**, 031903 (2009).

[12] L. Vina, S. Logothetidis, and M. Cardona, Phys. Rev. B **30**, 1979 (1984).

[13] M. Feneberg, R. A. Leute, B. Neuschl, K. Thonke, and M. Bickermann, Phys. Rev. B **82**, 075208 (2010).

[14] G. M. Prinz, A. Ladenburger, M. Schirra, M. Feneberg, K. Thonke, R. Sauer, Y. Taniyasu, M. Kasu, and T. Makimoto, J. Appl. Phys. **101**, 023511 (2007).

[15] J. Nipko and C. K. Loong, Phys. Rev. B **57**, 10550 (1998).

[16] M. Leroux, N. Grandjean, B. Beaumont, G. Nataf, F. Semond, J. Massies, and P. Gibart, J. Appl. Phys. **86**, 3721 (1999).

[17] H. B. Nam, J. Li, L. Nakarmi, J. Y. Lin, and H. X. Jiang, Appl. Phys. Lett. **82**, 1694 (2003).

[18] B. N. Pantha, N. Nepal, T. M. AlTahtamouni, M. L. Nakarmi, J. Li, J. Y. Lin, and H. X. Jiang, Appl. Phys. Lett. **91**, 121117 (2007).

[19] R. G. Banal, Dr. Thesis, Faculty of Engineering, Kyoto University, Kyoto, 2009.

[20] H. Y. Peng, M. D. McClukey, Y. M. Gupta, M. Kneissl, and N. M. Johnson, Phys. Rev. B **71**, 115207 (2005).

[21] R. Ishii, A. Kaneta, M. Funato, and Y. Kawakami, Phys. Rev. B , (submitted).

[22] G. Rossbach, M. Feneberg, M. Roppischer, C. Werner, N. Esser, C. Cobet, T. Meisch, K. Thonke, A. Dadgar, J. Blasing, A. Krost, and R. Goldhahn, Phys. Rev. B **83**, 195202 (2011).

Chapter 7

Conclusions

7.1 Conclusions

In this thesis, high-quality heteroepitaxial growth of AlN on SiC {0001} by molecular-beam epitaxy (MBE) was studied. Although a lattice mismatch between AlN and SiC is small (Δa ~0.9%), AlN grown on SiC had been reported to be highly defective. The author thought that it was due to heteropolytypic (2H/4H or 6H) and heterovalent (Ⅲ-V/IV-IV) structures. To overcome these problems, the author controlled the SiC-surface structure and initial growth process of AlN, and established high-quality AlN growth on SiC. Defect structures and optical properties in the AlN layers were also investigated in detail. The main conclusions in this study are summarized as follows.

Due to the polytype difference, AlN layers on SiC {0001} with 1-bilayer-high steps have planar defects, called stacking mismatch boundaries (SMBs). By controlling the step height of SiC to one-unit cell, the SMB can be eliminated. In Chapter 3, control of surface status of SiC {0001} was discussed. The author controlled the step heights of SiC {0001} by H_2-gas etching in a hot-wall chemical vapor deposition (CVD) reactor. Due to optimization of gas-etching conditions and off directions of the substrate, the 6-bilayer-high steps were achieved in the 30 % area of 2-inch 6H-SiC $(0001)_{\mathrm{Si}}$ wafers, and the 3-bilayer-high steps were uniformly achieved in whole area of them. 6H-SiC $(000\bar{1})_{\mathrm{C}}$ with 3-bilayer-high steps and 4H-SiC {0001} with 2-bilayer-high steps were uniformly obtained in the area of 50×50 μm^2. In addition, chemical conditions of SiC {0001} surfaces were studied. In terms of *in-situ* XPS measurements, it was revealed that residual oxygen on 4H- and 6H-SiC {0001} surfaces was removed by an *ex-situ* HF-chemical cleaning and *in-situ* Ga deposition-and-desorption process.

In Chapter 4, crystalline quality of AlN layers on SiC {0001} was improved especially by focusing on initial growth. First, growth conditions of Al-polar AlN on SiC $(0001)_{\mathrm{Si}}$ were optimized. AlN growth on SiC (0001) at low temperature (600–700°C) under a slightly Al-rich condition had a layer-by-layer growth mode from 10 to 30 sec after starting AlN growth. The full-width at half-maximum (FWHM) values of the (0002) and $(01\bar{1}2)$ ω-scan

diffraction peaks were 61 and 620 arcsec, respectively. In the AlN growth on 6H-SiC (0001) with 3- or 6-bilayer-high steps, the SMBs were not observed, but a high density of threading dislocations (TDs) was generated at the step edges of SiC before growth, called TD rows. Threading dislocation density (TDD) in the AlN layers was 2×10^{10} cm^{-2}. Furthermore, by the addition of a sacrificial oxidation process for SiC substrates with controlled step heights, stacking sequences of the topmost SiC surface were modified. In the AlN layer on 6H-SiC with the modified 3-bilayer-high steps, SMBs were generated at the step edges of SiC due to the change of stacking sequences of the topmost SiC surfaces. This is the direct evidence showing importance of SiC surface control.

For further reduction of TDD in AlN layers on 6H-SiC (0001), an initial growth control was studied. To reduce AlN/SiC interface energy, metallic-Ⅲ materials (Al or Ga) were deposited just before growth. The author found that 2ML-Ga pre-deposition just before AlN growth was very effective for early realization of the layer-by-layer growth mode (still not just after the growth). TDD in the AlN layer was decreased to 2×10^9 cm^{-2}. Next, a nitrogen-plasma stabilization process for 10 min before growth was focused on. In *in-situ* XPS measurements, it was found that slight active-nitrogen species reached the SiC surface with a closed plasma-cell shutter during the nitrogen-plasma stabilization process. The author considered that the unintentional nitrogen-plasma exposure was one of the causes for three-dimensional (3D) growth at a very initial stage of growth, and grew 300-nm-thick AlN just after nitrogen-plasma ignition, resulting in the layer-by-layer growth mode from the first atomic layer. The FWHM values of the (0002) and (01$\bar{1}$2) ω-scan diffraction peaks were 40 and 41 arcsec, respectively. TDD in the AlN layers was 4×10^8 cm^{-2}. Most TDs were generated at the step edges of SiC, and TDD generated on the terraces of SiC was 9×10^7 cm^{-2}. As far as the author knows, this is the best quality in heteroepitaxial growth of thin AlN on SiC. And, all impurity concentrations of Si, C, and O in the AlN layer were reduced to be under 1×10^{18} cm^{-3}.

N-polar AlN growth on SiC (000$\bar{1}$) was also investigated. The N-polar AlN had multinucleation growth, resulting in a rough surface. By decreasing supersaturation, i. e. nitrogen-plasma power, the smooth surface with a step-and-terrace structure was obtained: RMS roughness was 0.6 nm. TDD was reduced to 2×10^9 cm^{-2}.

In Chapter 5, extended-defect structures, such as SMBs and TD rows generated at the step edges of SiC, in AlN layers on SiC (0001) were investigated by transmission electron microscopy (TEM). The SMBs consisted of zigzag structures with ($\bar{2}$110) and (11$\bar{2}$0) planar defects. In particular, the ($\bar{2}$110) SMBs had the displacement vectors of $\mathbf{R}$=1/2[01$\bar{1}$1] with 2-nm-wide strained region. On the other hand, the TD rows consisted of many U-shaped dislocation loops, i. e. TD pairs with Burgers vectors of opposite directions. These TD pairs resulted from dislocations along the step edges of SiC. The author suggested that these dislocations were attributed to large accumulation of the strain energy in coalescence of AlN nuclei. A control of these dislocations is a key issue for further reduction of TDD.

AlN on the terraces of SiC was coherently grown. Critical thickness of AlN growth

on SiC was investigated by x-ray diffraction (XRD), laser Raman scattering spectroscopy, cathodoluminescence (CL), and TEM. The critical thickness of AlN growth on SiC is estimated to be 3.5 nm by Matthews-Blakeslee model. However, all experimental results showed that the critical thickness of AlN growth on SiC was over 700 nm. This abnormally-large critical thickness of AlN growth on SiC is attributed to low TDD, low growth temperature, and a layer-by-layer growth mode.

In Chapter 6, optical properties of AlN epilayers on SiC {0001} were characterized by CL and photoluminescence (PL). In the AlN layer coherently grown on 6H-SiC (0001), the peak energy of near-band-edge (NBE) emission was high (6.16 eV) at 300 K due to the biaxial strain, and well agree with theoretical estimation for coherent growth. A donor bound exciton (D^0X) peak was clearly separated from a free A-exciton (FX_A) peak for the PL measurement at 8.8 K. The small FWHM values of the D^0X and FX_A lines, which were 2.7 and 7.1 meV, respectively, were obtained due to the good crystalline quality. These results suggest the high-quality AlN layers in this study can be applicable for not only electronic devices but also optoelectronic devices.

7.2 Future work

Through this study, many aspects in AlN growth on SiC {0001} were revealed. However, several issues still remain and should be solved to improve performance of high-electron-mobility transistors (HEMTs) and deep-ultraviolet (UV) light-emitting diodes (LEDs). These issues and solutions are proposed as follows.

• Further reduction of TDD in AlN epilayers on SiC $(0001)_{Si}$:

In AlN growth on SiC (0001), TD rows generated at SiC-step edges are the most critical issues to achieve TDD less than 4×10^8 cm^{-2}. By eliminating the TD rows, TDD in the AlN layers will be reduced to 9×10^7 cm^{-2} (TDD on the SiC terrace).

One of the methods to eliminate the TD rows is a usage of SiC surface without steps. Powell *et al.* fabricated step-free mesa structures by homoepitaxial growth of SiC in a step-flow growth mode [1–3]. However, the step-free surface in the area over 100×100 μm^2 has not been achieved because screw-type TDs in the SiC epilayer cause spiral growth. Another method is to use a SiC (0001) substrate with smaller off angle ($\sim 0.1°$). The TDD in the AlN layer can be decreased because of the less density of the SiC-step edges. However, there is a limitation to reduce the off angle due to the residual crystal curvature of SiC bulk. Therefore, suppression of the TD row formation should be developed.

The TD rows are generated by coalescence of AlN nuclei at step edges of SiC due to the accumulation of the strain energy. If the AlN-nuclei coalescence at the step edges of SiC can be avoided, no TD rows would be generated. The author proposes growth-mode change during growth from a layer-by-layer-growth mode to a step-flow growth mode, as follows. First, for a 6H-SiC substrate with 6-bilayer-high steps, 6-bilayer-thick AlN layers are grown

on it in the layer-by-layer growth mode, as shown in Fig. 7.1 (a), because 2H-AlN growth from the first layer can avoid the generation of SMBs at the step edges of SiC (Section 4.3). After that, the growth mode is changed to the step-flow growth mode. The step-flow growth proceeds from the grown 6-bilayer-thick 2H-AlN layers, so that the AlN-nuclei coalescence at the step edges of SiC would be avoided (Fig. 7.1 (c)). The growth-mode change without growth interruption would be realized by migration enhanced epitaxy (MEE).

AlN layers on terraces of SiC has TDD of 9×10^7 cm^{-2}. The author anticipates that these TDs are caused by slight residual impurities on SiC surface and imperfection of its surface before growth. *In-situ* homoepitaxial growth of SiC and improvement of cleaning processes just before AlN growth is thought to be effective for further reduction of the TDD.

- **High-quality N-polar AlN growth on SiC $(000\bar{1})_C$:**

For AlGaN/GaN HEMTs, N-polar GaN films has higher potential than Ga-polar GaN films (Section 1.3.1). For templates of the N-polar GaN growth, the author grew N-polar AlN on SiC $(000\bar{1})$, achieving a step-flow growth mode and reduction of TDD by controlling supersaturation. However, the reduction of nitrogen-plasma power caused a slow growth rate, resulting in the high impurity concentration in the AlN layer. The MEE for N-polar AlN growth would be effective. Using MEE, Al-migration time on the surface would be increased, indicating that the growth mode can be changed from multinucleation growth to step-flow growth or layer-by-layer growth. The layer-by-layer growth mode is the most desirable to improve crystalline quality of N-polar AlN layers on SiC $(000\bar{1})$.

- **High-quality GaN growth:**

For the AlGaN/GaN HEMTs, high-quality GaN growth is necessary. As templates for GaN growth, high-quality AlN layers on SiC are thought to be suitable. The author tried to grow 300-nm-thick GaN on the 50-nm-thick AlN layer, realizing a smooth surface with a step-and-terrace structure. However, a high density of edge-type TDs ($\sim 10^{10}$ cm^{-2}) was generated in an initial growth stage of GaN due to the large lattice mismatch between GaN and AlN [1]. Then, AlGaN-graded growth (i. e., metamorphic growth with stepwise or linear changes) using a short-period super-lattice structure of AlN and GaN is thought to be necessary. The AlGaN-graded layer would be effective to annihilate the TDs at the AlN/GaN interface, like InGaAs-graded layers [4]. In addition, unlike the simultaneous supply, the alternate growth of AlN and GaN can control the Ga segregation in the AlGaN layer.

[1]The lattice mismatch is 3.5 % because 50-nm-thick AlN is coherently grown on SiC (Section 5.4).

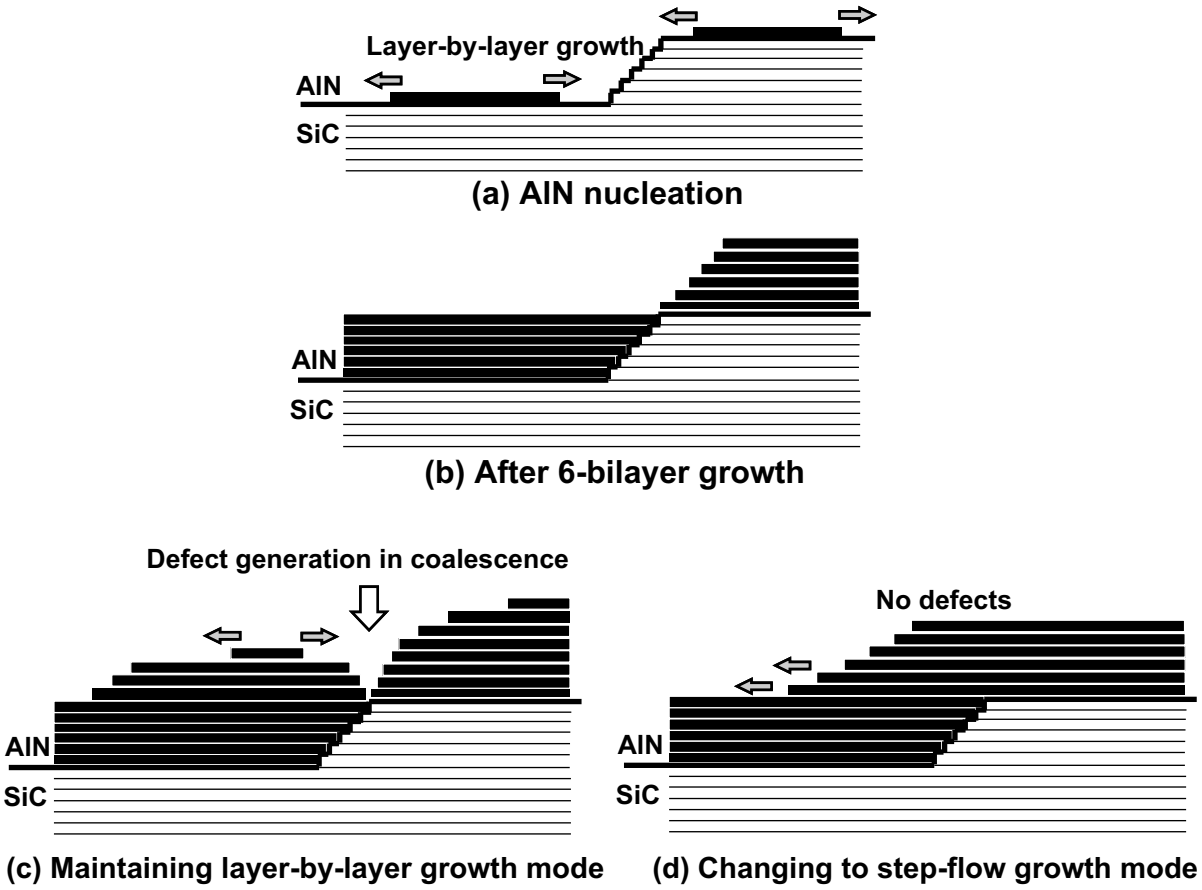

Figure 7.1: Model for eliminating TD rows in AlN growth on 6H-SiC (0001) with 6-bilayer-high steps. (a, b) AlN is grown in layer-by-layer growth mode until 6-bilayer heights. (c) Defects are generated at SiC-step edges in maintaining layer-by-layer growth mode. (d) No defects are generated in changing to step-flow growth mode after 6-bilayer growth.

References

[1] J. A. Powell, P. G. Neudeck, A. J. Trunek, G. M. Beheim, L. G. Matus, R. W. Hoffman, and L. J. Keys, Appl. Phys. Lett. **77**, 1449 (2000).

[2] Y. Chen, T. Kimoto, Y. Takeuchi, and H. Matsunami, J. Cryst. Growth **254**, 115 (2003).

[3] P. G. Neudeck, A. J. Trunek, D. J. Spry, J. A. Powell, H. Du, M. Skowronski, X. R. Huang, and M. Dudley, Chem. Vap. Deposition **12**, 531 (2006).

[4] R. Fischer, D. Neuman, H. Zabel, H. Morkoc, C. Choi, and N. Otsuka, Appl. Phys. Lett. **48**, 1223 (1986).

List of Publications

A. Full Length Papers and Letters

1. H. Okumura, M. Horita, T. Kimoto, and J. Suda
"Impact of Surface Step Heights of 6H-SiC (0001) Vicinal Substrates in Heteroepitaxial Growth of 2H-AlN,"
Appl. Surf. Sci. **254**, 7858 (2008).

2. H. Okumura, M. Horita, T. Kimoto, and J. Suda
"Observation of Novel Defect Structure in 2H-AlN Grown on 6H-SiC (0001) Substrates by Molecular-beam Epitaxy,"
Phys. Status Solidi (a) **206**, 1187 (2009).

3. H. Okumura, T. Kimoto, and J. Suda
"Reduction of Threading Dislocation Density in 2H-AlN Grown on 6H-SiC (0001) by Minimizing Unintentional Active-Nitrogen Exposure before Growth,"
Appl. Phys. Exp. **4**, 025502 (2011).

4. H. Okumura, T. Kimoto, and J. Suda
"Growth of Nitrogen-Polar 2H-AlN on Step-Height-Controlled 6H-SiC $(000\bar{1})$ Substrate by Molecular-Beam Epitaxy,"
to be published Jpn. J. Appl. Phys (2012).

5. H. Okumura, T. Kimoto, and J. Suda
"Displacement Vector of Stacking Mismatch Boundaries in 2H-AlN Grown on 6H-SiC (0001),"
to be submitted to Phys. Rev. (b).

6. H. Okumura, T. Kimoto, and J. Suda
"Generation Mechanism of Threading Dislocations in 2H-AlN on 6H-SiC (0001) with 3-Bilayer-High Steps,"
to be submitted to J. Appl. Phys.

7. H. Okumura, T. Kimoto, and J. Suda
   "Step Height of 6H-SiC (0001) with Different Miscut Directions by High-Temperature Hydrogen-Gas Etching,"
   in preparation.

8. H. Okumura, T. Kimoto, and J. Suda
   "Critical thickness of AlN Growth on 6H-SiC (0001) by Molecular-Beam Epitaxy,"
   in preparation.

B. Proceedings of International Conferences

1. H. Okumura, T. Kimoto, and J. Suda
   "Enhancement of Initial Layer-by-Layer Growth and Reduction of Threading Dislocation Density by Optimized Ga Pre-Irradiation in Molecular-Beam Epitaxy of 2H-AlN on 6H-SiC (0001),"
   Phys. Status Solidi (c) **7**, 2094 (2010).
   (*Proc. Intern. Conf. on Nitride Semiconductor 2009*, Jeju, Korea, 2009.)

C. Related Publications

1. K. Akiyama, Y. Ishii, S. Abe, H. Murakami, Y. Kumagai, H. Okumura, T. Kimoto, J. Suda, and A. Koukitu
   "Gravimetric Monitoring of Thrermal Decomposition and Hydrogen Etching Rates of 6H-SiC (0001) Si Face,"
   Jpn. J. Appl. Phys. **48**, 095505 (2009).